Semiconductors, Vol. 36, No. 10, 2002, pp. 1073–1076. From Fizika i Tekhnika Poluprovodnikov, Vol. 36, No. 10, 2002, pp. 1153–1156.

ATOMIC STRUCTURE AND NONELECTRONIC PROPERTIES OF SEMICONDUCTORS

Thermodynamic Stability of Bulk and Epitaxial $Ge_{1-x}Sn_x$ Semiconductor Alloys[1]

V. G. Deĭbuk* and Yu. G. Korolyuk

Chernivtsi National University, Chernivtsi, 58012 Ukraine

** e-mail: vdei@chdu.cv.ua*

Submitted February 7, 2002; accepted for publication February 28, 2002

Abstract—The total energy for an unconstrained and biaxially confined model of $Ge_{1-x}Sn_x$ alloys was calculated using molecular-dynamics simulation. This made it possible to study the thermodynamic stability of both disordered and ordered phases of the semiconductor alloys. A remarkable suppression of the phase separation in $Ge_{1-x}Sn_x$ due to biaxial strain was found. © *2002 MAIK "Nauka/Interperiodica".*

1. INTRODUCTION

The search for optoelectronic direct-gap materials on the basis of Group IV semiconductors has been stimulated in the past years by new crystal-growing technologies such as molecular-beam epitaxy and laser crystallization. The research efforts follow several basic lines. One of them consists in growing metastable alloys with a diamond structure and fundamental energy gap at the Γ-point (for example, Ge–Sn and Si–Sn alloys) [1, 2]. Under equilibrium growing conditions, Ge and Sn, as a rule, are normally not soluble components; however, alloys on their basis can be obtained using nonequilibrium growing techniques. $Ge_{1-x}Sn_x$ ($x < 0.3$) metastable semiconductor alloys were synthesized using pulsed UV laser crystallization [3].

Soma *et al.* [4] studied the effect of stress on the phase diagrams of Ge–Sn and Si–Sn alloys. They predicted the enlargement of the stability region of the Ge–Sn solid solution under external pressure. A common feature of the alloy epitaxies is the strain due to lattice mismatch and different thermal expansion coefficients. The epitaxial layer of a binary alloy grown pseudomorphically on a substrate becomes highly strained. The strain and compositional fluctuations influence all types of properties of the alloys including the miscibility.

In this paper, we present a theoretical study of the thermodynamic properties of strained bulk as well as epitaxial Ge–Sn alloys. We investigate the influence of biaxial strain on the miscibility of these alloys using molecular-dynamics simulation.

While basic physical properties of semiconductor alloys can be obtained by first-principles self-consistent calculations, computational simulation using molecular dynamics (MD) is helpful for understanding the stability of semiconductor alloys [5].

[1] This article was submitted by the author in English.

2. MOLECULAR-DYNAMICS SIMULATION

For the calculation of thermodynamic stability using molecular dynamics, first we have to determine the potential model. Among many empirical model potentials, which have been suggested for tetrahedral semiconductors, the Tersoff three-particle potential turned out to be the most successful for investigating many properties of semiconductor compounds [6].

The interatomic potential interaction energy of two neighboring atoms i and j has the form

$$V_{ij} = f_C(r_{ij})[a_{ij} f_R(r_{ij}) + b_{ij} f_A(r_{ij})], \quad (1)$$

where

$$f_R(r) = A\exp(-\lambda r), \quad (2)$$

$$f_A(r) = -B\exp(-\mu r), \quad (3)$$

$$f_C(r) = \begin{cases} 1, & r < R, \\ \frac{1}{2} + \frac{1}{2}\cos\left[\frac{\pi}{2}\frac{(r-R)}{(S-R)}\right], & R < r < S, \\ 0, & r > S, \end{cases} \quad (4)$$

and b_{ij} is a many-body order parameter describing how the bond-formation energy is affected by the local atomic arrangement due to the presence of other neighboring atoms (the k-atoms). This many-body function of atomic positions i, j, and k has the following form:

$$b_{ij} = \chi_{ij}(1 + \beta^n \zeta_{ij}^n)^{-1/2n}, \quad (5)$$

where

$$\zeta_{ij} = \sum_{k(\neq i,\, j)} f_C(r_{ik}) g(\theta_{ijk}) \exp(\lambda_3^3 (r_{ij} - r_{ik})^3), \quad (6)$$

1063-7826/02/3610-1073$22.00

$$g(\theta) = 1 + \frac{c^2}{d^2} - \frac{c^2}{d^2 + (h - \cos\theta)^2}, \quad (7)$$

$$a_{ij} = (1 + \alpha^n \eta_{ij}^n)^{-1/2n}, \quad (8)$$

$$n_{ij} = \sum_{k(\neq i, j)} f_C(r_{ik}) \exp(\lambda_3^3 (r_{ij} - r_{ik})^3), \quad (9)$$

ζ_{ij} is the effective coordination number, and $g(\theta)$ is a function of the angle between r_{ij} and r_{ik}, which has been fitted to stabilize the tetrahedral structure.

The parameters for Ge were taken from [6], and for Sn, these were derived from a gray-tin cohesion energy adjustment, which was equal to 3.12 eV per atom [7] and presented in our previous article [8]. Simulation was performed for systems with $N = 216$ particles, the initial positions of which were taken at tetrahedral sites of a cell, which are formed by $3 \times 3 \times 3$ unit cells of the diamond type. The periodic boundary conditions were used. This method was based on solving the Newton equation set using the fast form of the Verlet algorithm [9], which, being self-starting, does not lead to the accumulation of roundoff errors. Simulation is started from an initial structure, in which two kinds of atoms are randomly placed in a diamond lattice. After the system passed to the equilibrium state with a time step $\Delta t = 0.15 \times 10^{-15}$ s, we calculated the pair distribution function $g(r)$ for Ge, Sn, and $Ge_{0.74}Sn_{0.26}$ at various temperatures [8]. When $Ge_{1-x}Sn_x$ substitutional solid solutions are formed, the first peak of the pair distribution function splits into three peaks corresponding to the Ge–Ge, Ge–Sn, and Sn–Sn bonds. As temperature increases, the pair distribution function peaks become somewhat broader and shift slightly, which means that the conservation of the tetrahedral crystal structure is retained. In addition, the coordination number corresponding to the number of nearest neighbors was controlled in the course of simulation. Such behavior of the system is confirmed by the total energy as a function of the temperature.

3. BULK SEMICONDUCTOR ALLOYS

The lattice constants of the reference random alloy ($x = 0.5$) and the four ordered structures Ge, α-Sn, ZB-GeSn (zinc blende), and RH-GeSe (rhombohedral) were determined from the condition of minimal total energy as a function of volume (Fig. 1). Thus, at 300 K, from our calculation for Ge $a = 5.659$ Å (experimental value 5.657 Å [7]); and for Sn, $a = 6.490$ Å (experimental value 6.489 Å [7]). To check the stability of the investigated structures against segregation of the two constituents, we compare the total energy of the equilibrium ZB-GeSn, RH-GeSn, and disordered GeSn with the arithmetical mean of the total energies of Ge and Sn. Figure 1 shows that the ordered phases are more stable than the disordered phase, $\Delta E^{(D)} > \Delta E^{(O)}$. The random alloys have two tendencies toward phase transformations simultaneously, i.e., a tendency toward decomposition and a tendency toward superstructure formation.

For the disordered (D) binary alloy $Ge_{1-x}Sn_x$, the Helmholz mixing free energy ΔF as a function of x and T at a fixed pressure is given by

$$\Delta F(x, T) = F_{GeSn}(x, T) - (1 - x)F_{Ge}(T) - xF_{Sn}(T). \quad (10)$$

Then, ΔF can be written as

$$\Delta F = \Delta E - T\Delta S, \quad (11)$$

where ΔE is the mixing energy and ΔS is the mixing entropy defined similarly to ΔF. Since the magnitude of $\Delta(PV)$ is small at the normal pressure of about 1 atmosphere, ΔE and the mixing enthalpy ΔH are interchangeable. The calculated mixing energy ΔE as a function of composition at $T = 0$ K is represented in

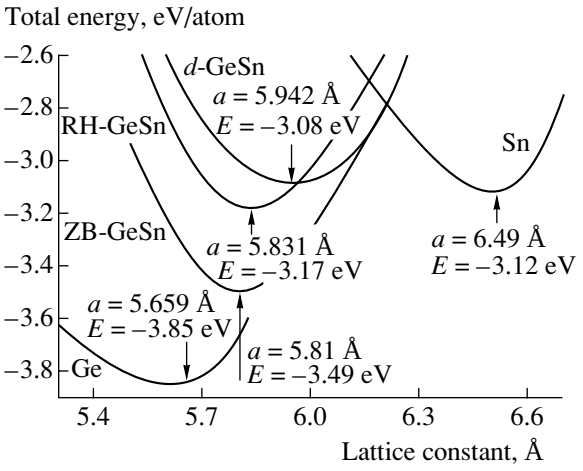

Fig. 1. Total energy of Ge, Sn, disordered (*d*-GeSn), rhombohedral (RH-GeSn) and zinc blende (ZB-GeSn) alloys at $x = 0.5$ as a function of volume.

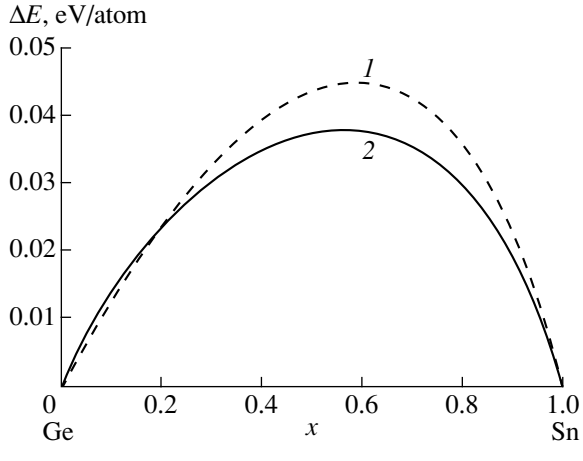

Fig. 2. The mixing energy ΔE as a function of composition x of $Ge_{1-x}Sn_x$ alloy at $T = 0$ K (curve *1* represents the pseudopotential calculation of Soma *et al.* [4] and curve *2* represents our calculation).

Fig. 2 in comparison with the pseudopotential calculations of Soma *et al.* [4]. The approximation $\Delta E = \Omega x(1-x)$ should introduce some error in the free energy calculation because our case extends beyond pair interactions. We obtain an interaction parameter of $\Omega_{Ge-Sn} = 11.86$ kcal/mol compared with the indirect calculated value from the experimental phase diagram $\Omega_{Ge-Sn} = 7.55$ kcal/mol [10] and the theoretical estimate $\Omega_{Ge-Sn} = 15.3$ kcal/mol [11]. The entropy of mixing is supposed to be equal to the configurational entropy in a regular-solution model, which is given by

$$\Delta S = -R[(1-x)\ln(1-x) + x\ln x]. \quad (12)$$

Figure 3 shows the mixing free energy of $Ge_{1-x}Sn_x$ as a function of x at four temperatures. These curves show that the alloys under consideration have a miscibility gap (MG). Below the critical temperature $T_C = 830$ K at $x_C = 0.62$, the excess free energy shows a common tangent line at two different x values, indicating the tendency for phase decomposition, i.e., the occurrence of a miscibility gap. Knowledge of the free energies allows the construction of a phase diagram. The T–x phase diagram for $Ge_{1-x}Sn_x$ is presented in Fig. 4. The binodal curve is the line in the (x, T) plane where the Ge- and Sn-rich disordered phases have equal chemical potentials μ. The spinodal line describes the limit of metastability of the disordered phase when $d^2F/dx^2 = d\mu/dx = 0$, with F being the free energy. For $T = 300$ K, the solubility limit of Sn(Ge) in Ge(Sn) is less than 2% (0%). The phase diagram also indicates that, in a wide range between spinodal and binodal curves, the random alloy may exist in a metastable phase. We find that the thermodynamically stable ground state corresponds to phase separation. We calculated the temperature limit of stability for ordered ZB and RH phases. The ordering temperatures are $T_O = 848$ K (for ZB-GeSn) and $T_O = 365$ K (for RH-GeSn).

At thermodynamic equilibrium, the system phase separates below T_C into Ge- and Sn-rich mixtures. If, however, phase separation is kinetically inhibited, metastable long-range ordering will persist below T_O.

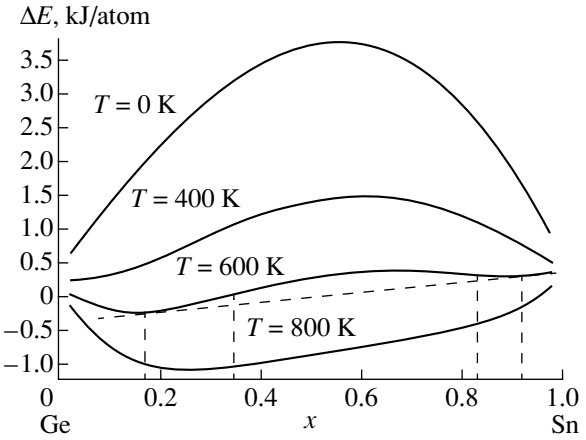

Fig. 3. The mixing free energy ΔF of $Ge_{1-x}Sn_x$ as a function of x at $T = 0$, 400, 600, and 800 K.

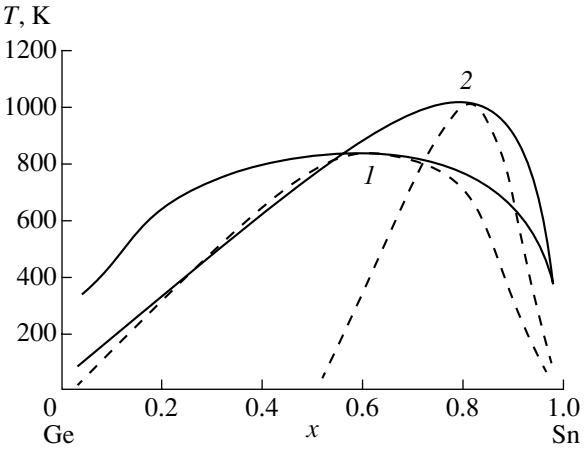

Fig. 4. T–x diagram for $Ge_{1-x}Sn_x$ alloy (*1*) without strain and (*2*) with biaxial strain $\varepsilon = 0.03$. Solid lines are binodal curves and dashed lines are spinodal curves.

4. EPITAXIAL SEMICONDUCTOR ALLOYS

We model a thin pseudomorphic epitaxial semiconductor alloy grown on a substrate (*s*) with a lattice constant a_s by setting the alloy lattice constant $a_\parallel$ parallel to the substrate equal to a_s and optimizing the MD calculated total energy through variation of the lattice constant $a_\perp$ in the direction perpendicular to the substrate. The excess free energy is decreased by the elastic energy due to build-up strain. Generally, the miscibility gap decreases. In the corresponding T–x diagram (Fig. 4), such a trend is indeed observed. For a biaxial strain of 3%, the critical temperature is about 1010 K at $x_C = 0.8$. The phase diagram becomes more asymmetric; simultaneously, the miscibility gap, as well as the region of spontaneous decomposition, reduce. One may indeed state that there is a tendency towards the suppression of phase separation in $Ge_{1-x}Sn_x$ due to elastic strain. This result explains why in $Ge_{1-x}Sn_x$ epilayers with an Sn content up to $x = 0.3$ evidence for phase separation has not been observed [3]. The enthalpy of formation ΔH of the epitaxial form of phase α is similar to that of the bulk form. Then, the substrate strain (*ss*) energy [12] is given by

$$\Delta E_{ss}^{(\alpha)} = H^{(E_p,\alpha)}[A_mB_n, a_\parallel = a_s] - H^{(\alpha)}[A_mB_n]. \quad (13)$$

Figure 5 shows our calculated enthalpies of the GeSn lattices matched to Ge. The effective enthalpy of formation of an epitaxial film (relative to lattice-matched products) can be written as

$$\delta H^{(E_p,\alpha)} = H^{(E_p,\alpha)}[A_mB_n, a_\parallel = a_s] - mH^{(\alpha)}[A, a_\parallel = a_s] - nH^{(\alpha)}[B, a_\parallel = a_s]. \quad (14)$$

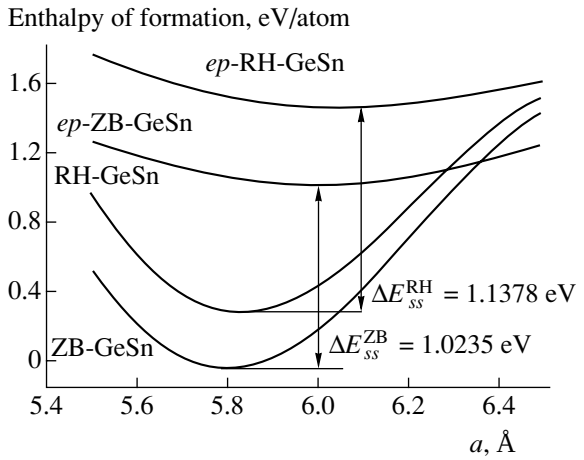

Fig. 5. The enthalpies of the formation of zinc-blende (ZB-) GeSn, rhombohedral (RH-) GeSn as a function of lattice constant a, and for epitaxially (*ep*-) confined (to a_{Ge} = 5.645 Å) ZB- and RH-GeSn.

Note that the stability of the ZB phase of GeSn is increased under epitaxial strain in comparison to RH-GeSn, i.e., $\Delta E_{ss}^{(ZB)} < \Delta E_{ss}^{(RH)}$. If phase separation is slow, metastable long-range ordering may occur. These special structures have a lower enthalpy than a disordered alloy of the same composition.

This study will surely lead to a better understanding of the physical properties of Sn–Ge alloys.

5. SUMMARY

Thus, we presented a molecular dynamics method to study unstrained and biaxially strained binary $Ge_{1-x}Sn_x$ alloys. Biaxial strain has been taken into account by fixing an in-plane lattice constant. We observe a wide miscibility gap for unstrained $Ge_{1-x}Sn_x$. The critical temperature is about 830 K. However, there is also a wide range of compositions where a random $Ge_{1-x}Sn_x$ alloy may exist in a metastable phase.

Biaxial strain is extremely important for the miscibility behavior of alloys. The miscibility gap, as well as the region of spontaneous decomposition, are reduced. In this case, the critical temperature is markedly raised. Highly ordered zinc-blende or rhombohedral phases are more stable against spinodal decomposition than the same random alloys. Analysis of the effective enthalpy of formation of an epitaxial films shows that the stability of the ZB-phase is increased under epitaxial strain in comparison with RH-GeSn and long-range ordering may occur.

REFERENCES

1. K. A. Mäder, A. Baldereschi, and H. von Känel, Solid State Commun. **69**, 1123 (1989).
2. M. Ferhat and A. Zaoui, Infrared Phys. Technol. **42**, 81 (2001).
3. S. Oguz, W. Paul, T. F. Deutsh, *et al.*, Appl. Phys. Lett. **43**, 848 (1983).
4. T. Soma and H. Matsuo Kagaya, Phys. Status Solidi B **147**, 109 (1988).
5. S. Matsumura, T. Inushima, and T. Shiraishi, J. Cryst. Growth **189**–**190**, 696 (1998).
6. J. Tersoff, Phys. Rev. B **39**, 5566 (1989).
7. A. Chen and A. Sher, *Semiconductor Alloys: Physics and Material Engineering* (Plenum, New York, 1995).
8. V. G. Deibuk and Yu. G. Korolyuk, Fiz. Tekh. Poluprovodn. (St. Petersburg) **35**, 298 (2001) [Semiconductors **35**, 283 (2001)].
9. H. Gould and J. Tobochnik, in *An Introduction to Computer Simulation Methods: Applications to Physical Systems* (Addison-Wesley, Reading, 1988; Mir, Moscow, 1990), Part 1.
10. G. B. Stringfellow, J. Phys. Chem. Solids **34**, 1749 (1973).
11. J. L. Martins and A. Zunger, Phys. Rev. B **30**, 6217 (1984).
12. J. L. Martins and A. Zunger, Phys. Rev. Lett. **56**, 1400 (1986).

Semiconductors, Vol. 36, No. 10, 2002, pp. 1077–1078. Translated from Fizika i Tekhnika Poluprovodnikov, Vol. 36, No. 10, 2002, pp. 1157–1158.

ATOMIC STRUCTURE AND NONELECTRONIC PROPERTIES OF SEMICONDUCTORS

The Effect of the Concentration of the Majority Charge Carriers and Irradiation Intensity on the Efficiency of Radiation-Defect Production in *n*-Si Crystals

T. A. Pagava and Z. V. Basheleĭshvili

Georgian Technical University, ul. M. Kostaza 77, Tbilisi, 380075 Georgia

Submitted July 3, 2001; accepted for publication March 7, 2002

Abstract—The effect of the concentration of the majority charge carriers (n) and the electron-flux density (φ) on the efficiency of radiation-defect production (η) in n-Si samples was studied. It is shown that the dependence $\eta(\varphi)$ features a maximum, which shifts to larger values of φ as n increases. This effect is explained by assuming that there is an optimal relation between the concentrations of primary defects produced per unit time and those of the free charge carriers, which charge these defects. *© 2002 MAIK "Nauka/Interperiodica".*

It has been shown experimentally that the electron-irradiation intensity (φ) affects the efficiency of radiation-defect production (η); however, there are certain contradictions between the data reported [1–4].

Zolotukhin *et al.* [5] studied the electron-flux dependence of the efficiency of A-center production $\eta_A(\varphi)$ in n-Si samples that had a resistivity $\rho = 60\ \Omega$ cm and were irradiated with 2.2-MeV electrons. It was found [5] that there existed a critical value φ_c, which separated the region where such a dependence was observed from the region where η_A was independent of φ ($\varphi_c = 5 \times 10^{12}$ cm^{-2} s^{-1}). The preliminary irradiation of the samples with protons in order to increase the number of macroscopic defects in crystals reduced φ_c to 2×10^{12} cm^{-2} s^{-1}; a preliminary plastic deformation brought about an increase in φ_c to 10^{13} cm^{-2} s^{-1}. The observed effect was attributed [5] to recombination of the Frenkel pairs' components at the crystal-lattice defects. A similar decrease in the efficiency of E-center production (η_E) was observed previously [6] for $\varphi_c = 5 \times 10^{12} - 2 \times 10^{13}$ cm^{-2} s^{-1}.

Pagava and Basheleĭshvili [7] studied n- and p-type Si samples with the same concentration of free charge carriers (6×10^{13} cm^{-3}). It was shown [7] that the dependence $\eta(\varphi)$ had a maximum at $\varphi_c = 5 \times 10^{12}$ cm^{-2} s^{-1} in the crystals of both types. Application of an electric field to the samples in the course of irradiation does not affect the value of φ_c; however, the dependence $\eta(\varphi)$ shifts to larger values of φ only in n-Si, which is attributed to a difference between the charge state of the primary radiation defects in the n- and p-type crystals.

In this paper, we report the results of studying n-Si crystals doped with phosphorus with concentrations of $n_1 = 10^{13}$ cm^{-3}, $n_2 = 6 \times 10^{13}$ cm^{-3}, and $n_3 = 2 \times 10^{14}$ cm^{-3} and grown by the float-zone method; the oxygen concentration in the crystals was $\sim 2 \times 10^{16}$ cm^{-3}. The samples were irradiated with 2-MeV electrons at room temperature.

The studies were conducted using the method of local irradiation with subsequent measurements of the volume photovoltage (U_{ph}) across the irradiated area of the sample. This method was described in detail elsewhere [8, 9].

As is well known, $U_{ph} \propto \partial\rho/\partial x$. The samples under investigation were irradiated with a fixed dose of electrons ($\Phi = 5 \times 10^{15}$ cm^{-2}); therefore, we have $U_{ph} \propto \eta$. The measurements were performed at room temperature in the region where the A centers were exhausted; therefore, the height of the potential barrier between the

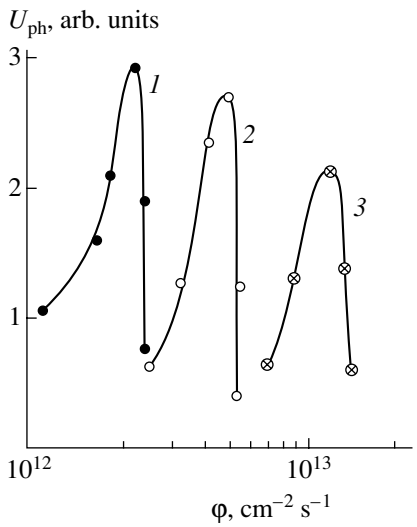

Dependences of the volume photovoltage U_{ph} on the flux density of 2-MeV electrons φ in locally irradiated n-Si samples. The charge-carrier (electron) concentration n = (*1*) 10^{13}, (*2*) 6×10^{13}, and (*3*) 2×10^{14} cm^{-3}. The irradiation dose $\Phi = 5 \times 10^{15}$ cm^{-2}.

1063-7826/02/3610-1077$22.00

irradiated and unirradiated parts of the sample was controlled by varying the concentration of acceptor centers with deeper levels (the E centers and divacancies V_2).

The measurements showed that, in contrast to the A centers [5], the dependences $U_{ph}(\varphi)$, i.e., the dependences of the efficiency of producing the E and V_2 centers on $\eta_{E, V_2}(\varphi)$ feature maxima in certain ranges of φ; these maxima shift to larger values of φ as η increases. In crystals with charge-carrier concentrations n_1, n_2, and n_3, we have $\varphi_c = 2 \times 10^{12}$, 5×10^{12}, and 10^{13} cm^{-2} s^{-1}, respectively (see figure). If we assume that a 2-MeV electron forms a single Frenkel pair in n-Si crystal, then the ratio n/N_V (where N_V is the concentration of vacancies formed per unit time) for the crystals with concentrations n_1, n_2, and n_3 is equal to 5, 12, and 20, respectively.

The presence of a peak in the curve $\eta(\varphi)$ in n-Si crystals and the shift of this peak along the φ axis as n varies suggests that there is an optimal relation between the concentrations of primary radiation defects formed per unit time and those of free charge carriers, which charge these defects.

REFERENCES

1. J. W. Corbett and G. D. Watkins, Phys. Rev. **138**, A555 (1965).
2. J. S. Blakemore, *Semiconductor Statistics* (Pergamon, Oxford, 1962; Mir, Moscow, 1969).
3. V. I. Kozhevnikov and V. V. Mikhnevich, Fiz. Tekh. Poluprovodn. (Leningrad) **15**, 1598 (1981) [Sov. Phys. Semicond. **15**, 924 (1981)].
4. P. F. Lugakov and V. V. Luk'yanitsa, Fiz. Tekh. Poluprovodn. (Leningrad) **18**, 345 (1984) [Sov. Phys. Semicond. **18**, 215 (1984)].
5. A. A. Zolotukhin, A. K. Kovalenko, T. M. Meshcheryakova, *et al.*, Fiz. Tekh. Poluprovodn. (Leningrad) **9**, 1201 (1975) [Sov. Phys. Semicond. **9**, 800 (1975)].
6. A. A. Zolotukhin, Author's Abstract of Candidate's Dissertation (IMET Akad. Nauk SSSR, Moscow, 1972).
7. T. A. Pagava and Z. V. Basheleĭshvili, Fiz. Tekh. Poluprovodn. (St. Petersburg) **33**, 542 (1999) [Semiconductors **33**, 508 (1999)].
8. L. S. Milevskiĭ and V. S. Garnyk, Fiz. Tekh. Poluprovodn. (Leningrad) **13**, 1369 (1979) [Sov. Phys. Semicond. **13**, 801 (1979)].
9. G. Tsintsadze, T. Pagava, V. Garnic, and Z. Basheleishvili, Bull. Georgian Acad. Sci. **160** (3), 450 (1999).

Translated by A. Spitsyn

Semiconductors, Vol. 36, No. 10, 2002, pp. 1079–1082. Translated from Fizika i Tekhnika Poluprovodnikov, Vol. 36, No. 10, 2002, pp. 1159–1162.

ATOMIC STRUCTURE AND NONELECTRONIC PROPERTIES OF SEMICONDUCTORS

Dependence of the Annealing Kinetics of *A* Centers and Divacancies on Temperature, Particle Energy, and Irradiation Dose for *n*-Si Crystals

T. A. Pagava

Georgian Technical University, ul. Kostaza 77, Tbilisi, 380075 Georgia

Submitted December 24, 2001; accepted for publication March 11, 2002

Abstract—*n*-Si crystals grown by the float-zone method with a phosphorus concentration of ~6×10^{13} cm^{-3} and irradiated with 2-MeV electrons and 25-MeV protons were studied. It is shown that the kinetics of the isochronous annealing of the *A* centers and divacancies (the annealing temperature and the rearrangement of radiation defects in the situation where the dissociation of one type of defects gives rise to more stable defects) depends in a complicated way on the energy, dose, and temperature of irradiation; i.e., this kinetics depends on the relation between the concentrations of various radiation defects and on the charge state of reacting primary radiation defects when they interact with each other, with impurity atoms, and with disordered regions. An increase in the concentration of divacancies in the temperature range of 180–210°C is attributed to the dissociation of disordered regions. © *2002 MAIK "Nauka/Interperiodica".*

Previous studies on the thermal stability of radiation defects showed that an increase in the oxygen concentration in silicon samples reduces the temperature of annealing of divacancies V_2 [1]. A dose dependence of the annealing temperature for the defects was also observed. The annealing of divacancies is completed at a temperature of T_{ann} = 190°C after irradiation with neutrons at a dose of $\Phi = 4 \times 10^{19}$ cm^{-2} [2].

It was shown by Berman *et al*. [3] that, in *n*-Si samples irradiated with 3.7-MeV protons, the annealing of divacancies occurred in two stages, one of which was observed at T_{ann} = 150°C and corresponded to the annealing of divacancies in disordered regions, and the other of which was observed at T_{ann} = 275–325°C and corresponded to the annealing of divacancies in the defect–impurity shell surrounding this region and also in the undamaged crystal host.

When analyzing the reported results of the aforementioned studies, one may conclude that the divacancy-annealing temperature depends on the concentration of sinks for the products of dissociation of these centers (vacancies). Along with impurity atoms, such sinks can be represented by disordered regions, whose size and concentration depend on the particle-energy and the dose of irradiation. According to this model, the dissociation of the less stable radiation defects (for example, the *E* centers and divacancies) in the course of isochronous heat treatment is bound to be accompanied by an increase in the concentration of stable *A* centers, which is indeed observed in the *n*-Si samples irradiated with large doses of γ-ray quanta [4].

We believe that the number of *A* centers formed in the course of isochronous annealing of *n*-Si samples irradiated with high-energy particles is controlled by the ratios σ_1/σ_2, N_E/N_A, and N_{V_2}/N_A. Here, σ_1 and σ_2 are the cross sections for the capture of vacancies by oxygen atoms and by disordered regions; and N_E, N_{V_2}, and N_A are the concentrations of *E* centers, divacancies, and *A* centers, respectively.

In this paper, we report the results of studying *n*-Si crystals grown by the float-zone method and doped with phosphorus to a concentration of 6×10^{13} cm^{-3}; the oxygen concentration determined from infrared-absorption measurements was ~2×10^{16} cm^{-3}. The samples were irradiated with 2-MeV electrons or 25-MeV protons at room temperature.

Concentrations of the *A* and *E* centers and divacancies V_2 in the course of isochronous annealing were determined from an analysis of the dependence of the majority-carrier concentration on the reciprocal temperature $1/T$ in the range T = 77–300 K.

The samples under investigation were bar-shaped with a surface area of 3 × 10 mm^2 and thickness of 1 mm. Isochronous annealing of irradiated samples was performed in the temperature range T_{ann} = 80–600°C with a step of 10°C. The samples were kept at a fixed temperature for 10 min. After each isochronous-annealing stage, the Hall method was used to measure the electron concentration N in the range of 77–300 K. Nonrectifying contacts for measuring the Hall voltage were formed by rubbing aluminum powder into the silicon surface.

As an example, Fig. 1 shows the dependences $N = f(1/T)$ in the as-grown crystal (curve *1*), after irradiation with 25-MeV protons with an integrated flux Φ = 8 ×

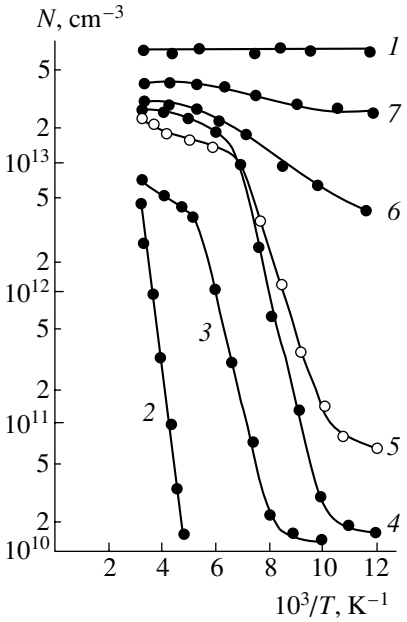

Fig. 1. Dependences of electron concentration on the reciprocal temperature in the *n*-Si crystals (*1*) before irradiation, (*2*) immediately after irradiation with 25-MeV protons with a dose of $\Phi = 8 \times 10^{12}$ cm^{-2}, and after subsequent heat treatments at T_{ann} = (*3*) 120, (*4*) 190, (*5*) 235, (*6*) 300, and (*7*) 400°C.

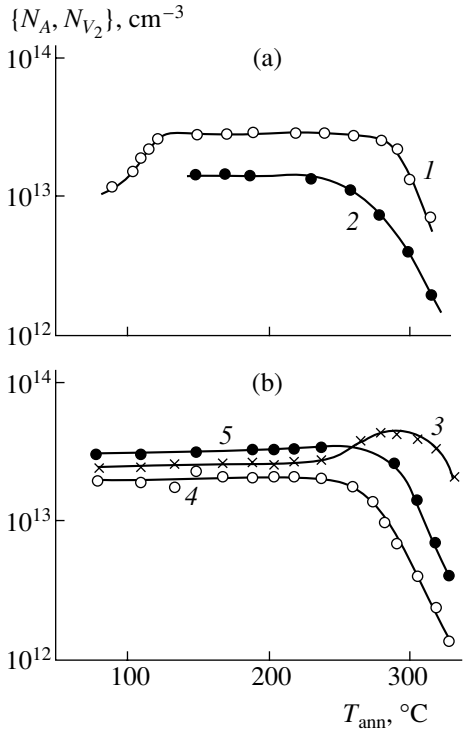

Fig. 2. Dependences of (*1*, *3*, *5*) the *A*-center and (*2*, *4*) divacancy concentrations on the temperature of isochronous heat treatments in the *n*-Si samples irradiated with 2-MeV electrons. (a) The irradiation temperature is 300 K, and the irradiation dose is $\Phi = 1.5 \times 10^{14}$ cm^{-2}; (b) the irradiation temperature is 523 K, and the irradiation dose is $\Phi = 5 \times 10^{14}$ cm^{-2}. Curve *5* corresponds to the heat-treatment duration of 60 min; in all other cases, it was 10 min.

10^{12} cm^{-2} (curve *2*), and after postirradiation heat treatments at T_{ann} = 120, 190, 235, 300, and 400°C (curves *3*–*7*, respectively). Curve *2* corresponds to the exhaustion of the acceptor centers that have a level at E_c – 0.4 eV, i.e., the *E* centers or divacancies. This means that all free electrons are trapped by the divacancies and *E* centers, whereas the *A* centers are neutral; as a result, it is impossible to determine N_A from the $N(1/T)$ curves. After annealing a certain fraction of the *E* centers ($T_{ann} \geq 100$°C), the *E* centers become charged, which makes it possible to monitor the variation in the concentration of these defects in the course of isochronous annealing (Fig. 1, curves *3*–*7*). If we determine the *A*-center concentration from curve *3* (after heat treatment at 120°C) as $N_A = N(250\ \text{K}) - N(100\ \text{K})$, i.e., as the difference between electron concentrations (ΔN) in the conduction band in the regions of exhaustion of the *A* centers and the phosphorus atoms, we can determine N_E by comparing curves *2* and *4* after the annealing out of the *E* centers, which is completed at $T_{ann} < 190$°C. It is well known that, when a single *E* center is formed, it removes two electrons from the conduction band [5] so that $N_E = \Delta N(250\ \text{K})/2$. For larger irradiation doses, when $N_{V_2} \geq N$, the *E* centers are most probably in a neutral state. After an *E* center is annealed, an electron is returned to the conduction band so that $N_E = \Delta N(250\ \text{K})$. The value of N_{V_2} is governed by the variation in the free-electron concentration at T = 250 K in the course of isochronous annealing in the range T_{ann} = 235–400°C (curves *5*–*7*). As is well known [5], a single divacancy traps two electrons from the conduction band at $T \leq 300$ K. The corresponding trapping levels are located at E_c – 0.4 eV and E_c – 0.54 eV; as a result, $N_{V_2} = \Delta N(250\ \text{K})/2$. A further increase in N to its initial value at 250 K in the course of heat treatment corresponds to the annealing of the V_2 + O complexes and makes it possible to determine the concentration of these centers (curves *7*, *1*).

As can be seen from Fig. 2a (curve *1*), the *A*-center concentration increases at $T_{ann} \geq 120$°C in the samples irradiated with 2-MeV electrons ($\Phi = 1.5 \times 10^{14}$ cm^{-2}); this phenomenon is attributed to interaction of the vacancies released as a result of decomposition of the *E* centers with oxygen impurity atoms. The ratio between the concentrations of dissociated *E* centers and the produced *A* centers is $\Delta N_E/\Delta N_A = 1.75$. Prior to annealing, we have $N_E/N_A = 3$. After annealing at $T_{ann} \geq 150$°C, $N_{V_2}/N_A = 0.6$, which is caused by an increase in N_A as a result of the dissociation of *E* centers in the region of 120°C. Under these conditions, an increase in N_A as a result of the dissociation of V_2 is not observed in the course of the heat treatment. In this case, the *A* centers are annealed out at ~300°C (Fig. 2a, curves *1*, *2*).

The exhaustion of the *E* centers and of the second V_2 level and also the *E*-center dissociation occur simulta-

neously in the range of 100–150°C. Therefore, it is impossible to monitor the variations in N_{V_2} using the $N(1/T)$ curves in the course of the *E*-center annealing. At low electron-irradiation doses ($\Phi = 1.5 \times 10^{14}$ cm^{-2}), the vacancies formed as a result of the *E*-center dissociation are charged negatively. It may be assumed that, due to electrostatic repulsion between negative vacancies, the efficiency of introducing divacancies is negligibly low; as a result, N_{V_2} does not increase.

In order to eliminate the effect of *E* centers, the samples were irradiated with electrons at a temperature of 250°C. It can be seen from Fig. 2b that the concentrations of the *A* and V_2 centers remain unchanged up to $T_{ann} = 250$°C. A further increase in the annealing temperature brings about a decrease in the V_2 concentration and, correspondingly, an increase in the number of *A* centers. An analysis of the experimental curves shows that a single *A* center is formed as a result of the decomposition of a single divacancy; i.e., $\Delta N_{V_2}/\Delta N_A = 1$ and $N_{V_2}/N_A \approx 1$.

If the heat-treatment duration is increased to 60 min, the negative annealing of *A* centers is not observed (Fig. 2b, curve *5*). Evidently, vacancies formed as a result of the dissociation of divacancies during the 1-h annealing come to the crystal surface; as a result, additional *A* centers are not formed during the rapid cooling of the samples.

In the crystals irradiated with 25-MeV protons ($\Phi = 2.7 \times 10^{12}$ cm^{-2}), the *A*-center concentration does not change when the *E* centers dissociate, whereas the temperature of the *A*-center annealing decreases to 240°C, which is attributed to the formation of positively charged disordered regions; the latter are efficient sinks for vacancies (negatively charged in *n*-Si [6, 7]) and reduce both the probability of the additional formation of *A* centers and the annealing temperature T_{ann} for these centers (Fig. 3, curve *1*). For the same reason, the annealing temperature for divacancies decreases to 220°C (Fig. 3, curve *4*). In this temperature range, an increase in the *A*-center concentration is not observed since $N_{V_2}/N_A = 0.5$.

In the samples irradiated with larger doses of protons ($\Phi = 8 \times 10^{12}$ cm^{-2}), the *A*-center concentration increases in the temperature region corresponding to *E*-center dissociation, in contrast to the samples irradiated with smaller proton doses. The *A*-center concentration decreases at $T_{ann} = 190$–220°C, a negative annealing of these centers is observed at $T_{ann} = 240$–300°C, and the *A* centers are completely annealed out at $T_{ann} = 300$–400°C (Fig. 3, curve *2*). An increase in the divacancy concentration is observed at $T_{ann} = 190$–210°C. The temperature corresponding to the onset of annealing of divacancies increases to 210°C (Fig. 3, curve *3*).

In the crystals irradiated with large doses of protons, the electron concentration in the conduction band is

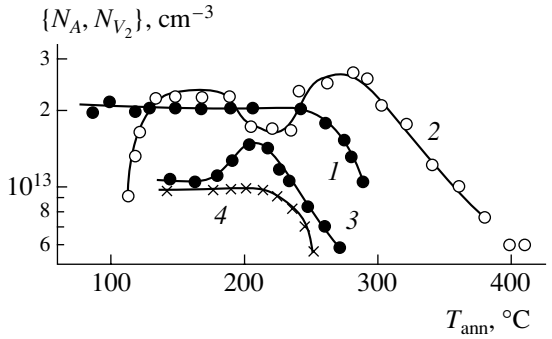

Fig. 3. Dependences of the (*1*, *2*) *A*-center and (*3*, *4*) divacancy concentrations on the temperature of isochronous heat treatment in the *n*-Si samples irradiated with 25-MeV protons. The dose of irradiation Φ = (*1*, *4*) 2.7×10^{12} and (*2*, *3*) 8×10^{12} cm^{-2}.

fairly low. Therefore, only a fraction of the vacancies formed as a result of the *E*-center dissociation are charged negatively in the early stages of isochronous heat treatment. As is well known [8], the disordered regions in *n*-Si are charged positively, which may account for a decrease in the efficiency of adsorption of vacancies by disordered regions. The supersaturation of the crystal with monovacancies in the regions where the *E* centers dissociate is relieved as a result of *A*-center formation (Fig. 3, curve *2*).

After the *E* centers are completely annealed out ($T_{ann} \geq 120$°C), the free-electron concentration increases. All vacancies formed in the course of heat treatment can be charged negatively. This brings about an increase in the efficiency of the adsorption of vacancies by disordered regions and a decrease in the annealing temperature for the *A* centers to 190°C (Fig. 3, curve *2*).

As is well known [9], isolated disordered regions in silicon crystals are annealed out at 260°C. Appreciable annealing sets in at 200°C. Apparently, the disordered regions are sources not only of monovacancies but also of divacancies, which accounts for an increase in the divacancy concentration ($\Delta N_{V_2} = 6 \times 10^{12}$ cm^{-3}) in the temperature range of 190–210°C (Fig. 3, curve *3*). We believe that, as the annealing temperature T_{ann} increases, the only products of the disordered-region dissociation are monovacancies. The annealing of divacancies V_2 also sets in in the undamaged part of the sample, which brings about the negative annealing of more stable *A* centers in the range $T_{ann} = 230$–280°C. The *A*-center annealing sets in at 300°C (Fig. 3, curve *2*).

Thus, the kinetics of annealing of the *A* centers and divacancies (the annealing temperature and rearrangement of disordered regions in the situation where the dissociation of one of these defects gives rise to more stable centers) depends, in a complicated manner, on the particle-energy and the dose and temperature of irradiation; i.e., it depends on the relation between the

concentrations of various point radiation defects and the charged state of vacancies and disordered regions.

REFERENCES

1. J. W. Corbett and G. D. Watkins, Phys. Rev. **138**, A555 (1965).
2. M. T. Lappo and V. D. Tkachev, *Radiation Defects in Semiconductors* (Belaruss. Gos. Univ., Minsk, 1972).
3. L. S. Berman, V. V. Voronkov, V. A. Kozlov, and A. D. Remenyuk, Fiz. Tekh. Poluprovodn. (St. Petersburg) **26** (8), 1507 (1992) [Sov. Phys. Semicond. **26**, 847 (1992)].
4. T. Nakano and Y. Inuishi, J. Phys. Soc. Jpn. **19**, 851 (1964).
5. V. V. Emtsev and T. V. Mashovets, *Impurities and Point Defects in Semiconductors* (Radio i Svyaz', Moscow, 1981).
6. L. S. Milevskiĭ and V. S. Garnyk, Fiz. Tekh. Poluprovodn. (Leningrad) **13**, 1369 (1979) [Sov. Phys. Semicond. **13**, 801 (1979)].
7. G. Tsintsadze, T. Pagava, V. Garnic, and Z. Basheleishvili, Bull. Georgian Acad. Sci. **160** (3), 450 (1999).
8. B. R. Gossick, J. Appl. Phys. **33**, 1816 (1960).
9. *Physical Processes in Irradiated Semiconductors*, Ed. by L. S. Smirnov (Nauka, Novosibirsk, 1977).

Translated by A. Spitsyn

Semiconductors, Vol. 36, No. 10, 2002, pp. 1083–1090. Translated from Fizika i Tekhnika Poluprovodnikov, Vol. 36, No. 10, 2002, pp. 1163–1170.

ATOMIC STRUCTURE AND NONELECTRONIC PROPERTIES OF SEMICONDUCTORS

Chalcogen Dimers in Silicon

A. A Taskin

Institute of Semiconductor Physics, Siberian Division, Russian Academy of Sciences, pr. Akademika Lavrent'eva 13, Novosibirsk, 630090 Russia

e-mail: taskin@thermo.isp.nsc.ru

Submitted January 16, 2002; accepted for publication March 14, 2002

Abstract—Structures, chemical properties, and chalcogen-dimer formation energies in silicon were investigated using quantum-chemical *ab initio* calculations by the Hartree–Fock method. The equilibrium geometrical configuration, electron-density distribution, and the parameters of the chemical bonding of lattice atoms were determined. Lattice relaxation around impurity defects is shown to contribute substantially to the total energy of a crystal. The chalcogen-dimer stability associated with a decrease in the total energy of a crystal, which accompanies its formation, was predicted. Estimates obtained for the dimer-formation energy agree well with available experimental data on their formation reactions. The geometrical configuration, and the electronic and chemical properties of impurity clusters involving up to six chalcogen atoms are discussed. © *2002 MAIK "Nauka/Interperiodica".*

1. INTRODUCTION

In the last decades, the system of chalcogen-doped (with sulfur, selenium, and tellurium—group-VI elements) silicon has been actively investigated in connection with its sensitivity to infrared (IR) radiation. In the present day, a vast experimental body of data associated with the study of its properties and behavior in crystal has been accumulated. The investigations were carried out using a wide assortment of experimental methods: deep-level transient spectroscopy (DLTS) [1–4], Hall-effect measurements [3, 5, 6], IR-absorption and photoconductivity measurements [6–12], capacitance and photocapacitance measurements [2, 3], secondary ion mass spectrometry (SIMS) and Rutherford backscattering spectroscopy (RBS) [13–16], electron spin resonance (ESR) [4, 17], electron–nuclear double resonance (ENDOR) [18, 19], radioactive-isotope-decay investigations [20], photoluminescence spectroscopy [21, 22], etc.

As a result of these investigations, it was established that isolated chalcogen atoms in silicon are deep-level doubly charged donors. The ionization energies of their ground states are equal to

$$\text{for } S^0(S^+)\text{: } 0.32\ (0.61\ \text{eV}),$$

$$\text{for } Se^0(Se^+)\text{: } 0.30\ (0.59\ \text{eV}),$$

$$\text{for } Te^0(Te^+)\text{: } 0.20\ (0.41\ \text{eV}).$$

The atoms occupy silicon lattice sites and have the point-group symmetry T_d. The wave functions of ground states are *S*-type functions and have the irreducible-representation symmetry A_1. In the singly ionized state, isolated chalcogen atoms are paramagnetic centers.

The chalcogen doping of silicon is accompanied by the formation of by-product complexes of which the S_2, Se_2, and Te_2 dimers have been most adequately studied. The dimers are doubly charged donors with the following ionization energies of their ground states:

$$\text{for } S_2^0(S_2^+)\text{: } 0.187\ (0.371\ \text{eV}),$$

$$\text{for } Se_2^0(Se_2^+)\text{: } 0.206\ (0.248\ \text{eV}), \text{ and}$$

$$\text{for } Te_2^0\text{: } 0.158\ \text{eV}.$$

Two chalcogen atoms occupying neighboring lattice sites represent a dimer structure. The symmetry of these complexes is D_{3d}. The symmetry of the ground-state wave functions is A_{1g}. In the singly ionized state, the dimers are paramagnetic centers. In the S–Se–Te sequence, the dimer formation becomes gradually less active.

The formation of more complicated complexes has been virtually unstudied; still, for certain temperature-treatment regimes for chalcogen-doped silicon wafers, more shallow donor states were observed: their ionization energy amounted to about 0.1 eV or less. These states are likely associated with the formation of more intricate complexes [3, 10, 12, 14, 23–28]. In many respects, chalcogen-doped silicon can be considered as a model for studying the processes of interaction between impurity defects in crystals that lead to the formation of impurity complexes [29, 30].

The purpose of this study is to calculate the energy of chalcogen-atom bonding when dimers are formed in silicon using nonempirical quantum-chemistry methods and to analyze the possibility of forming more complicated complexes.

2. CALCULATION METHOD

In this study, we calculated the electronic structure and analyzed the chemical properties of impurity defects in a silicon lattice using a cluster approximation of the Restricted Hartree–Fock (RHF) method [31, 32] implemented in the GAMESS (general atomic and molecular electronic structure system) software package [33].

It is well known that, contrary to the band methods for calculating impurity-defect properties in crystals, for example, using the formalism of the Green's functions including the localized perturbation introduced into a perfect crystal by an impurity atom [34–37], cluster calculations (in particular, by the Hartree–Fock method) yield only a qualitative description of the position of impurity-atom energy levels in a band gap [38–42]. Nevertheless, in recent years, calculations in "real space" using well-developed quantum-chemistry methods [43] have found ever wider application in describing systems with total or partial violation of lattice periodicity (crystals with isolated defects and deep-level impurities, amorphous materials, solid surfaces, and the interaction of these surfaces with molecules and atoms). The cluster approaches are used most successfully for calculating the properties associated with a variation in the total energy of a crystal containing intrinsic and impurity defects [42]: the geometrical configuration of the lattice around a defect (without restrictions of symmetry), the energy of diffusion barriers of defects in the crystal, the bonding energies of impurity complexes, etc.

In this study, we calculate variations in the total energy of a system when the arrangement of atoms in a cluster is varied. Further, the calculated results are used for analyzing the relaxation of a lattice around an impurity defect and also for estimating the bonding energy of impurity atoms in complexes. The character of the electron-density distribution in a cluster, calculated in various full-electron bases of atomic orbitals (AOs) [44], is represented in conventional terms of chemical bonding, i.e., of the bond orders between various atoms and their valences and charges (total atomic populations) [45–47].

Since the simulation of the behavior of impurity defects in a crystal is based on the local character of variation in physical properties introduced in the lattice by defects, it is necessary to use clusters of a reasonably large size in order to evade the influence of boundary atoms, whose dangling bonds are saturated by hydrogen atoms. In this study, the selection of cluster size, which is sufficient for analyzing the formation of chalcogen dimers in silicon, is based on the results of calculating the relaxation of a lattice around isolated chalcogen atoms in clusters with a tetrahedral symmetry: Si_5H_{12}, $Si_{17}H_{36}$, $Si_{29}H_{36}$, $Si_{35}H_{36}$, $Si_{47}H_{60}$, $Si_{71}H_{84}$, $Si_{87}H_{76}$, $Si_{99}H_{100}$, and $Si_{123}H_{100}$. An increase in the cluster size (beginning with $SSi_{16}H_{36}$, $SeSi_{16}H_{36}$, or $TeSi_{16}H_{36}$ with impurity atoms arranged at the center) does not profoundly affect the relaxation of the lattice around a chalcogen atom. The cause of this is that the AOs of an impurity atom are virtually totally located at the nearest neighbors. The minimum cluster size necessary for the calculation of properties of a crystal containing several impurity atoms must be such that there is no marked overlapping of contributions from the AOs of boundary silicon atoms and impurity atoms in the obtained self-consistent solution. For chalcogen atoms in silicon, this means that the boundary atoms of silicon in a cluster must be at least second neighbors.

3. RESULTS AND DISCUSSION

3.1. Homoatomic and Heteroatomic Molecules of Chalcogen Atoms

In order to select an adequate AO basis, to estimate the accuracy of calculations of physical properties, and to reveal differences in the formation of chemical bonds with the participation of chalcogen atoms in molecular and crystalline systems, we previously calculated properties of well-known molecules composed of silicon and chalcogen atoms. We calculated the following properties of such molecules: equilibrium spacings; eigenfrequencies; dissociation energies, which can be easily compared with experimentally determined values; and also properties characterizing the formation of chemical bonding—bond order, atomic valences in a molecule, and atomic charge (characterizing the electronegativity of atoms in compounds). For the calculations, we used conventional full-electron bases of AOs of various sizes—from STO-3G to 3-21G and 6-31G with the inclusion of supplementary *d* and *f* orbitals. We also carried out calculations in the SBK valence basis [48, 49] (using the Stevens–Basch–Krauss effective potential), which provided a level of accuracy for *ab initio* calculations.

As a rule, the accuracy of the obtained results increased with the size of the basis used. All the considered AO bases with the exception of the smallest ones (STO-3G) provide an acceptable accuracy of calculation of the basic physical properties of the molecules considered. In Table 1, we give the results of calculating equilibrium spacings, eigenfrequencies, and dissociation energies of Si_2, SiS, SiSe, SiTe, S_2, Se_2, and Te_2 molecules in the 3-21G(+1*d*) basis with allowance for correlation energies using the Møller–Plesset method of the second order (MP2) [50, 51] in comparison with experimental values of these quantities [52–54]. For all these molecules, the difference between the calculated and experimental values amounts to less than 2% for equilibrium spacings of atoms in a molecule, less than 5% for frequencies of eigenmodes, and from 8 to 13% for dissociation energies of molecules. The relatively lower accuracy in determining the dissociation energy is primarily associated with calculating the difference in the energy of two quite different systems—the molecules and two isolated atoms.

Table 1. Calculations of the ground-state symmetry, equilibrium spacings (r), eigenfrequencies (f), and dissociation energies (D) for the Si_2, SiS, SiSe, SiTe, S_2, Se_2, and Te_2 molecules in the 3-21G(+1d) basis with allowance made for the energy corrections by the MP2 method

Molecule (symmetry)	r, Å	r, Å experiment	f, cm^{-1}	f, cm^{-1} experiment	D, eV	D, eV experiment
Si_2 ($^3\Sigma_g^-$)	2.2505	2.25	516	511.0	2.79	3.224
Si–S ($^1\Sigma^+$)	1.936	1.929	774	749.5	5.87	6.45
Se–Se ($^1\Sigma^+$)	2.072	2.058	599	580.0	5.52	5.58
Si–Te ($^1\Sigma^+$)	2.31	–	491	–	4.44	–
S_2 ($^3\Sigma_g^-$)	1.91	1.8894	725	725.6	3.88	4.37
Se_2 ($^3\Sigma_g^-$)	2.2	2.166	388	385.37	3.70	3.411
Te_2 ($^3\Sigma_g^-$)	2.625	2.558	260	247.07	2.90	2.677

In heteroatomic molecules, the tendency toward a decrease in the electronegativity is observed in the chalcogen S–Se–Te sequence and manifests itself as a decrease in the negative charge at the chalcogen atom in the molecule as the atomic number increases. The formation of a stable chemical bond is characteristic of all the molecules. The bond order varies insignificantly for various chalcogen atoms and amounts to a value approximately equal to 2. It should be noted that the chalcogen atoms form stronger chemical bonds with silicon atoms in comparison with those formed between themselves.

3.2. Isolated Impurity Defects (S, Se, and Te) in Silicon

For calculating the properties of impurity defects in a crystal, chalcogen atoms were placed in a bounded cluster of silicon atoms simulating a crystal lattice. The dangling bonds of boundary silicon atoms were saturated with hydrogen atoms. The relaxation of lattice atoms around an impurity defect was determined by minimizing the total energy of the cluster.

The minimum of the total energy for a cluster containing a chalcogen atom corresponds to the displacement of four neighboring silicon atoms in the ⟨111⟩ direction. In this case, the defect symmetry remains tetrahedral (T_d). The relaxation proceeds almost entirely within the first coordination sphere. In its turn, the displaced silicon atoms only slightly change their spacing and angles relative to their neighboring silicon atoms (the displacement of silicon atoms in the second coordination shell is less than 0.01 Å). The displacement of the nearest neighboring silicon atoms is different for various chalcogen atoms (Fig. 1).

Lattice relaxation near an impurity atom leads to a significant decrease in the energy relative to an unrelaxed lattice, the interatomic spacings in which are equal to 2.35 Å. The magnitude of lattice relaxation increases in the S–Se–Te sequence (see Table 2 and Fig. 1). The energy variation associated with relaxation has the same tendency. For example, in the 3-21G(+1d) basis, the energy of a relaxed lattice for a S atom is less than the energy of an unrelaxed lattice by 0.17 eV; this difference is 0.50 eV for an Se atom and 1.65 eV for a Te atom (for a Si atom, this difference is less than 0.001 eV). As the basis size is varied, the qualitative pattern of relaxation is retained. In Table 2, we list the

Table 2. Equilibrium distances (in Å) from impurity atoms to the nearest neighboring silicon atoms calculated using various bases for a $ChSi_{16}H_{36}$ (Ch = Si, S, Se, or Te) cluster with the tetrahedral symmetry. In the upper row, the results of a similar calculation for a silicon atom formally considered as an impurity atom are listed

Impurities	STO-3G	SBK (+1d)	3-21G (1d)	6-31G (+1d)
Si	2.36	2.348	2.352	2.35
S	2.415	2.43	2.438	2.43
Se	2.50	2.50	2.475	2.486
Te	2.63	2.61	2.605	–

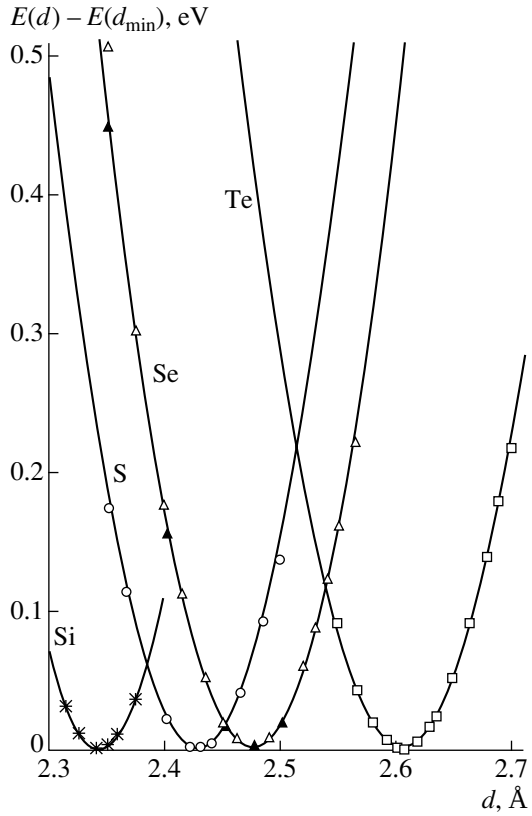

Fig. 1. Energy of $ChSi_{16}H_{36}$ (Ch = Si, S, Se, or Te) clusters calculated in the 3-21G(+1*d*) basis and reckoned from its minimum value in the case of a displacement of four silicon atoms neighboring the central impurity atom in the ⟨111⟩ direction; *d* is the spacing between a chalcogen atom and the nearest silicon atoms.

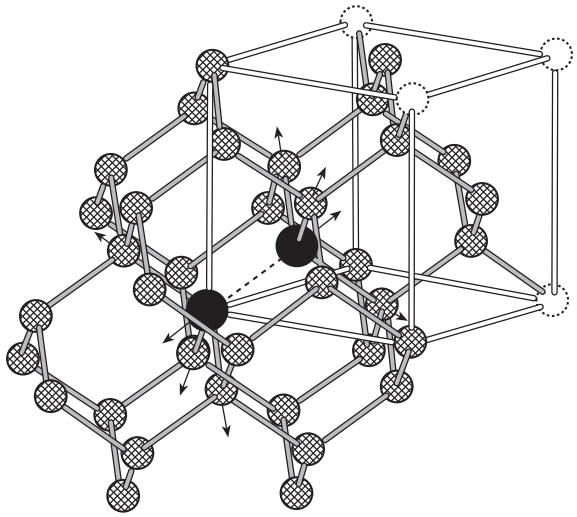

Fig. 2. Cluster of the $Ch_2Si_{36}H_{42}$ (Ch = Si, S, Se, or Te) type. Crosshatched spheres represent the silicon atoms; dark large spheres represent the chalcogen atoms (the hydrogen atoms are not shown). Rods represent the chemical bonds in the lattice (the dashed line corresponds to their absence). Also, a conditional cubic cell is singled out for the diamond lattice. The arrows show the displacement directions for atoms during the lattice relaxation.

equilibrium distances from chalcogen atoms to the nearest neighboring silicon atoms calculated in the STO-3G, SBK, 3-21G, and 6-31G bases. Taking into account the correlation corrections (MP2) leaves virtually intact the equilibrium spacings and the energies associated with relaxation.

An analysis of calculated one-electron states of chalcogen atoms in clusters shows that the highest occupied molecular orbitals (HOMOs) of clusters containing impurity atoms lie higher in energy than the HOMOs of similar silicon clusters and lower than their lowest unoccupied molecular orbitals (LUMOs); i.e., these states fall within a band gap. The energy necessary for electron transfer from an "impurity" level to the "conduction band" is much lower than the energy of the "valence-band–conduction-band" transition in a cluster. In spite of the fact that energies of one-electron Hartree–Fock states in cluster calculations have only a qualitative correspondence to the positions of levels in a real crystal, nevertheless, the calculation well reproduces the tendency of arrangement of energies of the ground state for isolated chalcogen atoms in silicon, which corresponds to the donor character of centers and to a decrease in the ionization energy for the ground state of the center in the S–Se–Te sequence.

The tetrahedral symmetry of isolated impurity defects and the symmetry A_1 of their ground state correspond to experimental data of investigations of ESR and optical transitions at centers related to chalcogen atoms in silicon. According to the calculations, the wave function of the ground state (HOMO) of chalcogen atoms in the substitutional position of the silicon lattice, which is virtually completely localized within the first coordination sphere, is governed by the contributions of the *s* states (with an insignificant admixture of *d* states) of a chalcogen atom and the sp^3 states of the neighboring silicon atoms.

The chemical bonds of isolated chalcogen atoms with the nearest neighboring silicon atoms in a lattice are partially ionic, remaining predominantly covalent. The electronegativity of chalcogens decreases in the S–Se–Te sequence. All four bonds of an impurity atom with neighboring silicon atoms are equivalent and have a bond order of ~0.5 (insignificantly increasing in the S–Se–Te sequence). The valence of chalcogen atoms in the silicon lattice is equal to ~2. For silicon atoms, the bond order between neighboring atoms is equal to ~1; the valence of the silicon atoms is equal to ~4.

3.3. Dimers S_2, Se_2, and Te_2

In order to calculate the properties of chalcogen dimers in a silicon crystal, we mainly used clusters that retained the D_{3d} symmetry of these impurity defects, in particular, the $Ch_2Si_{36}H_{42}$ clusters shown in Fig. 2.

The minimum of the total energy of this cluster containing two chalcogen atoms in the neighboring lattice sites corresponds to the symmetrical displacement of

these atoms in the ⟨111⟩ direction, which leads to an increase in the spacing between them. The three silicon atoms closest to each chalcogen atom are also displaced in the ⟨111⟩ direction. The symmetry of the defect remains as D_{3d}, and the displacement directions are shown by arrows in Fig. 2. In Fig. 3, we show the surface of total energy for a cluster (the potential-energy surface) containing an Se_2 dimer in relation to the distances r_1 (between selenium atoms) and Δr_2 (relative displacements of silicon atoms, which are neighbors with an impurity atom, from their sites in a perfect lattice). In Table 3, we give the results of calculations in the SBK and 3-21G(+1*d*) bases for the equilibrium spacings between chalcogen atoms in $Ch_2Si_{36}H_{42}$ corresponding to the minimum of the total energy of the cluster.

The relaxation of the lattice around a chalcogen dimer, as in the case of isolated impurity atoms, leads to a significant decrease in the total energy of the cluster. In the SBK(+1*d*) basis, the variation in energy is equal to 2.20 eV for the S_2, 3.13 eV for Se_2, and 7.61 eV for the Te_2 dimer; in the 3-21G(+1*d*) basis, similar variations of energy are equal to 2.19 eV for S_2, 2.82 eV for Se_2, and ~6.4 eV for Te_2.

The calculated one-electron values of the energies of the highest occupied orbitals for the chalcogen-atom dimers are located somewhat above the energy levels of the highest occupied orbitals for the corresponding isolated chalcogen atoms and remain within the "band gap." This fact is consistent with the experimentally observed character of the formation of more shallow donors in silicon when impurity centers involving two chalcogen atoms are formed [2, 4, 6].

The analysis of the electron-density distribution in clusters containing dimers reveals significant distinctions in the character of chemical-bond formation as compared with their chemical analogues—diatomic S_2, Se_2, and Te_2 molecules. The basic distinction consists in the absence of chemical bonding between chalcogen atoms in a dimer. The bond order between them is close to zero. The chalcogen atoms tend to move farther apart from one another and form stronger bonds with three neighboring silicon atoms. In this case, the order of bonds between chalcogen and silicon atoms becomes ~0.6–0.7 (in comparison with a value of ~0.5 for isolated chalcogen atoms forming bonds with four neighboring silicon atoms). The total valence of a chalcogen atom remains ~2.

To estimate the bonding energies of impurity atoms in a dimer, we calculated the total energies of identical clusters that differed in the mutual arrangement of chalcogen atoms in their lattices. Taking into account that variations in the electron density introduced by impurity defects are highly localized in space, even insignificantly spaced chalcogen atoms can be considered as isolated within a bounded cluster.

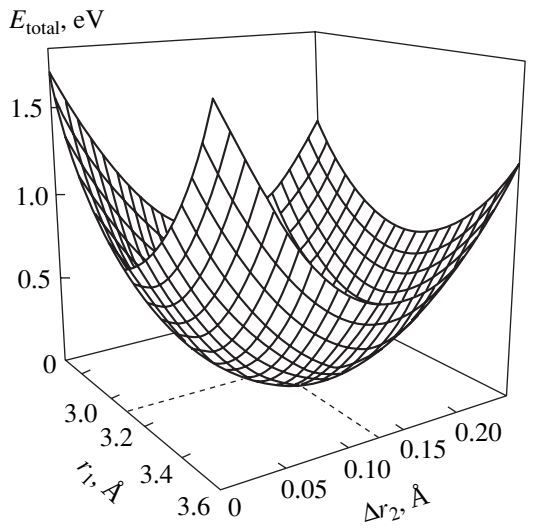

Fig. 3. Total-energy surface for the $Se_2Si_{36}H_{42}$ cluster containing the Se_2 dimer; r_1 is the spacing between selenium atoms, and Δr_2 is the displacement of a silicon atom neighboring a selenium atom relative to its position in a perfect lattice.

A comparison between the total energies of clusters in which chalcogen atoms reside at neighboring sites (dimers) and those of clusters in which chalcogen atoms are not nearest neighbors (two "isolated" atoms) shows that the energy of clusters containing a dimer is lower in comparison with that of similar clusters with "isolated" chalcogen atoms; i.e., dimer formation is energetically more favorable. For example, in the SBK(+1*d*) basis with allowance made for the relaxation of the lattice around impurity defects and with allowance made for the correlation corrections (MP2), the difference in energies associated with the formation of a dimer from two isolated chalcogen atoms amounted to 2.40, 1.90, and ~1.5 eV for S_2, Se_2, and Te_2, respectively. The obtained results are consistent with known tendencies in the formation of donor centers in silicon containing two chalcogen atoms. It is these tendencies that explain an increase in the concentration of these

Table 3. Equilibrium spacings r_1 between two chalcogen atoms located at the neighboring sites of the crystal lattice and equilibrium spacings r_2 between chalcogen atoms and the nearest silicon atoms for the $Ch_2Si_{36}H_{42}$ (Ch_2 = S_2, Se_2, or Te_2) cluster with the symmetry D_{3d}

Dimers	SBK		3-21G (1*d*)	
	r_1, Å	r_2, Å	r_1, Å	r_2, Å
S_2	3.13	2.36	3.08	2.33
Se_2	3.14	2.42	3.10	2.38
Te_2	3.27	2.53	3.20	2.50

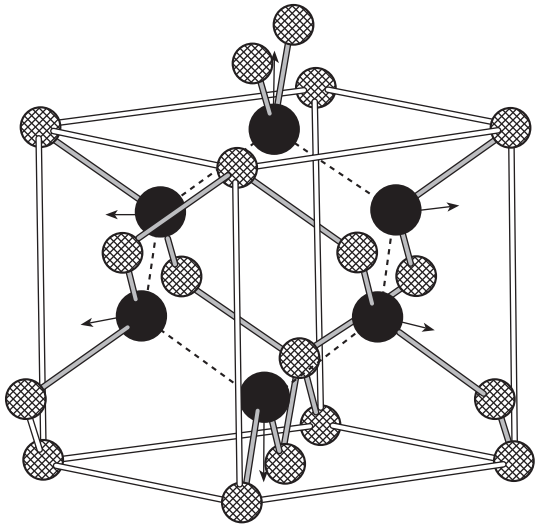

Fig. 4. Complex composed of six chalcogen atoms closed in a ring. The designations are the same as in Fig. 2.

centers with decreasing the temperature of technological treatment of chalcogen-doped samples and also an increase in the activity of their formation in the Te–Se–S sequence. The obtained estimates of dimer-formation energies are apparently very close to real values. In particular, from an analysis of experimental temperature dependences of the built-up kinetics of donor centers composed of two selenium atoms, we previously determined that the energy of formation of these centers is equal to ~1.4 eV [55]. It should be noted that the contribution of energies associated with the relaxation of the lattice around impurity defects to the dimer-formation energy is substantial and cannot be ignored when obtaining quantitative estimates of this value for chalcogens in silicon.

3.4. More Complicated Complexes

It is known that donors with shallower levels are observed in chalcogen-doped silicon under certain conditions of its technological treatment in addition to the donor centers associated with the isolated impurity atoms and dimers. The established special features of dimer formation enable us to assume that complexes composed of a larger number of chalcogen atoms can be formed in silicon; presumably, these complexes give rise to the shallower donor centers.

There are a number of difficulties in performing the calculation of complicated complexes with the methods used in this study. First, when a complex becomes considerably more complicated, the dimension of space of coordinates of impurity atoms and also of neighboring atoms of the lattice, which require optimization for determining their equilibrium positions, increases considerably. Second, for calculating the complex-formation energy as the energy difference for various spatial positions of impurity atoms within a single cluster (similar to the calculation of the dimer-formation energy), very large-size clusters are required. The *ab initio* calculations of clusters containing a large number of atoms in the full-electron bases require enormous computing resources and often are impracticable.

In these cases, an alternative is the calculations using semiempirical methods, which do not provide, however, the accuracy of the *ab initio* calculations and can be considered as auxiliary for estimating the tendencies in the properties of the systems under consideration.

The calculations which do not require determining the complex-formation energy, for example, when determining the relaxation of a lattice around a complex, can be fulfilled using relatively small clusters. For restricting the field of search for an equilibrium lattice configuration in the case of complicated complexes, the general pattern and tendencies established in calculations of less complicated complexes help considerably.

The results of our preliminary calculations of complicated complexes show that the formation of a complex involving three chalcogen atoms at neighboring lattice sites leads to an increase in the HOMO energy as compared with dimers and isolated impurity atoms, i.e., it leads to the formation of a more “shallow” donor.

As a whole, the special features of forming chemical bonds in a trimer are similar to those for chemical bonds in a dimer. The chalcogen atoms also do not form chemical bonds between them and tend to move farther apart from one another. A certain special feature is characteristic of the central impurity atom. In a trimer, this atom has only two nearest neighboring silicon atoms (contrary to three atoms for the boundary impurity atoms). Therefore, the central chalcogen atom is displaced in the ⟨100⟩ direction towards the nearest neighbors, forms only two, but stronger, chemical bonds, and remains bivalent in the silicon lattice.

The addition of each successive chalcogen atom to the impurity complex affects only slightly the considered pattern of forming chemical bonds. The complex-size increase leads to a steady increase in the HOMO energy as compared with that of the original complex; i.e., it leads to the formation of more and more shallow donors.

A substantial distinction in properties manifests itself in forming a closed complex. For the first time, such a complex can be formed in the silicon lattice for six impurity atoms topologically closed in a ring (Fig. 4). In this case, all six chalcogen atoms displaced in the ⟨100⟩ direction to the nearest silicon atoms and spaced from one another form two bonds each with neighboring silicon atoms. The relaxed cluster containing a ring of six chalcogen atoms features a much lower HOMO energy as compared with the cluster, which contains an isolated impurity atom. This means that the manifestation of the properties of a very deep donor (or a neutral center) should be expected for such a com-

plex. Furthermore, as follows from the calculations carried out using the PM3 semi-empirical method [56], a much greater energy must be released in the case of forming a closed ring of isolated chalcogen atoms than if a nonclosed complex involving the same number of atoms is formed. Apparently, the complex enclosed in a ring also represents a chemically inert formation in the silicon lattice. The addition of a successive impurity atom to the complex leads to the breaking of the existing bond between a chalcogen atom, and a silicon atom, which is energetically unfavorable.

4. CONCLUSION

The aforementioned results of the *ab initio* calculations of the equilibrium configuration, electronic structure, and chemical properties of impurity defects composed of chalcogen atoms in silicon enable us to make the following conclusions.

For isolated chalcogen atoms, the nearest neighboring silicon atoms are displaced in the ⟨111⟩ direction from an impurity atom, which retains the tetrahedral symmetry of the defect. The calculated displacement amounts to ~2.43 Å for S, ~2.48 Å for Se, and ~2.60 Å for Te atoms. The one-electron states of isolated chalcogen atoms in silicon qualitatively correspond to energy levels in the "band gap" of the corresponding donor centers. The chalcogen atoms form four equivalent chemical bonds with the nearest silicon atoms with a bond order of ~0.5 and have a total valence of ~2.

For dimers involving two chalcogen atoms at the neighboring lattice sites, these atoms are displaced from one another in the ⟨111⟩ direction. The equilibrium spacings between them are equal to ~3.08 Å for S, ~3.10 Å for Se, and ~3.20 Å for Te atoms. Three silicon atoms, closest to each chalcogen atom, are displaced (in the ⟨111⟩ directions) so that the distance to an impurity atom amounts to ~2.33 Å in S_2, ~2.38 Å in Se_2, and ~2.50 Å in Te_2. The symmetry of the defect is D_{3d}. The one-electron states of dimers correspond to donor centers having a lower ionization energy in comparison with isolated impurity atoms. It was shown that the chalcogen atoms in a dimer do not form chemical bonds between themselves (the bond order is close to zero) and form three equivalent bonds with the nearest silicon atoms (the bond order is ~0.6–0.7). The valence of each chalcogen atom in the dimer remains equal to ~2. The dimers in the silicon lattice are shown to be stable, which is associated with a decrease in the total energy of the crystal during dimer formation. The calculated formation energies are equal to ~2.4 eV for S_2, ~1.9 for Se_2, and ~1.5 eV for Te_2. For calculating the dimer-formation energy, consideration of the relaxation of the lattice around impurity atoms is important.

In the case of the formation of more complicated impurity defects containing chalcogen atoms, the manifestation of special features in the properties of closed complexes should be expected. In particular, they can differ by a substantially higher formation energy and display properties of a very deep donor (or even neutral) center.

REFERENCES

1. F. Richou, G. Pelous, and D. Lecrosnier, Appl. Phys. Lett. **31** (8), 525 (1977).
2. H. G. Grimmeiss, E. Janzen, and B. J. Skarstam, J. Appl. Phys. **51**, 3740 (1980); **51**, 4212 (1980).
3. S. D. Brotherton, M. J. King, and G. J. Parker, J. Appl. Phys. **52** (7), 4649 (1981).
4. H. G. Grimmeiss, E. Janzen, H. Ennen, *et al.*, Phys. Rev. B **24** (8), 4571 (1981).
5. R. Schaub, G. Pensl, M. Schulz, and C. Holm, Appl. Phys. A **34**, 215 (1984).
6. G. Pensl, G. Roos, C. Holm, and P. Wagner, in *Defects in Semiconductors*, Ed. by H. J. von Bardeleben, Mater. Sci. Forum **10-12**, 911 (1986).
7. H. G. Grimmeiss, E. Janzen, and K. Larsson, Phys. Rev. B **25**, 2627 (1982).
8. E. Janzen, K. Larsson, R. Stedman, and H. G. Grimmeiss, J. Appl. Phys. **53**, 7520 (1982).
9. E. Janzen and H. G. Grimmeiss, J. Phys. C **15**, 5791 (1982).
10. E. Janzen, R. Stedman, G. Grossmann, and H. G. Grimmeiss, Phys. Rev. B **29**, 1907 (1984).
11. E. Janzen, G. Grossmann, R. Stedman, and H. G. Grimmeiss, Phys. Rev. B **31**, 8000 (1985).
12. W. E. Krag, W. H. Kleiner, and H. J. Zeiger, Phys. Rev. B **33**, 8304 (1986).
13. O. Meyer, N. G. E. Johansson, S. T. Picraux, and J. W. Mayer, Solid State Commun. **8**, 529 (1970).
14. T. F. Lee, R. D. Pashley, T. C. McGill, and J. W. Mayer, J. Appl. Phys. **46** (1), 381 (1975).
15. G. Foti, S. U. Campisano, E. Rimini, and G. Vitali, J. Appl. Phys. **49**, 2569 (1978).
16. A. A. Taskin, B. A. Zaĭtsev, V. I. Obodnikov, and E. G. Tishkovskiĭ, Fiz. Tekh. Poluprovodn. (St. Petersburg) **34**, 318 (2000) [Semiconductors **34**, 312 (2000)].
17. R. Worner and O. F. Schirmer, Solid State Commun. **51** (9), 665 (1984).
18. J. R. Niklas and J. M. Speath, Solid State Commun. **46** (2), 121 (1983).
19. A. B. Van Oosten and C. A. J. Ammerlaan, Phys. Rev. B **38**, 13291 (1988).
20. N. Achtziger and W. Witthuhn, Phys. Rev. Lett. **75**, 4484 (1995).
21. T. G. Brown and D. G. Hall, Appl. Phys. Lett. **49**, 245 (1986).
22. T. G. Brown, P. L. Bradfield, and D. G. Hall, Appl. Phys. Lett. **51**, 1585 (1987).
23. J. C. Swartz, D. H. Lemmon, and R. Thomas, Solid State Commun. **36**, 331 (1980).
24. H. G. Grimmeiss and E. Janzen, Mater. Res. Soc. Symp. Proc. **14**, 33 (1983).
25. V. Kalyanaraman, M. M. Chandra, and V. Kumar, J. Appl. Phys. **54**, 6417 (1983).

26. E. V. Astrova, I. B. Bol'shakov, A. A. Lebedev, and O. A. Mikhno, Fiz. Tekh. Poluprovodn. (Leningrad) **19**, 597 (1985) [Sov. Phys. Semicond. **19**, 371 (1985)].
27. H. R. Vydyanath, J. S. Lorenzo, and F. A. Kroger, J. Appl. Phys. **49**, 5928 (1978).
28. N. Sclar, J. Appl. Phys. **52**, 5207 (1981).
29. E. Sorman, W. M. Chen, A. Henry, *et al.*, Phys. Rev. B **51**, 2132 (1995).
30. M. S. Yunusov, S. Karimov, B. L. Oksengendler, and A. Yusupov, Fiz. Tekh. Poluprovodn. (St. Petersburg) **31**, 708 (1997) [Semiconductors **31**, 605 (1997)].
31. R. McWeeny and B. T. Sutcliffe, *Methods of Molecular Quantum Mechanics* (Academic, New York, 1969; Mir, Moscow, 1972).
32. S. S. J. Roothaan, Rev. Mod. Phys. **23**, 69 (1951).
33. M. W. Schmidt, K. K. Baldridge, J. A. Boats, *et al.*, J. Comput. Chem. **14**, 1347 (1993).
34. A. Zunger and U. Lindefelt, Phys. Rev. B **26**, 5989 (1982).
35. A. Zunger and U. Lindefelt, Phys. Rev. B **27**, 1191 (1983).
36. F. Beeler, O. K. Anderson, and M. Scheffler, Phys. Rev. Lett. **55**, 1498 (1985).
37. F. Beeler, O. K. Anderson, and M. Scheffler, Phys. Rev. B **41**, 1630 (1990).
38. G. G. DeLeo, G. D. Watkins, and W. B. Fowler, Phys. Rev. B **23**, 1851 (1981).
39. G. G. DeLeo, G. D. Watkins, and W. B. Fowler, Phys. Rev. B **25**, 4962 (1982).
40. L. A. Hemstreet, Phys. Rev. B **15**, 834 (1977).
41. L. A. Hemstreet and J. O. Dimmock, Phys. Rev. B **20**, 1527 (1979).
42. S. K. Estreicher, Phys. Rev. B **60**, 5375 (1999).
43. R. P. Messmer, in *Semiempirical Methods of Electronic Structure Calculation*, Ed. by G. Segal (Plenum, New York, 1977; Mir, Moscow, 1980), Part B, p. 272.
44. E. R. Davidson and D. Feller, Chem. Rev. **86**, 681 (1986).
45. I. Mayer, Int. J. Quantum Chem. **29**, 73 (1986).
46. I. Mayer, Int. J. Quantum Chem. **29**, 477 (1986).
47. V. A. Veryazov, A. V. Leko, and V. A. Évarestov, Fiz. Tverd. Tela (St. Petersburg) **41**, 1407 (1999) [Phys. Solid State **41**, 1286 (1999)].
48. W. J. Stevens, H. Brasch, and M. Krauss, J. Chem. Phys. **81**, 6026 (1984).
49. W. J. Stevens, H. Brasch, M. Krauss, and P. Jansien, Can. J. Chem. **70**, 612 (1992).
50. M. J. Frish, M. Head-Gordon, and J. A. Pople, Chem. Phys. Lett. **166**, 275 (1990).
51. P. Carsky and I. Hubac, Theor. Chim. Acta **80**, 407 (1991).
52. *Handbook of Physical Quantities*, Ed. by I. S. Grigoriev and E. Z. Meilikhov (Énergoatomizdat, Moscow, 1991; CRC Press, Boca Raton, 1997).
53. K.-P. Huber and G. Herzberg, *Molecular Spectra and Molecular Structure* (Van Nostrand, New York, 1979; Mir, Moscow, 1984).
54. L. V. Gurvich, G. V. Karachevtsev, V. N. Kondrat'ev, Yu. A. Lebedev, V. A. Medvedev, V. K. Potapov, and Yu. S. Khodeev, *Bond-Breaking Energies. Ionization Potentials and Electron Affinity*, Ed. by Academician V. N. Kondrat'ev (Nauka, Moscow, 1974).
55. A. A. Taskin and E. G. Tishkovskiĭ, Fiz. Tekh. Poluprovodn. (St. Petersburg) **32**, 1306 (1998) [Semiconductors **32**, 1162 (1998)].
56. J. J. P. Stewart, J. Comput. Chem. **10**, 209 (1989).

Translated by V. Bukhanov

Semiconductors, Vol. 36, No. 10, 2002, pp. 1091–1096. Translated from Fizika i Tekhnika Poluprovodnikov, Vol. 36, No. 10, 2002, pp. 1171–1176.

ATOMIC STRUCTURE AND NONELECTRONIC PROPERTIES OF SEMICONDUCTORS

Chemical Bonding and Elastic Constants of Certain Ternary III–V Solid Solutions

V. G. Deĭbuk* and Ya. I. Viklyuk**

Chernivtsi National University, Chernivtsi, 580012 Ukraine

** e-mail: vdei@chnu.cv.ua*

*** e-mail: vyklyuk@mail.ru*

Submitted March 4, 2002; accepted for publication March 19, 2002

Abstract—The chemical bonding of GaP, InP, InAs, InSb, and InBi binary compounds was investigated as well as the modification of the bonding in $Ga_xIn_{1-x}P$, $InAs_xSb_{1-x}$, and $InSb_{1-x}Bi_x$ semiconductor alloys; this modification occurs as a result of variation in the composition characterized by the parameter x. An approach based on the consideration of the total valence charge density, the chemical-bonding polarity, and the transverse effective charge was used. The elastic constants of the aforementioned ternary solid solutions were calculated, and the influence of chemical-bonding modification on these constants was analyzed. Local strains and composition disordering in the alloys under consideration drastically affect the dependences of the quantities under investigation on solid-solution composition. Thus, the above effects cannot be neglected in investigating substitutional solid solutions. © *2002 MAIK "Nauka/Interperiodica".*

1. INTRODUCTION

Chemical bonding in III–V semiconductors is the subject of intensive experimental and theoretical investigations [1, 2]. Recently, interest in ternary solid solutions on the basis of III–V compounds has increased, which is caused by their wide use in optoelectronic devices and by the wide region of variation of their electronic properties.

Despite the semiempirical nature of the models which describe the chemical bonding in III–V materials, scientists have managed to gain insight into the diversity of properties of many compounds. In particular, the model of ionicity introduced by Phillips [4] predicted the existence of a critical ionicity value f_c, which separates more covalent tetrahedrally bonded crystals (zinc blende and wurtzite) with an ionicity $f_i < f_c$ from more ionic octahedrally bonded crystals (rock salt) with an ionicity $f_i > f_c$. It should be noted that, although the approaches for determining the ionicity proposed by Pauling [5], Phillips [4], and Harrison [6] yield good results, they require knowledge of empirical parameters.

Another approach for describing the chemical bonding is the notion of bonding polarity introduced in terms of the pseudopotential theory in [7] as a measure of the pseudopotential asymmetry. The introduced chemical-bonding polarity α_p made it possible to correctly explain many physical properties, in particular, mechanical properties and elastic constants.

In [8], the authors proposed using the measurement of asymmetry in the spatial distribution of a valence charge g as a parameter which represented the ionicity of bonding. The evolution of charge density in upper valence bands, as well as polarity and transverse effective charge, as a result of varying the composition of a solid-solution can yield a realistic pattern of the influence of diverse alloying effects (composition disordering, local strains, etc.) on the character of chemical bonding.

In this study, we present a theoretical analysis of the chemical-bonding modification in $Ga_xIn_{1-x}P$, $InAs_xSb_{1-x}$, and $InSb_{1-x}Bi_x$ semiconducting solid solutions. Such a choice of solid solutions is not accidental and is governed by the characteristic features of their band structure. For example, a band gap $E_g(x)$ has a characteristic minimum at $x = 0.37$ in $InAs_xSb_{1-x}$; here, the value of E_g is lower for a solid solution than it is for InAs and InSb binary compounds. In $Ga_xIn_{1-x}P$, the dependence $E_g(x)$ has a transition point ($x = 0.652$) at which the alloy transforms from a direct-gap one into an indirect-gap one. A characteristic feature of the $InSb_{1-x}Bi_x$ solid solution is the transition to the semimetallic state with $E_g = 0$ at $x = 0.4$.

The purpose of this study is to investigate the modification of the character of bonding in semiconductor alloys when the composition x is varied. We used an approach based on the consideration of total valence charge density, chemical-bonding polarity, and transverse effective charge. Furthermore, in this study, we calculated the elastic constants for the indicated ternary solid solutions and analyzed the influence of modification of chemical bonding on these constants.

1063-7826/02/3610-1091$22.00

2. CALCULATION PROCEDURE

We obtained the electronic band structure of binary III–V compounds by the method of local model pseudopotential in the plane-wave basis with allowance for spin–orbit interaction. The substitutional solid solutions were simulated in the approximation of modified virtual crystal, which takes into account the effects of composition disordering and local strains arising in alloys [9].

The total charge density $\rho(\mathbf{r})$ of valence electrons was calculated using a scheme of integration over symmetry points [10] according to

$$\rho(\mathbf{r}) = 2e\sum_{n,\mathbf{k}}|\psi_{n,\mathbf{k}}(\mathbf{r})|^2, \tag{1}$$

where $\psi_{n,\mathbf{k}}(\mathbf{r})$ is the electron wave function obtained from the solution of the secular equation, and n is the band number.

According to [8], the charge density can be divided into symmetric $\rho_S(\mathbf{r})$ and antisymmetric $\rho_A(\mathbf{r})$ components:

$$\begin{aligned}\rho_S(\mathbf{r}) &= \frac{1}{2}[\rho(\mathbf{r}) + \rho(-\mathbf{r})],\\ \rho_A(\mathbf{r}) &= \frac{1}{2}[\rho(\mathbf{r}) - \rho(-\mathbf{r})].\end{aligned} \tag{2}$$

Passing to the Fourier series

$$\rho(\mathbf{r}) = \sum_G \rho(\mathbf{G})e^{i\mathbf{G}\mathbf{r}}, \tag{3}$$

we form the Fourier components $\rho_S(\mathbf{G})$ and $\rho_A(\mathbf{G})$:

$$\begin{aligned}\rho_S(\mathbf{G}) &= \frac{1}{2}[\rho(\mathbf{G}) + \rho^*(\mathbf{G})],\\ \rho_A(\mathbf{G}) &= \frac{1}{2}[\rho(\mathbf{G}) - \rho^*(\mathbf{G})].\end{aligned} \tag{4}$$

The charge-asymmetry coefficient [8] is given by

$$g = \sqrt{\frac{S_A}{S_S}}, \tag{5}$$

where

$$\begin{aligned}S_S &= \sum_{\mathbf{G}}|\rho_S(\mathbf{G})|^2 = \frac{1}{\Omega}\int_\Omega \rho_S^2(\mathbf{r})d\mathbf{r},\\ S_A &= \sum_{\mathbf{G}}|\rho_A(\mathbf{G})|^2 = \frac{1}{\Omega}\int_\Omega \rho_A^2(\mathbf{r})d\mathbf{r},\end{aligned} \tag{6}$$

and Ω is the unit-cell volume.

The chemical-bonding polarity α_p [7] represents the asymmetry of the pseudopotential

$$\alpha_p = -\frac{V_3^A}{V_3^S}, \tag{7}$$

where V_3^A and V_3^S are the antisymmetric and symmetric form factors of the pseudopotential for $\mathbf{G} = \frac{2\pi}{a}(111)$.

The calculation of α_p enables us to find the transverse effective charge e_T^* [7]:

$$2e_T^* = -\Delta Z + \frac{8\alpha_p}{1+\alpha_p^2}, \tag{8}$$

where

$$\Delta Z = -Z_A + (1-x)Z_B + xZ_C. \tag{9}$$

The quantity e_T^* characterizes the infrared activity of phonons in materials and is a basic parameter which describes the dielectric properties of solids and can be used for classification of the crystal structure. Furthermore, this parameter is very sensitive to the influence of the anharmonic crystal potential. The contribution of anharmonic effects to the effective charge can manifest itself in solid solutions due to the fact that the composition disordering gives rise to significant anharmonicity. In addition, according to Harrison [6], the effective charge is equal to

$$Z^* = e_T^* - \frac{8}{3}\alpha_p(1-\alpha_p^2). \tag{10}$$

The elastic constants of solid solutions are parameters which give important information about the nature of chemical bonding. We calculated them according to [11] as

$$\begin{aligned}C_{11} &= \frac{\sqrt{3}}{4d^5}\Big[0.43\frac{\hbar^2}{m}(5+\lambda)(1-\alpha_p^2)^{3/2}\\ &\quad -\frac{3}{4}(1-\alpha_p^2)^{1/2}\Big|-0.81\frac{\hbar^2}{m}\Big|\Big],\\ C_{12} &= \frac{\sqrt{3}}{4d^5}\Big[0.43\frac{\hbar^2}{m}(3-\lambda)(1-\alpha_p^2)^{3/2}\\ &\quad +\frac{3}{4}(1-\alpha_p^2)^{1/2}\Big|-0.81\frac{\hbar^2}{m}\Big|\Big],\end{aligned} \tag{11}$$

where $d = \sqrt{3}\,a/4$ is the bond length (a is the lattice constant), and λ is the dimensionless parameter equal to 0.738 [11].

3. RESULTS OF CALCULATIONS AND DISCUSSION

The special features of band-gap variation with a change in the composition of $In_{1-x}Ga_xP$, $InAs_xSb_{1-x}$, and $InSb_{1-x}Bi_x$ solid solutions are shown in Fig. 1; in our previous studies [9, 12, 13], we analyzed these features in detail. However, the band gap doesn't correspond unambiguously to such an important parameter as the degree of ionicity of the bonding introduced by Phillips [4]. The search for a correlation between the band structure and the ionicity of the chemical bonding leads to the notion of a heterogeneous gap [14], which corresponds to the energy discontinuity in the electron density of states in the valence band at the point X of the Brillouin zone. In Table 1, we list the heterogeneous-gap values E_g in binary compounds obtained in our calculations of the band structure. If we proceed in the direction of the growth of the charge number of an anion with the cation fixed, the well-known tendency to decrease the degree f_i of the ionicity of bonding (first discovered by Phillips) is observed in the InP, InAs, InSb, and InBi sequence. However, this tendency is violated with respect to the heterogeneous gap, which somewhat incorrectly describes the special features of the chemical bonding.

We can gain insight into the modification of the chemical bonding for the tetrahedrally coordinated binary compounds by analyzing the charge-density distribution for valence electrons (Fig. 2). If the charge number of an anion increases, the maximum of the charge density $\rho(r)$ shifts to the bond midpoint leading to an increase in the degree of covalency and, therefore, to a decrease in the degree of ionicity. For the quantitative characteristic of the chemical bonding, it is convenient to use the notion of a charge-asymmetry coefficient g (5) as a direct measure of the ionicity of the bonding. The values of g that we calculated for binary compounds are given in Table 1 and agree satisfactorily with theoretical data [8]. Small discrepancies can be explained by differences in the methods used for the calculation of the band structure. In Fig. 3, we show the charge-asymmetry coefficient g as a function of the composition of the alloys under consideration. The consideration of such characteristic alloying effects as local strains and composition disordering leads to the nonlinear behavior of $g(x)$. The indicated factors only

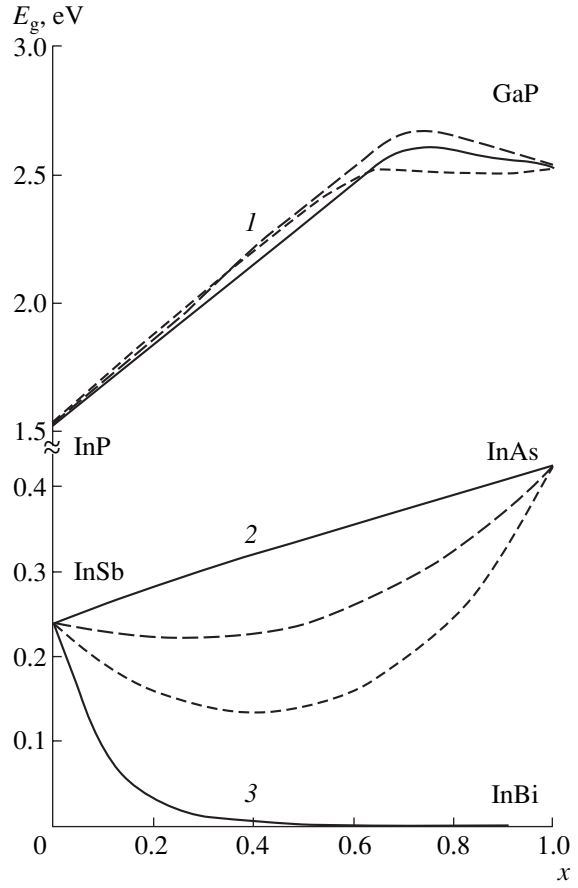

Fig. 1. Concentration dependences of the band gap E_g for (*1*) $In_{1-x}Ga_xP$, (*2*) $InAs_xSb_{1-x}$, and (*3*) $InSb_{1-x}Bi_x$ solid solutions. The calculation conditions: solid curves are the virtual-crystal approximation, the dashed curves are calculated taking into account internal local strains, and the dotted curves are obtained taking into account the internal local strains and the composition disordering.

Table 1. Lattice constant a, the band gap E_g, a heteropolar gap E_h, the degree f_i of ionicity, the polarity α_p, and the charge-asymmetry coefficient g for binary compounds

Compound	a, Å	E_g, eV	E_h, eV	f_i	α_p		g	
				[4]	[15]	our calculations	[8]	our calculations
GaP	5.45	2.53	5.07	0.327	0.31	0.438	0.371	0.398
InP	5.86	1.52	6.29	0.421	0.32	0.504	0.506	0.462
InAs	6.055	0.42	6.33	0.357	0.3	0.336	0.45	0.454
InSb	6.478	0.24	3.89	0.321	0.29	0.22	0.294	0.385
InBi	6.64	0	2.94	–	–	0.174	–	0.344

Note: Data from study [15] are experimental.

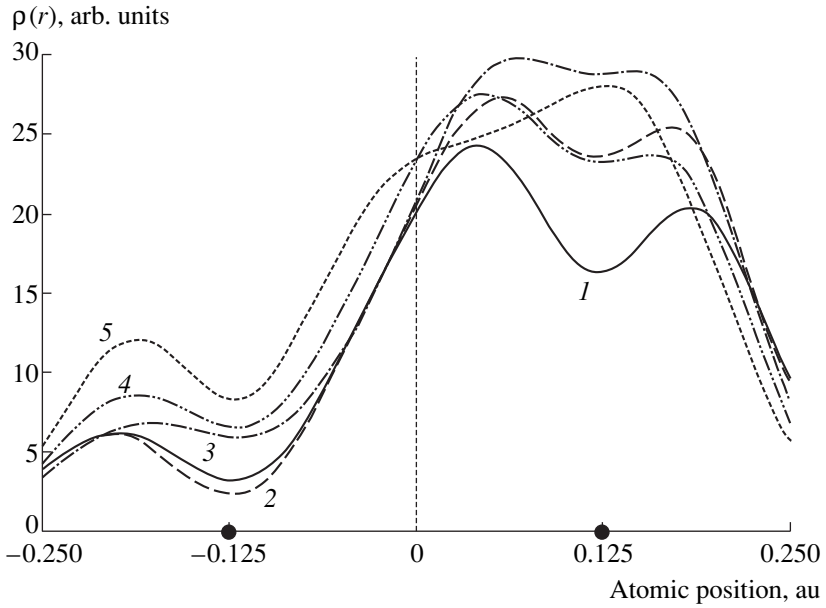

Fig. 2. Distributions of charge density for valence electrons in binary compounds along the [111] bond: (*1*) GaP, (*2*) InP, (*3*) InAs, (*4*) InSb, and (*5*) InBi. The positions of atoms are indicated in atomic units.

slightly affect the behavior of $E_g(x)$ in comparison with the virtual-crystal approximation in $In_{1-x}Ga_xP$ and $InSb_{1-x}Bi_x$, but their influence on the charge-density-asymmetry coefficient is rather profound. At the same time, the reverse situation is true for the $InAs_xSb_{1-x}$ alloy. We also note that the characteristic points in the reconstruction of the band structure for the solid solutions under consideration can be noticed in the concentration dependences $g(x)$ (Fig. 3).

As was noted in the Introduction, these points correspond to solid-solution compositions for which the following features can be observed:

(i) a transition of the conduction-band minimum from the point Γ of the Brillouin zone to the point *X* for $x = 0.652$ in $In_{1-x}Ga_xP$;

(ii) a minimum in the dependence $E_g(x)$ for $x = 0.37$ in $InAs_xSb_{1-x}$;

(iii) a transition to the zero-gap state for $x = 0.4$ in $InSb_{1-x}Bi_x$.

The polarity α_p is a concept which is also related to ionicity. However, as can be seen from expression (7), contrary to the charge-density-asymmetry coefficient, α_p represents the asymmetry of the pseudopotential at the point $G(111)$. The concentration dependences of the polarity in the alloys under consideration (Fig. 4) qualitatively resemble similar dependences $g(x)$ in Fig. 3. This fact can be attributed to a close correlation between the pseudopotential form factors and the corresponding quantities (6) which determine the charge-density asymmetry. In Fig 5, we compare the charge-asymmetry coefficient g with the polarity α_p for the binary semiconducting compounds under consider-

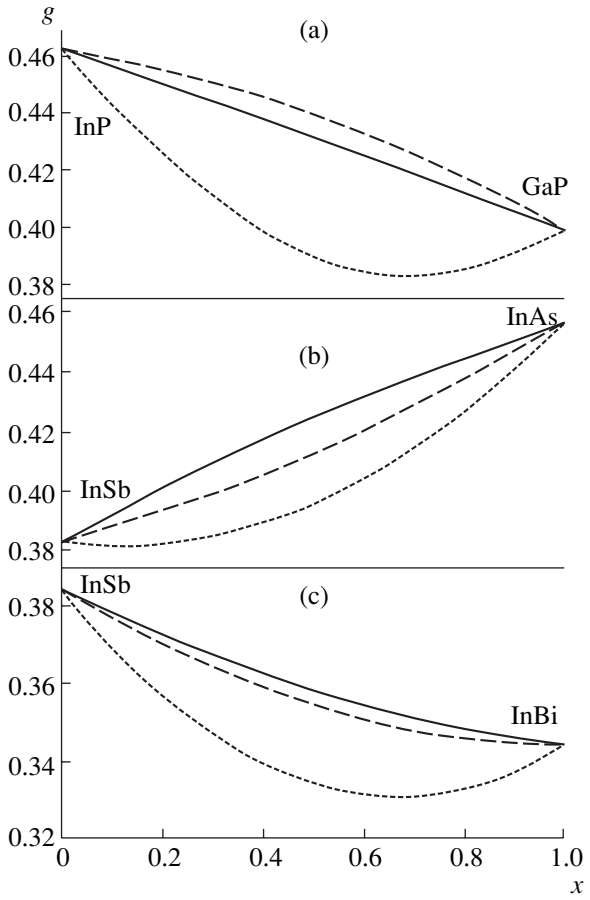

Fig. 3. Charge-asymmetry coefficient g as a function of a solid-solution composition x for (a) $In_{1-x}Ga_xP$, (b) $InAs_xSb_{1-x}$, and (c) $InSb_{1-x}Bi_x$. The conditions of calculation for solid, dashed, and dotted curves are the same as in Fig. 1.

ation. The linear correlation between these quantities justifies the use of the charge-density-asymmetry coefficient as a measure of the ionicity of chemical bonding. Furthermore, in our opinion, it is the quantity g that represents most completely the integral character of the spatial distribution of the valence charge in a crystal, in contrast to the polarity α_p, which is the ratio between antisymmetric and symmetric pseudopotential form factors only at a single point of the reciprocal space.

The transverse effective charge e_T^* is a fundamental quantity in the lattice dynamics of semiconductors; it determines the long-range component of the elastic constants in the long-wavelength region of the spectrum and can be measured experimentally. On the basis of relationships (8) and (9), we calculated e_T^* both for binary compounds and for the corresponding alloys. Good agreement between the obtained values of the transverse effective charge and experimental values (Table 2) gives grounds for predicting its variation in a solid solution. Evidently, this quantity is also influenced profoundly both by local strains and by composition disordering which occur in the semiconducting solid solutions and can be another quantitative characteristic of the ionicity of bonding. Approximating the calculated concentration dependence of the transverse effective charge for solid solutions, we obtain

$$e_T^* = 2.47x + 2.607(1-x) - 0.7x(1-x), \quad \text{for} \quad In_{1-x}Ga_xP, \tag{12}$$

$$e_T^* = 2.21x + 1.83(1-x) - 0.45x(1-x), \quad \text{for} \quad InAs_xSb_{1-x}, \tag{13}$$

$$e_T^* = 1.676x + 1.83(1-x) - 0.35x(1-x), \quad \text{for} \quad InSb_{1-x}Bi_x. \tag{14}$$

The obtained values of the polarity enable us to calculate the elastic constants for both binary compounds and their ternary substitutional solid solutions. In Table 2, we list values of the elastic constants C_{11} and C_{12} which we calculated for GaP, InP, InAs, InSb, and InBi binary compounds according to (11). The good agreement between these values and experimental data enables us to carry out an approximation for the corresponding solid solutions (C_{11} and C_{12} are given in units of 10^{-11} dyn/cm^2):

for $In_{1-x}Ga_xP$,

$$C_{11} = 14.3x + 10.2(1-x) + 6.1x(1-x),$$
$$C_{12} = 7.7x + 5.49(1-x) + 3.3x(1-x); \tag{15}$$

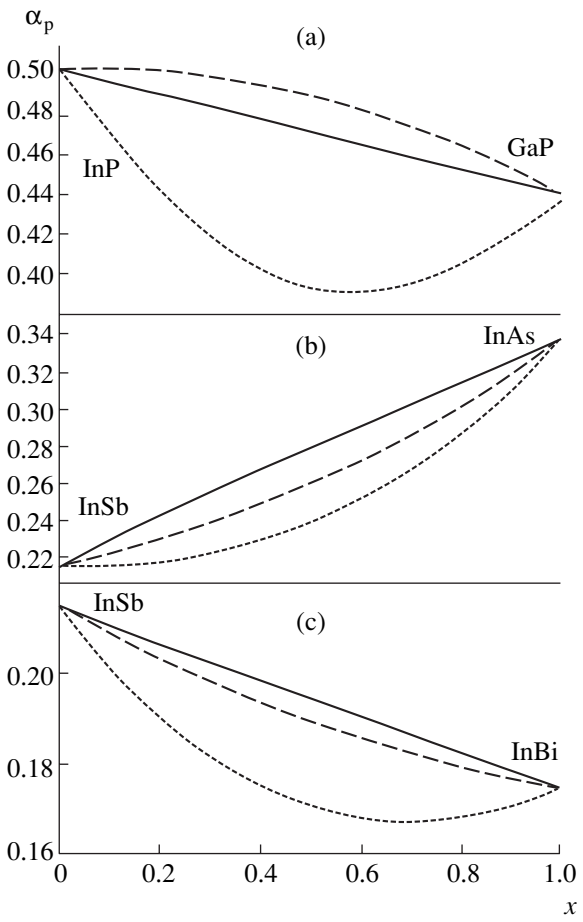

Fig. 4. Concentration dependences of the degree of polarity for the chemical bonding: (a) $In_{1-x}Ga_xP$, (b) $InAs_xSb_{1-x}$, and (c) $InSb_{1-x}Bi_x$.

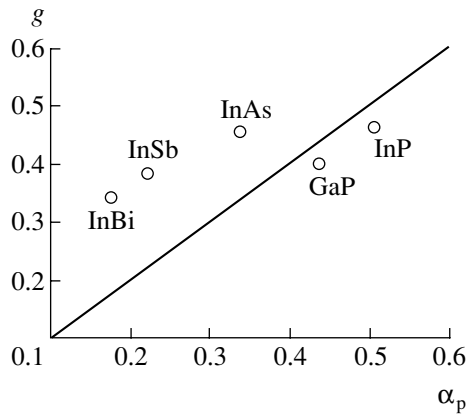

Fig. 5. Comparison of the polarity α_p and the charge-asymmetry coefficient g for binary compounds.

for $InAs_xSb_{1-x}$,

$$C_{11} = 8.391x + 6.967(1-x) + 1.4x(1-x),$$
$$C_{12} = 4.518x + 3.752(1-x) + 0.75x(1-x); \tag{16}$$

Table 2. Transverse effective charge e_T^*, effective charge Z^*, and elastic constants C_{11} and C_{12} for binary compounds

Compound	e_T^*		Z^*		C_{11}, 10^{-11} dyn/cm^2		C_{12}, 10^{-11} dyn/cm^2	
	[16]	our calculations	[6]	our calculations	[3]	our calculations	[3]	our calculations
GaP	2.04	2.47	1.01	1.526	14.39	14.3	6.52	7.7
InP	2.55	2.607	1.32	1.605	10.22	10.2	5.76	5.49
InAs	2.45	2.21	1.22	1.413	8.329	8.391	4.526	4.518
InSb	2.28	1.83	1.1	1.275	6.918	6.967	3.788	3.752
InBi	–	1.676	–	1.226	5.75*	5.803	3.1*	3.124

Note: Data from studies [3, 6, 16] are experimental. * Values obtained by the linear interpolation of data for In and Bi [17].

for $InSb_{1-x}Bi_x$,

$$C_{11} = 5.803x + 6.967(1-x) + 0.25x(1-x),$$
$$C_{12} = 3.124x + 3.752(1-x) + 0.13x(1-x). \quad (17)$$

4. CONCLUSIONS

Local strains and composition disordering in the alloys under consideration lead to an increase in elastic constants and to the nonlinearity of their dependences on the composition of a solid-solution. Thus, the above effects cannot be neglected in calculations of both effective charges and elastic constants for $In_{1-x}Ga_xP$, $InAs_xSb_{1-x}$, and $InSb_{1-x}Bi_x$ solid solutions. The obtained variations in the transverse effective charge and the elastic constants represent a variation in chemical bonding and, as a consequence, in the electron structure depending on the composition of an alloy.

REFERENCES

1. J. R. Chelikowsky, Phys. Rev. B **34**, 5295 (1986).
2. N. E. Christensen, S. Satpathy, and Z. Pawlowska, Phys. Rev. B **36**, 1032 (1987).
3. A. Chen and A. Sher, *Semiconductor Alloys: Physics and Materials Engineering* (Plenum, New York, 1995).
4. J. C. Phillips, *Bonds and Bands in Semiconductors* (Academic, New York, 1973).
5. L. Pauling, *The Nature of the Chemical Bond and the Structure of Molecules and Crystals* (Cornell University Press, Ithaca, 1960, 3rd. ed.).
6. W. A. Harrison, *Electronic Structure and the Properties of Solids: The Physics of the Chemical Bond* (Freeman, San Francisco, 1980; Mir, Moscow, 1983).
7. P. Vogl, J. Phys. C **11**, 251 (1978).
8. A. Garcia and M. L. Cohen, Phys. Rev. B **47**, 4215 (1993).
9. Ya. I. Viklyuk, V. G. Deĭbuk, and S. V. Zolotarev, Fiz. Tekh. Poluprovodn. (St. Petersburg) **36** (8), 925 (2002) [Semiconductors **36**, 863 (2002)].
10. D. J. Chadi and M. L. Cohen, Phys. Rev. B **8**, 6287 (1973).
11. N. E. Baranowski, J. Phys. C **17**, 6287 (1984).
12. V. G. Deĭbuk, Ya. I. Viklyuk, and I. M. Rarenko, Fiz. Tekh. Poluprovodn. (St. Petersburg) **33**, 289 (1999) [Semiconductors **33**, 293 (1999)].
13. V. G. Deĭbuk, Ukr. Fiz. Zh. **43**, 230 (1998).
14. J. R. Chelikowsky, T. J. Wagener, J. H. Weaver, and A. Jin, Phys. Rev. B **40**, 9644 (1989).
15. C. Falter, W. Ludwig, M. Selmke, and W. Zierau, Phys. Lett. A **105A**, 139 (1984).
16. K. Aoki, E. Anastassakis, and M. Cardona, Phys. Rev. B **30**, 681 (1984).
17. I. N. Frantsevich, *Elastic Constants and Elastic Moduli of Metals and Nonmetals* (Naukova Dumka, Kiev, 1982).

Translated by V. Bukhanov

Semiconductors, Vol. 36, No. 10, 2002, pp. 1097–1105. Translated from Fizika i Tekhnika Poluprovodnikov, Vol. 36, No. 10, 2002, pp. 1177–1185.

ATOMIC STRUCTURE AND NONELECTRONIC PROPERTIES OF SEMICONDUCTORS

The Nucleation of Coherent Semiconductor Islands during the Stranski–Krastanov Growth Induced by Elastic Strains

S. A. Kukushkin*, A. V. Osipov*, F. Schmitt, and P. Hess****

** Institute of Problems in Machine Science, Russian Academy of Sciences, Vasil'evskii ostrov, Bol'shoi pr. 61, St. Petersburg, 199178 Russia*

e-mail: oav@math.ipme.ru

*** Institute of Physical Chemistry, University of Heidelberg, INF 234, 69120 Heidelberg, Germany*

Submitted March 18, 2002; accepted for publication March 22, 2002

Abstract—The Ge island growth on the Si(100) and Si(111) surfaces was investigated through spectral ellipsometry in real time. It is found that both cases correspond to Stranski–Krastanov growth; i.e., a Ge wetting layer is initially formed, and only then do the islands of the new phase grow on the surface of this layer. However, the island nucleation on the (100) surface is accompanied by a substantial decrease in the wetting layer thickness, whereas, on the (111) surface, the islands nucleate and grow on the wetting layer of constant thickness. The Ge atoms on the (100) surface transfer from the wetting layer to islands, thus substantially decreasing the elastic energy of the system, but increasing the surface energy. For this reason, it is concluded that, in this case, it is the elastic energy which represents the fundamental driving force of the island nucleation. Thermodynamic and kinetic theories of island nucleation from the wetting layer under the effect of elastic energy are developed. A new notion of overstress is introduced by analogy with supersaturation and overcooling. The time evolution of the wetting layer thickness, the nucleation rate, and the island surface density of the new phase is described. The theoretical results are compared to experimental data obtained through ellipsometric simulation, and it is found that the theory and experiment are in good agreement. *© 2002 MAIK "Nauka/Interperiodica".*

1. INTRODUCTION

At present, the self-aligned Stranski–Krastanov growth of coherent semiconductor islands, which contain no lattice mismatch defects, is actively used for obtaining ordered structures with nanodimensional quantum dots (QDs) [1, 2]. The great interest in such structures is due to the prospects of their practical implementation in optoelectronics in relation to the localization of charge carriers in the vicinity of QDs [3]. In order to control the island shape during island growth, it is necessary to determine the driving force of nucleation. Two principle mechanisms exist. The first mechanism is the classic nucleation due to a high density of adsorbed atoms on the wetting-layer surface. The second mechanism is the nonclassic nucleation from the atoms of the wetting layer itself under the effect of elastic energy [1, 2, 4–7]. In the first case, the free energy of the island decreases due to the difference in chemical potentials of the atoms in the two-dimensional adsorbate gas and in the island itself. In the second case, the free energy decreases due to the difference between chemical potentials of the atoms in the wetting layer and in the island. In this case, the chemical potential is determined by the difference between the elastic energy and wetting energy. The island growth by the first mechanism occurs on a wetting layer of constant thickness. In the second case, the thickness of the wetting layer should decrease during the nucleation. The reason is that part of the atoms of the wetting layer transfer to islands primarily to decrease the elastic energy [1, 7].

The purpose of this study is to determine the driving force and the mechanism of island nucleation of a new phase for one of the classic Stranski–Krastanov systems (Ge-on-Si) and to develop the respective theory. The investigations were carried out for the growth on the Si(100) and Si(111) surfaces. It is well known that the growth mode for these surfaces is quite different [2]. To measure the wetting layer thickness and the total volume of islands in real time, spectroscopic ellipsometry was used.

2. DIAGNOSTICS OF ISLAND FORMATION BY SPECTROSCOPIC ELLIPSOMETRY

2.1. Experimental Procedure

The Ge films were deposited by chemical vapor deposition in a vacuum chamber equipped with a spectroscopy ellipsometer and a mass-spectrometer. Digermane Ge_2H_6, which was diluted with pure He, was used as the precursor in the pressure range from 4×10^{-6} to 3×10^{-5} mbar. The sample temperature was measured with an infrared pyrometer. Island dimensions and densities were measured using an atomic force microscope, which operated in the contact mode with ultralevel tips.

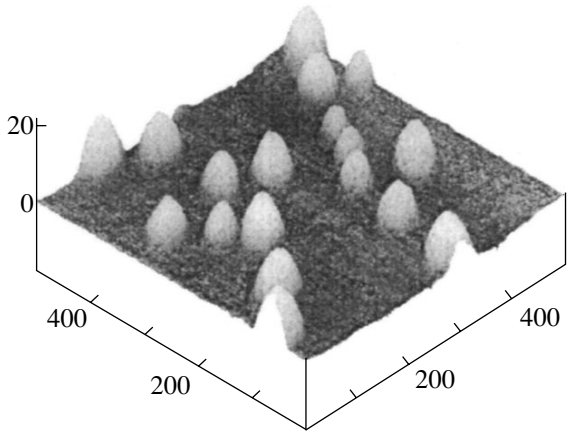

Fig. 1. Image of the Ge coherent islands on Si(100) at T = 500°C and the average deposition rate of 2 monolayers per minute; the image was obtained using an atomic force microscope. Dimensions along the axes are expressed in nanometers.

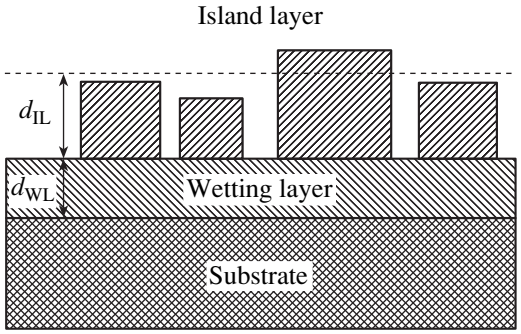

Fig. 2. Two-layer growing-film model based on the optical constants measured; d_{WL} and d_{IL} are the thicknesses of the wetting layer (WL) and the island layer (IL), respectively.

The *p*-Si(100) and *p*-Si(111) surfaces ($\rho > 300\ \Omega$ cm) with a cleavage angle less than 0.3° were used. The surfaces were cleaned using the Shiraki method and were faceted in pure NH_4F. The surfaces obtained, which were terminated with H, were then tested using infrared Fourier spectroscopy to obtain information on the homogeneity of surface chemical bonds of H.

2.2. Spectroscopy Ellipsometry

A Sopra-E54G-OMA ellipsometer with a rotating polarizer was used in the photon energy range of 1.2–4.7 eV. The angle of beam incidence was chosen close to 77°, which corresponds to the Brewster angle for crystalline Si at approximately the midpoint of the energy range given. The exact value of the angle of incidence was determined separately for each experiment using the best agreement of measured optical constants for Si and spectra given in the literature [8]. The optical constants of the film and substrate materials, which are necessary for ellipsometric simulation, were measured at the deposition temperature over the entire photon energy range. Ellipsometers with a time resolution from 1.5 to 3 s per spectrum were used.

2.3. Results of Experiments and Ellipsometric Simulation

The images obtained using an atomic force microscope demonstrate that the islands of the new phase are formed both at the (100) surface and at the (111) surface (Fig. 1). Specifically, for the Si(100) surface at T = 500°C, the average island height is about 10 nm and the base size is about 50 nm for a deposition rate of 2 monolayers per minute (the height of the coherent Ge monolayer on Si(100) $h_0 \approx 0.145$ nm). For the Si(111) surface, the size of the Ge islands is larger by a factor of 5–8. For example, at T = 570°C and a deposition rate of 0.35 bilayers per minute (the height of the coherent Ge bilayer on Si(111) $h_0 \approx 0.357$ nm), the island height is approximately 50 nm and the base size is approximately 400 nm. This means that the growth rate for the separate Ge island on the (111) surface is significantly higher compared to that on the (100) surface. The island surface density depends heavily on the precursor gas pressure. For the experiments described, this density was equal to 7×10^9 cm^{-2} for Si(100) and 0.5×10^9 cm^{-2} for Si(111).

It was found that the optical constants measured in real time agree best with simulation using the two-layer model (Fig. 2). According to this model, the growing film can be conventionally divided into two layers: the wetting layer (WL) and the island layer (IL). Each of these two layers consists of two Ge components and voids.

In order to calculate the optical constants for each layer, we used the Brüggemann approximation of the effective medium [9], which mixes these two components. Thus, four parameters of minimization were used for the ellipsometric simulation. These were the wetting layer thickness d_{WL}, the Ge fraction in the wetting layer c_{WL}, the island layer thickness d_{IL}, and the Ge fraction in the island layer c_{IL}. Mixing between Si and Ge was neglected, since the films were deposited at temperatures lower than the lowest temperature at which the interdiffusion between Ge and Si is observed (600°C). From the mathematical point of view, these two layers differ only in that the Ge content in the wetting layer (0.7–1.0) is noticeably higher compared to that in the island layer (0–0.3). In order to minimize the standard error, the quasi-Newton method was used, which is the most suitable for the minimization of ravine functions. This method makes it possible to clearly separate the wetting and island layers and determine the thickness of the wetting layer and the Ge concentration in it. For the island layer, it is impossible to separate the parameters d_{IL} and c_{IL}, since the correlation between them is too strong. However, their product $d_{IL}c_{IL}$, which specifies the total Ge amount in islands,

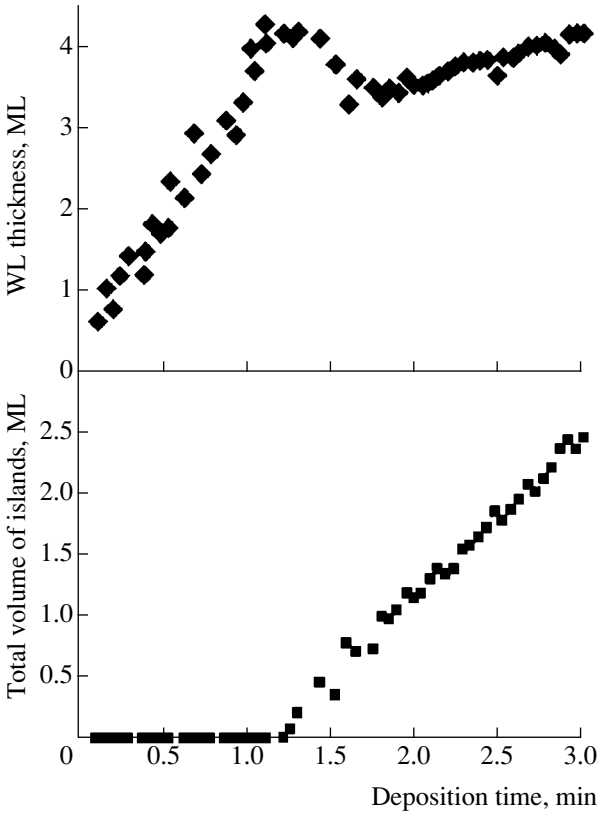

Fig. 3. Thickness of the wetting layer (WL) and the total Ge amount in the islands measured in monolayer (ML) units in relation to the deposition time for the Si(100) surface at T = 500°C. Experiment.

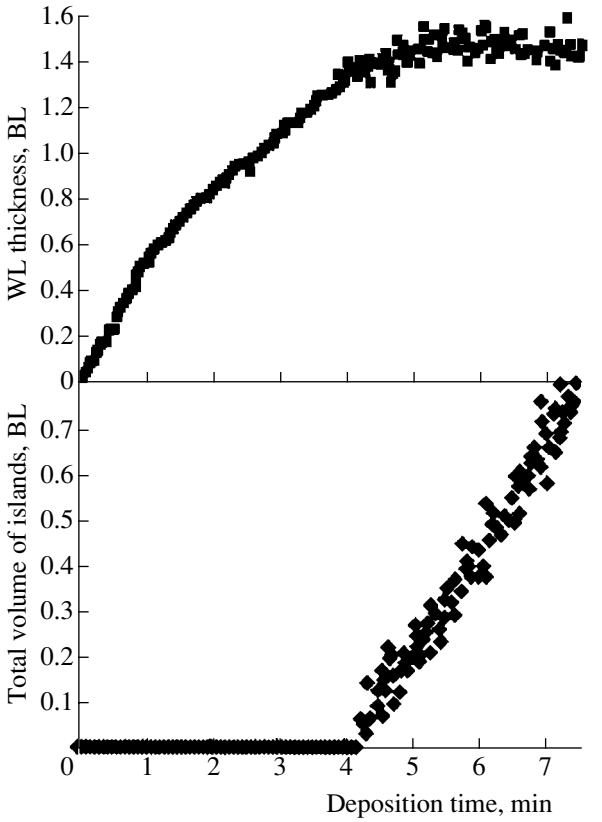

Fig. 4. Thickness of the wetting layer (WL) and the total Ge amount in the islands measured in bilayer (BL) units in relation to the deposition time for the Si(111) surface at T = 570°C. Experiment.

shows no strong correlation with the parameters of the wetting layer and can be determined easily. This is obviously associated with the fact that the upper boundary of the island layer is determined at a much lesser accuracy compared with the interface between the wetting and island layers.

The main results of the ellipsometry measurements in real time are as follows. The island nucleation of the new phase on the (100) surface is accompanied by a considerable decrease in the wetting-layer thickness (by ~1 monolayer) (see Fig. 3). Consequently, the nucleation proceeds mainly owing to the atoms of the wetting layer. This result is in good agreement with the results in [10], which were obtained for the Ge/Si(100) system at 600°C using Rutherford backscattering and atomic force microscopy. The main cause of this phenomenon consists in the fact that the wetting layer is in the overstressed metastable state. The nucleation of islands and an increase in their height is energetically favorable despite weakening the attraction of atoms to the substrate and increasing the free surface, since this leads to a considerable lowering of the elastic energy [1]. In other words, the dislocation-free mechanism of relaxation of the elastic energy, which is caused by the Si–Ge lattice mismatch (~4.2%), manifests itself in this system.

The island nucleation on the (111) surface proceeds in another way (Fig. 4). Here, the islands nucleate and grow on the wetting layer, which virtually retains its thickness. The growth apparently occurs due to the supersaturation by the atoms adsorbed at the wetting-layer surface; i.e., the classical growth mechanism is observed [4, 5]. The possible causes of distinctions between growth mechanisms were discussed, for example, in [2, 11].

In what follows, we develop a theory of island nucleation of the new phase from the overstressed metastable wetting layer.

3. THEORY

The following mechanism of the formation of coherent islands, which is based on our experimental data on the Ge-on-Si(100) growth, is considered. Initially, the layer-by-layer growth of the Ge film on the Si substrate occurs, since the Si surface energy is noticeably higher than the Ge surface energy, and wetting is favorable. However, Ge and Si have different lattice parameters, and the elastic energy increases with film growth (the elastic energy per atom is constant). The wetting energy per atom continuously decreases, since the Ge atoms are removed farther and farther apart from

the substrate. At the instant when the elastic energy per atom is equalized to the wetting energy per atom for the upper atoms of the wetting layer, the layer itself is in equilibrium. However, the wetting layer continues to grow and becomes metastable, making it possible for the elastic energy to relax. One of the possible ways of relaxation is nuclei formation on the wetting layer surface, since the higher clusters have a higher elastic energy compared with the lower clusters [11]. This process sets in when the nucleation barrier becomes low enough. Due to this, the nuclei formed grow and reduce the elastic energy of the film, and the wetting layer becomes thinner thus supplying the growing islands with atoms. After some time, the nucleation process will be completed, since a decrease in the wetting layer thickness will lead to heightening of the nucleation barrier. It is this process that will be described below.

3.1. Thermodynamic Model of the Formation of Coherent Islands

The free energy of the formation of a coherent island from the wetting layer is represented by three summands:

$$F = \Delta F_{\text{surf}} - (\Delta F_{\text{elas}} - \Delta F_{\text{att}}). \quad (1)$$

Here, ΔF_{surf} is an increase in the surface energy due to the formation of an additional surface of the film material, ΔF_{elas} is a decrease in the free energy due to the elastic energy relaxation within the island, and ΔF_{att} is an increase in the free energy due to weakening of the attraction (wetting) of the island atoms to the substrate. It is evident that the energy parenthesized in relationship (1) is the only driving force of this nucleation process. Each of the three quantities in relationship (1) depends not only on the number of atoms in the island but also on its shape. This is the distinction of this model from the classic theory of nucleation [5]. To calculate the ΔF_{surf}, ΔF_{elas}, and ΔF_{att} quantities, the simplest island configuration will be used below. Specifically, we assume that a parallelepiped-shaped island with a square base L and height H lies on the wetting strained layer with a height h. For such an island configuration with two parameters L and H, all results can be obtained in the analytical form. Let us calculate the free energy F as a function of two parameters: L and H.

Since the film's additional surface area caused by the formation of the parallelepiped-shaped island is equal to $4LH$, then

$$\Delta F_{\text{surf}} = 4\sigma_f LH, \quad (2)$$

where σ_f is the surface tension of the film material. The ΔF_{elas} quantity can be calculated in the context of the Ratsch–Zangwill model [12]. According to this model, the effective parameter of the lattice mismatch decreases as one passes from the bottom atomic layer to the top layer. This is caused by the fact that the top layer contains an additional number ($\Lambda/2$) of relaxed atoms at each island edge compared to the situation in the bottom layer [12]. For such an island shape, this means that the island elastic energy is equal to

$$F_{\text{elas}}^{\text{isl}} = \lambda\varepsilon_0^2 L^2 h_0 \sum_{k=0}^{H/h_0 - 1} \left(1 - \frac{\Lambda l_0}{L}\right)^{4k}, \quad (3)$$

since the effective parameter of the lattice mismatch for the kth layer is equal to [12]

$$\varepsilon_k = \varepsilon_0 \left(1 - \frac{\Lambda l_0}{L}\right)^{2k}. \quad (4)$$

Here, $\varepsilon_0 = (d_f - d_s)/d_s$ is the lattice mismatch between the film and a substrate, d_f is the lattice parameter for the film, d_s is the lattice parameter for the substrate, λ is the elastic modulus, h_0 is the height of the monolayer film, and l_0 is the average interatomic distance in the same layer. The sum involved in relationship (3) constitutes a geometric progression and, for this reason, can be calculated analytically as

$$F_{\text{elas}}^{\text{isl}} = \lambda\varepsilon_0^2 L^2 h_0 \frac{1 - \left(1 - \frac{\Lambda l_0}{L}\right)^{4H/h_0}}{1 - \left(1 - \frac{\Lambda l_0}{L}\right)^4}. \quad (5)$$

It was demonstrated that the results obtained from this model are in good agreement with the results of numerical simulation using the method of finite elements for $\Lambda = 3\pi/2$ [12]. For $3\pi l_0/2L \ll 1$, it is possible to use the approximation $(1 - 3\pi l_0/2L)^4 \approx 1 - 6\pi l_0/L$. For large values $4H/h_0$, it is possible to assume that

$$1 - (1 - 3\pi l_0/L)^{4H/h_0} \approx 1.$$

The latter approximation means that all atoms on the island top are relaxed, which is often observed experimentally for sufficiently tall islands. Since the elastic energy of the same number of atoms in the wetting layer is equal to

$$F_{\text{elas}}^{\text{WL}} = \lambda\varepsilon_0^2 L^2 H, \quad (6)$$

the gain in the elastic energy with island formation is equal to

$$\Delta F_{\text{elas}} = F_{\text{elas}}^{\text{WL}} - F_{\text{elas}}^{\text{isl}} \approx \lambda\varepsilon_0^2 L^2 H \left(1 - 6\pi \frac{h_0/l_0}{H/L}\right). \quad (7)$$

The attraction energy of the film atoms to the substrate can be calculated using the Müller–Kern model [13]. According to this model, the attraction energy of the film atoms, which lie immediately on the substrate, is determined by the difference in the specific interfa-

cial energies of the surfaces of the substrate (σ_s), the film (σ_f), and the interface between them (σ_{s-f}):

$$\Phi_\infty = \sigma_s - \sigma_f - \sigma_{s-f}. \quad (8)$$

If k monolayers of the film are positioned between the atoms of the film and the substrate, their attraction energy is lowered. Specifically, it is possible to consider that, for semiconductors, this lowering is exponential [13]:

$$\Phi(k) = \Phi_\infty e^{-k/k_0}, \quad (9)$$

where k_0 is the attenuation coefficient.

The expenditure of energy for island formation equals the difference in the attraction energy of atoms on the wetting layer surface,

$$F_{\text{elas}}^{\text{WL}} = \Phi_\infty e^{-h/h_0k_0}\frac{HL^2}{h_0} \quad (10)$$

and the attraction energy of island atoms,

$$\begin{aligned} F_{\text{att}}^{\text{isl}} &= \Phi_\infty \exp\left(\frac{-h/h_0+1}{k_0}\right)L^2\sum_{k=0}^{H/h_0-1} e^{-k/k_0} \\ &= \Phi_\infty \exp\left(\frac{-h/h_0+1}{k_0}\right)L^2\frac{1-e^{H/h_0k_0}}{1-e^{-1/k_0}}. \end{aligned} \quad (11)$$

The summation in relationship (11) is carried out analytically, since the sum represents a geometric progression. For $H/h_0 \gg (e^{1/k_0}-1)^{-1}$, $F_{\text{att}}^{\text{WL}}$ is much larger than $F_{\text{att}}^{\text{isl}}$. Consequently,

$$\Delta F_{\text{att}} \approx F_{\text{att}}^{\text{WL}}. \quad (12)$$

Thus, the free energy of formation of the parallelepiped-shaped island can be estimated as

$$\begin{aligned} F &\approx \Delta F_{\text{surf}} + F_{\text{elas}}^{\text{isl}} - (F_{\text{elas}}^{\text{WL}} - F_{\text{att}}^{\text{WL}}) \approx 4\sigma_f LH \\ &+ 6\pi\lambda\varepsilon_0^2 L^3\frac{h_0}{L_0} - \left(\lambda\varepsilon_0^2 - \frac{\Phi_\infty}{h_0}e^{-h/h_0k_0}\right)HL^2. \end{aligned} \quad (13)$$

The parenthesized expression in the last summand of relationship (13) evidently represents the difference in chemical potentials of the atoms on the wetting layer surface and in the island. If this difference is positive, island formation is possible in the system, since the gain in the elastic energy can be larger than its expenditure on overcoming the attractive forces and increasing the free energy. Otherwise, the wetting forces are stronger and the layer-by-layer growth of the film is observed. According to classical nucleation theory, we linearize this difference over the driving force of nucleation. For this purpose, let us introduce the equilibrium thickness of the wetting layer

$$h_{\text{eq}} = h_0k_0\ln\frac{\Phi_\infty}{\lambda\varepsilon_0^2h_0}. \quad (14)$$

If $h < h_{\text{eq}}$, then, according to the Müller–Kern criterion [13], layer-by-layer growth is observed. For $h > h_{\text{eq}}$, the transition $2D \longrightarrow 3D$ sets in, which is accompanied by decreasing the free energy due to the gain in the elastic energy. For this reason, the island formation depends on the quantity $\xi \equiv h/h_{\text{eq}} - 1$ in this case. By analogy with the concepts of supersaturation and overcooling, we will refer to the ξ quantity as the overstress. In this case, for small ξ, it is possible to use the approximation of the classical theory of nucleation:

$$\begin{aligned} \lambda\varepsilon_0^2 - \frac{\Phi_\infty}{h_0}e^{-h/h_0k_0} &= \lambda\varepsilon_0^2\left\{1-\exp\left[-\xi\ln\left(\frac{\Phi_\infty}{\lambda\varepsilon_0^2h_0}\right)\right]\right\} \\ &\approx \lambda\varepsilon_0^2\xi\ln\frac{\Phi_\infty}{\lambda\varepsilon_0^2h_0}. \end{aligned} \quad (15)$$

Finally, from relationships (13) and (15), we derive

$$\begin{aligned} F(L,H,\xi) &= 4\sigma_f LH \\ &+ 6\pi\lambda\varepsilon_0^2L^3\frac{h_0}{l_0} - \lambda\varepsilon_0^2\xi HL^2\ln\frac{\Phi_\infty}{\lambda\varepsilon_0^2h_0}. \end{aligned} \quad (16)$$

It is convenient to rewrite expression (16) in the dimensionless form using new variables: the number of atoms in the island $i = HL^2/h_0l_0^2$ and the characteristic ratio $\beta = H/L$,

$$\frac{F(i,\beta,\xi)}{k_BT} = ai^{2/3}\beta^{1/3} + b\frac{i}{\beta} - c\xi i. \quad (17)$$

Here, k_B is the Boltzmann constant, T is the temperature,

$$a = \frac{4\sigma_f(h_0l_0^2)^{2/3}}{k_BT}, \quad b = \frac{\kappa}{6\pi}\frac{h_0}{l_0}, \quad c = \kappa\gamma, \quad (18)$$

$\kappa = \lambda\varepsilon_0^0 h_0 l_0^2/k_BT$ is the elastic-to-thermal energy ratio, and $\gamma = \ln(\Phi_\infty/\lambda\varepsilon_0^2 h_0)$ is the constant characterizing the wetting-to-elastic force ratio. For the Ge island growth on the Si(100) surface, we have $\sigma_f = 800$ erg/cm^2, $\Phi_\infty = 450$ erg/cm^2 $= 1.27 \times 10^{12}$ dyn/cm, $\varepsilon_0 = 0.042$, $h_0 = 0.145$ nm, and $l_0 = 0.395$ nm. Consequently, $\kappa \approx 0.48$, $\gamma \approx 2.6$, and

$$a \approx 20, \quad b \approx 0.01, \quad c \approx 1.3. \quad (19)$$

From here on, we use these quantities for estimations in calculations. The dependence F/k_BT on i and β for these

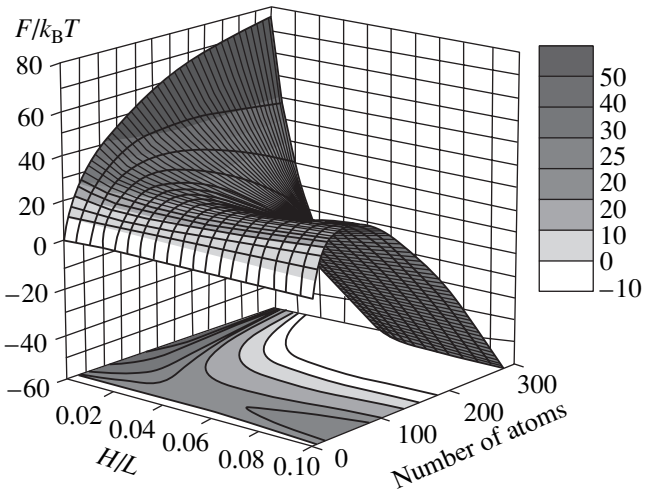

Fig. 5. Free-energy surface for the formation of a coherent island with a saddle point. The number of atoms in the island and the geometric proportion $\beta = H/L$ are plotted along the axis in the horizontal plane.

values of constants and for $\xi = 1.15$ is shown in Fig. 5. It can be seen that the free energy has a saddle point through which the nucleation actually proceeds [14].

To find the parameters of the saddle point, it is necessary to solve the set of equations $\partial F/\partial i = 0$, $\partial F/\partial\beta = 0$. In the case of the simplified expression (17) for the free energy, this can be done analytically:

$$i_c = \frac{3ba^3}{c^4\xi^4}, \quad \beta_c = \frac{3b}{c\xi},$$
$$H_0(\xi) = \frac{F(i_c, \beta_c, \xi)}{k_BT} = \frac{ba^3}{c^3\xi^3}. \tag{20}$$

It can be seen from expressions (18) and (20) that $H_0 \propto h_0/l_0$. For this reason, the formation of coherent islands on the (100) surface proceeds much more easily compared to the (111) surface, since the (111) surface is much denser. For example, $h_0/l_0 = 0.37$ for Ge/Si(100), whereas $h_0/l_0 = 1.4$ for Ge/Si(111). When $\xi = 1.15$ and the parameters a, b, and c have the above-indicated values, it is easy to estimate the parameters of the saddle point from expression (18): $i_c \approx 50$, $\beta_c \approx 0.02$, and $H_0 \approx 24$.

3.2. Nucleation Rate

Let us now calculate the formation rate of coherent islands. The main distinction from the classical one-parameter model of nucleation [5] is the fact that the free energy in this case depends on two parameters, i and β, rather than on one parameter. For this reason, thermal fluctuations affect both of these parameters, which leads to the two-parameter Zel'dovich equation

$$\frac{\partial g(i, \beta, t)}{\partial t} = D_i\frac{\partial}{\partial i}\left(\frac{\partial g}{\partial i} + \frac{1}{k_BT}\frac{\partial F}{\partial i}g\right) + D_\beta\frac{\partial}{\partial\beta}\left(\frac{\partial g}{\partial\beta} + \frac{1}{k_BT}\frac{\partial F}{\partial\beta}g\right). \tag{21}$$

Here, g is the distribution function of coherent islands by their size and shape; t is time; and D_i and D_β are the reciprocal times of variation per unit of i and β quantities, respectively (diffusivities in space of dimensions and shapes). The initial and boundary conditions for Eq. (21) are conventional; i.e.,

$$g(i, \beta, 0) = 0, \quad \left.\frac{g}{g_{eq}}\right|_{i\to 0} \longrightarrow 1, \quad \left.\frac{g}{g_{eq}}\right|_{\beta\to 0} \longrightarrow 1,$$
$$\left.\frac{g}{g_{eq}}\right|_{i\to\infty} \longrightarrow 0, \quad \left.\frac{g}{g_{eq}}\right|_{\beta\to 0} \longrightarrow 0, \tag{22}$$

where $g_{eq} = l_0^{-2}\exp(-F/k_BT)$ is the equilibrium function of island distribution. To solve Eq. (21) with conditions (22), it is sufficient to make allowance for the behavior of the F/k_BT function in the vicinity of the saddle point. For this reason, it is convenient to bring this function to the quadratic form

$$\frac{F(i, \beta, \xi)}{k_BT} = H_0 - A_{11}(i - i_c)^2 + A_{12}(i - i_c)(\beta - \beta_c) + A_{22}(\beta - \beta_c)^2, \tag{23}$$

$$A_{11} = \frac{c^5\xi^5}{27ba^5}, \quad A_{12} = \frac{2c^2\xi^2}{27b}, \quad A_{22} = \frac{2a^3}{27bc\xi}, \tag{24}$$

where H_0 is the nucleation-barrier height in k_BT units.

In order to eliminate the cross terms in Eq. (23) and, consequently, in the boundary conditions, let us introduce new variables

$$j = \sqrt{A_{11} + \frac{A_{12}^2}{2A_{22}}}(i - i_c), \tag{25}$$

$$\alpha = \sqrt{A_{22}}(\beta - \beta_c) + \frac{A_{12}}{2\sqrt{A_{22}}}(i - i_c). \tag{26}$$

In this case, Eq. (23) takes the form

$$\frac{F}{k_BT} = H_0 - j^2 + \alpha^2. \tag{27}$$

However, the cross terms now emerge in the kinetic equation (21). In order to eliminate them, it is necessary

to carry out the Lorentz transformation [15]

$$x = \frac{j + z\alpha}{\sqrt{1 - z^2}}, \quad y = \frac{zj + \alpha}{\sqrt{1 - z^2}}, \tag{28}$$

which leaves invariant quadratic form (27)

$$F/k_B T = H_0 - x^2 + y^2,$$

and then to choose the transformation parameter z so that the cross term in Eq. (21) approaches zero. This leads to the quadratic equation in z, which is solved analytically. As a result, an equation with separable variables is derived for the g function. This equation can be easily solved in the steady-state case for $\partial g/\partial t = 0$. This yields the steady-state nucleation rate

$$I(\xi) = Dl_0^{-4} Z e^{-H_0(\xi)}. \tag{29}$$

Here, D is the volume diffusivity in the wetting layer, and Z is the dimensionless Zel'dovich factor, which is calculated by the above method. The estimations demonstrate that this factor lies in the range of 0.1–10; for the above constants and the condition $D_\beta(i_c, \beta_c)/D_i(i_c, \beta_c) \ll 1$, we have $Z \approx 1$. For this reason, we assume in what follows that $Z = 1$.

The estimations of the time of attaining the steady-state solution (29) (they are performed similarly to the one-parameter case) demonstrate that it is in the range of 10^{-4}–10^{-2} s. This is much shorter compared to the characteristic time of nucleation of 1–10 s. For this reason, the quasi-steady-state approximation can be used for the nucleation rate

$$I(t) = Dl_0^{-4} \exp\left(-\frac{ba^3}{c^3 \xi^3(t)}\right). \tag{30}$$

3.3. Evolution of the Overstress

Thus, in order to describe the nucleation, it is necessary to calculate the time dependence of overstress $\xi(t)$. It is possible to do this using the law of conservation of matter on the substrate:

$$\frac{dh}{dt} = J(t) - l_0^2 h_0 \int_0^\infty v_i g(i, t) di. \tag{31}$$

Here, $J(t)$ is the flow of matter, which is directed to the substrate and increases the wetting layer thickness and, correspondingly, stresses in them; and $v_i \equiv di/dt$ is the rate of island growth due to elastic stresses. The elastic stresses in the wetting layer cause the diffusion of atoms to the island, since the stresses in the island are weaker than those in the layer. Let us estimate the rate of such growth v_i from the relationship

$$v_i = \frac{D}{k_B T l_0^2 h_0} \nabla\mu S. \tag{32}$$

Here, D is the diffusivity; $\nabla\mu$ is the gradient of the chemical potential, which is caused by the elastic stresses, at the island boundary; and S is the area across which the atoms are incorporated into the island. For small islands, only the surface atomic flux across the interface between the island and the wetting layer, which has a length $4L$ and thickness h_0, is significant. The bulk flux is less important due to the small dimensions of the island. The stress field around the island is a complex function of coordinates. For this reason, let us only roughly estimate the gradient of the chemical potential at the interface as

$$\nabla\mu \approx \frac{\Delta\mu}{\lambda_l L} = \frac{c k_B T \xi}{\lambda_l L}. \tag{33}$$

Here, $\Delta\mu$ is the difference between atomic chemical potentials for the layer and for the island, which is equal to $k_B T c \xi$ for islands whose size is much larger than the critical one. The λ_l quantity is the cutoff parameter of the elastic stresses, which indicates the magnitude of spread of the elastic perturbation from the island. Usually, $\lambda_l \gg 1$; we will assume that $\lambda_l = 10$. Finally,

$$v_i = \frac{4Dc\xi}{\lambda_l l_0^2}. \tag{34}$$

Substituting this expression into Eq. (31) and performing transformations, we obtain

$$\frac{d\xi}{dt} = j_0(t) - \frac{4Dh_0 c\xi}{l_l h_{eq}} N(t), \tag{35}$$

where $j_0(t) = J/h_{eq}$ is the elastic stress flow, and

$$N(t) = \int_0^\infty g(i, t) di = \int_0^t I(\xi(t')) dt'$$

is the surface density of the islands. Dividing this equation by ξ and taking a derivative with respect to time with allowance made for formula (30), we obtain the final equation for the evolution of the wetting-layer

$$\begin{cases} \xi'' - \xi'^2/\xi + j_0(t)\xi'/\xi - j_0'(t) = G(\xi), \\ \xi(0) = -1, \quad \xi'(0) = j_0(0), \end{cases} \tag{36}$$

where

$$G(\xi) = \begin{cases} (4h_0 c/h_{eq} v)\xi \exp(-ba^3/c^3\xi^3), & \xi > 0, \\ 0, & \xi \le 0. \end{cases} \tag{37}$$

This equation can be easily solved numerically for each $j_0(t)$. In this study, the following expression was used:

$$j_0(t) = (j_1 + j_2)/2 - [(j_1 - j_2)/2] \tanh[(t - t_0)/t_k];$$

it describes the transition from the flow j_1 to the flow j_2 ($j_1 > j_2$) in the time interval from $t_0 - t_*$ to $t_0 + t_*$. This expression approximately corresponds to the experi-

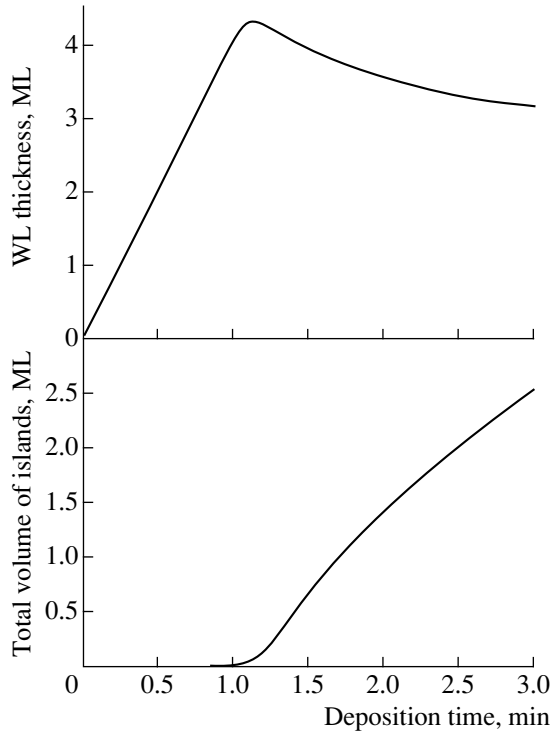

Fig. 6. Thickness of the wetting layer (WL) and the total Ge amount in the islands measured in monolayer (ML) units in relation to the deposition time for the Si(100) surface at T = 500°C. Calculation.

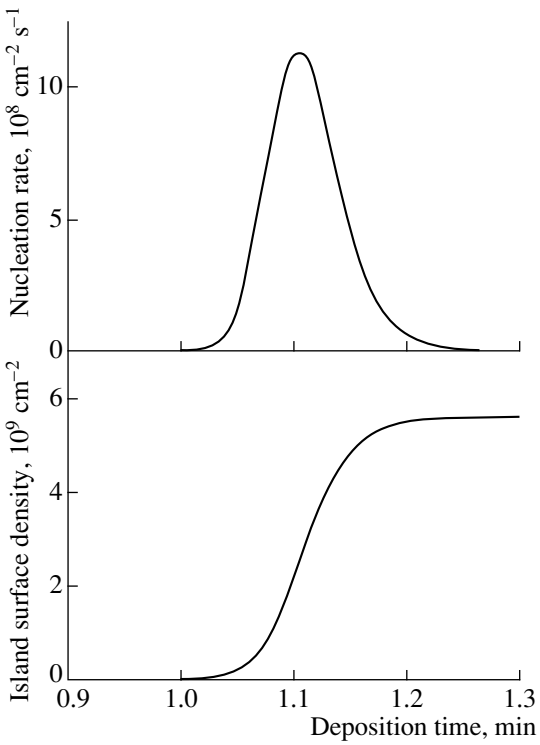

Fig. 7. Theoretical dependences of the nucleation rate and island surface density on the deposition time of Ge on the Si(100) surface at T = 500°C.

mental results which were obtained by simulating the ellipsometry data. A decrease in the flow during nucleation is apparently associated with the fact that the wetting layer becomes smoother and denser, which decreases the probability of incorporating the atoms in this layer. In addition, the formation of dislocations sets in, which also decreases the elastic stress.

For the numerical calculations, the following parameters were used: $D = 10^{-11}$ cm^2 s^{-1}, $j_1 = 2$, $j_2 = 1$, $t_* = 3$ s (the t_* quantity was chosen to be approximately equal to the time of reaching the highest nucleation rate), $h_{eq}/h_0 = 2$, $a = 20$, $b = 0.02$, $c = 1.3$, and $l_0 = 0.395$ nm. The largest overstress for these constants equals $\xi_{max} = 1.15$. The results of calculations based on Eq. (36) are shown in Figs. 6 and 7. It can be seen that the theoretical results are in good agreement with the ellipsometric experimental data (see Fig. 3). The final value of the surface density is also consistent with the experimental data. The main distinction between experiment and theory consists in the fact that the wetting layer begins to grow again at the final stage of deposition in actual systems. This can be explained by two factors. First, when the islands reach a certain size, the elastic stresses give rise to a kinetic barrier for incorporating the atoms into the islands [16]. In this case of self-restricting growth, the island growth rate v_i decreases and, correspondingly, the wetting layer thickness increases. Second, dislocation formation can set in in actual systems. The dislocations reduce the elastic stresses in the wetting layer and, correspondingly, increase h_{eq}. This can also lead to an increase in the wetting layer thickness.

4. CONCLUSION

Thus, based on the theoretical and experimental data obtained, the following conclusions can be made. The Ge islands on Si(100) nucleate from the atoms of the wetting layer itself, whereas, on Si(111), they nucleate from the atoms adsorbed on the wetting layer surface. During the growth on the (100) surface, the elastic stresses in the wetting layer constitute the driving force of the growth. In this case, nucleation is accompanied by a decrease in the wetting layer thickness. The thermodynamic model of the formation of coherent islands, which is based on the notion of overstress (by analogy with supersaturation and overcooling), adequately describes the experimental data on the evolution of coherent islands and a wetting layer.

ACKNOWLEDGMENTS

This study was supported in part by the Russian Foundation for Basic Research (project nos. 02-02-17216 and 02-03-32471) and the German Scientific Foundation DFG.

A. V. Osipov thanks the Humboldt Scientific Foundation (Germany) for financial support.

REFERENCES

1. V. A. Shchukin and D. Bimberg, Rev. Mod. Phys. **71**, 1125 (1999).
2. O. P. Pchelyakov, Yu. B. Bolkhovityanov, A. V. Dvurechenskiĭ, *et al.*, Fiz. Tekh. Poluprovodn. (St. Petersburg) **34**, 1281 (2000) [Semiconductors **34**, 1229 (2000)].
3. Zh. I. Alferov, Fiz. Tekh. Poluprovodn. (St. Petersburg) **32**, 3 (1998) [Semiconductors **32**, 1 (1998)].
4. A. V. Osipov, F. Schmitt, S. A. Kukushkin, and P. Hess, Phys. Rev. B **64**, 205 421 (2001).
5. S. A. Kukushkin and A. V. Osipov, Usp. Fiz. Nauk **168**, 1083 (1998) [Phys. Usp. **41**, 983 (1998)].
6. Yu. B. Bolkhovityanov, O. P. Pchelyakov, and S. I. Chikichev, Usp. Fiz. Nauk **171**, 689 (2001).
7. V. A. Shchukin, N. N. Ledentsov, P. S. Kop'ev, and D. Bimberg, Phys. Rev. Lett. **75**, 2968 (1995).
8. T. Yasuda and D. E. Aspnes, Appl. Opt. **33**, 7435 (1994).
9. G. E. Jellison, Thin Solid Films **234**, 416 (1993).
10. T. I. Kamins, G. Medeiros-Ribeiro, D. A. A. Ohlberg, and R. S. Williams, J. Appl. Phys. **85**, 1159 (1999).
11. I. Berbeizer, B. Gallas, A. Ronda, and J. Derrien, Surf. Sci. **412**/**413**, 415 (1998).
12. C. Ratsch and A. Zangwill, Surf. Sci. **293**, 123 (1993).
13. P. Müller and R. Kern, Appl. Surf. Sci. **102**, 6 (1996).
14. S. A. Kukushkin and A. V. Osipov, J. Phys. Chem. Solids **56**, 831 (1996).
15. F. M. Kuni and A. A. Melikhov, Teor. Mat. Fiz. **83**, 274 (1990).
16. M. Kästner and B. Voigtländer, Phys. Rev. Lett. **82**, 2745 (1999).

Translated by N. Korovin

Semiconductors, Vol. 36, No. 10, 2002, pp. 1106–1110. Translated from Fizika i Tekhnika Poluprovodnikov, Vol. 36, No. 10, 2002, pp. 1186–1190.

ATOMIC STRUCTURE AND NONELECTRONIC PROPERTIES OF SEMICONDUCTORS

Investigation of Vacancy-Type Complexes in GaN and AlN using Positron Annihilation

N. Yu. Arutyunov*, A. V. Mikhaĭlin*, V. Yu. Davydov, V. V. Emtsev**^, G. A. Oganesyan**, and E. E. Haller*****

** Institute for Electronics, Tashkent 700143, Uzbekistan*

*** Ioffe Physicotechnical Institute, Russian Academy of Sciences, Politekhnicheskaya ul. 26, St. Petersburg, 194021 Russia*

^e-mail: emtsev@pop.ioffe.rssi.ru

**** Department of Material Science and Engineering, University of California at Berkeley, CA 94720, Berkeley, USA*

Submitted February 28, 2002; accepted for publication April 1, 2002

Abstract—The momentum distribution of electron–positron pairs in GaN and AlN has been investigated for the first time by measuring the one-dimensional angular correlation of the annihilation radiation (1*D*-ACAR). The characteristic parameter of the electron density r_s' (the radius of the sphere occupied by an electron) estimated from the experimental data differs noticeably from r_s calculated in terms of a standard model of noninteracting particles: $r_s'(\mathrm{AlN}) \approx 1.28 r_s$, and $r_s'(\mathrm{GaN}) \approx 1.66 r_s$, where $r_s(\mathrm{AlN}) \approx 1.6091$ au, and $r_s(\mathrm{GaN}) \approx 1.6568$ au. The chemical nature of atoms in the environment of the annihilating positron in AlN and GaN was identified from the electron–positron ionic radius of Al^{3+}, Ga^{3+}, and N^{5+} cores, which were determined from the characteristics of the high-momentum component of 1*D*-ACAR curves. The analysis was based on a comparison of the electron–positron ionic radii with those considered standard for Al and Ga metals and the related compounds GaP, GaAs, and GaSb. A conclusion is made that positron annihilation dominates in the regions of vacancy-type "nitrogen antisite"–"vacancy" complexes, $[N_{Ga}^{+} V_{Ga}]$ and $[N_{Al}^{+} V_{Al}]$, in GaN and AlN, respectively.

1. INTRODUCTION

As is known, positrons emitted from a radioactive source into a sample under study are localized in the course of their thermalization in regions with negative effective charge [1]. This charge defines the electron density around a positron [1, 2] and the electron–positron ionic radius characterizing the chemical nature of atoms in the nearest environment of an annihilating positron [3, 4]. Different point defects in the material under study exert their influence on the annihilation parameters, so a positron can be regarded as a particle probing the electronic structure of a defect [5–7].

In this study, we made a successful attempt at probing the lattice point defects in AlN and GaN with positrons. Pairs of gamma quanta, emitted upon electron–positron annihilation from the vicinity of a defect, were detected by means of the high-precision measurement of angular correlations [8]. This technique for the detection of annihilating pairs [9] enables an estimation of the average density of the annihilating electrons and definite conclusions concerning the configuration in which Al and Ga ions are incorporated into the positron-sensitive defects in AlN and GaN.

2. EXPERIMENTAL PROCEDURE

The resolution of the precision spectrometer of angular correlations was ≈0.9 mrad [3]. A configuration with long collimator slits placed before the detectors of the annihilation-produced gamma quanta provided for the recording of the so-called one-dimensional angular correlation of the annihilation radiation (1*D*-ACAR) [8, 9]. In the range of detected angles $\Delta\theta \approx 6$–15 mrad, the statistical error of measurements, which allows correct determination of the electron–positron radius, varied from ≈1.1 to ≈5.3%. The screening of detectors and the device stability provided a very low background level, less than 0.4% of the count rate at the peak of the 1*D*-ACAR curve [3, 5]. The 1*D*-ACAR curves were recorded at a temperature of 18°C.

The derivative of the 1*D*-ACAR function with respect to momentum, which is necessary for the determination of the momentum distribution density of the electron–positron pairs, was calculated using a standard smoothing procedure of the 1*D*-ACAR spectra [8, 9]. An annealed chemically pure Al sample was used to determine the electron–positron radius of the Al^{3+} ion core, which served as a reference in the study of AlN. To determine reliable values of the electron–positron

ionic radius in GaN, its value was compared with the relevant data obtained for chemically pure Ga and binary semiconductors GaP, GaAs, and GaSb. Ga (of 99.99999% purity) samples were Czochralski-grown *n*-type GaP:S, GaAsP:Te, and GaSbP:S with a carrier density $n \approx (3\text{–}7) \times 10^{17}$ cm^{-3} at $T = 300$ K, and with a dislocation density no higher than $\approx 10^4$ cm^{-2}. The largest full width at half-maximum (FWHM) of the 1*D*-ACAR curves was $\theta_{1/2}(\mathrm{GaP}) \approx 5.1$ mrad, $\theta_{1/2}(\mathrm{GaAs}) \approx 4.95$ mrad, and $\theta_{1/2}(\mathrm{GaSb}) \approx 4.5$ mrad, which is typical of perfect crystals [4, 10].

3. 1*D*-ACAR AND THE ELECTRON MOMENTUM DISTRIBUTION IN ALN AND GAN

The 1*D*-ACAR curves for AlN and GaN are typical of crystals with ionic–covalent atomic bonding in the crystal lattice (see Fig.1). The absence of a specific "narrow" component in the 1*D*-ACAR curves attests to the very low probability of positronium formation and annihilation in the nitrides under study. Evaluation of the average density of valence electrons in terms of a model of noninteracting particles in an isotropic Fermi gas of electrons [1] yields $r_s(\mathrm{AlN}) \approx 1.6091$ au and $r_s(\mathrm{GaN}) \approx 1.6568$ au (r_s is the radius of a sphere occupied by an electron). The FWHM ($\theta_{1/2}$) of the 1*D*-ACAR spectral curve, which was calculated from the relation $\theta_{1/2}$ (mrad) $\approx 9.923 r_s^{-1}$ (au) [10], is slightly larger for AlN than for GaN: $\theta_{1/2}(\mathrm{AlN}) \approx 6.17$ mrad and $\theta_{1/2}(\mathrm{GaN}) \approx 5.99$ mrad. In both materials, the experimental $\theta_{1/2}$ values appeared to be smaller than the calculated ones: $\theta_{1/2}(\mathrm{AlN, exp.}) \approx 5.85$ mrad and $\theta_{1/2}(\mathrm{GaN, exp.}) \approx 4.9$ mrad.

For the electron densities specified above, the positron screening length is only weakly dependent on the chemical nature of atoms in the solid state; it equals ≈ 2 au [11]. The increased electron density around a positron slightly enhances the annihilation rate. This effect is manifested much more weakly in 1*D*-ACAR parameters than in the positron lifetime measurements [2], so it will not be discussed further.

A thermalized positron makes a relatively small contribution to the total momentum of the annihilating pair $p_{e^+e^-}$, and the principal parameters of the pair momentum distribution are determined by the electron momentum p_{e^-}. The probability of detecting a pair of annihilation quanta with a total momentum $p \approx p_{e^+e^-} \approx p_{e^-}$ is proportional to the average momentum:

$$I(\theta) \cong \int_0^\infty p\rho(p)dp, \qquad (1)$$

where $\rho(p)$ is the momentum distribution density for electrons, $p \approx p_z \approx \theta m_0 c$; θ is the detection angle of a pair of annihilation gamma quanta; p_z is the momentum component perpendicular to the axis of detector rotation that sets the angle of the recording of the annihilation radiation by detectors (for details, see [8] and references therein). In the nitrides under study, AlN and GaN, the function $\rho(p)$, reconstructed from the 1*D*-ACAR data, demonstrates a form typical of the Fermi distribution, which is usually observed in materials with a high ionic component in their chemical bonding (see Fig. 2 and Ref. [6]). The Fermi momentum p_F corresponds to the FWHM of the momentum distribution, it is about $(6.7\text{–}6.9) \times 10^{-3} m_0 c$ in AlN and $(5.0\text{–}5.2) \times 10^{-3} m_0 c$ in GaN.

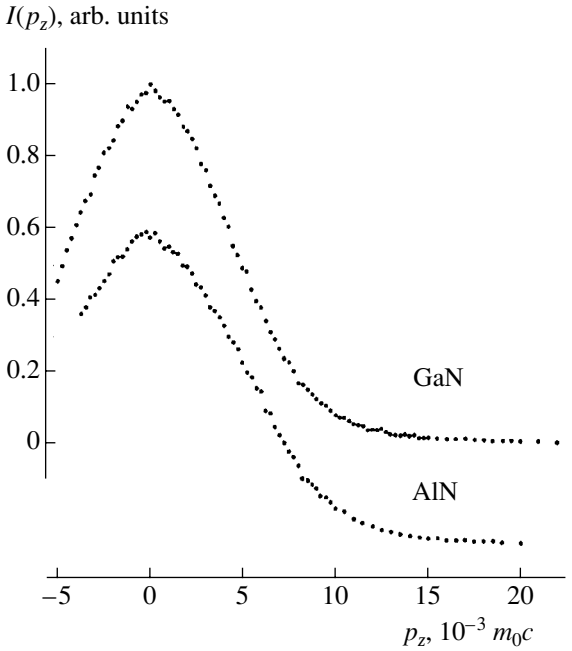

Fig. 1. 1*D*-ACAR curves for AlN and GaN (shifted along the ordinate axis for convenience): $I(\theta)$ is the count rate normalized to its maximum, $p_z \approx \theta m_0 c$, and θ the detection angle for a pair of annihilation-produced gamma quanta (p_z is the momentum component along the selected direction, see the text and [8, 9]).

The quantity r_s', estimated from the relation $p_F \approx 13.99/r_s'$ [1] using the above-listed p_F, appeared to be significantly smaller than r_s predicted from the model of noninteracting particles: $r_s'(\mathrm{AlN}) \approx 1.28 r_s$ and $r_s'(\mathrm{GaN}) \approx 1.66 r_s$ (see Fig. 3). Noteworthy is the considerable deviation of these data from the numerical values of the ratio $\{r_s'/r_s\}$ for reference "defect-free" materials, for which $\{r_s'/r_s\} \approx 1$. The discovery of a strong decrease in the electron density around a positron ($\approx 28\%$ for AlN and $\approx 66\%$ for GaN) indicates that positron annihilation proceeds in the vacancy-type defects.

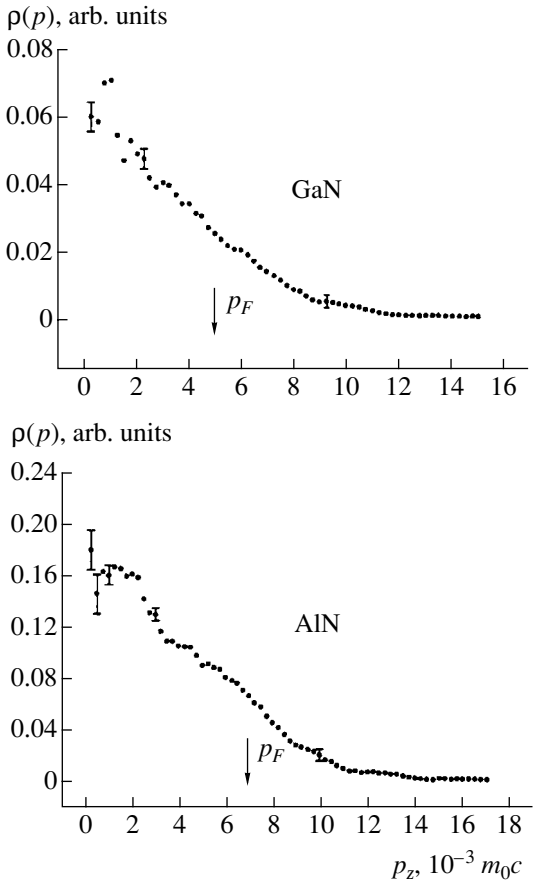

Fig. 2. The electron–positron pair momentum distribution density ρ(*p*) reconstructed from 1*D*-ACAR data for AlN and GaN; p_F is the Fermi momentum (see the text, and also [9] and references therein).

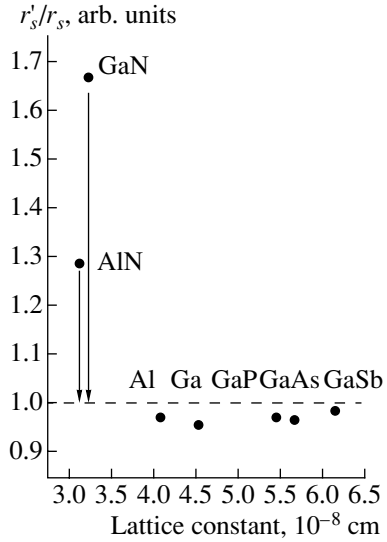

Fig. 3. The deviation of the electron density parameter r_s' obtained in 1*D*-ACAR measurements for nitrides and related materials from the r_s values calculated in terms of the standard model of independent particles [1]. Arrows indicate the decrease in electron density in AlN and GaN due to the positron annihilation in the vicinity of vacancy-type defects.

4. ANGULAR CORRELATION OF THE ANNIHILATION RADIATION EMITTED FROM THE VICINITY OF ALN AND GAN ION CORES

Pairs of quanta with a high total momentum are generated in the annihilation of positrons with ion core electrons; therefore, the momentum distribution density ρ(*p*) reconstructed from the 1*D*-ACAR data is not limited by the Fermi momentum p_F (see Figs. 1 and 2). Since the ion core shell electrons largely retain the atomic character of their wave functions, the momentum range $p > p_F$ contains information related to the chemical nature of atoms in whose cores positron annihilation proceeds. The numerical values $dI(p)/pdp \approx \rho(p)$ reconstructed from the experimental data for the range $0 \ll r < k_F^{-1}$ correlate well with the data calculated from the known relation [1, 4, 7, 12]:

$$\rho(p) \cong \text{const}\exp\left(-\left(\frac{\alpha p}{\eta}\right)^2\right), \qquad (2)$$

where $p = \hbar k$, $p_F = \hbar k_F$, k is the electron wave vector, and α is the most probable distance between the nucleus and the electron at the moment of its two-quantum annihilation with a positron. Usually, the electron–positron ionic radius $r_m \approx \alpha$ is determined, which is a parameter of the high-momentum component of an 1*D*-ACAR curve [1]. The data obtained in the investigations of the mentioned 1*D*-ACAR component for ionic crystals and oxides [1,12], metals [1, 4], diamond-like semiconductors [4, 7], and high-temperature superconductors [6] show that the r_m in the studied materials is approximately equal to the ionic radius of a core having the largest size and the smallest charge. To determine the chemical nature of atoms, the electron cores of which experience position annihilation in the nitrides under study, we have compared the r_m values for GaN and AlN with the data obtained from reference Al and Ga, and from diamond-like GaP, GaAs, and GaSb semiconductors related to our nitrides.

It was established that the parameters $r_m(Al^{3+}) \approx 0.519 \pm 0.011$ Å and $r_m(Ga^{3+}) \approx 0.584 \pm 0.015$ Å for Al and Ga correlate well with commonly accepted ionic radii, $r_i(Al^{3+}) \approx 0.53$ Å and $r_i(Ga^{3+}) \approx 0.62$ Å [13]. A similar situation was observed for the most perfect GaP and GaAs crystals, which are the closest structural analogues of the studied nitrides AlN and GaN (see Fig. 4). In this case, the ratios $r_m(GaP)/r_m(Ga^{3+})$ and $r_m(GaAs)/r_m(Ga^{3+})$ are close to unity: 1.0086 and 1.054, respectively. If the value $r_m(Ga^{3+}) \approx 0.584 \pm 0.015$ Å in Ga metal is used as a reference, the deviations are less than 1% for GaP and about 5% for GaAs. A somewhat larger deviation (≈7%) was obtained for GaSb, probably because of the presence of positron-sensitive vacancy-type defects in the sample (this problem will be discussed elsewhere).

Thus, the electron–positron ionic radius r_m in the studied semiconductors GaP, GaAs, GaSb is defined by the chemical nature of the outer 3*d* electron shell of Ga^{3+}, rather than by that of the P^{5+}, As^{5+}, or Sb^{5+} ion cores. The positron annihilation in Ga^{3+} ion cores is reliably detected in 1*D*-ACAR measurements, because a positron is localized during its lifetime in the region of effective negative charge of the P, As, or Sb chemical bonds and has four Ga atoms in the first coordination sphere; a similar conclusion is also valid for In^{3+} ion cores in "perfect" InP, InAs, and InSb single crystals [4].

Nevertheless, a different situation has been observed in the studied AlN and GaN samples (see Fig. 4). In this case, the ionic radius r_m differs significantly from the reference value: the ratio $r_m(\mathrm{AlN})/r_m(\mathrm{Al}^{3+})$ is about 1.249, and a somewhat smaller value of 1.108 is obtained for $r_m(\mathrm{GaN})/r_m(\mathrm{Ga}^{3+})$. In other words, the electron–positron radius of Al^{3+} and Ga^{3+} ion cores exhibits a considerable increase, by ≈25% in AlN and ≈11% in GaN. It is necessary to note that a similar result was obtained for GaN when related III–V compounds were used as reference samples: $\{r_m(\mathrm{GaN})/r_m(\mathrm{GaP})\} = 1.0986$ and $\{r_m(\mathrm{GaN})/r_m(\mathrm{GaAs})\} = 1.0986$. These two circumstances, the electron–positron ionic radius r_m increasing with respect to the selected reference value and the above-mentioned decrease of the electron density in the interatomic space around the positron, indicate that the annihilation of positrons with the electrons of Al^{3+} and Ga^{3+} ion cores proceeds in the regions of vacancy-type defects in AlN and GaN, respectively.

It should be emphasized here that, in spite of a considerable increase in r_m, its value characterizes the positron annihilation with the electrons of the outer shells of Ga^{3+} or Al^{3+} ion cores. This conclusion follows from a comparison of r_m with the ionic radius r_i: the ratio of these quantities is very close to unity, $\{r_m(\mathrm{GaN})/r_i(\mathrm{Ga}^{3+})\} \approx 1.044$ and $\{r_m(\mathrm{AlN})/r_i(\mathrm{Al}^{3+})\} \approx 1.2147$. Positrons virtually do not annihilate with the electrons of the N^{5+} ion core owing to a stronger Coulomb repulsion.

It is important to note that the obtained r_m values cannot be assigned to positron annihilation in isolated vacancies in the crystal lattice of the studied nitrides. Indeed, *isolated* Ga or Al vacancies do not include Ga^{3+} or Al^{3+} ions in their nearest environment, while positron capture by a positively charged *isolated* nitrogen vacancy is hardly probable.[1]

Therefore, the consistent interpretation of the whole set of experimental data demands that a hypothesis be put forward about positron annihilation in the region of a vacancy–impurity complex.[2]

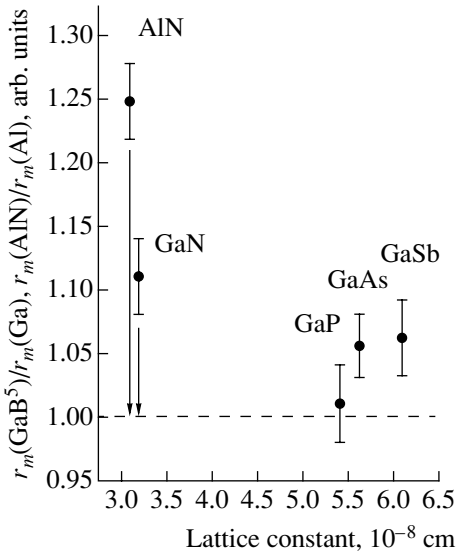

Fig. 4. The deviation of the electron–positron ionic radius r_m from the standard values obtained for Al^{3+} and Ga^{3+} ion cores in the corresponding metals. Arrows indicate an increase in the radius due to the positron annihilation in the vicinity of vacancy complexes, $[N_{\mathrm{Ga}}V_{\mathrm{N}}]$ in GaN and $[N_{\mathrm{Al}}V_{\mathrm{N}}]$ in AlN (see the text).

Let us assume that in the nitrides under study the complex consists of an anion vacancy and a cation and that the latter occupies an antisite position. In this configuration, a positron is localized in the free volume formed by three nitrogen cores and one cation core. Evidently, in this situation, positron annihilation in the region of charge associated with nitrogen atoms dominates, and the contribution to the angular correlation, made by the annihilation emission from cations, must be several times smaller than the observed one, which is in the range of 21–28% for the nitrides under study and the reference materials [4].

Thus, the discussed configuration of positron-sensitive defects seems of little use for the interpretation of experimental data.

In this context, a vacancy–impurity complex consisting of a cation vacancy, which has captured the nearest nitrogen atom with the formation of an antisite, and a nitrogen vacancy, $[N_{\mathrm{Ga}}V_{\mathrm{N}}]$ in GaN and $[N_{\mathrm{Al}}V_{\mathrm{N}}]$ in AlN, may deserve consideration. It is reasonable to assume that the effective charges of cation and anion vacancies are mutually compensated in a "nitrogen

[1] Calculations show that the wave function of a positron captured by an anion vacancy in binary compounds tends to extend into the interstitial space; bound states of a positron do not exist at all in isolated N, C, and O vacancies in GaN, SiC, and MgO compounds [2].

[2] Theoretically [2], an anion–cation divacancy forms the volume for the effective localization of a positron; the probability of the formation of isolated divacancies seems low in GaN and AlN, as well as in the majority of binary compounds whose chemical bonds have a high ionicity, though different models for multivacancy complexes are sometimes used for the interpretation of experimental data on radiation defects in semiconductor compounds (for more detail, see [14]).

atom antisite" + "nitrogen vacancy" complex; in this case, the free volume for a captured positron is formed by three cation cores (Ga^{3+} in GaN, Al^{3+} in AlN) and one nitrogen atom. This atomic environment provides conditions for the observed positron annihilation in the space between cation cores, where the characteristic length r_m is increased and the electron density is reduced. Here, it is necessary to note that similar complexes in GaN have been theoretically discussed in [15].

5. CONCLUSION

A pioneering study of 1*D*-ACAR curves in AlN and GaN nitrides has been performed. The electron density estimated from the obtained data on the electron–positron pair momentum distribution yields considerably lower values than the r_s predicted by the model of independent particles for an ideal Fermi gas: $r_s'(\mathrm{AlN}) \approx 1.28 r_s$ and $r_s'(\mathrm{GaN}) \approx 1.66 r_s$. The obtained data present convincing evidence that positron annihilation proceeds in the vicinity of vacancy-type defects.

The data analysis that draws on the results of systematical 1*D*-ACAR studies in Al and Ga metals and diamond-like GaP, GaAs, and GaSb semiconductors leads to the conclusion that the annihilation of positrons with the outer shell electrons of Ga^{3+} in GaN and Al^{3+} in AlN is dominant. A hypothesis of positron annihilation in the vicinity of vacancy complexes with a "nitrogen atom antisite" + "nitrogen vacancy" configuration, $[N_{\mathrm{Ga}}V_{\mathrm{N}}]$ in GaN and $[N_{\mathrm{Al}}V_{\mathrm{N}}]$ in AlN, is suggested.

ACKNOWLEDGMENTS

The study was financially supported by CRDF (grant no. RP1-2258).

REFERENCES

1. R. A. Ferrell, Rev. Mod. Phys. **28** (3), 308 (1956).
2. M. J. Puska, S. Mäkinen, M. Manninen, and R. M. Nieminen, Phys. Rev. B **39** (11), 7666 (1989).
3. N. Yu. Arutyunov, A. S. Baltenkov, V. B. Gilerson, and V. Yu. Trashchakov, Fiz. Tekh. Poluprovodn. (Leningrad) **20** (10), 1753 (1986) [Sov. Phys. Semicond. **20**, 1099 (1986)].
4. N. Yu. Arutyunov, in *Proceedings of International Positron Workshop, Univ. Bundeswehr, 1989,* Ed. by P. Sperr and G. Kogel.
5. N. Yu. Arutyunov, V. V. Emtsev, V. Yu. Trashchakov, and É. É. Rubinova, Fiz. Tekh. Poluprovodn. (Leningrad) **20**, 532 (1986) [Sov. Phys. Semicond. **20**, 349 (1986)].
6. V. F. Masterov, V. A. Kharchenko, and N. Yu. Arutyunov, Supercond.: Phys., Chem., Tech. **5**, 1211 (1992).
7. N. Yu. Arutyunov, Solid State Phenom. **57\58**, 4894 (1997).
8. V. I. Gol'danskiĭ, *Physical Chemistry of Positron and Positronium* (Nauka, Moscow, 1968).
9. A. T. Stewart, Can. J. Phys. **35**, 168 (1957).
10. N. Yu. Arutyunov, Mater. Sci. Forum **105\110**, 583 (1992).
11. A. D. Sakharov, Zh. Éksp. Teor. Fiz. **18**, 631 (1948).
12. N. Yu. Arutyunov, in *Positron and Positronium Chemistry,* Ed. by Y. C. Jean (World Scientific, Singapore, 1990).
13. J. P. Suchet, *Chemical Physics of Semiconductors* (Van Nostrand, New York, 1965; Metallurgiya, Moscow, 1969).
14. V. V. Emtsev and T. V. Mashovets, *Impurities and Point Defects in Semiconductors* (Radio i Svyaz', Moscow, 1981).
15. D. J. Chadi, Appl. Phys. Lett. **71**, 2970 (1997).

Translated by D. Mashovets

Semiconductors, Vol. 36, No. 10, 2002, pp. 1111–1113. Translated from Fizika i Tekhnika Poluprovodnikov, Vol. 36, No. 10, 2002, pp. 1191–1193.

ATOMIC STRUCTURE AND NONELECTRONIC PROPERTIES OF SEMICONDUCTORS

The Influence of Shallow Impurities on the Temperature Dependence of Microhardness and the Photomechanical Effect in Semiconductors

A. B. Gerasimov and G. D. Chiradze

Tsereteli State University, Kutaisi, 384000 Georgia

e-mail: irpdd@sanetk.net.ge

Submitted July 30, 2001; accepted for publication April 5, 2002

Abstract—The influence of a shallow-level donor impurity on the temperature dependence of microhardness and the photomechanical effect in single-crystal Si is investigated. It is demonstrated that, as the impurity concentration increases, the temperature dependence of the microhardness measured in the dark changes. The magnitude of the photomechanical effect and the temperature range of its existence decrease. The data obtained are explained on the basis of the mechanism of decreasing the microhardness with increasing the temperature due to increasing the density of phonons and antibonding quasiparticles. In this case, the concentration redistribution of antibonding quasiparticles that are induced by band-to-band transitions and transitions from impurity levels, which exert a different antibonding action, is responsible for the variations observed in the photomechanical effect. © *2002 MAIK "Nauka/Interperiodica".*

The mechanism of the photomechanical effect in semiconductors was suggested previously [1–5]. This effect consists in the variation in the microhardness of the material under illumination [6]. With the purpose of further investigating this mechanism, the influence of shallow-level impurities on the temperature dependence of microhardness and the photomechanical effect was investigated in this study using single-crystal Si.

Experiments were carried out using single-crystal dislocation-free Si(100):P with a dopant concentration of 2×10^{13}, 6×10^{16}, and 5×10^{18} cm^{-3}. The procedure for preparing the sample surface and microhardness measurements in the dark and under irradiation with white light were described previously [4]. The design of the heater, which allows attainment of the required temperatures of the samples under investigation, was also described previously [1]. The indenting load was equal to 25 g. For all measurements, the large diagonal of the Knoop pyramid coincided with the ⟨100⟩ direction in the (100) plane.

The experimental results are shown in Fig. 1. In the temperature range under investigation (T), it is conventionally possible to distinguish the low- and high-temperature regions, which are separated by the cross point of the temperature dependences of microhardness (H_k) for the intrinsic and extrinsic semiconductors. It can be seen that at low temperatures, the higher the concentration of impurity atoms, the lower the dark microhardness, whereas at high temperatures, the inverse relationship is observed. With increasing the impurity concentration, the magnitude of the photomechanical effect, which is determined as the difference between the dark microhardness and the microhardness under illumination, is decreased. The temperature range where the photomechanical effect exists also decreased.

To explain the experimental data obtained, it should be taken into account that a decrease in the microhardness of a semiconductor as the temperature is increased takes place due to an increase in the phonon density and the concentration of antibonding quasiparticles [3, 4, 7], which weaken chemical bonds.[1] In this case, thermally generated antibonding quasiparticles are responsible for a decrease in the dark microhardness, whereas the photogenerated antibonding quasiparticles are responsible for decreasing the microhardness under illumination.

Each electron or hole formed due to band-to-band transitions weakens the interatomic bond by the magnitude of the energy difference between E_0 and the relevant band edge [5]. Here, E_0 is the energy corresponding to the energy level of noninteracting atoms [9]. For this reason, the magnitude of this weakening is equal to $E_g(T)/2$, where $E_g(T)$ is the band gap of the semiconductor under investigation at a given temperature.[2] Due to this, an increase in the specific energy of chemical bonding for an intrinsic semiconductor crystal at a given temperature is as follows:

$$\Delta E \equiv \Delta E_{\text{in}} = (n_i + p_i)E_g(T)/2. \quad (1)$$

[1] For semiconductors, the valence band consists of bonding orbitals, whereas the conduction band consists of antibonding orbitals. For this reason, free electrons and holes in antibonding and bonding bands, respectively, are antibonding quasiparticles [8].

[2] For simplicity, no allowance is made for the difference in the weakening action of an electron and hole.

1063-7826/02/3610-1111$22.00 © 2002 MAIK "Nauka/Interperiodica"

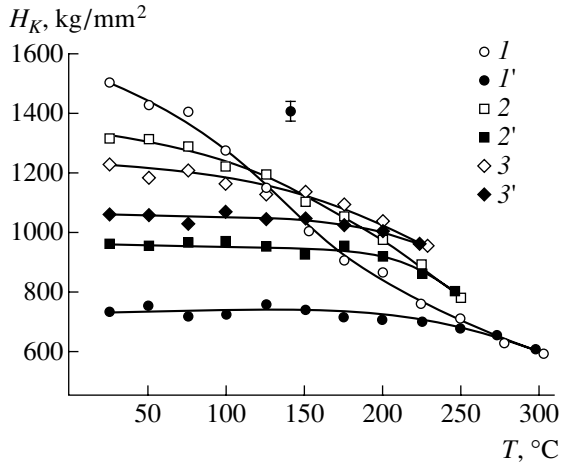

Fig. 1. Temperature dependence of the "dark" microhardness and the photomechanical effect in Si with a P concentration of (*1*, *1*') 2×10^{13}, (*2*, *2*') 6×10^{16}, and (*3*, *3*') 5×10^{18} cm^{-3}. (*1*–*3*) The measurements in the dark, and (*1*'–*3*') the measurements under illumination.

Here, n_i and p_i are the equilibrium electron and hole densities.

Additional antibonding quasiparticles, which are formed due to the ionization of impurity atoms, exist at room temperature in semiconductors which contain shallow impurity centers. It was demonstrated previously that these antibonding quasiparticles cause the microhardness of single-crystal Si to decrease [5]. In this case, it should be taken into account that the weakening of chemical bonds by antibonding quasiparticles in the presence of ionized impurities is less than for the antibonding quasiparticles formed only by band-to-band transitions in an intrinsic semiconductor. This is associated with the fact that the charge of the ionized impurity is screened by free carriers, and the interaction of antibonding quasiparticles with the bond charge is reduced. This variation in the bond energy can be estimated to a first approximation [10]. To do this, it is necessary to assume that each singly charged impurity atom effectively keeps one antibonding quasiparticle only, whose bond-weakening effect is less than that of antibonding quasiparticles which conventionally do not interact with the impurity. In this case, we may formally assume that there are two types of antibonding quasiparticles with a differing bond-weakening action. The antibonding quasiparticle, which is formed due to the ionization of a shallow impurity center, will weaken the interatomic bond by the magnitude $E_{\text{im}} < E_g(T)/2$. In this case, E_{im} does not coincide with the impurity-level energy.[3] The density of electrons that exert the lesser bond-weakening effect is equal to the impurity concentration.

[3] Evaluation of the bond-weakening effect of the electrons or holes generated from impurity atoms and its temperature and concentration dependence are the subjects of a special investigation which is presently being conducted.

The shallow-level impurities in semiconductors give rise to an electron or hole concentration in excess of the equilibrium one and, thus, change the ratio between the equilibrium electron n and hole p concentrations, since $np = n_i^2$ [11]. As a result, as is demonstrated below, these impurities affect the bond-weakening effect of electrons and holes. Indeed, if a semiconductor contains shallow-donor impurity atoms, which introduce an electron density of n_d into the conduction band, then the total electron density $n = n_i + n_d$. At the same time, the total hole density $p = n_i^2/n$, which is less than p_i. In this case, the total decrease in the specific energy of chemical bonds due to antibonding quasiparticles, which are formed by both band-to-band transitions and transitions from impurity levels, can be written for donors ($E_{\text{im}} = E_d$) as follows:

$$\Delta E \equiv \Delta E_{\text{im}} = n_i E_g(T)/2 + pE_g(T)/2 + n_d E_d. \quad (2)$$

Here, E_d is the energy by which one electron reduces the binding energy of the crystal due to the ionization of the impurity level.

Depending on the temperature of the semiconductor under investigation and the concentration of the shallow-donor impurity atoms in this semiconductor, if the inequality

$$p_i E_g(T)/2 < pE_g(T)/2 + n_d E_d \quad (3)$$

is fulfilled (or, similarly, $n_i E_g(T)/2 < nE_g(T)/2 + p_a E_a$ in the case of acceptor impurities), then the presence of impurities decreases the specific bond-weakening effect of antibonding quasiparticles, whereas, with the inverse inequality, this effect is enhanced. For the low-temperature range, when the densities n_i, p_i are low compared to n_d, inequality (3) is fulfilled. In this case, the microhardness in impurity semiconductors is determined mainly by antibonding quasiparticles with a smaller bond-weakening effect due to the presence of impurity atoms. However, if their concentration is sufficiently high, the microhardness is lower compared to that in an intrinsic semiconductor. For the high-temperature range, the inverse variant of inequality (3) is valid. In this case, the densities n_i and p_i are high enough to affect the microhardness of an extrinsic semiconductor. However, their bond-weakening effect, as was noted above, is reduced due to the presence of impurities. In a formal context, this is taken into account by decreasing the density of holes formed by the band-to-band transitions (in our experiment). For this reason, the microhardness of extrinsic semiconductors is higher compared to that in an intrinsic semiconductor at the same temperature. To date, no rigorous quantitative description of the microhardness dependence on the chemical-bond energy exists. In this context, we can rely on a qualitative comparison, i.e., on the correlation between variations in these quantities in relation to experimental conditions. The temperature dependences $1/\Delta E$ for Si with various concentrations of shallow

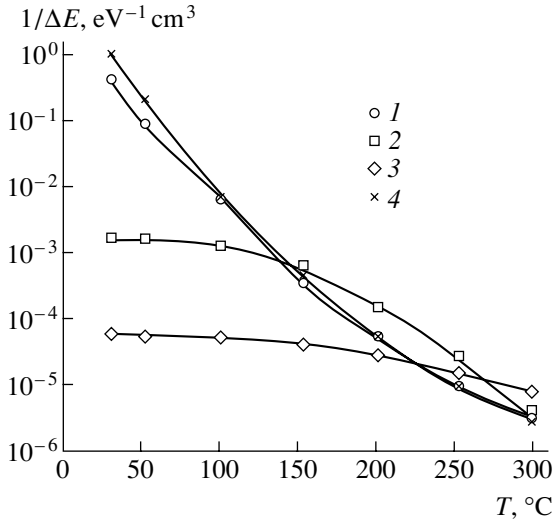

Fig. 2. Dependence of the inverse magnitude of a decrease in the specific energy of chemical bonds on temperature for Si with various concentrations of shallow donor impurities. Notations (*1*)–(*3*) are the same as in Fig. 1; (*4*) corresponds to an intrinsic semiconductor. As can be seen, the distinction between samples (*1*) and (*4*) is negligibly small. For this reason, sample (*1*) can actually be considered as intrinsic.

impurity atoms are shown in Fig. 2. The estimation yields $E_d = 10^{-4}$ eV, which is obtained from the equality condition $\Delta E_{\text{im}} = \Delta E_{\text{im}}$ for the cross point of the temperature dependences of microhardness for the extrinsic and intrinsic Si crystals. The comparison of Figs. 1 and 2 indicates that there is a correlation between variations in microhardness and $1/\Delta E$ in relation to the temperature and concentration of shallow impurity atoms.

Based on this reasoning, it is possible to evaluate the bond-weakening effect of antibonding quasiparticles that are photoexcited from ionized impurity atoms. This effect plays the main role in reduction of the photomechanical effect as the concentration of shallow impurity atoms increases, which was observed previously [5].

REFERENCES

1. A. B. Gerasimov, Z. V. Dzhibuti, and G. D. Chiradze, Soobshch. Akad. Nauk Gruz. **142**, 53 (1991).
2. A. B. Gerasimov, G. D. Chiradze, N. G. Kutivadze, *et al.*, Fiz. Tverd. Tela (St. Petersburg) **40**, 503 (1998) [Phys. Solid State **40**, 462 (1998)].
3. A. B. Gerasimov, G. D. Chiradze, N. G. Kutivadze, *et al.*, Proc. Tbilisi Univ., Ser. Phys. **34**, 86 (1999).
4. A. B. Gerasimov, G. D. Chiradze, and N. G. Kutivadze, Fiz. Tekh. Poluprovodn. (St. Petersburg) **35**, 70 (2001) [Semiconductors **35**, 72 (2001)].
5. A. B. Gerasimov and G. D. Chiradze, Fiz. Tekh. Poluprovodn. (St. Petersburg) **35**, 385 (2001) [Semiconductors **35**, 371 (2001)].
6. G. C. Kuchynski and R. H. Hochman, Phys. Rev. **108**, 946 (1957).
7. A. B. Gerasimov, G. D. Chiradze, N. G. Kutivadze, *et al.*, Proc. Tbilisi Univ., Ser. Phys. **34**, 79 (1999).
8. A. B. Gerasimov, Mater. Sci. Forum **65–66**, 47 (1990).
9. W. A. Harrison, *Electronic Structure and the Properties of Solids: The Physics of the Chemical Bond* (Freeman, San Francisco, 1980; Mir, Moscow, 1983), Vol. 1.
10. A. B. Gerasimov, Z. G. Bokhochadze, M. T. Vepkhvadze, *et al.*, Bull. Georgian Acad. Sci. **163**, 458 (2001).
11. V. I. Fistul', *An Introduction to the Physics of Semiconductors* (Vysshaya Shkola, 1984), p. 65.

Translated by N. Korovin

Semiconductors, Vol. 36, No. 10, 2002, pp. 1114–1122. Translated from Fizika i Tekhnika Poluprovodnikov, Vol. 36, No. 10, 2002, pp. 1194–1201.

ELECTRONIC AND OPTICAL PROPERTIES OF SEMICONDUCTORS

Neutron-Irradiation-Induced Effects Caused by Divacancy Clusters with a Tetravacancy Core in Float-Zone Silicon

P. F. Ermolov*, D. E. Karmanov, A. K. Leflat, V. M. Manankov, M. M. Merkin, and E. K. Shabalina

Institute of Nuclear Physics, Moscow State University, Vorob'evy gory, Moscow, 119899 Russia

** Fax: 7(095) 9395948*

Submitted January 30, 2002; accepted for publication March 11, 2002

Abstract—It is shown that the representation of neutron-irradiation-produced defects in the form of divacancy *D* clusters with a tetravacancy core adequately describes the observed neutron-irradiation-produced effects in float-zone silicon. It is also predicted that the complete-depletion voltage decreases for a dopant concentration exceeding a critical value; this decrease is due to "contraction" of the outer region of the cluster's space charge. The magnitude of the expected effect is determined by the factor $\sim[1 - (r_n/r_{cl})^3]^{-1}$, where r_n and r_{cl} are the radii of the core and cluster, respectively. © *2002 MAIK "Nauka/Interperiodica".*

1. INTRODUCTION

Numerous theoretical and experimental studies of ion-irradiated semiconductors [1–4] suggest that variation in the properties of these materials are generally caused by composite defects (complexes, clusters, and disordered regions) formed as a result of interaction of mobile primary radiation defects (vacancies and interstitial atoms) with each other and with previously formed defects. However, progress in studying the complex defects is retarded to a great extent by the lack of experimental tools for the observation and identification of the majority of complex defects, except for a comparatively small number of simpler defects, such as the *A* and *E* centers, divacancies, or the defects that possess specific properties (for example, paramagnetism in the case of tetravacancies). This makes it impossible to test quantitatively in full measure the existing theoretical models. As a result, theoretical models are, as a rule, approximate. The diffusion–reaction model of the stable-cluster formation can also be treated as a certain approximation because the role of the cascade stage of defect formation is underestimated in this model [2, 3]. However, quantitative tests for the applicability of this approximation have not been derived due to the severity of the problem. It is these difficulties that are apparently responsible for the lack of an adequate explanation of various neutron-irradiation-induced effects in float-zone silicon; these effects include the ultimate position (pinning) of the Fermi level [5, 6], conductivity-type inversion [7], the behavior of the effective concentration and the reverse current [8], and direct and reverse annealing [8–10].

The aim of this study is to present a model of neutron-irradiation-produced defects in float-zone silicon which adequately describes neutron-irradiation-induced effects.

Numerous experimental data indicate that [2, 11] the radiation defects with the highest concentration are divacancies, these being the main components of stable vacancy clusters. In the diffusion–reaction approximation, the kinetics of formation of a divacancy *D* cluster is governed essentially by the ratio between the vacancies' recombination and diffusion times $\lambda = \tau_R/\tau_D = D_V/\beta_{VV}N_VL^2$, where D_V and N_V are the diffusion coefficient and the concentration of vacancies, respectively; β_{VV} is the probability of an elementary recombination event; and L is the characteristic vacancy-cluster (the *V* cluster) size. In the case of a "freezing" *V* cluster, the radius of a divacancy cluster (a *D* cluster) is given by $L_2 \approx L[1 - 2\exp(1/\lambda)]$. In the case of irradiation with 1-MeV neutrons, the linear dimension of a *D* cluster is ~50 Å [12].

However, the interpretation of neutron-irradiation-induced effects on the basis of simple radiation defects (vacancies [13], divacancies [14], and impurity–vacancy pairs [15, 16]) using the "donor removal" and compensation models [7] leads to a discrepancy between the theory and experimental data [7, 17]. At the same time, an analysis of the spectra of the electron spin resonance (ESR) in irradiated silicon shows [18–20] that, in addition to divacancies and impurity–vacancy pairs, multivacancies are produced by fast neutrons. These multivacancies represent a family of defects formed from a chain of neighboring vacancies in a separate (110) plane (a zigzag configuration). These defects are

stable at room temperature and can give rise to localized bound states in the vicinity of the midgap. Among the multivacancies, the so-called Si-*P*3 centers were identified as tetravacancies [18, 19] and the Si-*P*1 centers, as pentavacancies [18–20]. According to a recent theoretical study [4] of the ring multivacancies V_m with $m = 1, \ldots, 7$, these defects, except for the hexavacancy, introduce deep levels into the band gap. The hexavacancy V_6 is not a vacancy-like defect and is electrically inactive.

Processing of the ESR spectra corresponding to the vacancy–oxygen (*V*O) complexes by the LCAO (linear combination of atomic orbitals) method shows [21] that bound states may appear in the band gap owing to splitting of the Si–Si molecular bond, which links the free sp^3 orbitals of two silicon atoms. The bound states correspond to bonding and antibonding orbitals. In the neutral charge state, there are two electrons with opposite spins at the bonding orbital. An additional trapped electron is located at the antibonding orbital. In this model, a positively charged divacancy V_2^+ is represented as a state with an unpaired electron at the bonding orbital; for a negatively charged divacancy V_2^-, such an electron is localized at the antibonding orbital. The ground state of a neutral divacancy V_2^0 is a singlet.

Measurements of the Hall constant show that, in float-zone silicon, the effect of pinning of the Fermi level at $E_v + 0.39$ eV is observed after irradiation with ^{60}Co γ quanta [5] or electrons [22, 23]; at the same time, the Fermi level is pinned at $E_v + 0.48$ eV after irradiation with fast neutrons [5, 24]. This effect was attributed to amphoteric properties of divacancies with the levels $E_2^- = E_v + 0.51$ eV (or $E_c - 0.54$ eV) and $E_2^+ = E_v + 0.27$ eV [6, 22, 23]. However, the results of other studies [24, 25] have indicated that divacancies introduce the level $E_2^- = E_c - 0.4$ eV into the band gap; consequently, the origin of the levels responsible for the pinning of the Fermi level at $E_v + 0.39$ eV should differ from that stated above. The pinning of the Fermi level indicates that the dominant role in the cluster should be played by multiply charged amphoteric centers. This means that both the Fermi level position and the equilibrium hole concentration in irradiated silicon are controlled by multiply charged centers (for example, divacancies or tetravacancies) and, at the same time, are independent of the concentrations of these defects and, consequently, of the integrated irradiation flux.

2. ELECTRONIC STRUCTURE OF MULTIVACANCIES

The one-electron approximation used in the analysis of ESR spectra [13] makes it possible to describe quite adequately the electronic structure of both isolated vacancies and defects composed of several vacancies. At the same time, it follows from theoretical estimations that the many-electron effects should be no less important than the Jahn–Teller effect itself; as a result, it is impossible to develop a complete quantitative theory without taking into account electron–electron interaction. However, the difficulty with taking into account the many-electron effects consists in the fact that the corresponding problem has to be solved self-consistently. To date, no exact solution to such problems has been found; various approximations have been used. Certain simplifications, including the defect-molecule model in the tight-binding approximation, make it possible to analyze systematically the dependence of the results on the relative strength of the electron–electron interaction. This strength depends only on the ratio between two parameters Δ/U, where Δ is the energy splitting of the one-electron states and U is the effective Coulomb energy of two electrons related to the defect; these two parameters can be used to express all the energy differences.

In the defect-molecule model, the multivacancies V_m in the zigzag configuration are represented in terms of the molecular bond Si(*A*)–Si(*B*) in the ⟨111⟩ direction with a distance d_{AB} between the atoms *A* and *B* at the end of the chain of vacancies in the (110) plane [19]. Corrections to the defect-molecule model specify the one-electron self-consistent calculations, which take into account both the charge state of the defects and the correlation effects. In the Haldane–Anderson model [26] used to study transition-metal impurities in covalent crystals in the Hartree approximation, the shift of the defect level E_d as the charge state of the defect is changed by a unit charge is given by

$$dE_L/dq = \theta_L dE_d/dq = \theta_L(J - J')dM_0/dq \approx E_g(1-2a)^2/nb, \quad (1)$$

where M_0 is the charge population of the defect site; J and J' are the intraatomic and interatomic Coulomb integrals; a and b are the coefficients of linear interpolation of contributions of the bands to the defect charge state ($a \approx b \approx 0.2$); n is the number of defect states; and θ_L is the degree of localization of the bound-state wave function ($\theta_L \approx 0.6$). For remote atoms, interatomic Coulomb terms J' vary in proportion to $\sim d_{AB}^{-1}$ ($J - J' = U = q^2/\varepsilon_{\text{eff}} d_{AB}$, where $\varepsilon_{\text{eff}} = \varepsilon$ is the dielectric constant). A value of dM_0/dq smaller than unity signifies that the change in the defect charge by unity results in a small variation in the electron occupancy of the lattice site at which this defect resides. This change in the charge state brings about a variation in the defect level E_d. As a result, the shift dE_L/dq is independent of the Coulomb contribution $U = J - J'$ and is equal to 0.22 eV for the average value of n ($n \approx 6$–12). This value of dE_L/dq is also corroborated by the results of more sophisticated calculations (by the pseudopotential method in terms of the local-density formalism; see, e.g., [27]) and is equal

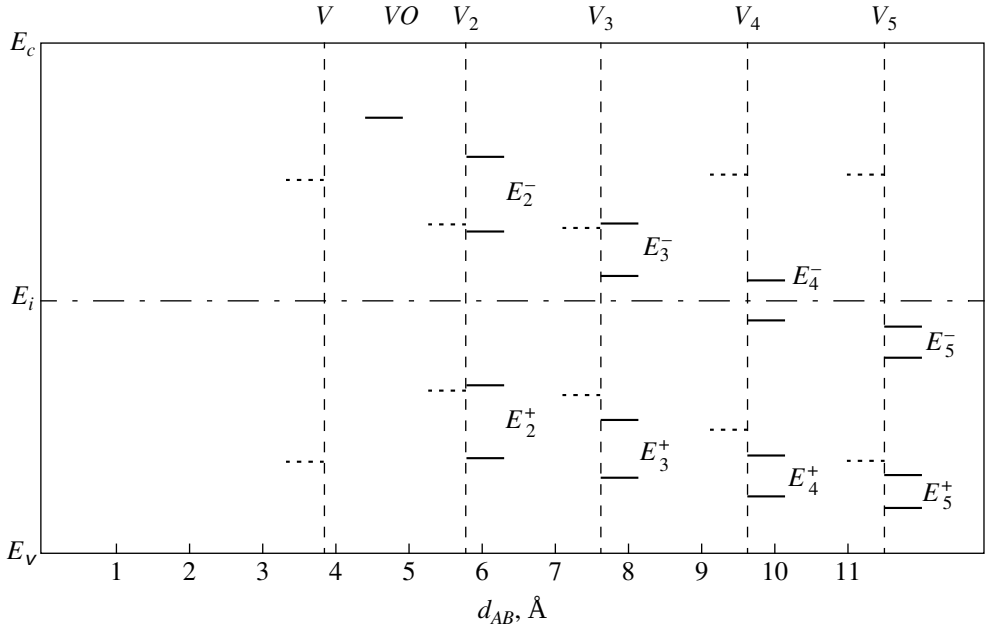

Fig. 1. Many-electron states of multivacancies in the neutral charge state V_m^0. The distance d_{AB} is calibrated by the number of vacancies between Si atoms at the end of the vacancy chain in the (110) plane.

to 0.21–0.25 eV for a vacancy. The inference that several charge states of the defect can give rise to localized states is confirmed experimentally by the example of vacancies and impurities of transition and other metals.

In the Hartree–Fock approximation and on the basis of the Slater determinants, the eigenstates of a two-center molecule are classified as $\pm(\Delta^2 + U^2/4)^{1/2}$ and $\pm U/2$, where Δ is the one-electron splitting which corresponds to the Si(*A*)–Si(*B*) bond and varies as $\sim d_{AB}^{-2}$ [28] ($\Delta \approx$ 1.2 eV for silicon). The symmetric and antisymmetric functions, which form the Slater determinants, are the basis functions of the representations Σ_g and Σ_u of the point-symmetry group C_{2v}. The multivacancies $V_2(D_{3d} \longrightarrow C_{2h})$ and V_4 have the C_{2h} symmetry, which is isomorphic to C_{2v} and, consequently, has the same representation. Such an approximation, which is simple to deal with in the two limiting cases corresponding to weak ($\Delta \gg U$) and strong ($\Delta \ll U$) correlations, are found to be extremely elaborate when the transition region $0 < (\Delta/U) < 1$ is to be considered carefully. The limiting case of weak correlation (of negligibly small intraatomic repulsion) $\Delta \gg U$ corresponds to a conventional energy-band spectrum with one-electron levels.

If the distances between the atoms Si(*A*) and Si(*B*) are large, we have $\Delta \ll U$ and the electron–electron interactions should be taken into account. The limiting case of strong correlation ($(\Delta/U) \longrightarrow 0$) implies that electrons tend to lower their energy and reside at different atoms. The ground state turns out to be degenerate. Excited states correspond to the pairing of electrons at the same atomic orbital and are located at $+U$ (for V_m^+ and V_m^0) and at $+2U$ (for V_m^-) in reference to the ground state. The ground state of a neutral multivacancy V_m^0 is a singlet. The spin $S = 1$ in such a system arises from a triplet excited state via thermal excitation. The many-electron states of neutral multivacancies V_m^0 are illustrated in Fig. 1. The ring-multivacancy levels, which are closest to the midgap (E_i) and are obtained by the [4] *ab initio* Hartree–Fock method and by the molecular-dynamic calculation based on the density functional, are also shown by the dotted line in Fig. 1. As can be seen from Fig. 1, multivacancies in the ring configuration do not form levels in the vicinity of the midgap. Thin lines in Fig. 1 indicate the levels of multivacancies V_m^0 for $\varepsilon_{\text{eff}} = (\varepsilon + 1)/2$. An analysis of the ESR spectra shows [18] that the difference between the spectra of the V_3 and V_5 multivacancies may be due to nonequivalence of the Si(*A*) and Si(*B*) atoms. An absence of the effects of motion for the Si-*P*3 center in the temperature range T = 77–300 K [18] is apparently also related to a large distance d_{AB} between the Si(*A*) and Si(*B*) atoms. If the relative magnitude of the interaction effects is characterized by a dimensionless ratio with the parameters δ/U, where δ is a variation in the energy of the one-electron state under the effect of the given distortion, the absence of motion effects for the Si-*P*3 centers signifies that multiplet splitting dominates over the Jahn–Teller effect when the distances between the Si(*A*) and Si(*B*) atoms are large. The difference in the spins of the Si-*P*3 ($S = 1$) and Si-*P*1 ($S = 1/2$) centers is apparently due to the fact that the pentavacancies have a ring configuration. A pentavacancy has six nonequivalent configura-

tions, five of which correspond to a configuration which is not ringlike. One of these has a zigzag configuration with a dissociation energy which is lower by 0.05 eV than that of the ring configuration [4]. Consequently, several metastable configurations can coexist. There is a single symmetrically nonequivalent configuration for a vacancy, divacancy, and trivacancy. A tetravacancy has four nonequivalent configurations, three of which correspond to a nonring configuration. This means that at least two metastable configurations can coexist. Consequently, the tetravacancy in the zigzag configuration may represent the most probable defect that forms the levels in the vicinity of the midgap and is responsible for the pinning of the Fermi level at $E_v + 0.39$ eV. As shown below, many experimental data can serve as indirect corroboration of this result, although, to date, there have been no direct measurements that identify the levels in the vicinity of the midgap. Experimentally, only the divacancy levels have been determined, in which case the Fermi level is pinned at $E_v + 0.48$ eV.

3. A CLUSTER MODEL FOR NEUTRON-IRRADIATION-INDUCED DEFECTS

A cluster model for the neutron-irradiation-produced defects in silicon was first suggested by Gossick [29]. In combination with the effective-medium method, this model (with certain corrections) is still widely used because it is relatively simple [2]. In the spherical approximation and for a uniform distribution of defects, Gossick used Poisson and electroneutrality equations for a system consisting of a cluster and a *n*-Si matrix to obtain

$$N_m(r_{cl}^3 - r_0^3) = N_{D0}(r_{scr}^3 - r_{cl}^3), \quad (2)$$

for $L_{Dm} \le r_{cl} \ll r_{scr}$; the depth and width of the potential shell were calculated to be

$$\varphi(r_{scr}) - \varphi(r_0) = \psi, \quad (3)$$

$$r_{scr}^3 = 3\varepsilon\varepsilon_0 r_{cl}\psi/qN_{D0}, \quad (4)$$

where $L_{Dm} = (\varepsilon\varepsilon_0 kT/q^2N_m)^{1/2}$ is the Debye screening length; ε_0 is the permittivity of free space; ε is the relative permittivity; $\varphi(r)$ is the potential, which is a solution to the Poisson equation; ψ is the difference between the Fermi energies outside and inside a cluster; q is the elementary charge; k is the Boltzmann constant; N_m is the electron concentration in a cluster; N_{D0} is the dopant concentration; r_{scr} is the outer radius of the space-charge region (SCR); r_0 is the inner radius of the SCR; and r_{cl} is the cluster radius. The asymptotic state of neutron-irradiated silicon is that of compensated intrinsic material. The quantities r_{cl} and ψ are specified, whereas the quantities r_0 and r_{scr} are unknown. It was assumed initially [29] that the potential shells were very deep, $q\psi \gg kT$, and that the penetration depth of electrons at the outer diameter $r = r_{scr}$ was negligibly small, $\Delta r \ll r_{csr}$. In more accurate models accounting for an additional contribution $\sim 2kT/q$ made by the tails of the majority-carrier distribution at the outer diameter of the potential shell, the quantity ψ is replaced by $\psi - 2kT/q$.

A detailed study of the defect-production mechanisms shows that the initial stage of the spatial–temporal separation of primary radiation defects (vacancies *V* and interstitial atoms *I*) is no less important in the formation of vacancy clusters than the diffusion–reaction stage. The latter includes the intracascade annealing (recombination) of closely spaced *V–I* pairs and the subsequent diffusion–reaction mechanism, which accounts for a large difference in the diffusivities of vacancies and interstitial atoms. For both mechanisms of the diffusion–reaction stage, only a small fraction of the defects (*V* and *I*) initially formed in a cascade survives. In fact, the concentration of closely spaced *V–I* pairs is higher than their average concentration since, as the energy of the defect-producing particle becomes lower, the mean distance between successive collisions decreases. Therefore, there is a high probability that the closely spaced *V–I* pairs annihilate or the closely spaced vacancies combine into the V_2 or V_m complexes. Since the annihilation of *V–I* pairs is limited by diffusion with an activation energy that is higher than the barrier for the trapping of a vacancy by another vacancy [30], the reaction $V + V \longrightarrow V_2$ will be dominant. Initially, a divacancy *D* cluster is formed from a two-vacancy *V* cluster ($V + V \longrightarrow V_2$); then, a tetravacancy *T* cluster is formed from two divacancy *D* clusters ($V_2 + V_2 \longrightarrow V_4$). Since the divacancies are almost immobile at room temperature, the $V_2 + V_2 \longrightarrow V_4$ reaction limited by the interaction event can proceed only for the divacancies separated by a distance no larger than the corresponding capture radius. The formation rate of tetravacancies is proportional to the squared concentration of divacancies, so that the main part of a *T* cluster is formed in the *D*-cluster region where the divacancy concentration is highest (i.e., in the central region). For short-range forces of interaction between identical defects (divacancies) with concentration $N_2 \approx 10^{20}$ cm^{-3}, the tetravacancy concentration is estimated at $\sim 10^{19}$ cm^{-3}. Consequently, divacancies and tetravacancies will be mainly formed in appreciable concentrations, with the divacancy concentration being predominant. This is consistent with the data on the ion irradiation of silicon (the highest concentration of divacancies is $\sim 7 \times 10^{19}$ cm^{-3} [3], and that of tetravacancies is $\sim 4 \times 10^{19}$ cm^{-3} [31]).

The previous consideration indicates that a cluster consists of divacancies with traces of tetravacancies at the cluster center. A space-charge region (SPR) is formed around the cluster as a result of a difference in the Fermi level positions within and outside the cluster.

The energy diagram of a structure consisting of a cluster and SPR is illustrated in Fig. 2. In the spherical

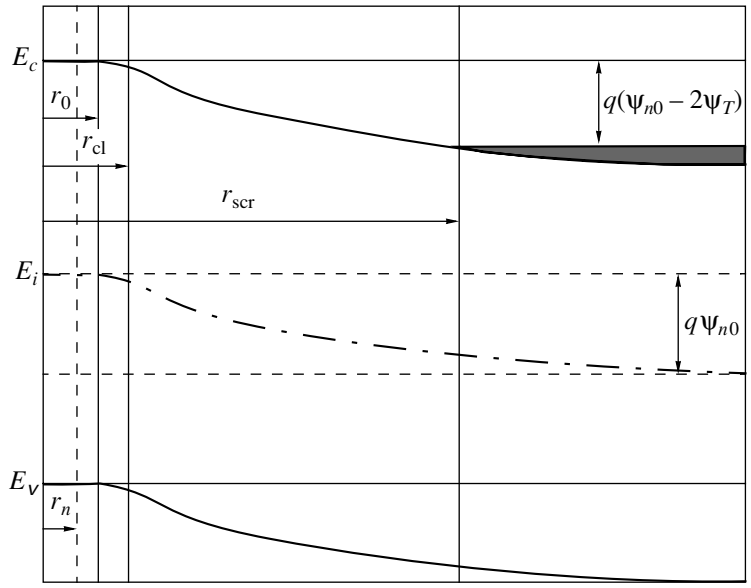

Fig. 2. Potential contour of the conduction and valence bands in a cluster and in its surroundings. The region corresponding to the electron penetration ~2*kT* is hatched.

approximation, this structure fills a $(1 - \eta)$ fraction of the crystal volume; here, $\eta = \exp(-v_{scr}\Sigma_{eff}\Phi)$ is the undamaged fraction of the crystal volume, v_{scr} is the SCR volume according to (4), $\Sigma_{eff} = n_{cl}\Sigma$, $\Sigma = \sigma_{Si}N_{Si}$ is the macroscopic scattering cross section of neutrons in silicon, n_{cl} is the average number of clusters, and Φ is the integrated flux of neutrons. The product of the donor concentration in *n*-Si by the undamaged fraction of the *n*-Si volume is the effective donor concentration: $N_{D_{eff}} = N_{D_0}\eta$.

Similarly, the fraction of the crystal volume unoccupied by clusters is given by $\chi = \exp(-v_{Cl}\Sigma_{eff}\Phi)$, and the fraction of the crystal occupied by clusters is $(1 - \chi) \approx v_{cl}\Sigma_{eff}\Phi$ since $v_{cl}\Sigma_{eff}\Phi \ll 1$, where v_{cl} is the cluster volume. The system consisting of a cluster and SCR occupies the volume $v_a = (4\pi/3)r_0^3$, which is governed by the negative (inner) part of the SCR. According to (2)–(4), the number of negatively charged defects in the unit solid angle for $r_{scr} \gg r_{cl}$ and $\Delta r = r_{cl} - r_0 \ll r_{cl}$ is given by

$$N_m(r_{cl}^3 - r_0^3) = N_{D_0}(r_{scr}^3 - r_{cl}^3) = 3\varepsilon\varepsilon_0 r_{cl}\psi_n/q, \quad (5)$$

where N_m is the average concentration of defects in a cluster within the range $\Delta r = r_{cl} - r_0$, $\psi_n = \psi_{n0} - 2\psi_T$, $q\psi_T = kT$, and ψ_{n0} is the Fermi level position in reference to the midgap in *n*-Si. The condition $\Delta r = r_{cl} - r_0 \ll r_{cl}$ implies a plane approximation to the solution of the Poisson equation in the range $r_0 < r < r_{cl}$. It follows from (5) that the inner radius of the SCR is given by

$$r_0 = r_{cl}(1 - 3\varepsilon\varepsilon_0\psi_n/qN_m r_{cl}^2)^{1/3}. \quad (6)$$

Taking into account that $N_2(r_0^3 - r_n^3) > N_{nm}r_n^3$, where N_{nm} is the defect concentration in the cluster core and r_n is the core radius, we obtain the effective acceptor concentration $N_{A_{eff}}$ as the product of the divacancy concentration N_2 by $v_{an}\Sigma_{eff}\Phi$, where $v_{an} = (4\pi/3)(r_0^3 - r_n^3)$; i.e.,

$$N_{A_{eff}} = (4\pi/3)N_2[r_{cl}^2(1 - 3\varepsilon\varepsilon_0\psi_n/qN_2r_{cl}^2) - r_n^3]\Sigma_{eff}\Phi. \quad (7)$$

The resulting effective carrier concentration up to inversion is given by

$$N_{eff} = N_{eff.c} = N_{Deff} + N_{Aeff.c} = N_{D0}\exp(-c\Phi) + b_c\Phi, \quad (8)$$

where the acceptor-introduction constant is represented as

$$b = b_c = (4\pi/3)N_2\Sigma_{eff}[r_{cl}^2(1 - 3\varepsilon\varepsilon_0\psi_n/qN_2r_{cl}^2) - r_n^3], \quad (9)$$

and the donor-removal constant is given by

$$c = v_{scr}\Sigma_{eff} = 4\pi\varepsilon\varepsilon_0 r_{cl}\psi_n\Sigma_{eff}/qN_{D0}. \quad (10)$$

After inversion ($\Phi > \Phi_{inv}$), the effective charge-carrier concentration is independent of impurities in Si and is governed only by the cluster radius r_{cl} and by the lowest impurity concentration N_{D0min} ($\psi_{nmin} = 2\psi_T$) $\approx 2.4 \times 10^{11}$ cm^{-3} (T = 300 K) at which a depletion region can exist; i.e., we have

$$N_{eff} = N_{Aeff.a} = b_a\Phi, \quad (11)$$

where the acceptor-introduction constant b is given by

$$b = b_a = (4\pi/3)N_2\Sigma_{\text{eff}}[r_{\text{cl}}^3(1-3\varepsilon\varepsilon_0\psi_{n\min}/qN_2r_{\text{cl}}^2)-r_n^3]. \quad (12)$$

For $N_{D0} \approx (2\text{–}50)\times 10^{11}$ cm^{-3}, $r_{\text{cl}} \approx 20$ Å, $N_2 \approx 7\times 10^{19}$ cm^{-3}, and $\Sigma_{\text{eff}} \approx 0.33$ cm^{-1}, the values of c and b calculated using formulas (9), (10), and (12) are in good agreement with experimental data: $c \approx (5\text{–}80)\times 10^{-14}$ cm^2, $b_a \approx 0.05$ cm^{-1}, and $b_c \approx 0.012\text{–}0.015$ cm^{-1}. Since we do not specify a precise distribution of defects, the defect concentration N_m and the radii of the cluster r_{cl} and SCR r_{scr} are effective (average) quantities.

Representation of neutron-irradiation-produced defects as insulator inclusions is quite realistic if $v_{\text{scr(cl)}}\Sigma_{\text{eff}}\Phi \ll 1$, and it is approximate in the vicinity of inversion, in which case $v_{\text{scr}}\Sigma_{\text{eff}}\Phi \approx 1$. The inversion-inducing integrated flux Φ_{inv} can be determined from the condition $N_{D_{\text{eff}}} = N_{A_{\text{eff}}}$; i.e.,

$$N_{D0}\exp(-c\Phi_{\text{inv}}) = b_c\Phi_{\text{inv}}. \quad (13)$$

The value of Φ_{inv} can be determined approximately from the condition $N_{D_{\text{eff}}} = N_{D0\min}$

$$\Phi_{\text{inv}} = (1/c)\ln(N_{D0}/N_{D0\min}). \quad (14)$$

It is also noteworthy that, according to (5), the clusters are stable if the defect concentration in them and the cluster radius satisfy the condition

$$N_m r_{\text{cl}}^2 \geq 10^6 \text{ cm}^{-1}, \quad (15)$$

i.e., if the cluster secures the equilibrium potential at a value larger than $2\psi_T$ at the point $r_0 = 0$.

The presence of the cluster core manifests itself if the dopant concentrations N_{D0} are such that the SCR inner radius reaches the core radius r_n. As $N_{D0}(\psi_{n0})$ increases, the depletion radius r_0 (6) decreases; correspondingly, the quantity $\Delta r_{0n} = r_0 - r_n$ also decreases. If $\Delta r_{0n} \longrightarrow 0$, a negative charge fills the entire cluster volume. This means that the amount of negative charge of divacancies in a D cluster is insufficient for maintaining the total potential $\psi = \psi_{n0}$. The dopant concentration $N_{D0n}(\psi_{n0n})$, at which the negative charge fills the entire cluster volume, can be determined from equality (6) for $r_0 = r_n$; i.e.,

$$\psi_{nn} = (qN_2r_{\text{cl}}^2/3\varepsilon\varepsilon_0)[1-(r_n/r_{\text{cl}})^3]. \quad (16)$$

A further increase in $N_{D0}(\psi_{n0})$ would result in a decrease in the SCR radius: $r_{\text{scr}\,n} < r_{\text{scr}}$, where $r_{\text{scr}\,n}$ is the SCR radius in the presence of the core. It follows from (8) that the relative variations in the ratio $(r_{\text{scr}}/r_{\text{scr}\,n})^3$ and, correspondingly, in c and b [see (9), (10), (12)] are defined by the quantity

$$R = (r_{\text{scr}}/r_{\text{scr}\,n})^3 = [1-(r_n/r_{\text{cl}})^3]^{-1} = qN_2r_{\text{cl}}^2/3\varepsilon\varepsilon_0\psi_{nn}. \quad (17)$$

For the core radius $r_n \approx (0.7\text{–}0.9)r_{\text{cl}}$, we have $R \approx 1.5\text{–}3.7$; at the same time, $N_{D0n} \approx 8\times 10^{12}$ cm^{-3} for $r_n = 0.8r_{\text{cl}}$. According to the effective-medium model, a decrease in the SCR radius brings about an increase in effective conductivity and a reduction in the charge-carrier scattering; consequently, the charge collection becomes more efficient. Conceivably, it is this effect that causes the parameters c and b to decrease in the samples with a resistivity of $\rho \leq 500$ Ω cm [10, 32]; however, further experimental verification is needed.

The behavior of the reverse current is also consistent with the suggested cluster model. In the Shockley–Read approximation for recombination, the major contribution to the generation current is made by clusters; i.e.,

$$\Delta I \propto q\sigma v_T n_i N_m v_{\text{cl}} n_{\text{cl}}\Sigma\Phi/2\cosh(x). \quad (18)$$

Here,

$$\alpha = q\sigma v_T n_i N_m v_{\text{cl}} n_{\text{cl}}\Sigma/2\cosh(x) \quad (19)$$

is the degradation constant; $\sigma \approx \sigma_n \approx \sigma_p$ are the capture cross sections for electrons and holes, respectively; N_m (N_{nm}) is the multivacancy concentration in a cluster (the cluster core); v_T is the thermal velocity; n_i is the charge-carrier intrinsic concentration; $\cosh(x) = (e^x + e^{-x})/2$; and $x = (E_i + E_m)/kT$, where E_m and E_i are the multivacancy energy level and the midgap energy, respectively. Assuming that v_T and n_i have typical values, the level $E_4^- \approx E_c - 0.5$ eV, $\sigma \approx \sigma_p \approx 2\times 10^{-14}$ cm^2, $r_{\text{cl}} = 25\times 10^{-8}$ cm, $\Sigma = 0.165$ cm^{-1}, $n_{\text{cl}} = 2\text{–}3$, and $N_{nm} = 4\times 10^{19}$ cm^{-3}, we find that the degradation constant is approximately equal to $\alpha \approx 4\times 10^{-17}$ A/cm. At the same time, assuming that the clusters consist mainly of divacancies, the level $E_2^- = E_c - 0.4$ eV [14, 23], and $N_m = 7\times 10^{19}$ cm^{-3}, we find that the value of α is smaller by more than two orders of magnitude: $\alpha(E_2^-) \approx 10^{-18}$ A/cm. Consequently, in the case of irradiation with neutrons, the reverse current is governed by tetravacancies, which are predominant in the central region of the clusters, since the tetravacancy energy levels are located closer to the midgap. In this situation, the degradation constant α should be independent of the impurity concentration in silicon and constant in the range of moderate integrated fluxes of neutrons, protons, and pions [8].

The suggested model includes a single variable parameter, i.e., the *D*-cluster radius r_{cl}. The constants *c*, *b*, and Φ_{inv} are functions of N_m, r_{cl}, and $\psi_n(N_{D0})$. For each type of irradiating particle and for each initial *n*-Si, we have a unique set of the constants α, *c*, *b*, and Φ_{inv}. The cluster model makes it possible to predict qualitatively and quantitatively the behavior of neutron-irradiated float-zone silicon in relation to the inherent properties of this material, external conditions, and time.

4. DIRECT AND REVERSE ANNEALING

In the cluster model, annealing is conceived as a multistage process of cluster disintegration: direct annealing is caused by the disintegration of the *D*-cluster core (immediately after irradiation with neutrons, the *D*-cluster core consists of tetravacancies), whereas reverse annealing is related to *D*-cluster disintegration with the subsequent formation of multivacancies. The kinetics of the latter process has a mixed character relative to the reaction type. Evolution of the *D*-cluster core may bring about both an increase and a decrease in the number of vacancies, depending on which annealing process is dominant (i.e., whether it involves external or internal annihilation) [3]. Predominance of one or the other process is governed by the decomposition of small-size defect complexes, which are the sources of separate vacancies and interstitial atoms. The ESR data indicate that both types of sources are present. Such sources for vacancies can be the Si-*A*5 centers, whereas, for interstitial atoms, these sources can be represented by di-interstitials (the Si-*P*6 centers), which dissociate at the same temperatures $T \approx 150$–170°C ($E_a \approx 1.1$ eV) [18, 20] as the Si-*A*5 centers and tetravacancies. A low annealing temperature of tetravacancies, which is equal to the activation temperature for the formation of the Si-*P*1 centers (pentavacancies), $T = 150$–170°C, indicates that the processes which involve internal annihilation are predominant; these processes result in the disruption of tetravacancies and the formation of trivacancies ($V_4 + I \longrightarrow V_3$). In this case, the decomposition of the Si-*P*6 di-interstitial center into two interstitial atoms ($I_2 \longrightarrow I + I$) at $T = 150$–170°C [33] leads to the annihilation of a vacancy in a tetravacancy and to the formation of trivacancies, which interact with stable divacancies and form pentavacancies ($V_3 + V_2 \longrightarrow V_5$). The pentavacancies that formed via external annihilation according to the bimolecular reaction $V_4 + V \longrightarrow V_5$ should have a low concentration since they possess a lower enthalpy of formation and a lower concentration of the centers that act as sources of vacancies for their formation. Apparently, the spin $S = 1/2$ of the Si-*P*1 centers indicates that these centers (pentavacancies) have, predominantly, the ring configuration. The kinetics of the internal-annihilation processes is governed by the characteristics of the reactions $V_m + I \longrightarrow V_{m-1}$, which accompany the decomposition of interstitial defects ($I_2 \longrightarrow I + I$). The interstitial-generation kinetics can be monomolecular, bimolecular, or diffusion-controlled. Monomolecular reactions proceed under the conditions of high thermal stability of interstitial defects, so that the effective concentration of free interstitial atoms is limited by the decomposition rate of their sources. The final result of annealing is governed by the total number of accumulated interstitial atoms. Thus, the characteristics of the decomposition of the point-defect source ultimately govern the annealing kinetics for a multivacancy cluster.

However, it is hardly possible to observe such a decomposition process in the explicit form, because this process is accompanied by the disintegration of the divacancy *D* cluster; the latter process occurs with the subsequent diffusion-controlled buildup of separate multivacancies, which are distributed throughout the crystal. It can be shown [3] that, in this case as well, the final result consists in the buildup of Si-*P*3 and Si-*P*1 centers. It follows from this reasoning that reverse annealing is caused by the decomposition of the *D* clusters and by the buildup of tetravacancies and pentavacancies. In the limiting case of high integrated fluxes of neutrons, the buildup of multivacancies (mainly, pentavacancies) in the ring configuration should be the predominant process; as a result, the asymptotic state of irradiated silicon will correspond to the compensated intrinsic material.

5. RADIATION RESISTANCE

It follows from the foregoing analysis that one can enhance the radiation resistance of a silicon detector by varying the asymptotic state of the cluster. For example, this can be attained by introducing centers that have large capture cross sections for vacancies and interstitial atoms and prevent the formation of divacancies and tetravacancies. It has been shown [2] that, if the conditions $\beta_{VO} > \beta_{VV}$ and $\lambda \ll 1$ are satisfied for the probabilities of elementary events of reactions $V + O \longrightarrow VO$ (O is any impurity, including oxygen) and $V + V \longrightarrow V_2$, the cluster consists of divacancies, whereas the *V*O complexes are dominant at the periphery of the cluster. Competition of the correlated-pair (*V*–*I*) recombination will affect the output of the reaction $V + O \longrightarrow VO$. Consequently, the rate of the latter reaction will depend on the energy of irradiating particles, i.e., on the separation parameter δ, which appears in the generation function for correlated pairs $\varphi(r) = \varphi_0 \exp[-\delta(r - r_V)]$. If the reaction rates are diffusion-limited, then, in order for these rates to be comparable, the impurity (oxygen) concentration should be $N_O \geq (r_V^2 \delta / r_O) N_V$, where r_V and r_O are the radii of capture by a vacancy and oxygen atom, respectively. In this case, it should be expected that, if the reaction $V + O \longrightarrow VO$ is not controlled by the recombination of correlated pairs (*V*–*I*), the reaction rate is proportional to $\propto N_O$, whereas, if this reaction is controlled by the recombination, the rate is propor-

tional to $\propto N_O^x$, where $0 < x < 1$. Since $\delta_n < \delta_p$ (for neutron and proton irradiation, respectively), the clusters should be less sensitive to the introduction of oxygen under neutron irradiation than in the case of proton irradiation, which is inconsistent with experimental data. As was mentioned above, the cause of this might be related to the fact that the initial stage of the spatial–temporal separation of *V* and *I* defects was ignored; i.e., the dependence of the cross sections of reactions (or the reaction rate constants) on the time and coordinates was ignored. An increased probability of vacancy capture by another vacancy and divacancy formation depend predominantly on the characteristics of interaction of the defect-forming particles with the crystal's atoms (i.e., on the impact parameter), rather than on the separation parameter δ (i.e., on the energy of the above particles). As the energy of the defect-producing particle decreases, the impact parameter and the collision rate with the largest energy transfer, which differs for neutrons and protons, increase. The domination of the reaction $V + V \longrightarrow V_2$ over other reactions leads to the fact that tetravacancies are formed in the central part of a cluster, whereas vacancies are formed in the remaining part of the cluster. This is confirmed by the independence of the degradation constant on the oxygen concentration and by the dependence of the depletion voltage on the oxygen concentration in the case of irradiation with protons. Indeed, since the reverse current is governed by tetravacancies, which are dominant at the center of the cluster, all variations in the characteristics at the periphery of the cluster are of no importance. The depletion voltage is governed by divacancies whose concentration is low at the periphery of the clusters. The presence of oxygen reduces the divacancy-formation rate due to the capture of vacancies and brings about a decrease in the *D*-cluster radius and, correspondingly, in the constants *b* [see (9), (12)] and *c* (10).

6. CONCLUSION

Agreement of the calculated values of the parameters α, *b*, *c*, and Φ_{inv} with experimental data validates the suggested cluster model. This model is based on the representation of neutron-irradiation-produced defects as divacancy *D* clusters with a tetravacancy core. The energy structure is calculated in the defect-molecule model. Identification of the energy levels in the vicinity of the midgap is of fundamental importance since it is these levels that govern the characteristics of irradiated detectors. However, this issue has not been resolved until now. Explaining the neutron-irradiation-induced effects on the basis of divacancies or V_2O oxygen complexes has not been corroborated experimentally.

It follows from the suggested model that the main defects responsible for radiation resistance and neutron-irradiation-induced effects are divacancies and tetravacancies. Tetravacancies are responsible for the behavior of reverse current, whereas divacancies govern the depletion voltage. At the same time, the oxygen-containing complexes do not give rise to observable radiation effects; nevertheless, these complexes aid in enhancing radiation resistance by reducing the formation rate of multivacancies, which control resistance to radiation.

The proposed model makes it possible to predict qualitatively and quantitatively the behavior of neutron-irradiated float-zone silicon in relation to the inherent properties of this material and external conditions. The effect of contraction of a cluster's outer space-charge region if the dopant concentration exceeds a certain critical value is also predictable (16). This effect may reduce the depletion voltage by a factor of $R \sim [1 - (r_n/r_{cl})^3]^{-1}$.

REFERENCES

1. *Physical Processes in Irradiated Semiconductors*, Ed. by L. S. Smirnov (Nauka, Novosibirsk, 1977).
2. V. L. Vinetskiĭ and G. A. Kholodar', *Radiation Physics of Semiconductors* (Naukova Dumka, Kiev, 1979).
3. *Radiation Effects in Semiconductors* (Nauka, Novosibirsk, 1979).
4. J. L. Hastings, S. K. Estreicher, and P. A. Fedders, Phys. Rev. B **56** (16), 10215 (1997).
5. I. D. Konozenko, A. K. Semenyuk, and V. I. Khivrich, Phys. Status Solidi **35**, 1043 (1969).
6. V. L. Vinetskii, Phys. Status Solidi **41**, K93 (1970).
7. E. Fretwurst *et al.*, Nucl. Instrum. Methods Phys. Res. A **326**, 357 (1993).
8. G. Lindström, M. Moll, and E. Fretwurst, Nucl. Instrum. Methods Phys. Res. A **426**, 1 (1999).
9. R. Wunstorf *et al.*, Nucl. Instrum. Methods Phys. Res. A **315**, 149 (1992).
10. H.-J. Ziock *et al.*, Nucl. Instrum. Methods Phys. Res. A **342**, 96 (1994).
11. C. E. Barnes, Radiat. Eff. **8**, 221 (1971).
12. V. A. J. van Lint, R. E. Leadon, and J. E. Colwell, IEEE Trans. Nucl. Sci. **19**, 181 (1972).
13. G. D. Watkins, J. Phys. Soc. Jpn., Suppl. 2 **18**, 22 (1963).
14. G. D. Watkins and J. W. Corbett, Phys. Rev. **138**, A543 (1965); Phys. Rev. **138**, A555 (1965).
15. G. D. Watkins and J. W. Corbett, Phys. Rev. **134**, 1359 (1964).
16. Y. H. Lee and J. W. Corbett, Phys. Rev. B **13** (6), 2653 (1976).
17. D. F. Daly and H. E. Noffke, Radiat. Eff. **8**, 203 (1971).
18. Wan Jung and G. S. Newell, Phys. Rev. **132** (2), 648 (1963).
19. K. L. Brower, Radiat. Eff. **8**, 213 (1971).
20. Y. H. Lee, Y. M. Kim, and J. W. Corbett, Radiat. Eff. **15**, 77 (1972).
21. G. D. Watkins and J. W. Corbett, Phys. Rev. **121** (4), 1001 (1961).
22. G. A. Kholodar and V. L. Vinetskii, Phys. Status Solidi A **30**, 47 (1975).

23. V. L. Vinetskii, G. N. Eritsyan, and R. A. Melkonyan, Phys. Status Solidi A **52**, 441 (1979).
24. P. F. Lugakov, T. A. Lukashevich, and V. V. Shusha, Phys. Status Solidi A **74**, 445 (1982).
25. J. Krynicki, J. C. Bourgoin, and G. Vassal, Rev. Phys. Appl. **14**, 481 (1979).
26. F. D. Haldane and P. W. Anderson, Phys. Rev. B **13**, 2553 (1976).
27. G. A. Baraff, E. O. Kane, and M. Schluter, Phys. Rev. Lett. **43**, 956 (1979).
28. W. A. Harrison, in *Festkörperprobleme* (Advances in Solid State Physics), Ed. by J. Treusch (F. Viewig, Braunschweig, 1977), Vol. 17.
29. B. R. Gossick, J. Appl. Phys. **30** (8), 1214 (1959).
30. F. F. Morehead and B. L. Crovden, Radiat. Eff. **6** (1), 27 (1970).
31. N. N. Gerasimenko, A. V. Dvurechenskiĭ, and G. P. Lebedev, Fiz. Tekh. Poluprovodn. (Leningrad) **7** (12), 2297 (1973) [Sov. Phys. Semicond. **7**, 1530 (1973)].
32. B. Dezillie, V. Eremin, and Z. Li, Nucl. Instrum. Methods Phys. Res. A **426**, 114 (1999).
33. Y. H. Lee, Appl. Phys. Lett. **73** (8), 1119 (1998).

Translated by A. Spitsyn

Semiconductors, Vol. 36, No. 10, 2002, pp. 1123–1127. Translated from Fizika i Tekhnika Poluprovodnikov, Vol. 36, No. 10, 2002, pp. 1202–1206.

ELECTRONIC AND OPTICAL PROPERTIES OF SEMICONDUCTORS

Electronic Properties of Liquid Tl_2Te, Tl_2Se, Ag_2Te, Cu_2Te, and Cu_2Se Alloys

V. M. Sklyarchuk and Yu. O. Plevachuk*

Ivan Franko National University, Lviv, 79044 Ukraine

** e-mail: plevachk@iap.franko.lviv.ua*

Submitted February 7, 2002; accepted for publication February 21, 2002

Abstract—The dependences of the electrical conductivity $\sigma(T)$ and thermoelectric power $S(T)$ of Cu_2Te, Cu_2Se, Ag_2Te, Tl_2Te, and Tl_2Se liquid semiconductors were experimentally studied at high temperatures and pressures (up to 25 MPa). The melts were shown to exhibit a minima in the dependences $\sigma(T)$ and a maximum in $S(T)$ at the stoichiometric composition M_2X (where M = Tl, Ag, Cu; X = Te, Se). The results were interpreted on the basis of the Mott model with *sp–d* hybridization, taking into account the metal *d* state position with respect to the Fermi level. © *2002 MAIK "Nauka/Interperiodica".*

1. INTRODUCTION

The study of electronic properties of chalcogenide-based melts is an important and, at the same time, difficult problem, since pure tellurium is intermediate between a metal and semiconductor, while liquid selenium changes its properties from dielectric to semiconductor. Most tellurium- and selenium-based melts are semiconductors that are metallized on heating. The dependences of the electrical conductivity on the carrier concentration exhibit a minimum, while the corresponding dependence of the thermoelectric power has a maximum in the stoichiometric composition region. Interest in Cu-, Ag-, and Tl-based melts is caused by the fact that tallium, being a group-III element exhibits properties of group-I elements, to which Cu and Ag noble metals belong [1]. This is caused by the fact that the valence 6*d* electrons of Tl have a very low energy. Silver and (to a greater degree) copper differ from tallium in that their populated *d* states have a sufficiently high energy; therefore, in addition to the *s* electron, *d* electrons can also be involved in bond formation. Many papers [2–4] are dedicated to the *sp–d* hybridization effect; however, deep insight into the electronic properties has not yet been achieved.

2. EXPERIMENTAL

The measurements were carried out by a contact four-point probe method under pressure from argon (up to 25 MPa) to preserve a constant composition of the samples under study. We used multizone two-radius measuring cells made of boron nitride and shaped as vertical cylindrical containers. Point graphite electrodes were embedded into the cell walls along the axis. The temperature was measured using WRe5/WRe20 thermocouples connected to the electrodes. A high-temperature furnace with three independently controlled heating elements allowed a uniform temperature field over the sample height or the necessary temperature gradient to measure the thermoelectric power. The equipment and measuring procedure used are described in [5] in detail.

3. RESULTS

3.1. Cu_2Te and Cu_2Se Melts

The experimental results on the temperature dependence of the conductivity $\sigma(T)$ and the thermoelectric power $S(T)$ of Cu_2Te and Cu_2Se melts are shown in Figs. 1 and 2. Immediately after melting, the

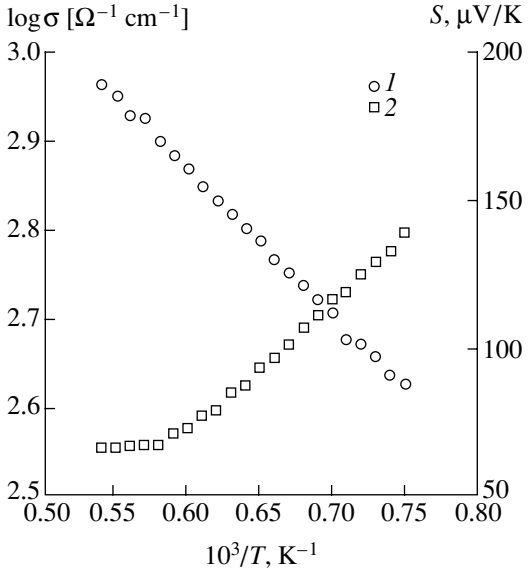

Fig. 1. Temperature dependences of the Cu_2Te melt conductivity (*1*) and thermoelectric power (*2*).

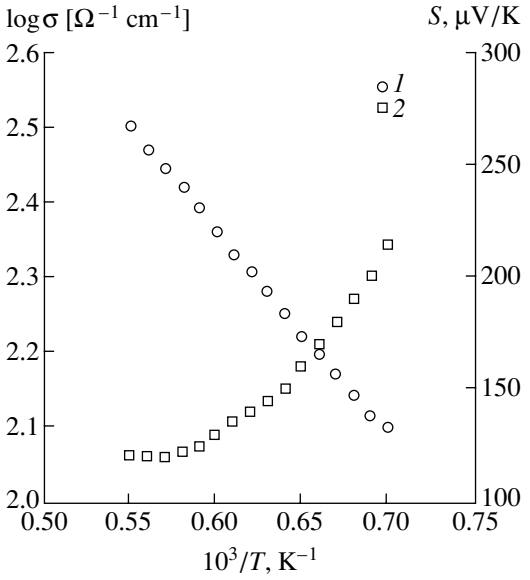

Fig. 2. Temperature dependences of Cu_2Se conductivity (*1*) and thermoelectric power (*2*).

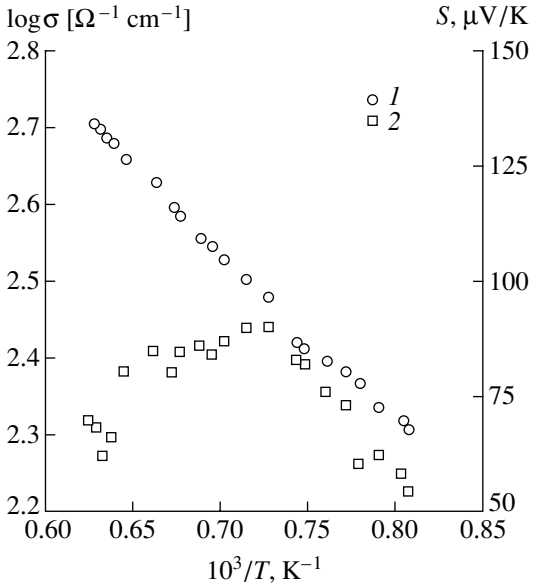

Fig. 3. Temperature dependences of Ag_2Te conductivity (*1*) and thermoelectric power (*2*).

quantity σ takes values of 500 Ω^{-1} cm^{-1} for Cu_2Te and 120 Ω^{-1} cm^{-1} for Cu_2Se. The activation energies $E(0)$ calculated from the experimental $\sigma(T)$ data are 0.33 and 0.55 eV for Cu_2Te and Cu_2Se, respectively. In the region of the melting point, the thermoelectric power is equal to 130 μV/K for Cu_2Te and 180 μV/K for Cu_2Se. As the temperature increases, the thermoelectric power decreases and levels off at 70 and 100 μV/K at 1670 and 1620 K for Cu_2Te and Cu_2Se, respectively.

3.2. Ag_2Te Melt

The data on $\sigma(T)$ and $S(T)$ of the Ag_2Te melt (see Fig. 3) indicate that the conductivity retains semiconductor properties in the entire temperature range under consideration with $E(0) = 0.45$ eV and that there is insignificant deviation from the dependence $\sigma(T) \propto \exp(1/T)$ above 1600 K. The thermoelectric power dependence on temperature $S(T)$ is not typical of semiconductor melts. The positive value of S indicates a dominant contribution of holes to charge transport processes. Immediately after melting, the thermoelectric power takes the value of 50 μV/K. Upon further heating, $S(T)$ increases to 90 μV/K and then decreases. This behavior indicates that complicated processes occur in the formation of the electron spectrum during heating. The absolute values of $\sigma(T)$ and $S(T)$ and their character give grounds to argue that the 4*d* band of silver is actively involved in the formation of the Ag_2Te electron spectrum.

3.3. Tl_2Te and Tl_2Se Melts

The experimental data on the conductivity $\sigma(T)$ and the thermoelectric power $S(T)$ of Tl_2Te (Fig. 4) and Tl_2Se (Fig. 5) melts indicate that the conductivity retains an exponential dependence typical of semiconductors in almost the entire temperature range under consideration, with the activation energy $E(0) = 0.49$ and 0.35 eV for Tl_2Te and Tl_2Se, respectively. Insignificant deviations from the linear dependence $\log\sigma = f(1000/T)$ are observed only above 1400 K for Tl_2Se and above 1000 K for Tl_2Te. In this case, the thermoelectric power S decreases in absolute value from |–140| μV/K to the level of |–40| μV/K for Tl_2Te with $E(0) = 0.28$ eV. For Tl_2Se, the value of S decreases in

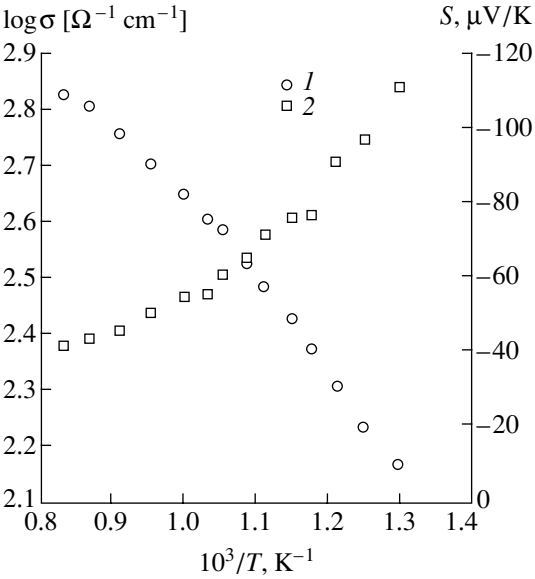

Fig. 4. Temperature dependences of Tl_2Te conductivity (*1*) and thermoelectric power (*2*).

magnitude from |–290| μV/K to the level of |–80| μV/K with $E(0) = 0.5$ eV. The negative value of S for both alloys suggests a dominant electron contribution to the charge transport mechanism. We also call attention to the fact that both the behavior of $\sigma(T)$ and $S(T)$ for Tl_2Se in contrast to Tl_2Te, is not typical of liquid semiconductors. This is probably caused by the fact that Tl_2Se is characterized by an appreciable fraction of the ionic conduction component, which amounts to 6.8% at 710 K [6].

The results obtained for all the systems under consideration call for a deeper analysis of the influence of the *d* band on the formation of the electron spectrum of the melts. However, we can already argue that the *d* band of metals has a significant effect on electron spectrum formation for liquid semiconductors.

4. DISCUSSION

The results for all the melts conform well to previous data [1–4]; however, there is disagreement in their interpretation. In our opinion, this is caused by different approaches to the interpretation of the charge transport properties. We calculated the Lorentz number (some values of L/L_0, where $L_0 = \pi^2/3(k/e)^2$, are given in Table 1) for the case of arbitrary degeneracy in the approximation of scattering by acoustic vibrations using thermoelectric power S data [7]. The very wide variation in L (also taking into account the fact that $L/L_0 \longrightarrow 1$ as the temperature increases) indicates that the degree of degeneracy of electron gas increases. The calculated Lorentz numbers were used to evaluate the electron component of the heat conductivity χ_{el} (Table 2). The calculated values of $\chi_{el}(T)$ (see Fig. 6) point to a certain role of bipolar heat transport, which disappears as the density of states in the pseudogap increases. Taking into account the increase in the degree of degeneracy of electron gas, we can argue that the system converts from the semiconductor state to the metal one.

As is known [9], the conductivity and thermoelectric power of a liquid semiconductor can be written as

$$\sigma(T) = \sigma_0 \exp\left(-\frac{E(0) - 2\gamma T}{2kT}\right),$$
$$S(T) = \left(-\frac{k}{e}\right)\left(\frac{E(0) - 2\gamma T}{2kT} + 1\right), \quad (1)$$

where $E(0)$ is the activation energy and γ is its temperature coefficient. We note that insignificant downward deviations from the linear dependence $\log\sigma = f(1000/T)$ are observed for Tl_2Te and Tl_2Se melts above 900 and 1400 K, respectively, which is described in [10] in detail.

The dependence of the thermoelectric power of all the melts is more intricate. The linear dependence $S = f(1000/T)$ is observed in the low-temperature region, while an insignificant deviation from linearity followed by leveling off is observed in the high-temperature region. This behavior is characteristic of all the melts, except for Ag_2Te, where S initially increases and then decreases. The dependence $S(T)$ for all the melts levels

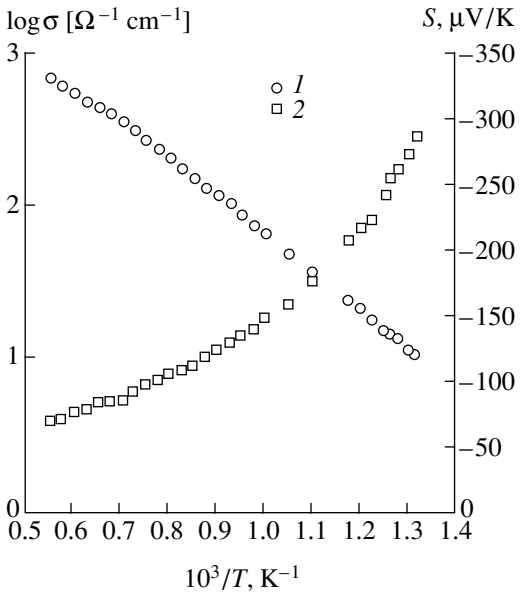

Fig. 5. Temperature dependences of the Tl_2Se conductivity (*1*) and thermoelectric power (*2*).

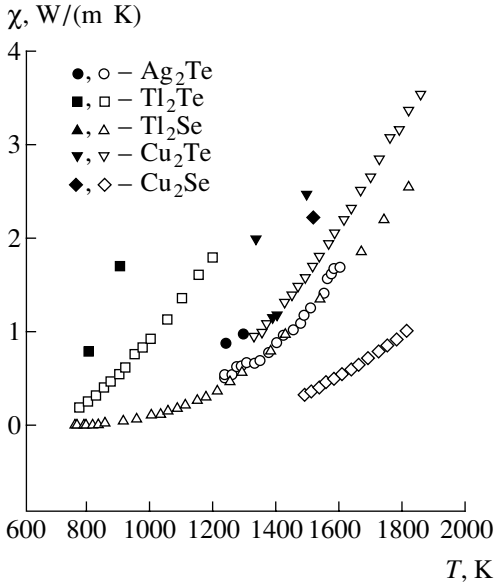

Fig. 6. Temperature dependences of the heat conductivity (*1*) of Cu_2Te, Cu_2Se, Ag_2Te, Tl_2Te, and Tl_2Se melts. Open and closed symbols correspond, respectively, to the calculated electronic component of the heat conductivity and the experimental data on the total heat conductivity of Cu_2Te, Cu_2Se, Ag_2Te [2], and Tl_2Te [8] melts.

Table 1. Calculated values of the temperature dependence of the Lorentz number L and the density of states $N(E_F)$ at the Fermi level for Cu_2Te, Cu_2Se, Ag_2Te, Tl_2Te, and Tl_2Se melts

Tl_2Te				Tl_2Se				Ag_2Te			
T, K	L/L_0	$N(E_F)$, 10^{-28} eV^{-1} m^{-3}	$\frac{dN(E_F)}{dE_F}$, 10^{-28} eV^{-2} m^{-3}	T, K	L/L_0	$N(E_F)$, 10^{-28} eV^{-1} m^{-3}	$\frac{dN(E_F)}{dE_F}$, 10^{-28} eV^{-2} m^{-3}	T, K	L/L_0	$N(E_F)$, 10^{-28} eV^{-1} m^{-3}	$\frac{dN(E_F)}{dE_F}$, 10^{-28} eV^{-2} m^{-3}
800	0.79	0.35	0.86	800	0.64	0.1	0.62	1200	0.89	0.38	0.35
900	0.85	0.47	0.77	900	0.68	0.17	0.68	1300	0.85	0.42	0.46
1000	0.89	0.56	0.62	1000	0.71	0.22	0.68	1400	0.84	0.48	0.53
1100	0.92	0.64	0.54	1100	0.74	0.29	0.68	1500	0.82	0.54	0.63
1200	0.93	0.69	0.48	1200	0.77	0.36	0.66	1600	0.85	0.61	0.55
				1400	0.81	0.5	0.62				
				1600	0.83	0.59	0.58				
				1800	0.86	0.7	0.54				

Cu_2Te				Cu_2Se			
T, K	L/L_0	$N(E_F)$, 10^{-28} eV^{-1} m^{-3}	$\frac{dN(E_F)}{dE_F}$, 10^{-28} eV^{-2} m^{-3}	T, K	L/L_0	$N(E_F)$, 10^{-28} eV^{-1} m^{-3}	$\frac{dN(E_F)}{dE_F}$, 10^{-28} eV^{-2} m^{-3}
1300	0.72	0.55	1.21	1500	0.68	0.33	0.79
1400	0.75	0.59	1.03	1600	0.71	0.37	0.69
1500	0.78	0.65	0.89	1700	0.74	0.42	0.63
1600	0.82	0.69	0.72	1800	0.75	0.47	0.64
1700	0.84	0.75	0.65				
1800	0.86	0.8	0.62				

Table 2. Calculated values of the temperature dependence of the electronic component of the heat conductivity of Cu_2Te, Cu_2Se, Ag_2Te, Tl_2Te, and Tl_2Se melts

Ag_2Te		Tl_2Te		Tl_2Se		Cu_2Se		Cu_2Te	
T, K	χ_{el}, W/(m K)	T, K	χ_{el}, W/(m K)	T, K	χ_{el}, W/(m K)	T, K	χ_{el}, W/(m K)	T, K	χ_{el}, W/(m K)
1250	0.57	800	0.26	800	0.2	1350	1.04	1500	0.88
1300	0.65	900	0.56	900	0.055	1400	1.21	1600	0.55
1400	0.91	1000	0.95	1000	0.12	1450	1.43	1700	0.77
1500	1.25	1100	1.39	1100	0.23	1500	1.63	1800	0.99
1550	1.44	1200	1.81	1200	0.39	1600	2.16		
1600	1.7			1400	0.93	1700	2.71		
				1600	1.58	1800	3.1		
				1800	2.48				

off at a value below 86 μV/K, which is interpreted in [8] as a transition to the metal state. However, a somewhat different approach to the determination of the transition criterion is considered in [1], where it is based on the specific dependence of the conductivity at the band edge. We considered these approaches in [12] and reason that these have no basic differences. In our opinion, the variation in the properties in the transitional region

is of significance, since quantitative estimations are rather subjective.

An important fact is that the degree of degeneracy of electron gas increases, as well as the density of states at the Fermi level, in the course of the heating of the melts under study. In this case, we can write

$$\sigma(T) = \frac{e^2h^3l}{81\pi m^2}[N(E_F)]^2,$$
$$S(T) = \frac{2\pi^2k^2T}{3}\frac{1}{e}\frac{1}{N(E_F)}\frac{dN(E_F)}{dE_F}, \quad (2)$$

where l is the free path length comparable to the interatomic spacing and $N(E_F)$ is the density of states at the Fermi level.

An analysis of formulas (2) shows that σ increases due to an increase in the density of states at the Fermi level, and S is given by

$$\frac{1}{N(E_F)}\frac{dN(E_F)}{dE_F}.$$

The absolute values of $N(E_F)$ and $dN(E_F)/dE_F$ calculated using the data in [13] are listed in Table 1. The density of states $N(E_F)$ increases with temperature for all the melts. This factor controls the conductivity behavior. A somewhat different pattern is observed when analyzing the data on $dN(E_F)/dE_F$. For Tl_2Te, Cu_2Te, and Cu_2Se, the value of $dN(E_F)/dE_F$ decreases as temperature increases, which controls the dependences $S(T)$; in contrast, the run of the $dN(E_F)/dE_F$ curves for Tl_2Se and Ag_2Te is more intricate, which manifests itself in the dependences $S(T)$. In the latter melts, the ion component probably plays a certain role; this component is also involved in the transport processes.

5. CONCLUSION

An analysis of the electronic structures of copper, silver, and tallium atoms shows that the filled 3*d* shell of copper is closer to the 4*d* states than the 4*d* shell of silver to the 5*d* states. Therefore, the 4*d* states of silver and (to a greater degree) the 3*d* states of copper can overlap with the valence band, which results in a change in the density of states near the band edge. The density of states N_v in the valence band increases more rapidly than that of N_c in the conduction band. This probably explains the fact as to why the thermoelectric power of Ag_2Te, Cu_2Te, and Cu_2Se is positive, in contrast to Tl_2Te and Tl_2Se where it is negative. Thus, the *sp–d* hybridization effect is more pronounced in the sequence Tl, Ag, and Cu; and this controls the dynamics of the electronic properties studied.

REFERENCES

1. M. Cutler, *Liquid Semiconductors* (Academic, New York, 1977).
2. A. R. Regel' and V. M. Glazov, *Physical Properties of Electronic Melts* (Nauka, Moscow, 1980).
3. E. A. Dancy, Trans. Metall. Soc. AIME **233**, 270 (1965).
4. B. I. Kazandzhan and Yu. I. Selin, Dokl. Akad. Nauk SSSR **216** (1), 67 (1974) [Sov. Phys. Dokl. **19**, 301 (1974)].
5. Yu. Plevachuk and V. Sklyarchuk, Meas. Sci. Technol. **12** (1), 23 (2001).
6. T. Usuki, J. Phys. Soc. Jpn. **62** (2), 634 (1993).
7. I. A. Smirnov and V. I. Tamarchenko, *Electron Heat Conductivity in Metals and Semiconductors* (Nauka, Leningrad, 1977).
8. V. I. Fedorov and V. I. Machuev, Fiz. Tverd. Tela (Leningrad) **12**, 631 (1970) [Sov. Phys. Solid State **12**, 484 (1970)].
9. N. F. Mott and E. A. Davis, *Electronic Processes in Non-Crystalline Materials* (Clarendon, Oxford, 1971; Mir, Moscow, 1974).
10. V. Sklyarchuk and Yu. Plevachuk, Z. Metallkd. **91**, 71 (2000).
11. J. E. Enderby and A. C. Barnes, Rep. Prog. Phys. **53**, 85 (1990).
12. V. Sklyarchuk and Yu. Plevachuk, J. Alloys Compd. **312** (1/2), 25 (2000).
13. A. C. Barnes and C. Guo, J. Phys.: Condens. Matter **6** (23A), A229 (1994).

Translated by A. Kazantsev

Semiconductors, Vol. 36, No. 10, 2002, pp. 1128–1131. Translated from Fizika i Tekhnika Poluprovodnikov, Vol. 36, No. 10, 2002, pp. 1207–1210.

ELECTRONIC AND OPTICAL PROPERTIES OF SEMICONDUCTORS

Dependence of GaN Photoluminescence on the Excitation Intensity

V. N. Bessolov, V. V. Evstropov, M. E. Kompan, and M. V. Mesh

Ioffe Physicotechnical Institute, Russian Academy of Sciences, Politekhnicheskaya ul. 26, St. Petersburg, 194021 Russia

Submitted December 4, 2001; accepted for publication April 9, 2002

Abstract—The dependence of the edge photoluminescence (PL) intensity on the excitation intensity in (0001) HVPE-grown GaN samples has been studied. The specific behavior found is that, at a low excitation level, the dependence is markedly superlinear, namely, superquadratic, and at high excitation levels it is nearly linear. A model accounting for the observed superquadratic behavior is proposed which is based on the identity of the recombination processes in the surface space charge region (SCR) under optical excitation with those in the SCR of the Schottky barrier or a *p–n* junction under current flow conditions. The superquadratic dependence is obtained analytically under the assumption that the nonradiative recombination channel is associated with multiple-hopping tunneling along a dislocation, which is formed by a chain of carrier localization centers and crosses the SCR. The experimental dependence of the PL intensity on the excitation intensity is a power-law function. The distance between the neighboring localization centers, i.e., the period of the potential along the dislocation, is determined as ~ 4.1 nm. © *2002 MAIK "Nauka/Interperiodica".*

1. Epitaxial GaN layers are widely used in the production of short-wavelength optoelectronic devices. The luminescence quantum yield is related to the epitaxial layer (epilayer) quality through, among other things, the ratio between the intensities of the radiative and nonradiative recombination of carriers; however, the mechanisms of nonradiative recombination in GaN epilayers grown using different techniques (metal-organic chemical vapor deposition (MOCVD), molecular beam epitaxy (MBE), hydride-chloride vapor phase epitaxy (HVPE)) are still unclear.

One of the factors affecting the epilayer quality is the lattice mismatch between the wurtzite GaN epilayer and 6H-SiC (~4%), Al_2O_3 (~15%), or Si (~22%) substrate. This results in a high density of misfit dislocations in GaN layers during heteroepitaxy. It is also known that the misfit dislocation density increases as the lattice mismatch between the layer and substrate increases and decreases as the epilayer thickness increases. In particular, HVPE epitaxy provides for the fabrication of GaN layers more than 100 μm thick on a sapphire (Al_2O_3) substrate, with the mismatch dislocation density at the layer surface an order of magnitude smaller than that at the heterointerface [1].

It is worth noting that in studies of luminescence attention is usually drawn mainly to the spectral characteristics of recombination radiation. However, in the situations where the spectral bands are broad and unstructured, the study of band shapes yields little information. The goal of the present study is to investigate nonradiative recombination by analyzing the behavior of luminescence intensity as a function of the intensity of excitation radiation.

2. Samples with relatively intensive luminescence were chosen for study. This allowed the recording of emission–excitation characteristics in a luminescence intensity range that varied by as many as three orders of magnitude. GaN layers were grown by HVPE. The GaN layer deposited on a sapphire substrate was more than 100 μm thick, with an electron density $n_n = 5 \times 10^{18}$ cm^{-3}; the respective values for the GaN layer on the 6*H*-SiC substrate were 3 μm and 5×10^{17} cm^{-3}.

The photoluminescence (PL) was excited with a pulsed nitrogen laser (the emission wavelength λ = 337 nm, the pulse width was 6 ns). The luminescence was excited and detected on the free surface of layers. The measurements were done at room temperature. The object of interest was the dependence of the PL intensity Φ on the photoexcitation intensity I.

In our case, a specific problem complicating the recording of $\Phi(I)$ dependences was the lack of standard ultraviolet photodetectors of nanosecond pulses with sufficient linearity in a wide range of intensities. We used a special technical approach involving the simultaneous recording of the luminescence band and the excitation line on one and the same scale. For this, a portion of the exciting radiation was directed to the monochromator input, with its intensity preliminarily attenuated to the necessary value by an adjustable filter for this wavelength. A family of luminescence spectra was recorded at an excitation intensity that varied in the range of 0.01–7 W cm^{-2} by the known neutral filters and grids. Consequently, the ratio of the intensities of the exciting and luminescent radiation was recorded each time with the same detector under the same conditions.

1063-7826/02/3610-1128$22.00

This method allowed us to minimize the possible influence of detector nonlinearity on the obtained data.

3. The samples under study exhibited luminescence spectra typical of GaN. The photon energy in the PL spectrum peak was $h\nu = 3.397$ eV for both GaN layers. The full width at half-maximum (FWHM) for the GaN/sapphire layer was significantly larger than that for GaN/SiC (Fig. 1), which presumably can be related to the effect of not only interband but also of donor–acceptor recombination, which is in agreement with the higher doping level of the GaN/sapphire layer.

For both layers, the dependence of the luminescence intensity on the excitation intensity is superlinear at a low excitation level and it can be described by the power-law dependence $\Phi \propto I^n$, where $n \approx 3.3$. At a high excitation level, this dependence is nearly linear: $n = 1.0$ for the layers on SiC and $n = 1$ for the layers on sapphire. In this case, the small sublinearity of the $\Phi(I)$ characteristic for the GaN/sapphire layer is presumably defined by the contribution of donor–acceptor recombination. The relationship between the Φ and I intensities can be approximated by a single simple formula accounting for the existence of two portions (Fig. 2):

$$I = k_1\Phi^{m_1} + k_2\Phi^{m_2}, \quad (1)$$

where the fitting parameters for the GaN/sapphire layer are $m_1 = 1.1$, $m_2 = 0.3$, $k_1 = 0.4$, and $k_2 = 1.3$, and those for GaN/SiC are $m_1 = 1.0$, $m_2 = 0.3$, $k_1 = 0.4$, and $k_2 = 6.6$. As is seen, the upper portions virtually coincide (m_1 and k_1 are nearly equal for both samples). The difference between the dependences for the two samples is observed only at the lower superlinear portion, in the k_2 value. The transition from the superlinear to the virtually linear portion in the layers on sapphire occurs at a lower excitation level than for the GaN/SiC layers (Fig. 2).

4. Superlinear dependences of the luminescence intensity on the excitation intensity were observed in GaN layers previously. For example, studies of cathodoluminescence from a 2-μm-thick MOCVD-grown GaN layer on a sapphire substrate have shown that the intensity of the edge luminescence increases with the excitation level by the power law $\Phi \propto I^n$ with the exponent $n = 2$ [2]. To the authors' knowledge, dependences with an exponent $n > 2$ were not observed.

In discussing the results, we shall use an analogy between the luminescence under optical pumping in the surface space-charge region (SCR) and the luminescence under current pumping in the SCR of a *p*–*n* junction. Let us present the necessary data. The depth of light absorption in GaN under the energy of exciting photons ($h\nu = 3.68$ eV) is 0.1 μm. The SCR width W, in our case, is not less than 0.05 μm, and the diffusion length of the minority carriers is ~0.5 μm [3]. Thus, the depth of the light absorption is less than the width of the carrier collection region (the photosensitive region) $W + L_p$, where L_p is the diffusion length of holes.

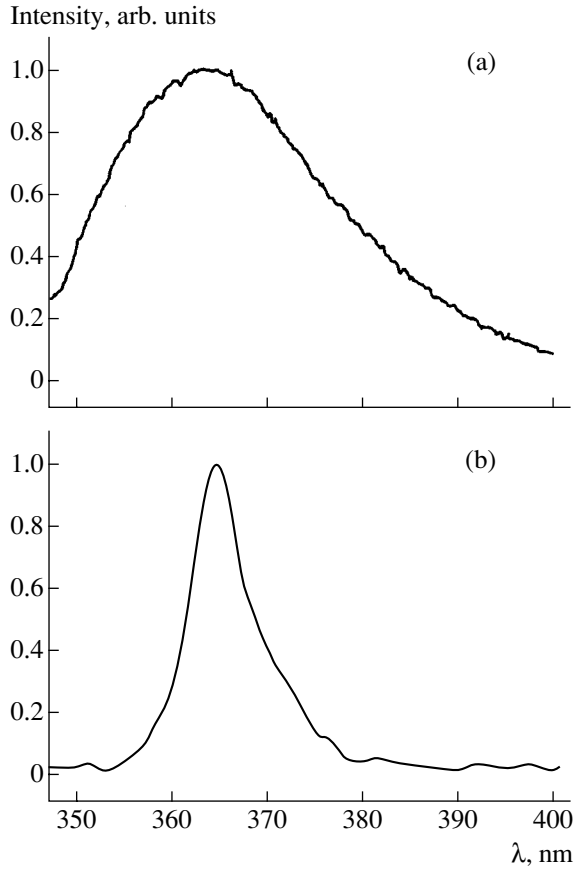

Fig. 1. PL spectra of GaN layers grown on (a) sapphire and (b) SiC substrate.

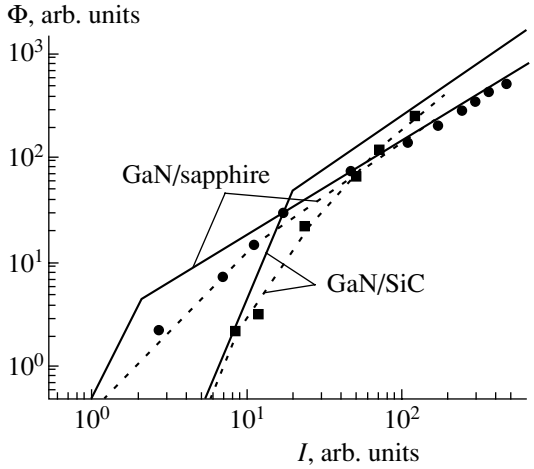

Fig. 2. Luminescence intensity vs. the excitation intensity for GaN layers on sapphire and SiC. Points: experiment; dashed lines: approximation (1); solid lines: asymptotes of the approximating curves.

The excitation radiation diminishes the band bending which existed in the dark and induces a photovolt-

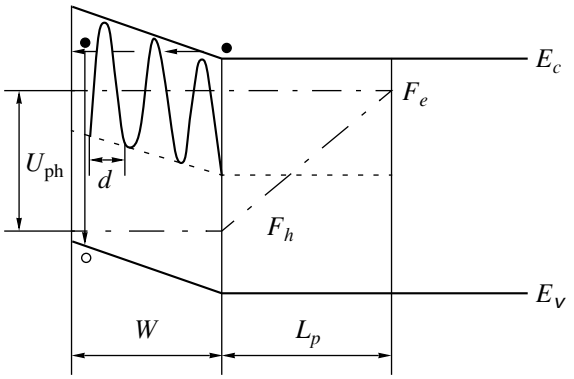

Fig. 3. The energy diagram of the surface region of an *n*-type semiconductor in the absorption of exciting light in the photosensitive region ($W + L$). Horizontal arrows: isoenergetic tunneling hopping of an electron; vertical arrow: electron–hole recombination.

age U_{ph} equal to the difference between the quasi-Fermi levels for electrons, Fe_e, and holes, F_h (Fig. 3). Since the light is totally absorbed in the photosensitive region $W + L_p$, the energy diagram of the surface region is the same as in a forward-biased Schottky barrier. The recombination processes in the surface SCR are the same as in the SCR of a Schottky barrier or a *p–n* junction under forward bias. The nature of the recombination flows is identical in all these cases; therefore, to obtain an analytical $\Phi(I)$ dependence, we shall regard the intensity of optical pumping as an analogue of the driving current, i.e., an analogue of the forward current J in a *p–n* junction. In the case under consideration, the equivalent forward current J consists of two components associated with thermal injection and tunneling:

$$J = J_{01}\exp(eU_{ph}/kT) + J_{02}\exp(eU_{ph}/\varepsilon), \qquad (2)$$

where $\varepsilon > 2kT$ is the characteristic energy of the tunneling component. In turn, the interband luminescence is defined by the thermal injection process; therefore, its intensity Φ is described by a thermal-injection-like dependence on the photovoltage U_{ph}:

$$\Phi = \Phi_0\exp(eU_{ph}/kT). \qquad (3)$$

Excluding U_{ph} from (2) and using (3), we obtain a relationship between the luminescence intensity Φ and the forward current J:

$$J = p_1\Phi + p_2\Phi^{kT/\varepsilon}, \qquad (4)$$

where $p_A = J_{01}/\Phi_0$, $p_2 = J_{02}/\Phi_0^{kT/\varepsilon}$.

The derived dependence (4) gives the sought-for $\Phi(I)$ characteristic, since the forward current J is equivalent to the optical excitation intensity I. The maximum power density of the optical pumping $I = 7$ W cm^{-2} corresponds to the driving current density $J = eI/h\nu \approx 2$ A cm^{-2}. Dependence (4) corresponds to the experimental characteristics $\Phi(I)$ (1) for GaN/sapphire and GaN/SiC if we disregard the contribution of the donor–acceptor recombination responsible for a small sublinearity in the upper portion and the broadening of the PL spectrum.

Let us thoroughly consider the lower portions of the $\Phi(I)$ characteristics. As follows from a comparison of (1) with (4), $kT/\varepsilon = m_2 = 0.3$. It is seen that $\varepsilon = nkT$, where $n = 1/m_2 = 3.3$, i.e., $n > 2$, which provides evidence in favor of the tunneling recombination mechanism. The value $\varepsilon = 82.5$ meV is the same for both layers, which infers one and the same tunneling mechanism.

According to the well-known model of tunneling across an SCR [4], ε depends on W and, consequently, on the density n_n ($\varepsilon \propto 1/W \propto \sqrt{n_n}$). In terms of multiple-hopping tunneling along dislocations, where a dislocation is modeled by a chain of potential wells separated with parabolic barriers [5], ε is defined only by the type of dislocation crossing the space charge region and is independent of density n_n. Therefore, the coincidence of ε in two layers with different n_n densities correlates with the model of tunneling along the dislocation.

Let us discuss this situation, namely, the equality of ε and the difference between the k_2 coefficients. The model assumes a series of isoenergetic tunneling jumps of an electron with subsequent recombination (Fig. 3). The current along the dislocation line is defined by the frequency of the last tunneling jump, since the barrier is the highest and, consequently, the barrier penetrability is the lowest for this jump. The current density is proportional to the dislocation density. In terms of the model [5], the quantity ε in (2) and, consequently, in (4) is related to the parameter r, which characterizes the dislocation type:

$$\varepsilon = \frac{\hbar}{\pi}\sqrt{\frac{r}{m^*}}, \qquad (5)$$

where r is the curvature of a parabolic barrier at its top, and m^* is the effective mass of a tunneling carrier ($m^* = 0.2m_0$ for an electron [6]). Hence, we can find the width d of a barrier with its height equal to half the band-gap width:

$$d = (E_g/r)^{1/2}, \qquad (6)$$

where $E_g = 3.39$ eV is the band gap [7]. The value $\varepsilon = 82.5$ meV yields $r = 0.03$ J m^{-2} = 0.2 eV nm^{-2}, and the width $d = 4.1$ nm. The equal ε values in both types of layers indicate that the dislocations crossing the SCR and defining the tunneling mechanism of recombination are of the same kind.

According to this model, the preexponential factor J_{02} for the tunneling component of the current is proportional to the density ρ of dislocations crossing the space charge region, $J_{02} \propto \rho$. Thus, we can see from (1) and (4) that $k_2 \propto p_2 \propto p$, which allows for a comparison

of the dislocation densities near the surface of the layers. A comparison of parameters k_2 in relation (1), which describes the experimental characteristics, shows that the dislocation density at the surface of the GaN/sapphire layer is 5 times lower than for GaN/SiC. We believe that this is due to the greater thickness of the GaN layer on sapphire, since the density of the mismatch dislocations at the GaN/sapphire interface is known to be higher than at the GaN/SiC interface [8]. This explanation is in agreement with the known fact that the spectral position of the edge photoluminescence band can depend on the thickness of the GaN epilayer [9].

5. We conclude that GaN layers of different thicknesses grown on different substrates (sapphire and SiC) exhibit similar $\Phi(I)$ characteristics. The dependence is superquadratic (with the exponent above 2) at a low excitation intensity, and at a higher intensity it is virtually linear. To account for this behavior, a model for the multistage nonradiative recombination of carriers via multiple-hopping tunneling along a dislocation was proposed. The model makes it possible to compare the dislocation densities in different layers and determine the period of the potential along a dislocation.

ACKNOWLEDGMENTS

We thank Yu.V. Zhilyaev and V.A. Dmitriev for providing the GaN epilayers used in this study. One of the authors (V.N.B.) is grateful to a program of the Russian Ministry of Industry, Science, and Technology (project no. 40.012.1.1.1153) for financial support.

REFERENCES

1. E. A. Stach, M. Kelsh, E. C. Nelson, *et al.*, Appl. Phys. Lett. **77**, 1819 (2000).
2. S. O. Kucheyev, M. Toth, M. R. Phillips, *et al.*, Appl. Phys. Lett. **79**, 2154 (2001).
3. Z. Z. Bandic, P. M. Bridger, E. C. Piquette, and T. C. McGill, Appl. Phys. Lett. **73**, 3276 (1998).
4. B. L. Sharma and R. K. Purohit, *Semiconductor Heterojunctions* (Pergamon, Oxford, 1974; Sov. Radio, Moscow, 1979).
5. V. V. Evstropov, M. Dzhumaeva, Yu. V. Zhilyaev, *et al.*, Fiz. Tekh. Poluprovodn. (St. Petersburg) **34**, 1357 (2000) [Semiconductors **34**, 1305 (2000)].
6. A. S. Barker and M. Ilegems, Phys. Rev. B **7**, 743 (1973).
7. M. E. Levinshtein, S. L. Rumyantsev, and M. S. Shur, *Properties of Advanced Semiconductor Materials* (Wiley, New York, 2001).
8. S. Koynov, M. Torf, S. Fisher, *et al.*, J. Appl. Phys. **82**, 1890 (1997).
9. P. W. Yu, C. S. Park, and S. T. Kim, J. Appl. Phys. **89**, 1692 (2001).

Translated by D. Mashovets.

Semiconductors, Vol. 36, No. 10, 2002, pp. 1132–1135. Translated from Fizika i Tekhnika Poluprovodnikov, Vol. 36, No. 10, 2002, pp. 1211–1214.

SEMICONDUCTOR STRUCTURES, INTERFACES, AND SURFACES

Photosensitivity of Structures Based on I–III$_n$–VI$_m$ Ternary Compounds Containing Ordered Vacancies

I. V. Bodnar'*, V. Yu. Rud', Yu. V. Rud'***, and M. V. Yakushev******

** Belarussian State University of Information Science and Radio Engineering, ul. Brovki 17, Minsk, 220072 Belarus*

*** St. Petersburg State Technical University, Politekhnicheskaya ul. 29, St. Petersburg, 195251 Russia*

**** Ioffe Physicotechnical Institute, Russian Academy of Sciences, Politekhnicheskaya ul. 26, St. Petersburg, 194021 Russia*

e-mail: rudvas@spbstu.ru

***** University of Strathclyde, G40NG Glasgow, UK*

Submitted February 4, 2002; accepted for publication February 13, 2002

Abstract—Homogeneous crystals of $CuIn_3Se_5$, $CuGa_3Se_5$, and $CuGa_5Se_8$ ternary compounds were grown, and their physical and chemical properties were investigated. Photosensitive structures were fabricated for the first time on the basis of these compounds, and the spectral dependence of the relative quantum photoconversion efficiency was measured. The bandgap of these compounds was also estimated, and it was shown that direct interband transitions are typical in them. It was found that the content and chemical nature of atoms forming an elementary cell in a I–III$_n$–VI$_m$ ternary compound control the relevant band gap. © *2002 MAIK "Nauka/Interperiodica".*

1. INTRODUCTION

Ternary I–III–VI$_2$ semiconductor compounds and their solid solutions have been widely investigated with the aim of developing high-efficiency thin-film solar cells. In particular, structures based on $CuInSe_2$ with a photoconversion efficiency as high as 18% have been fabricated [1, 2]. Up to now, the fundamental properties of I–III–VI$_2$ compounds have been controlled mainly by the formation of solid solutions. However, the study of interactions in I–III–VI systems showed that, along with well-known I–III–VI$_2$ phases, they can also contain many ordered phases of the I–III$_n$–VI$_m$ type, including phases with ordered vacancies [3–7]. Tsang *et al.* [3] calculated from first principles the domains of stability of such compounds and assumed that these phases are formed due to a spatial translation of a single cell of defect pairs for different numbers of I–III–VI$_2$ cells. The wide investigation of such phases has been recently started with the aim of using them as a basic tool in controlling fundamental properties of ternary chalcogenides [6, 7]. Evidently, the physical and technical investigations, aiming to synthesize such materials, make it possible to relate the fundamental properties of these materials to their atomic composition and analyze the possibility of forming nanostructures in I–III–VI systems.

The aim of this study is to develop methods for the formation of single-phase samples of I–III$_n$–VI$_m$ compounds and to fabricate photosensitive structures on the basis of these. The results of first investigations of the photosensitivity spectra of Schottky barriers are reported. These investigations made it possible to determine the band gap for a number of such phases and to measure some of their photoelectric properties.

2. GROWTH OF CRYSTALS

In order to grow the crystals of $CuIn_3Se_5$, $CuGa_3Se_5$, and $CuGa_5Se_8$ ternary compounds, high-purity atomic components were used (Cu of 99.999% purity, and In, Ga, and Se of 99.9999% purity). These components in the ratios Cu : In (Ga) : Se = 1 : 3 : 5 for $CuIn_3Se_5$ ($CuGa_3Se_5$) and Cu : Ga : Se = 1 : 5 : 8 for $CuGa_5Se_8$ with a total mass of 20–25 g were loaded into double quartz cells with conically shaped bottoms (for $CuIn_3Se_5$ and $CuGa_3Se_5$). A quartz holder was sealed into the cells from below to attach them to a vibrator. After evacuation to the residual pressure of 10^{-3} Pa, a cell was placed into a single-zone furnace with a preset temperature gradient. First, the temperature in the furnace was increased to 900 K at a rate of ~50 K/h, and then the cell was kept at this temperature for 2 h with the vibrator switched on. Then, the temperature was increased at the same rate to 1280–1300 K (for $CuIn_3Se_5$) and 1420–1450 K (for $CuGa_3Se_5$) with the vibrator switched on, and the formed melt was kept in

1063-7826/02/3610-1132$22.00 © 2002 MAIK "Nauka/Interperiodica"

Table 1. Results of X-ray spectroscopic microprobe analysis of $CuIn_3Se_5$, $CuGa_3Se_5$, and $CuGa_5Se_8$ ternary compounds

Compound	Cu, at. %		In, at. %		Ga, at. %		Se, at. %	
	calculation	experiment	calculation	experiment	calculation	experiment	calculation	experiment
$CuIn_3Se_5$	11.18	11.42	33.31	32.88	–	–	55.51	55.70
$CuGa_3Se_5$	11.11	10.98	–	–	33.33	33.16	55.56	55.86
$CuGa_5Se_8$	7.15	7.22	–	–	35.71	35.43	57.14	57.35

these conditions for an hour. After that, the vibrator was switched off and the melt was subjected to planar crystallization by decreasing the furnace temperature to 1070 K at a rate of 2–3 K/h. A homogenizing annealing was carried out at this temperature for 120 h.

Crystals of $CuGa_5Se_8$ were grown by the two-temperature method (horizontal variant) with subsequent planar melt crystallization. Metal components of the above-mentioned purity were loaded into a quartz boat that was then positioned in one of the cell ends. Selenium, taken in excess (in order to form vapor pressure of ~1 bar above the melt), was positioned in the opposite end of the cell. After evacuation and sealing off, the cell was positioned in a horizontal two-zone furnace in such a way as to place the boat with metal components in the "hot" zone, where the temperature was rapidly (for ~2 h) increased to ~1400 K. Then, the temperature of the "cold" zone was increased to 900 K and kept at this value for 2 h to produce a reaction between the metal components and the Se vapor. After being kept constant for 2 h, the temperature was increased at the same rate to 1100 K and kept at this value for an hour. Then, planar melt crystallization was carried out by decreasing the temperature to 1170 K at a rate of 2 K/h with subsequent annealing of $CuGa_5Se_8$ crystals for 240 h.

As a result, we obtained single-crystal $CuIn_3Se_5$ and $CuGa_3Se_5$ ingots of 12 mm in diameter and ~40 mm in length. The ingots of $CuGa_5Se_8$ were homogenous along their length and polycrystalline with large crystallites (separate crystallites were as large as $8 \times 4 \times 3$ mm^3 in size).

3. X-RAY MEASUREMENTS

The composition of the grown crystals was determined by X-ray spectroscopic microprobe analysis. The results are listed in Table 1. It can be seen that the experimental data are in agreement with the results of calculations.

The structure and parameters of the unit cell were determined by X-ray diffraction analysis. Diffraction patterns were recorded using a DRON-3M diffractometer (filtered X-rays emitted by a copper anode). The measurements showed that the $CuIn_3Se_5$, $CuGa_3Se_5$, and $CuGa_5Se_8$ ternary compounds crystallize in the defect-containing chalcopyrite structure. The parameters of the unit cell, calculated by the least squares method over lines, for which $2\theta > 60°$, are in good agreement with available published data [8–10]. The resolution of large-angle lines on the diffraction patterns indicates that the grown crystals are in equilibrium.

4. SURFACE-BARRIER STRUCTURES

In order to fabricate photosensitive structures, we used wafers that were cut from the grown crystals, mechanically ground and polished, and then subjected to polishing etching. Wafers with mirror-like cleavage planes were also used. In this case, no surface treatment was carried out.

The measurements we carried out showed that photosensitive structures can be fabricated by the thermal vacuum deposition of thin In, Cu, or Au layers on the surfaces of $CuIn_3Se_5$, $CuGa_3Se_5$, and $CuGa_5Se_8$ crystals. Ohmic contacts were prepared by soldering the wires using a Ga-based alloy. The spectra of the relative quantum photoconversion efficiency η (ratio of a short-circuit photocurrent to the number of incident photons) were measured by using continuous or modulated (at a frequency of 20 Hz) radiation from an incandescent lamp with the subsequent filtering of monochromatic radiation by a SPM-2 quartz-prism monochromator. The formed structures made it possible to obtain a spectral resolution of ≈1 meV.

5. RESULTS AND DISCUSSION

The measurements of static current–voltage (*I–V*) characteristics of the surface-barrier structures revealed that the contacts made by the deposition of pure In, Cu, and Au on the surfaces of $CuIn_3Se_5$, $CuGa_3Se_5$, and $CuGa_5Se_8$ crystals reproducibly show rectifying properties under a negative bias applied to the crystals. For a reverse bias U of ≈10 V (in magnitude), the rectification factor did not exceed 2. The forward portion of the *I–V* characteristic follows the law

$$U = U_0 + IR$$

at $U > 10$ V.

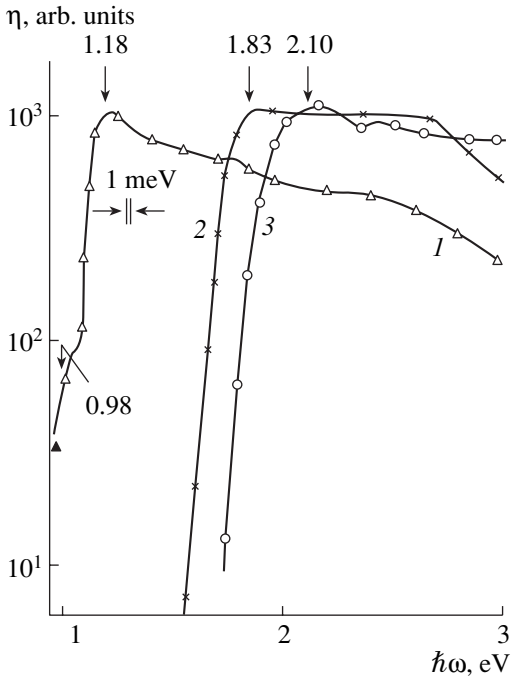

Fig. 1. Spectral dependences of relative quantum photoconversion efficiency of (*1*) $In/CuIn_3Se_5$, (*2*) $In/CuGa_3Se_5$, and (*3*) $In/CuGa_5Se_8$ surface-barrier structures exposed at 300 K to unpolarized light from a source facing the barrier side.

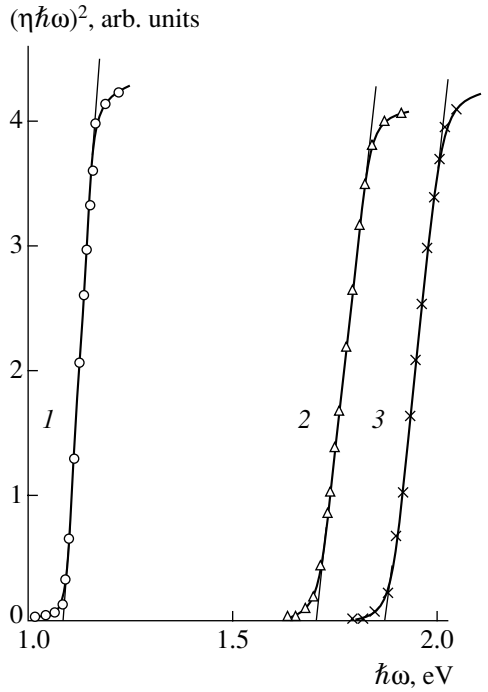

Fig. 2. Dependences $(\eta\hbar\omega)^2 = f(\hbar\omega)$ for (*1*) $In/CuIn_3Se_5$, (*2*) $In/CuGa_3Se_5$, and (*3*) $In/CuGa_5Se_8$ surface-barrier structures.

Typical values of residual resistance R_0 are listed in Table 2. In accordance with these data, $CuIn_3Se_5$, $CuGa_3Se_5$, and $CuGa_5Se_8$ crystals that were used to fabricate surface-barrier structures are compensated semiconductors with a sufficiently high resistivity.

When the fabricated Schottky barriers are illuminated, the photovoltaic effect is reproducibly observed. It is worth noting that the photovoltage sign did not depend on the geometric layout of the recording scheme or on the changes in the location of the light probe over the structure surface. This allowed us to assume that photogenerated carriers are separated by an active region, which is formed due to the deposition of metal layers on ternary compounds. The values of highest photovoltaic sensitivity S_U for Schottky barriers formed on $CuIn_3Se_5$, $CuGa_3Se_5$, and $CuGa_5Se_8$ compounds are listed in Table 2 for the first time. Generally, the maximum value of S_U was obtained when the illumination source faced the metallized side. The highest photovoltage (~0.3 V) was detected on $In/CuGa_3Se_5$ barriers illuminated with an incandescent lamp of power $P \approx 80$ W.

Table 2. Photoelectric properties of $In/CuIn_3Se_5$, $In/CuGa_3Se_5$, and $In/CuGa_5Se_8$ structures

Structure	R_0, Ω	S_U, V/W	E_g, eV	ħω, eV
$In/CuIn_3Se_5$	2×10^8	100	1.08	1.18
$In/CuGa_3Se_5$	2×10^9	400	1.70	1.8–2.5
$In/CuGa_5Se_8$	5×10^8	750	1.87	2.1–3.2

Figure 1 shows typical spectral dependences of the relative quantum photoconversion efficiency η for $In/I–III_n–VI_m$ Schottky barriers under illumination at 300 K by a source facing the metallized side. What engages our attention is the broad-band character of the photosensitivity spectra of the Schottky barriers. The location of the long-wavelength edge in the photosensitivity spectra is determined by the atomic composition and values of *n* and *m* in the chemical formula of the semiconductors used to form the Schottky barriers. The long-wavelength edge of the photosensitivity spectra in $(\eta\hbar\omega)^2 = f(\hbar\omega)$ coordinates can be linearly approximated (Fig. 2). On the basis of the data reported in [8], this makes it possible to attribute the long-wavelength edge to direct interband transitions in the semiconductor used to form the barrier. The energy value obtained by the extrapolation of the $(\eta\hbar\omega)^2$ curve to zero can be attributed to the band gap E_g (see Table 2). As can be seen, substituting In for Ga in the chemical composition of a semiconductor results in an increase in the band gap, which is typical of $I–III–VI_2$ compounds. Similar behavior is characteristic of the band gap in $CuGa_3Se_5$ and $CuGa_5Se_8$ compounds as *n* increases from 3 to 5 and *m* increases from 5 to 8 (see Table 1).

In the case of $In/CuIn_3Se_5$ Schottky barriers, the long-wavelength edge of the η spectrum has a clear

kink (Fig. 1, curve *1*), which can be attributed to photoactive absorption with the participation of deep levels related to lattice defects (these levels are spaced at 0.2 eV from one of the free bands). It is worth noting that the existence of such levels has been previously pointed out for structures based on $CuInSe_2$. No similar features were detected in the η spectra of other ternary compounds of this group (see Fig. 1, curves *2*, *3*).

The broad-band character of the photosensitivity spectra of barrier structures based on I–III$_n$–VI$_m$ ternary compounds with ordered vacancies, recorded under illumination using a source facing the contact side, indicates that the quality of the Schottky barriers formed for the first time on the new materials is rather high. Indeed, the most clearly defined short-wavelength falloff is only typical of structures based on $CuIn_3Se_5$ (Fig. 1, curve *1*). The full width at half-maximum δ of the spectra of these structures was found to be rather large ($\approx$900 meV). As for the other compounds of the I–III$_n$–VI$_m$ group, the value of this parameter is even larger, because the η spectra of the barrier structures based on them show virtually no short-wavelength falloff in a wide spectral region (Fig. 1, curves *2*, *3*).

It is also worth noting that the photoelectric parameters of the Schottky barriers in the new semiconductors with ordered vacancies, listed in Table 1, are stable (no degradation was observed). These parameters were reproduced well for samples cut from different zones of the grown crystals.

6. CONCLUSION

On the basis of pioneering physical and technical investigations, homogenous crystals of $CuIn_3Se_5$, $CuGa_3Se_5$, and $CuGa_5Se_8$ ternary compounds were grown to fabricate photosensitive structures. It was found that the band gap of these compounds is governed by their atomic composition and the ratios between atoms of Groups III and VI. This makes it possible to use these compounds for the fabrication of photosensitive structures capable of operating in controlled spectral ranges.

ACKNOWLEDGMENTS

This study was supported by INTAS, project no. 2001-283.

REFERENCES

1. T. Negami, Solid State Phenom. **67**–**68**, 349 (1999).
2. B. Esene, M. Wagner, D. Wolf, and G. Muller, J. Cryst. Growth **198**/**199**, 321 (1999).
3. S. B. Tsang, S. H. Wei, A. Zunger, and H. Katayama-Yoshida, Phys. Rev. B **57**, 9642 (1998).
4. S. H. Wei, S. B. Tsang, and A. Zunger, Appl. Phys. Lett. **72**, 3199 (1998).
5. N. M. Gasanly, A. Serpengurel, A. Audinly, *et al.*, J. Appl. Phys. **85**, 3198 (1999).
6. I. V. Bodnar', V. F. Gremenok, V. Yu. Rud', and Yu. V. Rud', Fiz. Tekh. Poluprovodn. (St. Petersburg) **33**, 805 (1999) [Semiconductors **33**, 740 (1999)].
7. G. Martin, R. Marques, S. M. Wasim, and R. Guevara, Jpn. J. Appl. Phys., Suppl. **39** (1), 44 (2000).
8. S. M. Sze, *Physics of Semiconductors Devices* (Wiley, New York, 1981; Mir, Moscow, 1984).
9. *Physicochemical Properties of Semiconductor Materials: a Handbook* (Nauka, Moscow, 1975).
10. J. L. Shay and J. H. Wernick, *Ternary Chalcopyrite Semiconductors: Growth, Electronic Properties, and Applications* (Pergamon, Oxford, 1975).

Translated by Yu. Sin'kov

Semiconductors, Vol. 36, No. 10, 2002, pp. 1136–1137. Translated from Fizika i Tekhnika Poluprovodnikov, Vol. 36, No. 10, 2002, pp. 1215–1216.

SEMICONDUCTOR STRUCTURES, INTERFACES, AND SURFACES

Effect of the State of the Silicon Surface on Hydrogen Sensitivity of Pd/*n*-Si Barrier Structures

V. M. Kalygina, L. S. Khludkova, V. I. Balyuba, and T. A. Davydova

Kuznetsov Siberian Physicotechnical Institute, Tomsk State University, Tomsk, 634050 Russia

Submitted January 8, 2002; accepted for publication March 11, 2002

Abstract—The influence exerted by the thermal annealing of silicon, prior to the deposition of a palladium contact, on the hydrogen sensitivity of palladium–⟨natural oxide⟩–silicon structures was studied. It is shown that structures based on annealed silicon have a much higher sensitivity to hydrogen and a shorter response time when compared with structures based on silicon not subjected to annealing. The results obtained are discussed in terms of structural transformations occurring at the silicon–⟨natural oxide⟩ interface during thermal treatment. © *2002 MAIK "Nauka/Interperiodica".*

It has been shown that palladium–⟨natural oxide⟩–silicon structures can be used as effective detectors of hydrogen [1–4]. As is known, mechanical stresses arise at the silicon–⟨natural oxide⟩ interface because of the lattice mismatch between the contacting phases [5]. These stresses may dramatically change the properties of both the semiconductor and the oxide and thereby affect the characteristics of device structures. These stresses can be relieved by thermal annealing. This communication presents the results obtained from studying the influence exerted by the thermal treatment of silicon prior to the deposition of a palladium contact on the hydrogen sensitivity of palladium–⟨natural oxide⟩–silicon structures.

Pd/*n*-Si structures were fabricated on the basis of silicon epitaxial layers with a doping level of 1×10^{12} cm^{-3}. The barrier contact was formed by the thermal evaporation of palladium in a vacuum at a residual pressure of 10^{-3} Pa. The contact area was 1×10^{-2} cm^2. Two types of structures were studied. In fabricating the structures of the first type, palladium was deposited onto silicon with a thin layer of natural oxide on its surface. In fabricating structures of the second type, on whose surface natural oxide was also present, silicon was subjected, prior to depositing palladium, to vacuum annealing at 500°C for 10 min. The current–voltage (*I–V*) characteristics of the structures were measured at room temperature in a hermetically sealed chamber filled with air or a hydrogen/air gas mixture containing 1 vol % H_2.

Figure 1 shows the forward *I–V* characteristics of structures of the first (curve *1*) and second (curve *2*) types. At biases in the range 0.05–0.25 V, the forward *I–V* characteristic is described by an exponential dependence which can be represented analytically as

$$I = SAT^2 \exp\left(-\frac{\varphi_B}{kT}\right)\exp\left(\frac{qV}{nkT}\right),$$

where *S* is the contact area; *A*, the effective Richardson constant; *T*, absolute temperature; *k*, the Boltzmann constant; φ_B, the barrier height; *q*, the elementary charge; and *n*, the nonideality factor.

The coefficient *n* is 1.2 and 1.9 for structures of, the first and second types respectively. The Φ_B value found from the *I–V* characteristics (at $A = 110$ A cm^{-2} K^{-2}) is, respectively 0.78 and 0.75 eV. Thus, the Pd/*n*-Si barrier structures fabricated on the basis of annealed silicon are characterized by a larger nonideality factor and a somewhat lower barrier height compared with the structures obtained on unannealed silicon.

Upon letting hydrogen into the measuring chamber, the forward current increased for both types of structures. The structures of the second type exhibited a

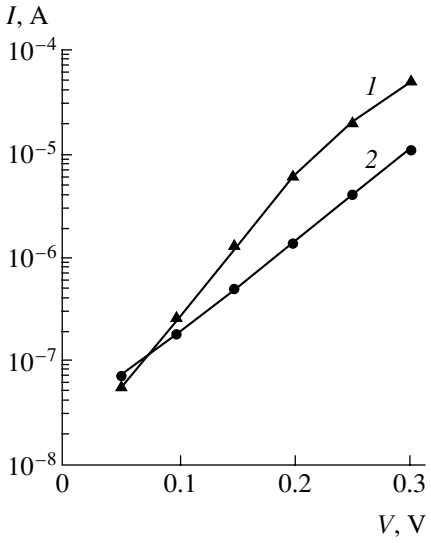

Fig. 1. Forward *I–V* characteristics of Pd/*n*-Si structures based on (*1*) unannealed and (*2*) annealed silicon, measured in air.

1063-7826/02/3610-1136$22.00 © 2002 MAIK "Nauka/Interperiodica"

much higher sensitivity to hydrogen than those of the first type. For the latter, the forward current at a voltage of 0.05 V increased 2–3-fold under the action of an air mixture containing 1 vol % H_2, whereas for the former, the increase was by a factor of 20–30. The ratio of currents in a medium with and without hydrogen, I_H/I, decreased for both types of structures with increasing bias. The maximum I_H/I values were observed at voltages of 0.05–0.10 V.

Figure 2 presents the time dependences of the rise in current, $\Delta I = I_H - I$, upon letting hydrogen into the measuring chamber. The current was measured under a forward bias of 0.05 V. It can be seen that the time in which a stationary value is attained (3–4 min) is an order of magnitude shorter for structures of the second type (curve *2*) compared with that for structures of the first type (curve *1*).

Thus, Pd/*n*-Si structures based on silicon annealed in a vacuum at 500°C have a much higher sensitivity to hydrogen and a shorter response time compared with structures based on unannealed silicon.

The results obtained can be accounted for in terms of structural transformations occurring in the course of annealing in the natural oxide layer and adjacent regions of silicon. Thermal annealing leads to the relaxation of mechanical stresses at the silicon–⟨natural oxide⟩ interface, which is accompanied by defect formation. Since defects are, as a rule, gas adsorption centers on the real surface of silicon [6], an increase in their concentration upon thermal treatment must improve the sensitivity of Pd/*n*-Si structures to hydrogen. Indirect confirmation of the increase in the defect concentration at the silicon–⟨natural oxide⟩ interface in the experiments carried out in this study is the fact that the nonideality factor increases and the barrier height in the Pd/*n*-Si structures decreases upon the thermal treatment of silicon.

The shorter response time of Pd/*n*-Si structures based on annealed silicon is presumably due to a decrease upon annealing in the density of slow states at the silicon–⟨natural oxide⟩ interface. As noted in [7], slow interfacial states, whose recharging times are as long as minutes and even hours, virtually disappear upon heating silicon samples in a vacuum at temperatures higher than 230°C. Therefore, the time of equilibration in surface charging as a result of adsorption of hydrogen atoms becomes shorter.

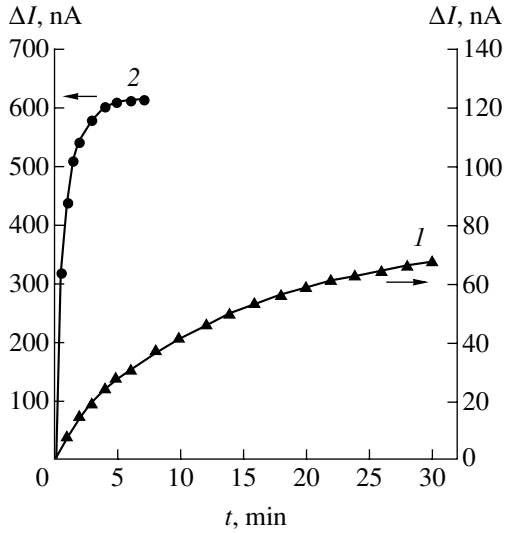

Fig. 2. Variation of the current with time after letting hydrogen in the measuring chamber for Pd/*n*-Si structures based on (*1*) unannealed and (*2*) annealed silicon.

Thus, the investigation performed demonstrated that the thermal treatment of silicon prior to depositing a palladium contact markedly improves the characteristics of gas sensors based on Pd/*n*-Si barrier structures.

REFERENCES

1. A. Diligenti, M. Stagi, and V. Ciuti, Solid State Commun. **45**, 347 (1983).
2. M. C. Petty, Solid-State Electron. **29**, 89 (1986).
3. G. G. Kovalevskaya, M. M. Meredov, E. V. Russu, *et al.*, Zh. Tekh. Fiz. **63** (2), 185 (1993) [Tech. Phys. **38**, 149 (1993)].
4. V. I. Gaman, P. N. Drobot, M. O. Duchenko, and V. M. Kalygina, Poverkhnost', No. 11, 64 (1996).
5. S. A. Litvinenko, V. V. Mitrofanov, and V. I. Sokolov, Zh. Tekh. Fiz. **51** (4), 828 (1981) [Sov. Phys. Tech. Phys. **26**, 490 (1981)].
6. V. G. Litovchenko, Poluprovodn. Tekh. Mikroélektron., No. 9, 92 (1972).
7. V. S. Vavilov, V. F. Kiselev, and B. N. Mukashev, *Defects in the Bulk and at the Surface of Silicon* (Nauka, Moscow, 1990).

Translated by M. Tagirdzhanov

Semiconductors, Vol. 36, No. 10, 2002, pp. 1138–1145. Translated from Fizika i Tekhnika Poluprovodnikov, Vol. 36, No. 10, 2002, pp. 1217–1224.

SEMICONDUCTOR STRUCTURES, INTERFACES, AND SURFACES

Electrical Properties of Narrow-Gap HgMnTe Schottky Diodes

L. A. Kosyachenko*, A. V. Markov, S. É. Ostapov, I. M. Rarenko, V. M. Sklyarchuk, and Ye. F. Sklyarchuk

Chernivtsi National University, Chernivtsi, 58012 Ukraine

** e-mail: lakos@chv.ukrpack.net*

Submitted January 30, 2002; accepted for publication March 11, 2002

Abstract—The electrical properties of Al/$Hg_{1-x}Mn_xTe$ (x = 0.08–0.1) Schottky barriers have been studied. Specific features related to a narrow band gap and to a strong difference between the effective masses of carriers have been revealed. The principal parameters defining the characteristics of a diode structure, as well as the tunneling and above-barrier (diffusion) carrier transport, are determined. The obtained experimental and theoretical data demonstrate the high detectivity of the diodes under study. *© 2002 MAIK "Nauka/Interperiodica".*

1. INTRODUCTION

The prospect of using a $Hg_{1-x}Mn_xTe$ solid solution as a material for IR detectors, which feature a higher stability of the crystal lattice and surface than those based on $Hg_{1-x}Cd_xTe$, was predicted theoretically [1] and confirmed experimentally as early as the 1980s [2]. A detailed analysis of possible charge transport mechanisms in $Hg_{1-x}Mn_xTe$ *p–n* junctions has shown that, judging by key photoelectric parameters, they should not rank below $Hg_{1-x}Cd_xTe$ detectors [3]. This conclusion was confirmed by studies of $Hg_{1-x}Mn_xTe$ photodiodes with n^+–*p* junctions fabricated using ion etching of single crystals with *p*-type conduction [4, 5].

However, the fabrication of multielement photodetectors with *p–n* junctions encounters the problem of poor reproducibility of single element parameters in all the steps of device fabrication: ion etching, multilayer metallization, surface passivation, etc. Meanwhile, the possibility of using $Hg_{1-x}Mn_xTe$ Schottky diodes as IR detectors, which are characterized by a simpler fabrication technology and, moreover, possess certain advantages over *p–n* junctions (higher working frequency, higher sensitivity in the short-wavelength spectral range, etc.) have received virtually no attention.

In this communication, we report the results of a study of the electrical properties and detectivity of Schottky diodes based on $Hg_{1-x}Mn_xTe$ with a band gap $E_g \approx 0.1$ eV, i.e., those suitable as detectors of radiation in the 8–14 μm atmospheric window.

2. SINGLE CRYSTALS

The samples were fabricated from *p*-type $Hg_{1-x}Mn_xTe$ single crystals grown by modified zone melting with subsequent annealing in mercury vapor. Wafers 0.8–1 mm thick were cut from an ingot of 15 mm in diameter, lapped, and thoroughly polished. Though the Mn content in the synthesis was chosen so as to obtain a band gap E_g = 0.1 eV at the liquid nitrogen temperature, the E_g value appeared to be nonuniform in the ingot, as well as over the area of single wafers. The inhomogeneity of the $Hg_{1-x}Mn_xTe$ composition is demonstrated by Fig. 1, which presents optical absorption data obtained from different portions of the middle part of the ingot at room temperature (T = 300 K). The absorption coefficient α was determined from transmission data recorded with a beam of 1–2 mm in diameter (with multiple reflections taken into account). The

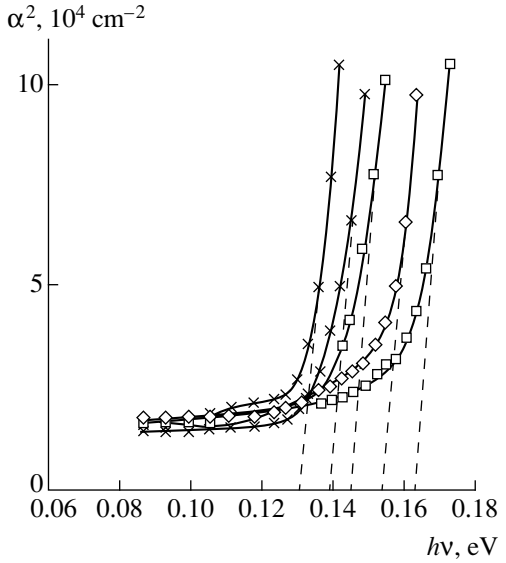

Fig. 1. Optical absorption at different parts of wafers cut from the central portion of the $Hg_{1-x}Mn_xTe$ ingot. T = 300 K.

coordinate system in the figure (α^2 vs. the photon energy $h\nu$) was chosen based on the assumption that $\alpha \propto (h\nu - E_g)^{1/2}$ near the fundamental absorption edge in a semiconductor with direct interband transitions, which is the case for $Hg_{1-x}Mn_xTe$ [6].

As seen from Fig. 1, the cutoff at the photon energy axis yields E_g values in the range 0.13–0.163 eV (T = 300 K), which, in accordance with the well-known semi-empirical relation

$$E_g(x, T) = -0.253 + 3.446x + 4.9 \times 10^{-4}T - 2.55 \times 10^{-3}xT, \quad (1)$$

corresponds to x = 0.088–0.100. At T = 77 K (the operation temperature for this type of diodes), E_g = 0.069–0.111 eV, according to the same relation. So strong a variation in the band gap with a relatively small (~1%) variation in x is due to the step dependence of E_g on the Mn content in narrow-gap $Hg_{1-x}Mn_xTe$ compounds.

3. FABRICATION OF DIODE STRUCTURES

Schottky diodes were produced by sputtering Al in a vacuum chamber with the residual pressure below 10^{-5} Torr. Prior to the rectifying contact formation, a wafer was chemically treated in bromomethanol and rinsed in deionized water. Immediately before the metal sputtering, the wafer surface was etched for ~10 min with Ar ions at an accelerating voltage of ~500 V and a current density of 4–5 mA cm^{-2}. When a metal is deposited onto a surface treated in this manner, the electrical properties of the contact depend on the work function of the metal. An ohmic contact is formed with metals with a high work function (Au or Ni), whereas Al, whose work function is smaller, always forms a nonlinear, and only in some cases a rectifying, contact. This fact correlates with the general concept of processes at the metal–semiconductor contacts. To form the Schottky barrier, the work function of a semiconductor with *p*-type conduction must be higher than the work function of a metal (naturally, if the screening by carriers captured by surface states is ignored). However, namely the presence of Mn in the material under study causes a low density of these states [7].

At the same time, the observed dependence of the metal–semiconductor contact properties on the nature of a metal indicates that the ion etching performed under the above-described conditions does not produce an *n*-layer at the sample surface, which could happen [4, 5]. If this did occur, the deposition of Au or Ni would not eliminate the nonlinearity or rectification caused by the *p*–*n* junction. Ohmic contacts on the substrate were fabricated by sputtering Ni onto the area not subjected to ion etching.

4. CURRENT–VOLTAGE CHARACTERISTICS OF Al/$Hg_{1-x}Mn_xTe$ DIODES

The current–voltage (*I*–*V*) characteristics of the studied Schottky diodes differ widely in their current strength and type of dependence of current on bias,

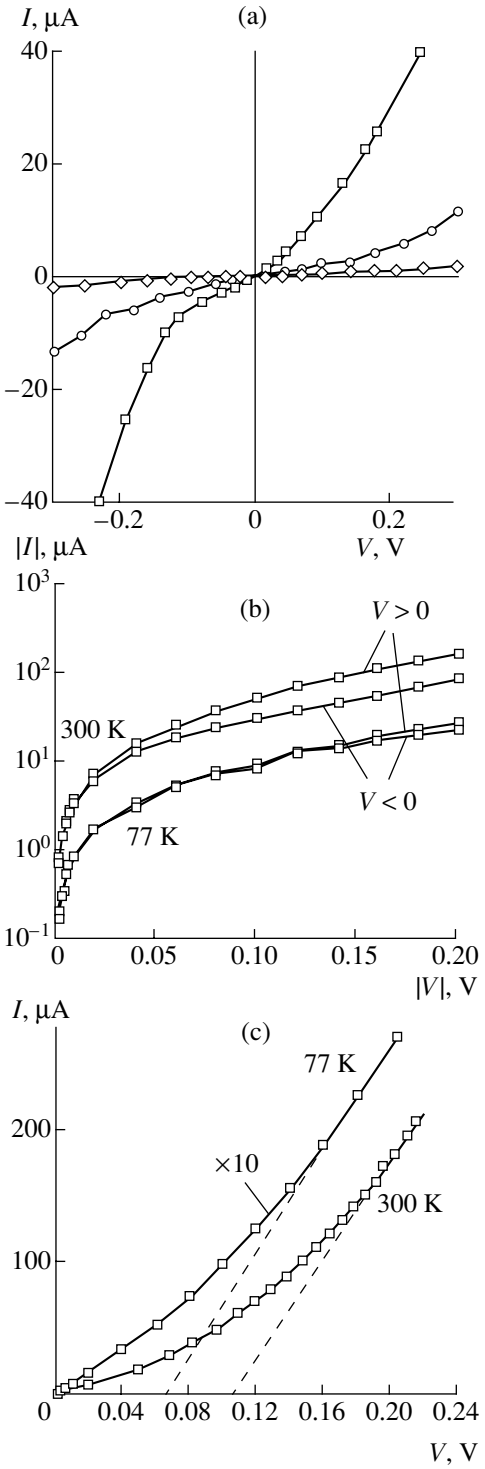

Fig. 2. *I*–*V* characteristics of (a) several Al/HgMnTe diodes at 77 K; (b) one of the diodes at 77 and 300 K; (c) forward portions for the same diode in the range of high current.

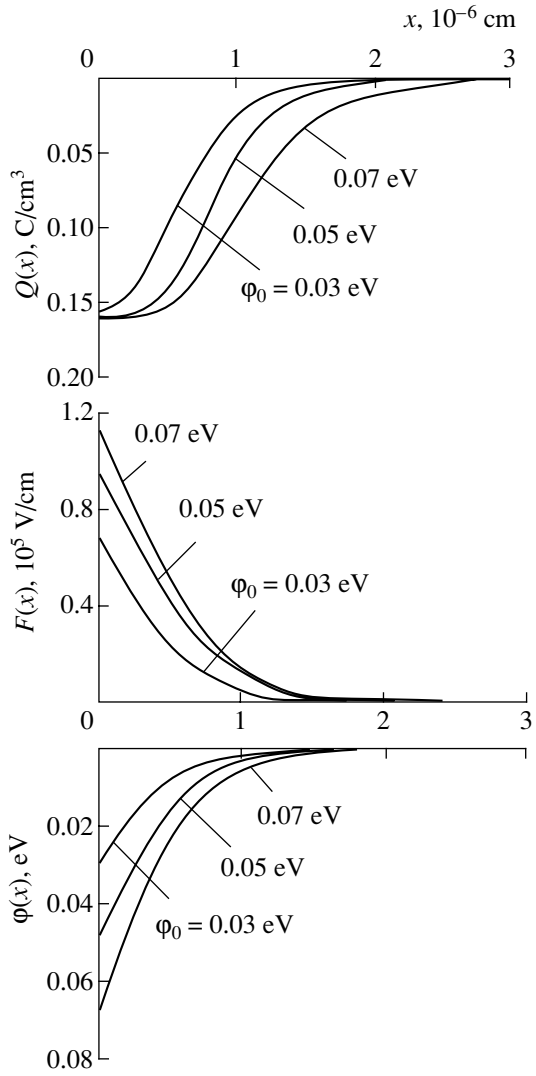

Fig. 3. Distribution of charge $Q(x)$, electric field intensity $F(x)$, and potential energy of carriers $\varphi(x)$ in a p-$Hg_{1-x}Mn_xTe$ Schottky diode. $E_g = 0.1$ eV, $N_a = 10^{16}$ cm^{-3}, $T = 77$ K.

depending on the Mn content and acceptor density in $Hg_{1-x}Mn_xTe$. Later, we present the results obtained in the study of Al/$Hg_{1-x}Mn_xTe$ diodes for a solid solution with $x \approx 0.1$, to which $E_g = 0.11$ eV corresponds at 77 K, i.e., the practically important cut-off wavelength of ~ 11 μm.

Figure 2a shows typical *I–V* characteristics recorded at $T = 77$ K for several diodes 150 μm in diameter. As seen, the *I–V* curves are nonlinear in all the cases but the rectification is weak. At best, the ratio of the forward to reverse current does not exceed several units.

Another characteristic feature of the studied Al/$Hg_{1-x}Mn_xTe$ diodes is that the rectification becomes worse at lower temperatures. This is illustrated by Fig. 2b, where the *I–V* curves for one of the diodes are plotted in convenient semilog coordinates, regardless of the bias voltage and current direction. As seen, at 77 K, the forward and reverse currents virtually coincide. At 300 K, the forward current is several times higher than the reverse, but only for an elevated bias. For other diodes, the forward current can be slightly higher than the reverse one, but sometimes the forward and reverse portions intersect.

In Fig. 2c, the forward characteristics are plotted on a linear scale, which allows us to reveal a linear portion of the $I(V)$ dependences under high current (the current density of ~ 0.5 A cm^{-2} corresponds to the current of 100 μA). Consequently, in this range of currents, the contact potential V_c is compensated by the applied bias and, therefore, $V \approx V_c + IR_s$, where R_s is the series resistance (in this case, the crystal resistance). Judging from the offset in Fig. 2c, the barrier height at 300 K is 0.11 eV ($E_g = 0.16$ eV), and with the temperature lowered to 77 K, it decreases to 0.07 eV ($E_g = 0.11$ eV), which seems quite probable and reasonably correlates with the temperature variation of the band gap. It is necessary to note, nevertheless, that full compensation of the contact potential is impossible; therefore, it may only be asserted that the barrier height at 300 and 77 K is not lower than the cited values.

5. SPECIFICS OF THE ELECTRIC FIELD DISTRIBUTION IN A SCHOTTKY DIODE BASED ON A NARROW-GAP SEMICONDUCTOR

The simulation of the electrical characteristics of a Schottky diode presumes a knowledge of the distributions of the carrier density $Q(x)$, electric field intensity $F(x)$, and potential energy of carriers $\varphi(x)$ in the SCR. If the space charge density is assumed to be uniform (as is usually done), the field intensity decreases linearly, and the potential, quadratically, with the coordinate x directed from the interface to the semiconductor bulk. However, in a narrow-gap semiconductor, the uniformity of the charge density can be distorted in the barrier layer of the Schottky diode owing to the strong effect of free carriers, which is similar to what occurs in a *p–n* junction [5]. This assertion is confirmed by calculations, and the results are presented in Fig. 3.

The dependences $Q(x)$, $F(x)$, and $\varphi(x)$ have been found from the solution to the Poisson equation on the assumption that the space charge in the depleted region is defined by ionized acceptors, $-eN_a$, and holes in the valence band $+eN_v\exp\{-[|\varphi(x)| + \Delta\mu]/kT\}$, where N_a is the acceptor density; N_v and $\Delta\mu$, the effective density-of-states in the valence band and the energy distance between the Fermi level and the valence band top; e, the elementary charge; and k, the Boltzmann constant. The calculations were done for $E_g = 0.1$ eV, $N_a = 10^{16}$ cm^{-3}, and three values of the barrier height: $\varphi_0 = 0.03$, 0.05, and 0.07 eV. As seen, with holes in the valence band taken into account, the space charge density in the depleted region is not uniform but varies continuously

with the coordinate. Consequently, the field intensity dependence on x deviates from linearity. The behavior of the potential also deviates from the quadratic law (naturally, this does not manifest itself so clearly).

It is evident that the special features of the $Q(x)$, $F(x)$, and $\varphi(x)$ dependences presented in Fig. 3 must be taken into account in calculations of current, and the approximation of the linear variation (and even more so, uniformity) of the electric field in the Schottky diode based on a narrow-gap semiconductor [8] is too crude. In the strict sense, if the bands are strongly bent near the interface, the space charge of electrons in the conduction band must also be taken into account. However, in the case under study this effect is insignificant even at maximal barrier height. This is accounted for by a much lower density of states in the conduction than in the valence band, due to the very small effective electron mass ($\sim 10^{-2} m_0$ at $E_g \approx 0.1$ eV). The Schottky barrier in n-type $Hg_{1-x}Mn_xTe$ presents the opposite case, where the holes in the valence band can play a principal role in the formation of a space charge (which is confirmed by our calculations). Naturally, similar calculations for $Q(x)$, $F(x)$, and $\varphi(x)$ in a wide-gap semiconductor (e.g., for $E_g = 1$ eV with equal electron and hole effective masses $m_e = m_h = m_0$) shows that taking into account free carriers of both types is quite unnecessary in this case.

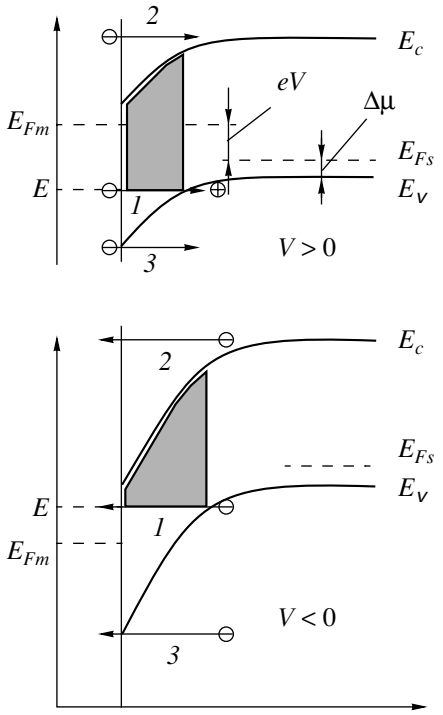

Fig. 4. The band diagram of an Al/HgMnTe contact at (top) forward and (below) reverse bias. Arrows indicate the discussed components of current: (*1*) tunneling, (*2*) above-barrier electron, (*3*) above-barrier hole; the potential barrier for electron tunneling is hatched.

6. CALCULATION OF *I–V* CHARACTERISTICS

The observed poor rectification and relatively weak temperature dependence of the forward and reverse currents indicate that the electrical properties of the diodes under study are primarily defined by the tunneling. Figure 4 shows an energy diagram of the $Al/Hg_{1-x}Mn_xTe$ contact and the discussed metal–semiconductor tunnel transitions. With an increase in the forward bias, the range of tunneling gradually shifts downwards and finally merges with the energy interval of the above-barrier transport of carriers (in standard terminology, this is the hole diffusion current). At the same time, the contribution of the above-barrier electron current (the electron diffusion current), which is usually ignored when the band curvature is moderate, increases. A calculation similar to the one made for a p–n junction [5] shows that the current defined by the generation–recombination in the SCR (the depleted layer) is negligible as compared with the tunneling and diffusion components. Hence, in terms of an actual model, the diode current is defined by the sum of tunneling and diffusion currents.

Using the dependence of potential $\varphi(x)$ which was determined in Section 5, we can calculate the tunnel transparency coefficient of a potential barrier for an electron of energy E as [9]

$$D(E, V) = \exp\left(-\frac{2\sqrt{2m_r}}{\hbar}\int_{x_1}^{x_2}\sqrt{\varphi(x, V) - E}\,dx\right), \quad (2)$$

where m_r is the reduced electron mass, and x_1 and x_2 are the so-called turning points. In the chosen reference system (see Fig. 4, the energy is reckoned from the Fermi level in a metal E_{Fm}),

$$D(E, V) = \exp\left(-\frac{2\sqrt{2m_r}}{\hbar}\int_{x_1}^{x_2}\sqrt{E_g - \Delta\mu - eV - \varphi(x) - E}\,dx\right), \quad (3)$$

where $\Delta\mu$ is the distance between the Fermi level E_{Fs} in the semiconductor and the valence band top E_v (defined by the given acceptor density), $x_1 = 0$, and x_2 is found from the condition of zero radicand in (3). When $\varphi(x)$ is known, the tunneling current can be calculated as

$$I_{tun} = A\frac{em^*kT}{2\pi^2\hbar^3}\int_{-\varphi_0-\Delta\mu}^{-\Delta m - eV}[f_m(E) - f_s(E)]D(E, V)\,dE, \quad (4)$$

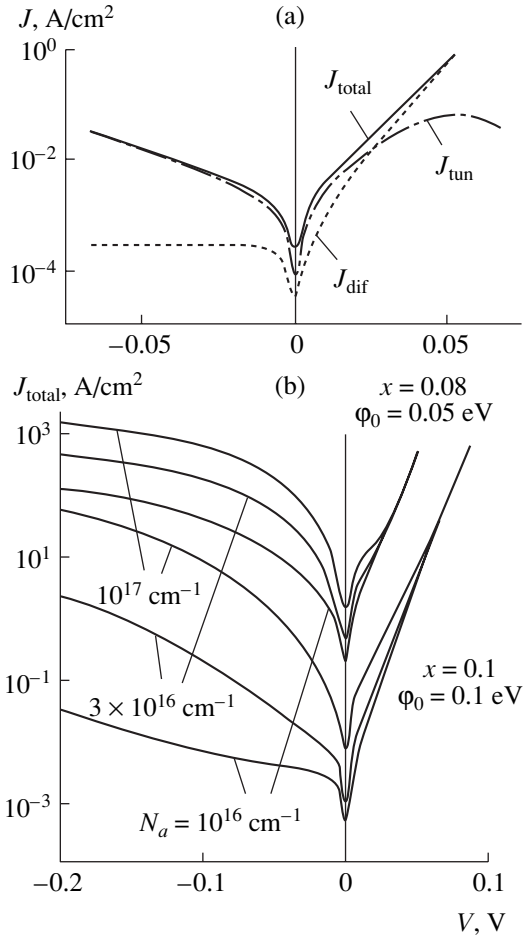

Fig. 5. (a) Calculated density of the tunneling and diffusion current vs. bias, $J(V)$, for an Al/$Hg_{1-x}Mn_xTe$ diode with x = 0.09, φ_0 = 0.1 eV, $N_a = 3 \times 10^{16}$ cm^{-3}, at T = 77 K; (b) total current density, $J_{total}(V)$, calculated with the parameters specified.

where A is the diode area, and $f_m(E) = \ln\{1 + \exp(-E/kT)\}$ and $f_s(E) = \ln\{1 + \exp[-(E + eV)/kT]\}$ are the probabilities of the occupation of the level E with an electron in the metal and semiconductor, respectively. The expressions for $f_m(E)$ and $f_s(E)$ differ from the Fermi–Dirac function, because only the velocity component perpendicular to the junction plane is important for tunneling, while the lateral components can have arbitrary values (these expressions are obtained through integration over all the possible values of the transverse velocity component, i.e., from $-\infty$ to $+\infty$). The difference $f_m(E) - f_s(E)$ in relation (4) accounts for the counterflow of electrons from the semiconductor to the metal at forward bias, and from the metal to the semiconductor at reverse bias, which is significant in the near-zero range of voltages ($|V| < kT/e$) that are important for detector applications. It is necessary to note, thereupon, that frequently used relations obtained for tunneling currents under the condition $|eV| \gg \varphi_0$ are inapplicable at small biases [8].

Using the same approach, we now apply the relation (4) to calculate the above-barrier hole current; to do this, we assume $D(E,V) = 1$ and set the integration limits as $-(\varphi_0 + \Delta\mu)$ to $-\infty$ (several kT below $-(\varphi_0 + \Delta\mu)$ is enough). Naturally, this calculation yields a result coinciding with the relation for the thermionic current, $I = A(em_hk^2/2\pi^2\hbar^3)T^2\exp[-(\varphi_0 + \Delta\mu)/kT] = AA^*T^2\exp[-(\varphi_0 + \Delta\mu)/kT]$ [9], which is obtained through the analytical integration of (4) (A^* is the effective Richardson constant). A similar relation can also be obtained for the above-barrier electron current by replacing the effective hole mass m_h with an electron mass m_e and the barrier height for holes $\varphi_0 + \Delta\mu$ with that for electrons $E_g - \Delta\mu$ (see Fig. 4).

If we assume that the current in the diodes under study is the sum of the tunneling and above-barrier hole currents, the calculated values of current under high forward bias are strongly overestimated as compared with the experiment (by more than 3 orders of magnitude). It is necessary to assume, therefore, that the barrier height is larger than the value obtained from the cutoff in Fig. 2c. It is also necessary to keep in mind that the above-barrier electron current becomes substantial when the band bending is strong. Since the above-barrier hole current is proportional to $m_h\exp[-(\varphi_0 + \Delta\mu)/kT]$, and the electron current, to $m_e\exp[-(E_g - \Delta\mu)/kT]$, the latter can exceed the hole current when $\varphi_0 > E_g - 2\Delta\mu - kT\ln(m_e/m_h)$. In general, both the electron and hole currents must be considered.

Figure 5a presents the tunneling and above-barrier currents calculated at 77 K and the acceptor density $N_a = 3 \times 10^{16}$ cm^{-3} with account taken for the aforesaid. The figure presents, in an illustrative form, the relation between the tunneling (J_{tun}) and diffusion (J_{dif}) components of the current density. Under reverse and small forward bias, the above-barrier current is considerably less than the tunneling. However, the rise of the tunneling current becomes slower under higher forward bias, and, at V approaching φ_0/e, the tunneling current decreases, which is accounted for by the above-mentioned narrowing of the tunneling region and its downward shift on the energy scale. At the same time, the contribution of the over-barrier diffusion current increases, so that under a forward bias of 0.02–0.03 V these current components become comparable, and under a higher forward voltage the diffusion current dominates. This circumstance allows us to determine, with reasonable precision, the barrier height φ_0 that yields the best agreement between the calculated current and the experimental data in the range of high forward bias. As would be expected, in this case the band curvature near the semiconductor surface becomes so strong that the above-barrier electron current dominates over the hole current (e.g., at E_g = 0.11 eV, φ_0 = 0.1 eV, instead of φ_0 = 0.07 eV determined from the cut-off in Fig. 2c). Strong band bending is also demonstrated by the fact that the capacitance of the diodes under study

is virtually independent of the bias voltage. This fact is accounted for by the influence of free carriers (in this case, electrons), which are responsible for the deviation from the standard dependence of the Schottky diode capacitance C on bias, $C \propto (\varphi_0 - eV)^{1/2}$, similarly to what is observed in n^+–p junctions in $Hg_{1-x}Mn_xTe$ [5].

Now, when all the necessary parameters are known, we can calculate the I–V characteristic of a $Al/Hg_{1-x}Mn_xTe$ diode as the sum of tunneling and above-barrier currents (electron and hole), varying the Mn content and the acceptor density to a reasonable extent. The computer program is organized so that the calculation begins from the determination of the charge and potential distributions; to do this, we specify the barrier height φ_0 determined from the forward diode characteristic in the range of high current (Fig. 3 only illustrates the changes in the I–V curve at varied φ_0). With φ_0 set in this way, the program accounts for both the electron and hole above-barrier currents, and, thereby, their relation to one another.

The results shown in Fig. 5b account for the experimentally observed specificities of the diode characteristics. As seen, the I–V characteristic changes drastically when x, φ_0, and N_a are varied. The diode exhibits a reasonably fair rectification at $x = 0.1$, $\varphi_0 = 0.1$ eV, $N_a = 10^{16}$ cm^{-3} (the forward current is several orders of magnitude higher than the reverse one); by contrast, the reverse current exceeds the forward current at $x = 0.08$, $\varphi_0 = 0.05$ eV, and $N_a = 10^{17}$ cm^{-3}. The main reason for this evolution of the I–V characteristic is the increasing role of tunneling as compared with the above-barrier transport of carriers (the exceeding of the reverse current over the forward current in the so-called backward diodes is also accounted for by the tunneling [3, 9]).

As follows from Figs. 5b and 5a, the reverse and forward currents become nearly equal at $x = 0.09$–0.1, $\varphi_0 \approx 0.07$ eV, and $N_a = (3$–$10) \times 10^{16}$ cm^{-3}, which correlates with the experimental data presented in Fig. 2b. The model used also accounts for the temperature dependences of the I–V characteristic of $Al/Hg_{1-x}Mn_xTe$ diodes. Figure 6 shows the calculated I–V characteristics at 77 and 300 K for a diode with $x = 0.1$, $\varphi_0 = 0.1$ eV, and $N_a = 10^{16}$ cm^{-3}.

As seen, at 77 K, the rectification is absent, and, at room temperature, of the forward current is several times higher than the reverse current, which is actually observed in the experiment (we do not show the current in the range $V > 0.08$–0.10 V, because, in this case, account must be taken of the voltage drop in the diode bulk). A comparison of the data presented in Figs. 2 and 6 shows that the calculated and measured current values are close to one another (the diode area was 2×10^{-4} cm^2). Evidently, even better coincidence between the calculation and the experiment can be obtained with parameter fitting. We believe that this would be too artificial, because many of the semiconductor parameters

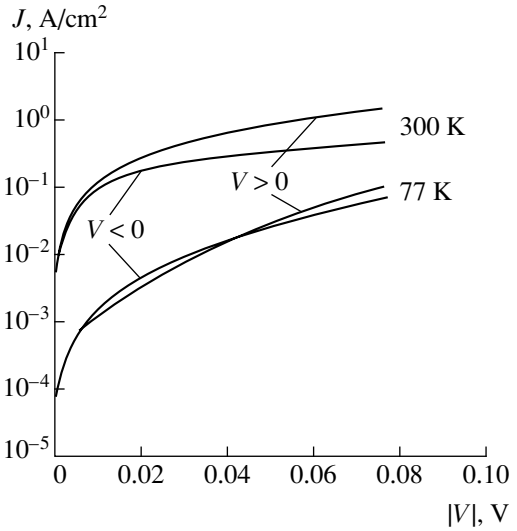

Fig. 6. Calculated forward and reverse current at 77 and 300 K for an $Al/Hg_{1-x}Mn_xTe$ diode with $x = 0.1$, $\varphi_0 = 0.1$ eV, and $N_a = 10^{16}$ cm^{-3}.

(especially the effective carrier mass, the band gap, and the dielectric constant) are specified by inexact empirical relations. On the other hand, the consistency of the calculated and experimental data in Fig. 6 shows that the proposed model provides a convincing explanation for describing the properties of the diodes under study.

7. DETECTIVITY OF $Al/Hg_{1-x}Mn_xTe$ DIODES

Poor rectification and the deviation from an "ideal" I–V characteristic (when the forward current no longer behaves as $I \propto \exp(eV/kT)$) are commonly regarded as evidence of low device quality. Nevertheless, we shall estimate the possibility of using $Al/Hg_{1-x}Mn_xTe$ diodes as IR detectors for the wavelength range 8–14 μm.

The principal parameter of an IR detector is its detectivity D^*, defined by the conductance of a diode structure and by the background radiation. Traditionally, the detectivity of a detector is defined as the product of its differential resistance under zero bias by the active area, i.e., the so-called R_0A product:

$$D^* = \frac{e\eta\lambda_c}{hc}\left[\frac{4kT}{R_0A} + 2e^2\eta\phi_B\right]^{-1/2}, \qquad (5)$$

where η is the quantum efficiency of the detector and ϕ_B, the irradiation from the environment (the number of photons in the Planck radiation, which are incident per unit area and absorbed by the semiconductor per unit time, i.e., in the wavelength range below the λ_c cutoff). Conventionally, η is assumed to be 0.5–0.7, and ϕ_B equals 6.5×10^{17} cm^{-2} s^{-1} for $\lambda_c = 11$ μm at 300 K and an angle of aspect of 180°.

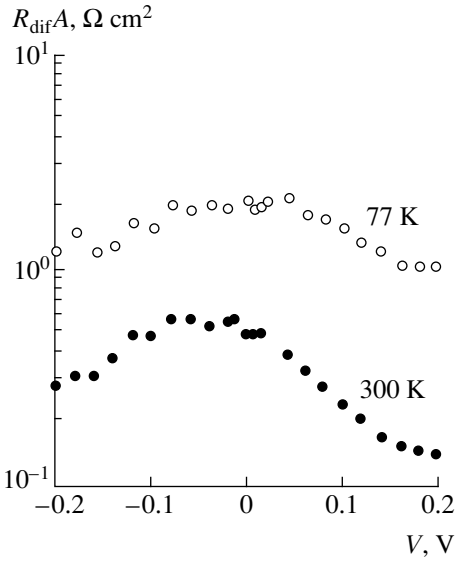

Fig. 7. Differential resistance multiplied by the diode area vs. bias for an Al/$Hg_{0.9}Mn_{0.1}Te$ Schottky diode at 77 and 300 K.

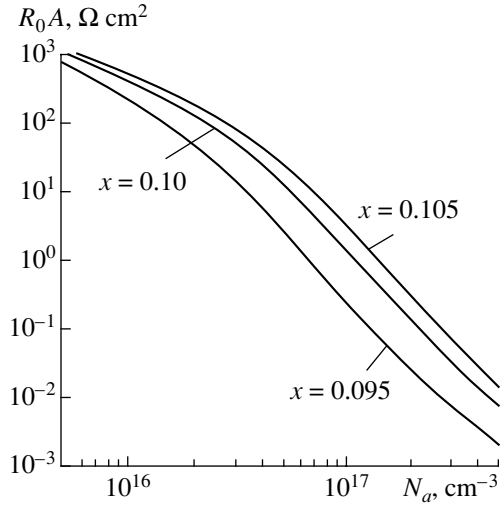

Fig. 8. Dependence of R_0A on the acceptor density calculated for Al/$Hg_{1-x}Mn_xTe$ diodes with different compositions of the solid solution and, correspondingly, different cutoff wavelengths of 10, 11, and 13 μm at 77 K.

Figure 7 presents the measured differential resistance of an Al/$Hg_{1-x}Mn_xTe$ diode at two temperatures. At 77 K and zero bias (the operating conditions for these detectors), $R_0A \approx 2\ \Omega\ cm^2$. For this value of R_0A, the first term in square brackets in relation (5) is ~8 times less than the second. This means that the diode detectivity is defined by the background radiation at 300 K and the angle of aspect of 180°; i.e., it is close to its limiting value $D^* \approx 3.6 \times 10^{10}$ cm $Hz^{1/2}$ W^{-1} (the so-called background-limited infrared photodetector mode (BLIP)) [3].

It might seem that the room-temperature detectivity of an Al/$Hg_{1-x}Mn_xTe$ detector is also high ($R_0A \approx$ 0.6 Ω cm^2). However, we should not forget that the band gap of $Hg_{1-x}Mn_xTe$ increases to 0.16 eV at 300K, which means that the cutoff wavelength becomes $\lambda_c \approx$ 7 μm. For this λ_c, the background irradiation ϕ_B decreases by a factor of ~5 in comparison with λ_c = 11 μm. Consequently, the room-temperature D^* is far from the limiting value.

It is noteworthy that the value $R_0A \approx 2\ \Omega\ cm^2$ at 77 K refers to a medium-quality sample (the diode with the highest currents, Fig. 2a); for the best diodes, this quantity can be several times higher. The sufficiently good quality of Al/$Hg_{1-x}Mn_xTe$ diodes as IR detectors is also confirmed by the results of calculations. Figure 8 shows R_0A vs. the acceptor density N_a at 77 K for three compositions of the solid solution: x = 0.095, 0.1, and 0.105, which correspond to the industrially important range of the cutoff wavelength $\lambda_c \approx$ 13, 11, and 10 μm, respectively. As seen, the calculated R_0A exceeds 10 Ω cm^2 at $N_a = 3 \times 10^{16}$ cm^{-3}, and even at $N_a = (5–10) \times 10^{16}$ cm^{-3} it is over 2–3 Ω cm^2 (which corresponds to the BLIP mode).

Naturally, the Schottky diode on a 0.8- to 1-mm-thick crystal with a ~1-μm metallic layer is not applicable as a radiation detector. Nevertheless, the problem of radiation input into the barrier region of a diode can be resolved by several methods. The barrier structure can be fabricated in a thin epitaxial $Hg_{1-x}Mn_xTe$ layer grown on a transparent substrate made of CdTe or, for better lattice matching, $Cd_{1-x}Mn_xTe$. Another way to resolve the problem is the fabrication of an Al contact in the form of a thin-stripe grid. With an acceptor density of 3×10^{16} cm^{-3}, the Fermi level in the crystal bulk lies at about 0.03 eV above the valence band top. This means that for a barrier height of 0.07 eV or more, the Fermi level at the crystal surface lies close to the conduction band; i.e., the conductance of the surface layer can be sufficient for the areas between the stripes of the grid to be active.

8. CONCLUSION

The study of the optical properties of *p*-$Hg_{1-x}Mn_xTe$ single crystals shows considerable inhomogeneity in the composition of the material and, correspondingly, in the band gap in different parts of an ingot and even within a single wafer. The specific features of the Al/$Hg_{1-x}Mn_xTe$ Schottky diodes under study are a nonlinear *I–V* characteristic, the lack of rectification at 77 K, and poor rectification at 300 K. The calculations of the tunneling and above-barrier currents with account taken of the special features of the potential distribution in the barrier region of the Schottky diode in a narrow-gap semiconductor account for the behavior of the diodes. The differential conductance of Al/$Hg_{1-x}Mn_xTe$ diodes corresponds to a detectivity of $D^* \approx 3 \times 10^{10}$ cm $Hz^{1/2}$ W^{-1}, which is close to the limit for the industrially important cutoff wavelength λ_c = 11 μm

under the conditions of background irradiation at 300 K with an angle of aspect equal to 180°.

ACKNOWLEDGMENTS

We are grateful to S.Yu. Paranchin and O.A. Bodnaruk for providing the $Hg_{1-x}Mn_xTe$ single crystals used for this study.

REFERENCES

1. J. K. Furdyna, Proc. SPIE **409**, 43 (1983).
2. P. Becla, J. Vac. Sci. Technol. A **4**, 2014 (1986).
3. A. Rogalski, Infrared Phys. **31**, 117 (1991).
4. L. A. Kosyachenko, I. M. Rarenko, Sun Weiguo, and Lu Zheng Xiong, Solid-State Electron. **44**, 1197 (2000).
5. L. A. Kosyachenko, A. V. Markov, S. É. Ostapov, and I. M. Rarenko, Fiz. Tekh. Poluprovodn. (St. Petersburg) **35**, 1326 (2001) [Semiconductors **35**, 1270 (2001)].
6. L. A. Kosyachenko, I. M. Rarenko, O. O. Bodnaruk, *et al.*, Semicond. Phys. Quantum Electron. Optoelectron. **2**, 31 (1999).
7. S. G. Gasan-Zade, I. P. Zhad'ko, O. E. Zinchenko, *et al.*, Fiz. Tekh. Poluprovodn. (St. Petersburg) **26**, 1100 (1992) [Sov. Phys. Semicond. **26**, 615 (1992)].
8. V. V. Zav'yalov, V. F. Radantsev, and T. I. Deryabina, Fiz. Tekh. Poluprovodn. (St. Petersburg) **26**, 688 (1992) [Sov. Phys. Semicond. **26**, 388 (1992)].
9. S. M. Sze, *Physics of Semiconductor Devices* (Wiley, New York, 1981; Mir, Moscow, 1984), Vol. 1.

Translated by D. Mashovets

Semiconductors, Vol. 36, No. 10, 2002, pp. 1146–1153. Translated from Fizika i Tekhnika Poluprovodnikov, Vol. 36, No. 10, 2002, pp. 1225–1232.

LOW-DIMENSIONAL SYSTEMS

Anisotropy of Magnetooptical Absorption of Quantum Dot–Impurity Center Complexes

V. D. Krevchik, A. B. Grunin, and R. V. Zaĭtsev

Penza State University, Penza, 440017 Russia

e-mail: physics@diamond.stup.ac.ru

Submitted January 10, 2001; accepted for publication March 5, 2002

Abstract—The magnetooptical properties of ⟨quantum dot⟩–⟨impurity center⟩ complexes formed in a transparent insulator host were studied. In order to describe one-electron states of a quantum dot, a parabolic model of the confinement potential was used. In terms of the zero-range potential model in the effective-mass approximation, the coefficient of extrinsic absorption of light polarized parallel and perpendicular to the direction of an external magnetic field (longitudinal and transverse polarizations, respectively) was calculated taking into account variance in the quantum-dot size. It was shown that, in the case of longitudinal polarization, the edge of the extrinsic-absorption band shifts in a magnetic field to shorter wavelengths and the absorption coefficient increases several times. In the case of transverse polarization, the quantum-dimensional Zeeman effect is observed in the extrinsic-absorption spectrum. It was also shown that the anisotropy of the magnetooptical absorption is a nonmonotonic function of the frequency of light and does not depend critically on the impurity-level position. © *2002 MAIK "Nauka/Interperiodica".*

1. INTRODUCTION

The magnetooptical properties of ⟨quantum dot⟩–⟨impurity center⟩ (QD–IC) complexes formed in a transparent insulator host are of interest in connection with the problem of the development of photodetectors with a controlled operating frequency and maximum sensitivity in the extrinsic-absorption region. The magnetooptical absorption of multiwell quantum systems (GaAs–$Ga_{0.75}Al_{0.25}As$) with the participation of D^- states was experimentally studied in [1]. In order to analyze experimental data, the variational approach is commonly used for describing the localized state of an electron at a D^- center [2]. This approach has a number of well-known drawbacks, among which the most significant is the uncertainty in choosing the trial wave functions. The authors of [3] theoretically investigated magnetooptical absorption in a semiconductor quantum well (QW) which was caused by transitions of electrons from the D^- state to the Landau levels. The bonding state was described in terms of the zero-range potential model [4, 5]. However, when the absorption coefficient was calculated, it was implicitly assumed that a localized electronic state is formed only by the states of the low-lying QW subband. Apparently, this is correct only in the quantum-mechanical limit, when $L \ll a_d$ (L is the QW width, and a_d is the effective Bohr radius). In the case of semiconductor QDs, when $R_0 \ll a_d$ (R_0 is the QD radius), the question arises as to the applicability limits of the effective-mass concept when the energy spectrum of an impurity electron is calculated. We have shown previously (see [6, 7]) that the zero-range potential model makes it possible to derive an analytical solution for the wave function of a localized carrier, as well as to analyze the effect of positional disorder in semiconductor QWs and QDs, characterized by a parabolic potential profile, with no limitations imposed on the number of QW or QD states participating in the formation of the localized state.

The aim of this work is to theoretically investigate the magnetooptical absorption of QD–IC complexes formed in a transparent insulator host. The cases of longitudinal and transverse polarization of light relative to the magnetic field direction are considered. The impurity potential is approximated by the zero-range potential of intensity $\gamma = 2\pi/\alpha$ [7]:

$$V_\delta(\mathbf{r}, \mathbf{R}_a) = \gamma\delta(\mathbf{r} - \mathbf{R}_a)[1 + (\mathbf{r} - \mathbf{R}_a)\nabla_\mathbf{r}], \qquad (1)$$

where α is determined by the binding energy E_i of an electronic state localized at a similar IC in a massive semiconductor; IC is located at a point $\mathbf{R}_a = (x_a, y_a, z_a)$. As is known (see [5]), such a model is appropriate for the description of D^- states, which correspond to the attachment of an extra electron to a shallow-level donor. The Lippmann–Schwinger equation has an analytical solution for the wave function $\Psi_\lambda(\mathbf{r}, \mathbf{R}_a)$ of an electron localized at the QD short-range potential with a parabolic profile [7]

$$\Psi_\lambda(\mathbf{r}, \mathbf{R}_a) = C\exp\left(-\frac{r^2 + R_a^2}{2a^2}\right)$$

$$\times \int_0^\infty dt\, e^{-(\varepsilon_a + 3/2)t}(1 - e^{-2t})^{-3/2} \qquad (2)$$

1063-7826/02/3610-1146$22.00

$$\times \exp\left\{-\frac{e^{-2t}(r^2 + R_a^2) - 2e^{-t}(\mathbf{r}, \mathbf{R}_a)}{a^2(1 - e^{-2t})}\right\}.$$

Here,

$$C = \left[-\frac{\partial}{\partial \varepsilon_a} G(R_a, R_a; \varepsilon_a) a^3\right]^{1/2}$$

is the normalization factor; $\varepsilon_a = |E_\lambda|/\hbar\omega_0$; $E_\lambda = -\hbar^2\lambda^2/2m^*$ is the IC binding energy; m^* is the effective electron mass; ω_0 is the confinement-potential characteristic frequency that is related to the QD radius R_0 and the amplitude of the QD potential U_0 as follows: $2U_0 = m^*\omega_0^* R_0^2$; and $a = \sqrt{\hbar/m^*\omega_0}$. The equation that defines the dependence of the energy of the IC binding state E_λ on the QD parameters and IC position R_a can be written as [7]

$$\sqrt{\eta^2 + \frac{3}{2}\beta^{-1}} = \eta_i - \sqrt{\frac{2}{\beta\pi}}\int_0^\infty dt \exp[-(\beta\eta^2 + 3/2)t] \times \left\{\frac{1}{2t\sqrt{2t}} - \frac{1}{(1 - e^{-2t})^{3/2}} \exp\left[-\frac{R_a^*\beta^{-1}}{2}\frac{(1 - e^{-t})}{(1 + e^{-t})}\right]\right\}, \quad (3)$$

where $\eta^2 = |E_\lambda|/E_d$ and $\eta_i^2 = |E_i|/E_d$ are parameters describing the binding-state energy of an IC located in a QD and bulk semiconductor, respectively; $E_d = m^*e^4/(32\pi^2\hbar^2\varepsilon_0^2\varepsilon^2)$ is the effective Bohr energy with allowance made for the effective mass m^* and dielectric constant ε; $\beta = R_0^*/4\sqrt{U_0^*}$; $R_0^* = 2R_0/a_d$; $U_0^* = U_0/E_d$; and $R_a^* = R_a/a_d$. In order to describe one-electron states in a QD, we will use the confinement potential of the form $V(r) = m^*\omega_0^2 r^2/2$. It is worth noting that, for the theoretical description of one-electron states in a QD, the hard-wall model is often used; i.e., the confinement potential is chosen as a spherically symmetric potential well with infinitely high walls. A more accurate approach to the confinement-potential form requires finding a self-consistent solution to Poisson and Schrödinger's equations. The analysis of the numerical solutions of these equations for a QW [8] shows that the confinement potential is nearly parabolic, but with the lower part truncated. Therefore, the parabolic form of the potential can be considered as quite realistic when there is a choice of the confinement-potential form. The parabolic potential form is convenient for the theoretical study of optical properties of quasi-zero-dimensional structures in magnetic fields, because, as will be shown below, such a potential makes it possible to obtain explicit formulas for the coefficients of extrinsic absorption of light in the cases of both longitudinal and transverse polarization with allowance made for variance in the QD size. We consider the case of strong localization of an impurity electron when $\lambda a \gg 1$ ($\lambda^2 \equiv 2m^*|E_\lambda|/\hbar^2$). This allows us to assume that the one-electron states in the quantizing magnetic field are not distorted by the impurity potential. In the asymmetric gauge of the vector potential $\mathbf{A} = [\mathbf{B}, \mathbf{r}]/2$, the wave functions of one-electron states $\Psi_{n_1, m, n_2}(\rho, \varphi, z)$, which are not perturbed by the impurity, and the relevant energies E_{n_1, m, n_2} take the form [9]

$$\Psi_{n_1, m, n_2}(\rho, \varphi, z) = \frac{1}{a_1^{|m|+1}} \times \left[\frac{(n_1 + |m|)!}{2^{n_2 + |m| + 1} n_1! n_2! \pi\sqrt{\pi}(|m|!)^2 a}\right]^{1/2} \times \rho^{|m|} \exp\left[-\left(\frac{\rho^2}{4a_1^2} + \frac{z^2}{2a^2}\right)\right] H_{n_2}\left(\frac{z}{a}\right) F\left(-n_1, |m| + 1, \frac{\rho^2}{2a_1^2}\right) \exp(im\varphi), \quad (4)$$

$$E_{n_1, m, n_2} = \frac{|e|B\hbar m}{2m^*} + \hbar\omega_0(n_2 + 1/2) + \hbar\sqrt{\omega_0^2 + \frac{e^2B^2}{4m^{*2}}}(2n_1 + |m| + 1), \quad (5)$$

where ρ, φ, and z are cylindrical coordinates; $H_n(x)$ are Hermitean polynomials [10]; $F(\alpha, \beta, x)$ is the degenerate hypergeometric function [10]; $a_1^2 = a^2/2\sqrt{1 + a^4/4a_B^4}$; $a_B = \sqrt{\hbar/m^*\Omega}$ is the magnetic length; $n_1, n_2 = 0, 1, 2, \ldots$ are quantum numbers associated with Landau levels and energy levels of a spherically symmetric oscillator potential well; and $m = 0, \pm1, \pm2, \ldots$ is the magnetic quantum number. In what follows, we will consider the case of a weak magnetic field, so that the effect of the magnetic field on the impurity ground state in a QD can be ignored. This assumption is correct when $|E_\lambda| + (3/2)\hbar\omega_0 \gg \hbar\Omega$ ($\Omega = |e|B/m^*$ is the cyclotron frequency, $|e|$ is the elementary charge, and B is the magnetic induction).[1] Since positional disorder occurs in a QD containing IC [7]; i.e., the binding energy of IC is a decreasing function of its coordinate, the above restriction imposed on **B** can be somewhat relaxed in the case of an impurity located at the center of a QD. In this case, substitution of $\mathbf{R}_a =$

[1] A theoretical study of the photoionization of deep-level ICs in a bulk semiconductor in the presence of an external quantizing magnetic field was carried out in [10, 11].

(0, 0, 0) into (2) and the use of the integral representation of the Whittaker function [12] yield [7]

$$\Psi_\lambda(r) = C\left(\frac{r^2}{a^2}\right)^{-3/4}\Gamma\left(\frac{\varepsilon_a + 3/2}{2}\right)W_{-\varepsilon_a/2,\,1/4}\left(\frac{r^2}{a^2}\right). \quad (6)$$

Here, $\Gamma(x)$ is the gamma function, $W_{\kappa,\mu}(x)$ is the Whittaker function [12], $C = \{2\sqrt{\pi}\,\Gamma(\varepsilon_a/2 + 7/4)a^3[(\varepsilon_a/2 + 3/4)(\Psi(\varepsilon_a/2 + 7/4), \text{ and } \Psi(\varepsilon_a/2 + 1/4)) - 1]/[(\varepsilon_a + 3/2)^2\Gamma(\varepsilon_a/2 + 1/4)]\}^{-1/2}$; $\Psi(x)$ is the logarithmic derivative of the gamma function [12]. As far as we know, no experimental study of the extrinsic absorption of light in semiconductor structures with QDs in the presence of an external quantizing magnetic field has been carried out. However, the modern δ-doping technique (see review in [13]) apparently makes it possible to carry out such studies.

2. ABSORPTION OF LIGHT IN THE CASE OF LONGITUDINAL POLARIZATION

Let us consider the absorption of light of a QD–IC complex when $\mathbf{B} \parallel \mathbf{e}_\lambda$ ($\mathbf{e}_\lambda$ is the unit polarization vector). We assume that (i) the values of all characteristic lengths of the problem are large compared with the lattice constant and (ii) the location of the ground-state level of the IC is rather asymmetric relative to the midgap. It follows from this that the extrinsic absorption of light in a QD can be considered in terms of the effective-mass method in the one-band approximation. The effective Hamiltonian for interaction with the light-wave field $\hat{H}_{\text{int}}^{(s)}$ in the case of longitudinal (relative to the magnetic-field direction) polarization $\mathbf{e}_{\lambda s}$ can be written as

$$\hat{H}_{\text{int}}^{(s)} = \lambda_0\sqrt{\frac{2\pi\hbar^2\alpha^*}{m^{*2}\omega}I_0}e^{i\mathbf{qr}}(\mathbf{e}_{\lambda s}, \hat{\mathbf{P}}), \quad (7)$$

where λ_0 is the local-field coefficient, α^* is the fine-structure constant taking account of permittivity ε, I_0 is the intensity of light, ω is its frequency, q is the magnitude of the wave vector, and $\hat{\mathbf{P}}$ is the electron-momentum operator. The matrix element $M_{f\lambda}^{(s)}$, which determines the oscillator strength of the optical dipole transition of an electron from the ground state of the impurity center $\Psi_\lambda(r)$ to states $\Psi_{n_1, m, n_2}(\rho, \varphi, z)$ of the discrete spectrum of a QD, is given by

$$M_{f\lambda}^{(s)} = \frac{(-1)^n i\pi\lambda_0}{2^{n-1}n!a_1}\sqrt{\frac{\alpha^* I_0}{\omega}}\beta a^2$$

$$\times\frac{[(2n+1)!]^{1/2}\Gamma(\beta/2 + n)[\Gamma(\beta/2 - 1/2)]^{1/2}}{[\Gamma(\beta/2 + 1)]^{1/2}\{(\beta/2)[\Psi(\beta/2 + 1) - \Psi(\beta/2 - 1/2)] - 1\}^{1/2}}$$

$$\times(E_{n_1, 0, 2n+1} - E_\lambda)\sum_{k=0}^{n_1}(-1)^k C_{n_1}^k\left(1 + \frac{a^4}{4a_B^4}\right)^{k/2} \quad (8)$$

$$\times\frac{2^{k+1}\Gamma(k+2)}{(1 + \sqrt{1 + a^4/4a_B^4})^{k+1}}\frac{1}{\Gamma(\beta/2 + n + k + 2)}$$

$$\times F\left(\frac{\beta}{2} + n, k + 1; \frac{\beta}{2} + n + k + 2, 1 - \frac{2}{1 + \sqrt{1 + a^4/4a_B^4}}\right),$$

where $F(\alpha, \beta; \gamma, z)$ is the Gaussian hypergeometric function [12], and $C_{n_1}^k$ are binomial coefficients. Equation (8) accounts for selection rules that arise when calculating the integral

$$\int_{-\infty}^{\infty} u\exp[-(1+t)u^2]H_{n_2}(u)du$$

$$= \begin{cases} 0, & \text{if} \quad n_2 \neq 2n+1, \quad n = 0, 1, 2, \ldots, \\ (1+t)^{-3/2-n}\sqrt{\pi}\dfrac{(2n+1)!}{n!}(-1)^n t^n, & \\ \text{if} \quad n_2 = 2n+1. & \end{cases} \quad (9)$$

It follows from (9) that, in the case of longitudinal polarization of light, optical transitions from the impurity level are possible only to states with odd values of the quantum number n_2. The coefficient of extrinsic absorption of light $K^{(s)}(\omega)$ with account of variance of the QD size[2] can be written as

$$K^{(s)}(\omega) = \frac{2\pi N_0}{\hbar I_0}\sum_{n_1, n}\sum_m \delta_{m,0}\int_0^{3/2} duP(u)$$

$$\times\left|M_{f\lambda}^{(s)}\right|^2\frac{1}{\hbar\omega_0\beta^*(X - \eta^2)} \quad (10)$$

$$\times\delta\left[\frac{(2n + 3/2) + \sqrt{1 + \beta^{*2}u^2/a^{*4}}(2n_1 + 1)}{\beta^*(X - \eta^2)} - u\right],$$

where $\delta_{m,0}$ is the Kronecker delta:

[2] It is assumed that the variance arises during phase decomposition of a supersaturated solid solution and can be satisfactorily described by the Lifshitz–Slyozov formula [14]

$$P(u = R_0/\overline{R_0}) = \begin{cases} \dfrac{3^4 eu^2\exp[-1/(1-2u/3)]}{2^{5/3}(3+u)^{7/3}(3/2-u)^{11/3}}, & u < 3/2, \\ 0, \quad u > 3/2, & \end{cases}$$

where e is the natural logarithm base; and R_0 and $\overline{R_0}$ are the QD radius and its mean value, respectively.

$$\delta_{m,0} = \begin{cases} 1, & \text{if } m = 0, \\ 0, & \text{if } m \neq 0; \end{cases}$$

N_0 is the concentration of QDs in the insulator host; $P(u)$ is the Lifshitz–Slyozov function [14]; $\delta(z)$ is the Dirac delta function; $X = \hbar\omega/E_d$ is the photon energy in units of effective Bohr energy; $\beta^* = \overline{R_0^*}/4\sqrt{U_0^*}$; $\overline{R_0^*} = 2\overline{R_0}/a_d$; and $a^* = a_B/a_d$. In order to perform integration in (10), the roots of the argument of the Dirac delta function should be found. As a result, we obtain

$$\frac{(2n + 3/2) + \sqrt{1 + \beta^{*2}u^2/a^{*4}}(2n_1 + 1)}{\beta^*(X - \eta^2)} = 0. \quad (11)$$

It is easy to verify that only one root of Eq. (11), u^*_{n,n_1}, satisfies the energy conservation law for the considered optical transitions:

$$u^*_{n,n_1} = \frac{(2n + 3/2)(X - \eta^2)}{\beta^*[(X - \eta^2)^2 - (1/a^{*4})(2n_1 + 1)^2]} \quad (12)$$
$$+ \frac{(2n_1 + 1)\sqrt{(X - \eta^2)^2 + (1/a^{*4})[(2n + 3/2)^2 - (2n_1 + 1)^2]}}{\beta^*[(X - \eta^2)^2 - (1/a^{*4})(2n_1 + 1)^2]}.$$

Taking into account (12), we can write the expression for the coefficient of extrinsic absorption of longitudinally polarized light as

$$K^{(s)}(\omega) = K_0\beta^* X \sum_{n_1, n} \frac{(2n_1 + 1)(2n + 1)!}{2^{2n+1}(n!)^2} \frac{(2b_{n,n_1} + 3/2)^2}{\Gamma(b_{n,n_1} + 7/4)}$$
$$\times \frac{\Gamma(b_{n,n_1} + 1/4)\Gamma^2(b_{n,n_1} + 3/4 + n)}{\{(b_{n,n_1} + 3/4)[\Psi(b_{n,n_1} + 7/4) - \Psi(b_{n,n_1} + 1/4)] - 1\}}$$
$$\times \frac{u^{*4}_{n,n_1}\exp[-1/(1 - 2u^*_{n,n_1}/3)]}{(u^*_{n,n_1} + 3)^{7/3}(3/2 - u^*_{n,n_1})^{11/3}}$$
$$\times \left|\beta^* u^*_{n,n_1}[(2n_1 + 1)^2/a^{*4} - (X - \eta^2)^2] + (2n + 3/2)(X - \eta^2)\right|^{-1} \quad (13)$$
$$+ \left[\sum_{k=0}^{n_1} (-1)^k C^k_{n_1} \frac{2^{k+1}\Gamma(k + 2)}{\Gamma(b_{n,n_1} + 11/4 + n + k)} \right.$$
$$\times \frac{[\beta^*(X - \eta^2)u^*_{n,n_1} - (2n + 3/2)]^{k+1}}{[\beta^*(X - \eta^2)u^*_{n,n_1} + 2(n_1 - n) - 1/2]^{k+1}}$$
$$\times F(b_{n,n_1} + 3/4 + n, k + 1; b_{n,n_1} + 11/4 + n + k,$$
$$\left. 1 - \frac{2(2n_1 + 1)}{\beta^*(X - \eta^2)u^*_{n,n_1} + 2(n_1 - n) - 1/2}\right)\Bigg]^2,$$

where $K_0 = (3^4 \times 2^{1/3})\pi^3\alpha^*\lambda_0^2 e a_d^2 N_0$ and $b_{n,n_1} = \beta^*\eta^2 u^*_{n,n_1}/2$. Figure 1 shows the spectral dependence of the coefficient of extrinsic absorption of light $K^{(s)}(\omega)$ for the optical transition with the maximum oscillator strength ($n_1 = 0$, $n_2 = 1$) in borosilicate glass with inclusions of InSb crystallites. In this case, $m^* = 0.0133m_0$ (m_0 is the free-electron mass), $\varepsilon = 18$, $\overline{R_0} = 35.9$ nm, $U_0 = 0.2$ eV, $|E_\lambda| = 5.6 \times 10^{-2}$ eV, and $N_0 = 10^{15}$ cm^{-3}. Curves *1* and *2* in Fig. 1 are plotted for $B = 0$ and 12.8 T, respectively. It can be seen that, in a magnetic field, the edge of the extrinsic-absorption band (absorption threshold) shifts to shorter wavelengths, which is caused by the dynamics of the Landau level. The shift follows the law

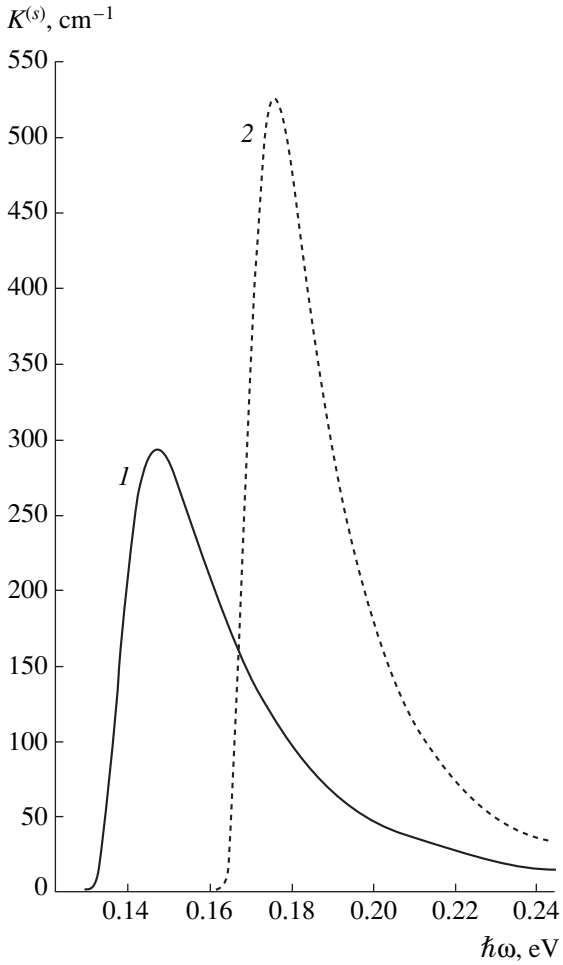

Fig. 1. Spectral dependence of the coefficient of extrinsic absorption of longitudinally polarized light $K^{(s)}(\omega)$ for the optical transition with the maximum oscillator strength ($n_1 = 0$, $n_2 = 1$, $m = 0$) in borosilicate glass colored with InSb crystallites, for $B =$ (*1*) 0 and (*2*) 12.8 T.

$X_{\text{th}} \approx \eta^2 + 8\sqrt{U_0^*}(3/2 + \sqrt{1 + 9\overline{R_0^*}^2/64U_0^* a^{*4}})/3\overline{R_0^*}$ and can be as large as ~0.034 eV (see curve *2*). In addition, the coefficient of the extrinsic absorption of light increases (compare curves *1* and *2*). This effect can be qualitatively explained by a decrease in the dimensionality of the oscillator spherical well with increasing magnetic field. Indeed, since $a_B \ll a$, the confinement of carrier motion in the *xy* plane, caused by "weakening" of the QD potential, can be considered as a perturbation. A decrease in the dimensionality of the QD potential increases overlap of the wave functions of the initial and final states, increasing, correspondingly, the possibility of the optical transition. Thus, the variation of *B* makes it possible to change the lateral confinement of the system and, therefore, control the extrinsic absorption of light.

3. ABSORPTION OF LIGHT IN THE CASE OF TRANSVERSE POLARIZATION

Let us consider the absorption of light by a QD–IC complex when $\mathbf{B} \perp \mathbf{e}_\lambda$. The effective Hamiltonian for interaction with the light-wave field $\hat{H}_{\text{int}}^{(t)}$ in the case of transverse (relative to the magnetic-field direction) polarization $\mathbf{e}_{\lambda t}$ can be written as

$$\hat{H}_{\text{int}}^{(t)} = \lambda_0 \sqrt{\frac{2\pi\hbar^2\alpha^*}{m^{*2}\omega} I_0} e^{i\mathbf{qr}} \left[(\mathbf{e}_{\lambda t}, \hat{\mathbf{P}}) - \frac{|e|B}{2} [\mathbf{e}_{\lambda t}, \mathbf{r}]_z \right]. \quad (14)$$

In the dipole approximation, the matrix element $M_{f\lambda}^{(t)}$ of the transition under consideration can be written as

$$M_{f\lambda}^{(t)} = \frac{(-1)^n i\pi\lambda_0 \exp(\mp i\vartheta)}{2^{n+1} n! a_1^2} \sqrt{\frac{\alpha^* I_0}{\omega}} \beta a^3$$
$$\times \frac{[(2n)!]^{1/2} (n_1+1)^{1/2} \Gamma(\beta/2+n) [\Gamma(\beta/2-1/2)]^{1/2}}{[\Gamma(\beta/2+1)]^{1/2} \{(\beta/2)[\Psi(\beta/2+1) - \Psi(\beta/2-1/2)] - 1\}^{1/2}}$$
$$\times \left((E_{n_1, \pm 1, 2n} - E_\lambda) \pm \frac{|e|B\hbar}{2m^*} \right) \sum_{k=0}^{n_1} (-1)^k C_{n_1}^k \left(1 + \frac{a^4}{4a_B^4} \right)^{k/2} \quad (15)$$
$$\times \frac{2^{k+1}\Gamma(k+2)}{(1+\sqrt{1+a^4/4a_B^4})^{k+2}} \frac{1}{\Gamma(\beta/2+n+k+2)}$$
$$\times F\left(\beta/2+n, k+2; \beta/2+n+k+2, 1 - \frac{2}{1+\sqrt{1+a^4/4a_B^4}} \right).$$

Here, ϑ is the polar angle of the transverse-polarization vector $\mathbf{e}_{\lambda t}$. In this case, selection rules arise when the following integrals are calculated:

$$\int_0^{2\pi} \exp(-im\varphi)\cos(\varphi - \vartheta) d\varphi = \begin{cases} \pi \exp(\mp i\vartheta), & \text{if } m = \pm 1, \\ 0, & \text{if } m \neq \pm 1; \end{cases} \quad (16)$$

$$\int_0^{2\pi} \exp(-im\varphi)\sin(\varphi - \vartheta) d\varphi = \begin{cases} \mp \pi i \exp(\mp i\vartheta), & \text{if } m = \pm 1, \\ 0, & \text{if } m \neq \pm 1; \end{cases} \quad (17)$$

$$\int_{-\infty}^{\infty} \exp\left[-(1+t)\frac{z^2}{a^2} \right] H_n\left(\frac{z}{a}\right) dz = \begin{cases} 0, & \text{if } n_2 \neq 2n, \quad n = 0, 1, 2, \ldots, \\ (-1)^n \sqrt{\pi} a \dfrac{(2n)!}{n!} t^n (1+t)^{-n-1/2}, & \text{if } n_2 = 2n. \end{cases} \quad (18)$$

It can be seen from (16)–(18) that optical transitions from the impurity level are allowed only to states with the quantum number $m = \pm 1$ and even quantum numbers n_2. The coefficient of extrinsic absorption of transversely polarized light, $K^{(t)}(\omega)$, can be written as

$$K^{(t)}(\omega) = \frac{2\pi N_0}{\hbar I_0}$$
$$\times \sum_{n_1, nm=-1} \sum^{1} \delta_{|m|,1} \int_0^{3/2} du P(u) \left| M_{f\lambda}^{(t)} \right|^2 \frac{1}{\hbar\omega_0 \beta^* (X - \eta^2)} \quad (19)$$
$$\times \delta \left[\frac{(2n+1/2) + \sqrt{1 + \beta^{*2} u^2 / a^{*4}} (2n_1 + 2)}{\beta^* (X - \eta^2)} + \frac{mu}{a^{*2}(X - \eta^2)} - u \right].$$

The equation for determining the roots of the argument of the Dirac δ function is

$$\frac{(2n+1/2) + (2n_1+2)\sqrt{1 + \beta^{*2} u^2 / a^{*4}}}{\beta^* (X - \eta^2)} + \frac{mu}{a^{*2}(X - \eta^2)} - u = 0. \quad (20)$$

In accordance with the selection rules for the magnetic quantum number, in the case of transverse polar-

ization, Eq. (20) has only two roots $u_{n_1,n,\pm1}$ satisfying the energy conservation law for the optical transition under consideration:

$$u_{n_1,n,-1} = \frac{(2n+1/2)[1+a^{*2}(X-\eta^2)]}{(\beta^*/a^{*2})\{[1+a^{*2}(X-\eta^2)]^2-(2n_1+2)^2\}} + \frac{(2n_1+2)\sqrt{[1+a^{*2}(X-\eta^2)]^2+(2n+1/2)^2-(2n_1+2)^2}}{(\beta^*/a^{*2})\{[1+a^{*2}(X-\eta^2)]^2-(2n_1+2)^2\}} \quad (21)$$

$$u_{n_1,n,+1} = \frac{(2n+1/2)[a^{*2}(X-\eta^2)-1]}{(\beta^*/a^{*2})\{[a^{*2}(X-\eta^2)-1]^2-(2n_1+2)^2\}} + \frac{(2n_1+2)\sqrt{[a^{*2}(X-\eta^2)-1]^2+(2n+1/2)^2-(2n_1+2)^2}}{(\beta^*/a^{*2})\{[a^{*2}(X-\eta^2)-1]^2-(2n_1+2)^2\}} \quad (22)$$

As a result, the coefficient of extrinsic absorption of transversely polarized light $K^{(t)}(\omega)$ can be represented as

$$K^{(t)}(\omega) = K_0\beta^* a^{*6} X\Bigg[\Bigg(1-\frac{1}{a^{*2}X}\Bigg)^2 \times \sum_{n_1,n}\frac{(2n)!(n_1+1)(2n_1+2)^2}{2^{2n}(n!)^2}\frac{(2c_{n_1,n,-1}+3/2)^2}{\Gamma(c_{n_1,n,-1}+7/4)} \times \frac{\Gamma(c_{n_1,n,-1}+1/4)\Gamma^2(c_{n_1,n,-1}+3/4+n)}{\{(c_{n_1,n,-1}+3/4)[\Psi(c_{n_1,n,-1}+7/4)-\Psi(c_{n_1,n,-1}+1/4)]-1\}} \times \frac{u^4_{n_1,n,-1}\exp[-1/(1-2u_{n_1,n,-1}/3)]}{(u_{n_1,n,-1}+3)^{7/3}(3/2-u_{n_1,n,-1})^{11/3}} \times \Big|\beta^*\{(2n_1+2)^2-[1+a^{*2}(X-\eta^2)]^2\}u_{n_1,n,-1} + (2n+1/2)a^{*2}[1+a^{*2}(X-\eta^2)]\Big|^{-1} \times \Bigg[\sum_{k=0}^{n_1}(-1)^k C^k_{n_1}\frac{2^{k+1}\Gamma(k+2)}{\Gamma(c_{n_1,n,-1}+11/4+n+k)} \times \frac{\{\beta^*[1+a^{*2}(X-\eta^2)]u_{n_1,n,-1}-(2n+1/2)a^{*2}\}^{k+3/2}}{\{\beta^*[1+a^{*2}(X-\eta^2)]u_{n_1,n,-1}+a^{*2}[2(n_1-n)+3/2]\}^{k+2}} \times F\Bigg(c_{n_1,n,-1}+\frac{3}{4}+n, k+2; c_{n_1,n,-1}+\frac{11}{4}+n+k, 1-\frac{2(2n_1+2)a^{*2}}{\beta^*[1+a^{*2}(X-\eta^2)]u_{n_1,n,-1}+a^{*2}[2(n_1-n)+3/2]}\Bigg)\Bigg]^2$$

$$+\Bigg(1+\frac{1}{a^{*2}X}\Bigg)^2\sum_{n_1,n}\frac{(2n)!(n_1+1)(2n_1+2)^2}{2^{2n}(n!)^2}\frac{(2c_{n_1,n,+1}+3/2)^2}{\Gamma(c_{n_1,n,+1}+7/4)} \times \frac{\Gamma(c_{n_1,n,+1}+1/4)\Gamma^2(c_{n_1,n,+1}+3/4+n)}{\{(c_{n_1,n,+1}+3/4)[\Psi(c_{n_1,n,+1}+7/4)-\Psi(c_{n_1,n,+1}+1/4)]-1\}} \times \frac{u^4_{n_1,n,+1}\exp[-1/(1-2u_{n_1,n,+1}/3)]}{(u_{n_1,n,+1}+3)^{7/3}(3/2-u_{n_1,n,+1})^{11/3}} \times \Big|\beta^*\{(2n_1+2)^2-[a^{*2}(X-\eta^2)-1]^2\}u_{n_1,n,+1} + (2n+1/2)a^{*2}[a^{*2}(X-\eta^2)-1]\Big|^{-1} \times \Bigg[\sum_{k=0}^{n_1}(-1)^k C^k_{n_1}\frac{2^{k+1}\Gamma(k+2)}{\Gamma(c_{n_1,n,+1}+11/4+n+k)} \times \frac{\{\beta^*[a^{*2}(X-\eta^2)-1]u_{n_1,n,+1}-(2n+1/2)a^{*2}\}^{k+3/2}}{\{\beta^*[a^{*2}(X-\eta^2)-1]u_{n_1,n,+1}+a^{*2}[2(n_1-n)+3/2]\}^{k+2}} \times F\Bigg(c_{n_1,n,+1}+\frac{3}{4}+n, k+2; c_{n_1,n,+1}+\frac{11}{4}+n+k, 1-\frac{2(2n_1+2)a^{*2}}{\beta^*[a^{*2}(X-\eta^2)-1]u_{n_1,n,+1}+a^{*2}[2(n_1-n)+3/2]}\Bigg)\Bigg]^2,$$

where $c_{n_1,n,\pm1} = \beta^*\eta^2 u_{n_1,n,\pm1}/2$. Figure 2 shows the spectral dependence of the coefficient of extrinsic absorption of transversely polarized light $K^{(t)}(\omega)$ calculated by formula (23) for the optical transition with the maximum oscillator strength ($m = \pm1$, $n_1 = n_2 = 0$) in borosilicate glass with inclusions of InSb crystallites. Curves *1* and *2* are plotted for the same values of the parameters of a QD and impurity center, as in the case of longitudinal polarization. It can be seen that, in a magnetic field, the extrinsic-absorption band (curve *1*) splits into a Zeeman doublet (curve *2*). Notably, the height of the absorption peak associated with the optical transition to the state with $m = -1$ is several times smaller than that of the peak associated with the transition of an electron to the state with $m = +1$. Apparently, such asymmetry is due to displacement of the wave function of an electron associated with the state with energy $E_{0,-1,0}$ from the oscillator spherically symmetric potential well. Indeed, since $E_{0,-1,0} < E_0$ (E_0 is the QD ground-state energy), in accordance with the uncertainty relation, the electron-localization radius in this case should exceed the characteristic oscillator length $a = \sqrt{\hbar/m^*\omega_0}$. Figure 3 shows the spectral dependence of the anisotropy of the magnetooptical absorption $K^{(s)}/K^{(t)}$ for the same two-phase system as in the previous case. The anisotropy is pronounced near the thresh-

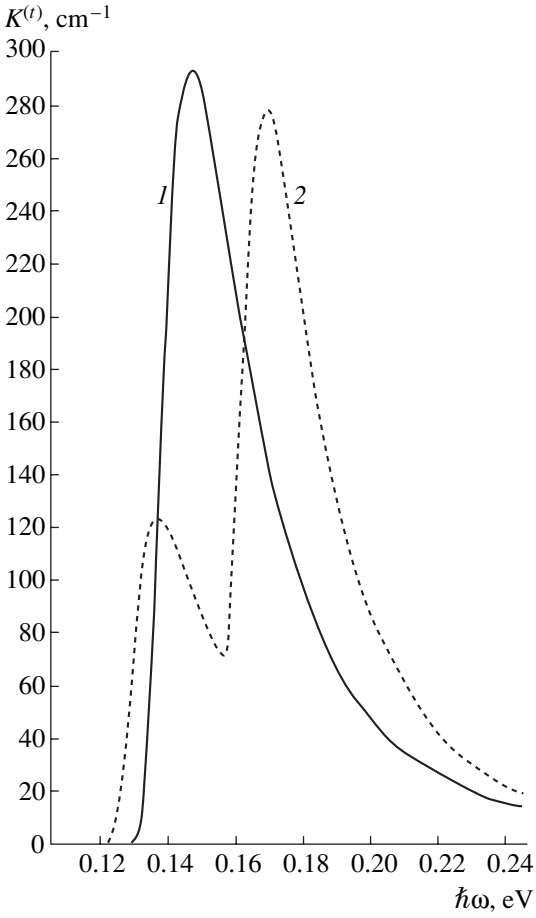

Fig. 2. Spectral dependence of the coefficient of extrinsic absorption of transversely polarized light $K^{(t)}(\omega)$ for the optical transition with the maximum oscillator strength ($n_1 = 0$, $n_2 = 0$, $m = \pm 1$) in borosilicate glass colored with InSb crystallites, for B = (*1*) 0 and (*2*) 3.7 T.

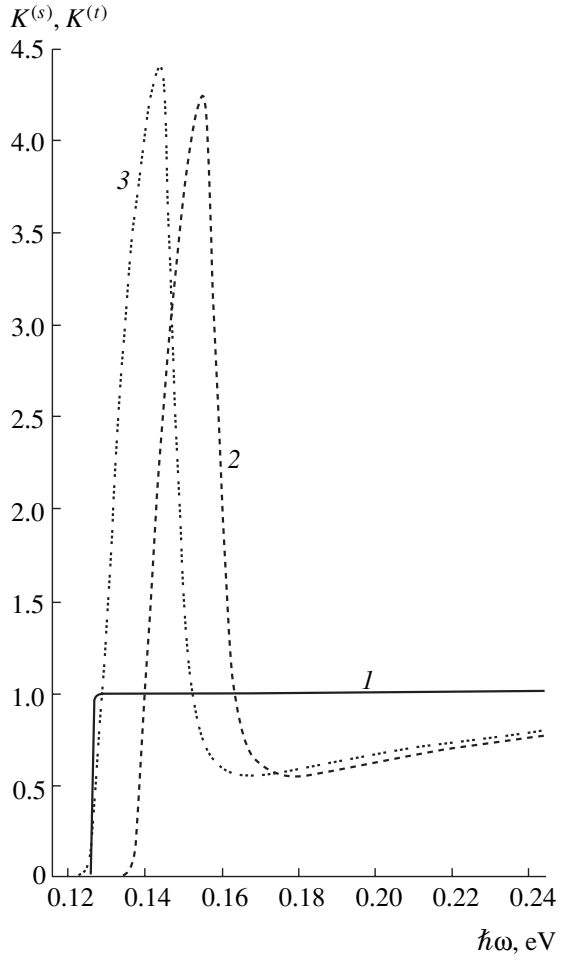

Fig. 3. Spectral dependence of the anisotropy of extrinsic absorption of light $K^{(s)}/K^{(t)}$ for B = (*1*) 0, (*2*) 3.7, and (*3*) 3.6 T and for $|E_\lambda|$ = (*2*) 5.6×10^{-2} and (*3*) 4.4×10^{-2} eV.

old of the extrinsic absorption of longitudinally polarized light (see curve *2*) and depends only slightly on the impurity-level location $|E_\lambda|$ (compare curves *2* and *3*).

4. CONCLUSION

We have carried out a theoretical study of the magnetooptical absorption of QD–IC complexes in an insulator host. The zero-range potential model was used for the impurity potential, while the QD was described in terms of a parabolic confinement potential. The amplitude of the QD potential U_0 is an empirical parameter. Characteristic features of the spectra of extrinsic absorption of longitudinally and transversely (relative to the magnetic-field direction) polarized light were studied. It was found that, in the case of longitudinal polarization, the edge of the extrinsic-absorption band shifts in a magnetic field to shorter wavelengths, while the light-absorption coefficient increases several times. In the case of transverse polarization, the quantum-dimensional Zeeman effect was observed in the extrinsic-absorption spectra. The anisotropy of magnetooptical absorption is a nonmonotonic function of the frequency of light. As in the case of quasi-one-dimensional nanostructures [15], a magnetic field can appreciably affect lateral geometric confinement. This is of particular interest in the context of the fabrication of photodetectors based on two-phase systems with a controlled extrinsic-absorption band.

REFERENCES

1. S. Huant, S. P. Najda, and B. Etienne, Phys. Rev. Lett. **65**, 1486 (1990).
2. M. Fujito, A. Natori, and H. Yasunada, Phys. Rev. B **51**, 4637 (1995).
3. É. P. Sinyavskiĭ and S. M. Sokovnich, Fiz. Tekh. Poluprovodn. (St. Petersburg) **34**, 844 (2000) [Semiconductors **34**, 815 (2000)].
4. V. D. Krevchik and É. Z. Imamov, Fiz. Tekh. Poluprovodn. (Leningrad) **17**, 1235 (1983) [Sov. Phys. Semicond. **17**, 780 (1983)].

5. A. A. Pakhomov, K. V. Khalipov, and I. N. Yassievich, Fiz. Tekh. Poluprovodn. (St. Petersburg) **30**, 1387 (1996) [Semiconductors **30**, 730 (1996)].

6. V. D. Krevchik, R. V. Zaĭtsev, and V. V. Evstifeev, Fiz. Tekh. Poluprovodn. (St. Petersburg) **34**, 1244 (2000) [Semiconductors **34**, 1193 (2000)].

7. V. D. Krevchik and R. V. Zaĭtsev, Fiz. Tverd. Tela (St. Petersburg) **43**, 504 (2001) [Phys. Solid State **43**, 522 (2001)].

8. T. Martin and S. Feng, Phys. Rev. Lett. **64**, 1971 (1990).

9. L. D. Landau and E. M. Lifshitz, *Course of Theoretical Physics*, Vol. 3: *Quantum Mechanics: Non-Relativistic Theory* (Nauka, Moscow, 1974; Pergamon, New York, 1977).

10. D. S. Bulyanitsa and A. A. Grinberg, Fiz. Tekh. Poluprovodn. (Leningrad) **11**, 806 (1977) [Sov. Phys. Semicond. **11**, 474 (1977)].

11. V. A. Grinberg, Fiz. Tekh. Poluprovodn. (Leningrad) **8**, 1000 (1974) [Sov. Phys. Semicond. **8**, 648 (1974)].

12. *Higher Transcendental Functions (Bateman Manuscript Project)*, Ed. by A. Erdelyi (McGraw-Hill, New York, 1953; Nauka, Moscow, 1974), Vols. 1, 2.

13. A. Ya. Shik, Fiz. Tekh. Poluprovodn. (St. Petersburg) **26**, 1161 (1992) [Sov. Phys. Semicond. **26**, 649 (1992)].

14. I. M. Lifshitz and V. V. Slezov, Zh. Éksp. Teor. Fiz. **35** (2), 479 (1958) [Sov. Phys. JETP **8**, 331 (1959)].

15. V. A. Geĭler, V. A. Margulis, and L. I. Filina, Zh. Éksp. Teor. Fiz. **113**, 1376 (1998) [JETP **86**, 751 (1998)].

Translated by Yu. Sin'kov

Semiconductors, Vol. 36, No. 10, 2002, pp. 1154–1158. Translated from Fizika i Tekhnika Poluprovodnikov, Vol. 36, No. 10, 2002, pp. 1233–1236.

LOW-DIMENSIONAL SYSTEMS

Dependence of the Optical Gap of Si Quantum Dots on the Dot Size

V. A. Burdov

Nizhni Novgorod State University, pr. Gagarina 23, Nizhni Novgorod, 630600 Russia

e-mail: burdov@phys.unn.runnet.ru

Submitted September 5, 2001; accepted for publication March 11, 2002

Abstract—The dependence of the optical gap of Si quantum dots, embedded in a SiO_2 insulator host, on the dot size was calculated in terms of an envelope-function approximation. It is shown that consideration of the finiteness of the SiO_2 band gap and an abrupt change in the effective mass at the Si–SiO_2 interface significantly decreases the optical gap of quantum dots in comparison with a model in which the potential barriers for electrons and holes are assumed to be infinitely high. The obtained results are in good agreement with the experimental data. © *2002 MAIK "Nauka/Interperiodica".*

INTRODUCTION

The optical properties of heterostructures with Si quantum dots (QDs) of small size (a few nanometers) have been intensively studied with the aim to obtain emission in the near-infrared or even visible spectral region. In connection with this, it is of interest to calculate the energy of the basic optical transition in such systems and analyze the dependence of this energy (or frequency) on the QD size.

It is worth noting that a number of attempts to carry out such calculations by using the effective-mass approximation (or **kp**-method) [1–3] have already been made in terms of a model with infinitely high potential barriers. However, many authors (including those of [3]) pointed out that this approximation yields highly overestimated values when applied to small-size QDs (smaller than 6–8 nm). Hence, more complex and powerful methods were used for such QDs (which, however, are rather difficult to apply to larger QDs for different reasons, including an abrupt increase in the volume of computations). Examples of such methods are the tight-binding model [3–8], pseudopotential method [9–11], and local-density approximation [12]. In addition to this, several authors (see, for example, [5]), pointed out that, for spherical dots, the dependence of the optical gap on the QD radius R does not follow the R^{-2} law, which is typical of the effective-mass approximation, but turns out to be weaker ($R^{-1.39}$ law was reported in [5]).

In this study, the optical gap of spherically shaped Si QDs positioned in a layer of fused SiO_2 was calculated by the **kp** method. We will show that this method can be used for QDs much smaller than 6–8 nm in size under a number of conditions. Specifically, the anisotropy of the dispersion law for electrons and holes should be taken into account more strictly, compared with the way it was done in [1–3]. In addition to this, one should take into account the finiteness of the potential-barrier height for both types of carriers (as it was already pointed out in [12]) and the abrupt change in the effective mass at the QD boundary.

MATHEMATICAL SIMULATION AND CALCULATIONS

The calculations show that, as well as in bulk Si, spin–orbit interaction rather weakly affects the energy spectrum by forming two levels in the valence band, the energy difference between which is 0.04 eV. Thus, this interaction can be ignored, and, in terms of an envelope-function approximation for the valence band, the Hamiltonian can be written as follows [13]:

$$\hat{H}_{ij}^{(h)} = \delta_{ij}\left(\hat{H}_{0h} + \frac{\hbar^2}{2m_0}\frac{L-M}{3}(\hat{\mathbf{k}}^2 - 3\hat{k}_j^2)\right) + (\delta_{ij}-1)\frac{\hbar^2}{2m_0}N\hat{k}_i\hat{k}_j. \quad (1)$$

Here δ_{ij} is the Kronecker delta; the indices i and j run from 1 to 3; m_0 is the free-electron mass; and the values of L, M, and N are 6.8, 4.43, and 8.61, respectively [14]. The Hamiltonian $\hat{H}_{0h}$ is an isotropic operator; i.e.,

$$\hat{H}_{0h} = -\frac{\hbar^2}{2m_h}\hat{\mathbf{k}}^2, \quad (2)$$

where $m_h = 3m_0/(L + 2M)$ is the effective hole mass ($\sim 0.19m_0$), and the magnitudes of the wave vector and the energy are reckoned from the Γ point.

For the conduction band of Si, a model in which the constant-energy surface is assumed to have the form of an ellipsoid of revolution with longitudinal and transverse effective masses is commonly used. This model is

obtained by expanding the dispersion relation in the vicinity of one of six equivalent points related to the energy minimum. However, this model is not appropriate for our aims, because the characteristic values of energies of dimensional quantization in a nanocluster of a few nanometers in size appreciably exceed the difference between the energy at the X point, where two energy branches cross each other, and that at the point related to the energy minimum. For such energies, the form of the constant-energy surface appreciably differs from an ellipsoid of revolution and a deviation from the parabolic dependence begins to play a significant role in the dispersion law.

For this reason, we shall follow the author of [15] and write the Hamiltonian for the conduction band in the form of a 2×2 matrix operator in the vicinity of one of three physically nonequivalent X points of the Brillouin zone, for example, in the vicinity of the X point related to the [0, 0, 1] direction (for the other two X points, the Hamiltonian can be written in a similar way):

$$\hat{H}_{11}^{(e)} = \hat{H}_{22}^{(e)} = \hat{H}_{0e} + \frac{\hbar^2}{6}\left(\frac{1}{m_t} - \frac{1}{m_l}\right)(\hat{\mathbf{k}}^2 - 3\hat{k}_z^2),$$

$$\hat{H}_{12}^{(e)} = (\hat{H}_{21}^{(e)})^{\dagger} \tag{3}$$

$$= \hbar^2(1/m_t - 1/m_0)\hat{k}_x\hat{k}_y + i(\hbar^2 k_0/m_l)\hat{k}_z,$$

where m_t and m_l are the transverse and longitudinal effective masses equal to $0.19m_0$ and $0.92m_0$, respectively; the magnitude of the wave vector and the energy are reckoned from the X point; and the Hamiltonian $\hat{H}_{0e}$ is also an isotropic operator

$$\hbar\hat{H}_{0e} = \frac{\hbar^2}{2m_e}\hat{\mathbf{k}}^2, \tag{4}$$

where $m_e = 3m_l m_t/(2m_l + m_t)$ is the effective electron mass. The value of $k_0 = 0.144(2\pi/a)$ (where $a = 0.543$ nm is the lattice constant) determines the distance in the $\mathbf{k}$ space from the X point to the nearest electron-energy minimum in the Brillouin zone. The matrix form of the Hamiltonian in this case, as well as in the case of the valence band, is the result of degeneracy of the energy spectrum at the X point (but now each X point is doubly degenerate).

In order to calculate the ground-state energies of electrons and holes, we will use perturbation theory, having chosen Hamiltonians (2) and (4), respectively, as the basic approximation. We will consider as perturbations the off-diagonal matrix elements of Hamiltonian operators (1) and (3), as well as the anisotropic components of the main-diagonal elements. Thus, it is necessary to solve the following matrix equation (the matrix dimension is 3×3 and 2×2 for the valence and conduction bands, respectively):

$$\hat{H}_{ij}F_j(\mathbf{r}) = \mathscr{E}F_i(\mathbf{r}), \tag{5}$$

where $F_j(\mathbf{r})$ are envelope functions and $\mathscr{E}$ is the energy. We will seek the envelope functions in the form of an expansion in the eigenfunction basis $|\alpha\rangle$ of the zero-order-approximation Hamiltonian (2) or (4) for holes or electrons, respectively:

$$F_j(\mathbf{r}) = \sum_{\alpha} C_{j\alpha}|\alpha\rangle. \tag{6}$$

Here, $|\alpha\rangle$ stands for the states of the unperturbed problem and j is the Bloch function index.

The substitution of expansion (6) into Eq. (5) yields an equation for the determination of energies $\mathscr{E}$ and expansion coefficients $C_{j\alpha}$:

$$(\mathscr{E} - E_\beta)C_{i\beta} = \sum_{\alpha}\sum_{j} C_{j\alpha}V_{ij}^{\beta\alpha}, \tag{7}$$

where E_β are the eigenvalues of the $\hat{H}_{0h}$ or $\hat{H}_{0e}$ operators in the $|\beta\rangle$ state and $V_{ij}^{\beta\alpha} = \langle\alpha|\hat{V}_{ij}|\beta\rangle$ are the matrix elements of the perturbation operator.

Direct calculation shows that, in spite of the strong anisotropy of the electron and hole energy branches, the perturbation series converge quite rapidly, and even the first-order corrections do not exceed a few percent. Therefore, we will ignore second-order corrections from here on.

First of all, we will calculate the ground-state energy of holes in the valence band. The zero-order approximation yields

$$\mathscr{E}_h = -\frac{\hbar^2 k_h^2}{2m_h}, \tag{8}$$

where k_h is the solution to the equation

$$kR\cot(kR) = 1 - \frac{m_h}{m^*} - \sqrt{\frac{m_h}{m^*}(w_h^2 - k^2R^2)}, \tag{9}$$

the parameter $w_h^2 = 2m_h V_h R^2/\hbar^2$, V_h is the height of the potential barrier for holes in the valence band, and m^* is the effective hole mass in the vicinity of the potential barrier. In general, $m^{-1}(r)d\Psi/dr$ differs from the effective hole mass in the QD. Deriving (9), we used the condition for continuity of the wave function at the QD boundary and the condition for continuity of the flow, which can be reduced to the condition of continuity of the $m^{-1}(r)d\Psi/dr$ ratio when there is a coordinate dependence of the mass. First of all, it is worth noting that, in the zero-order approximation, the expression for energy (8) and Eq. (9) can also be derived for electrons of the conduction band by replacing the "h" subscript with the "e" subscript in (8) and (9).

The corrections to (8) can be calculated conventionally using the perturbation theory for degenerate states [16], since even the ground state in the valence band is triply degenerate. Notably, only one ground *s* state should be retained on the right side of Eq. (7) in the sum over α. However, the mean value of the perturbation operator in the ground state vanishes; i.e., there are no first-order corrections to the energy. The second-order corrections (the *d* states of the $\hat{H}_{0h}$ operator are involved in the formation of these) differ from zero but are too small, as was already mentioned above. Thus, expression (8) should be considered as final for the ground-state energy of holes.

The structure of the ground state of electrons in the conduction band is more complicated. Since the perturbation operator contains $\hat{k}_z$ components that are linear in the operator, hybridization of the *s* and p_z states of the unperturbed system becomes possible (the p_x and p_y states couple with each other but fail to couple with the *s* and p_z states). For this reason, both *s* and p_z states should now be retained in the sum in Eq. (7). The solution of the secular equation yields a doubly degenerate ground-state energy (most likely, double degeneracy in the conduction band is not removed due to the full symmetry of the constant-energy surface relative to the *X* point)

$$\mathscr{E}_e = \frac{E + E_1 - V}{2} - \sqrt{\left(\frac{E_1 - E - V}{2}\right)^2 + U^2}, \qquad (10)$$

where E and E_1 are the energies of the s and *p* states, respectively:

$$E = \frac{\hbar^2 k_e^2}{2m_e}, \quad E_1 = \frac{\hbar^2 k_1^2}{2m_e}. \qquad (11)$$

The value of k_e is determined from Eq. (9), where the "*h*" subscript should be replaced throughout with the "*e*" subscript, as was already mentioned above. The value of k_1 can be derived from the equation

$$\frac{(kR)^2}{1 - kR\cot(kR)} = 2(1 - m_e m^*) - \frac{w_e^2 - (kR)^2}{1 + \sqrt{(w_e^2 - k^2R^2)m^*/m_e}}. \qquad (12)$$

The parameters V and U are the magnitudes of the diagonal and off-diagonal perturbation matrix elements

$$\frac{\hbar^2}{6}\left(\frac{1}{m_t} - \frac{1}{m_l}\right)\langle p_z|\hat{\mathbf{k}} - 3\hat{k}_z^2|p_z\rangle, \quad i\frac{\hbar^2 k_0}{m_l}\langle s|\hat{k}_z|p_z\rangle,$$

respectively. The values of these parameters are equal to

$$V = \frac{\hbar^2 k_1^2}{6A^2}\left(\frac{1}{m_t} - \frac{1}{m_l}\right)\left[\frac{\sin 2x}{2} - 2(1 - 2x^2/5)j_0^2(x) + \frac{4x}{5}j_0(x)j_1(x)\right] + \frac{\hbar^2 k_1^2}{6A^2}\left(\frac{1}{m_t} - \frac{1}{m_l}\right)j_1^2(x)$$

$$\times \frac{5x^2(c+2) - 4(x^2-6)(c+1)^2 - 9c^3 - 24c^2 - 48c - 24}{5(c+1)^2},$$

$$U = \frac{2\hbar^2 k_0}{\sqrt{3}m_l RA}$$

$$\times \frac{zx^2(c+b)(c+1)[j_0(x)\cos z - j_0(z)\cos x] - c^2 x j_1(x)}{(c+b)(c+1)\sqrt{1 + \sin^2 z - j_0(2z)}},$$

where $j_0(t)$ and $j_1(t)$ are spherical Bessel functions of the first kind with argument t,

$$x = k_1 R, \quad z = k_e R,$$

$$c = \sqrt{\frac{m^*}{m_e}(w_e^2 - x^2)}, \quad b = \sqrt{\frac{m^*}{m_e}(w_e^2 - z^2)},$$

$$A^2 = 1 + j_0(2x) - 2j_0^2(x) + \frac{c+2}{(c+1)^2}x^2 j_1^2(x).$$

The dependence $\mathscr{E}_e(R)$, as well as $\mathscr{E}_h(R)$, cannot be written in an explicit form, because Eqs. (9) and (12) are transcendental. However, the numerical solution of these equations for different QD radii is not a particular problem, and this makes it possible to calculate the dependence of the optical gap on *R*:

$$\mathscr{E}_g(R) = \Delta_{\Gamma X} + \mathscr{E}_e(R) - \mathscr{E}_h(R), \qquad (13)$$

where $\Delta_{\Gamma X}$ is the difference in the energies at the *X* point of the conduction band and at the Γ point of the valence band. In accordance with the data reported in [15], $\Delta_{\Gamma X} = 1.215$ eV.

RESULTS AND DISCUSSION

The figure shows $\mathscr{E}_g$ as a function of the inverse radius of a QD. The solid line shows the dependence $\mathscr{E}_g(R)$ for the model with infinitely high potential barriers V_e and V_h. Triangles *1* correspond to the model with barriers of finite height and an effective mass in the vicinity of the barrier, *m**, which is equal to the effective mass of carriers in Si, i.e., to m_e and m_h for electrons and holes, respectively. Circles *2* show the dependence $\mathscr{E}_g(R)$ for the model with barriers of finite height and *m** equal to the free-electron mass m_0 (which is, apparently, realistic). The band gap of fused SiO_2 is 8.7 eV. In accordance with the data reported in [17], the

height of the potential barrier for electrons is 3.2 eV. Hence, the barrier height for holes equals 4.3 eV (taking into account that $\Delta_{\Gamma X}$ should be subtracted).

It is worth noting that, even in the infinite-barrier approximation, the dependence of the optical gap on R will not be of the const $+R^{-2}$ kind due to hybridization of the *s* and *p* states. It is easy to show that, in this case, the energies E and E_1 and the matrix element V depend quadratically on R^{-1}, and the matrix element U is proportional to R^{-1}, which, in accordance with (10), yields some intermediate (between R^{-1} and R^{-2}) dependence for the optical gap.

In general, the potential barriers for both electrons and holes are rather high and exceed the values of $\mathscr{E}_e$ and $\mathscr{E}_h$ by an order of magnitude. However, as can be seen from the figure, even such high barriers cannot be assumed to be infinite with sufficient accuracy. Indeed, the difference between the energies of electrons and holes from the corresponding values yielded by the model with infinite barriers ranges from 15 to 65%, depending on R. Naturally, the effect of the finite-barrier height is especially profound in the small-size areas, where the deviation from the parabolic dependence (on R^{-1}) of both triangles *1* and circles *2* increases with R^{-1}, thus increasing the correction, which now contains R^{-3} components and higher (in magnitude) powers of R.

The abrupt change in the effective mass at the QD boundary also appreciably affects the location of the energy levels of electrons and holes. As can be seen from the figure, when $m^* = m_0$, the correction for all radii exceeds that obtained in the case of constant effective mass by a factor of 2.

A comparison of the results of this study with the calculations carried out by more complex methods shows very good agreement for QDs larger than 1.5 nm in size. For example, the values of the optical gap, calculated by the tight-binding method in [4, 5, 8], the pseudopotential method in [11], and in the local-density-functional approximation in [12], virtually coincide with the values of $\mathscr{E}_g(R)$ obtained here for $m^* = m_0$. The data obtained in [6] and [10] (using the tight-binding and pseudopotential methods, respectively) differ from that reported here by approximately 10–15%, but in different ways: the tight-binding method yields smaller values of the gap, while the pseudopotential method yields larger values.

The experimental data reported in [5, 6, 10, 18–21] are also in good agreement with the results of this study. There is virtually complete agreement with the experimental data on luminescence and optical absorption reported in [5, 18] and [10], respectively. Somewhat smaller values of the optical gap compared with the results reported here (on the whole, by 10–20%) were reported in [6, 19–21], where luminescence in Si nanocrystals was experimentally studied. The scatter in the experimental data may be caused by the different methods for preparating QDs, which can hardly be taken into account in a theoretical model.

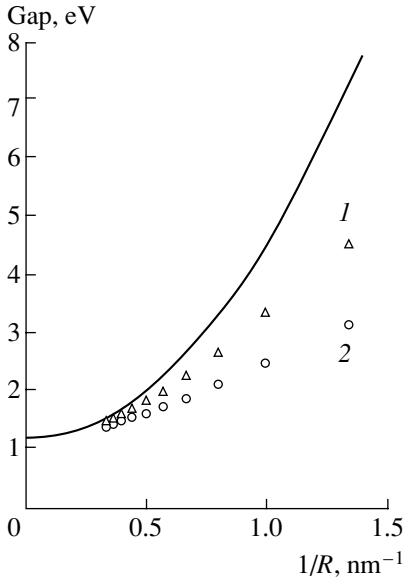

Optical gap as a function of the inverse QD radius, calculated in terms of models with infinite potential barriers (solid curve), (*1*) finite potential barriers (3.2 and 4.3 eV for electrons and holes, respectively) and constant effective mass, and (*2*) finite potential barriers (3.2 and 4.3 eV for electrons and holes, respectively) and abrupt change in the effective mass.

CONCLUSION

We have shown that, even for small-size QDs, the envelope approximation yields good agreement with the data derived from both experiments and other calculation methods. The advantage of the envelope approximation is that, being essentially an analytical method, it does not require as large an amount of computations as more complex calculation methods do.

ACKNOWLEDGMENTS

This study was supported by the Russian Foundation for Basic Research, project no. 00-02-17488.

REFERENCES

1. T. Takagahara and K. Takeda, Phys. Rev. B **46**, 15578 (1992).
2. J. B. Khurgin, E. W. Forsythe, G. S. Tompa, and B. A. Khan, Appl. Phys. Lett. **69**, 1241 (1996).
3. Y. M. Niquet, C. Delerue, G. Allan, and M. Lannoo, Phys. Rev. B **62**, 5109 (2000).
4. S. Y. Ren and J. D. Dow, Phys. Rev. B **45**, 6492 (1992).
5. C. Delerue, G. Allan, and M. Lannoo, Phys. Rev. B **48**, 11024 (1993).
6. N. A. Hill and K. B. Whaley, Phys. Rev. Lett. **75**, 1130 (1995).

7. K. Leung and K. B. Whaley, Phys. Rev. B **56**, 7455 (1997).
8. C. Delerue, M. Lannoo, and G. Allan, Phys. Rev. Lett. **84**, 2457 (2000).
9. L.-W. Wang and A. Zunger, J. Chem. Phys. **100**, 2394 (1994).
10. S. Ogut and J. R. Chelikowsky, Phys. Rev. Lett. **79**, 1770 (1997).
11. A. Franceschetti and A. Zunger, Phys. Rev. B **62**, 2614 (2000).
12. B. Delley and E. F. Steigmeier, Appl. Phys. Lett. **67**, 2370 (1995).
13. A. I. Anselm, *Introduction to Semiconductor Theory* (Nauka, Moscow, 1978; Prentice-Hall, Englewood Cliffs, 1981).
14. M. Voos, Ph. Uzan, C. Delalande, *et al.*, Appl. Phys. Lett. **61**, 1213 (1992).
15. A. A. Kopylov, Fiz. Tekh. Poluprovodn. (Leningrad) **16**, 2141 (1982) [Sov. Phys. Semicond. **16**, 1380 (1982)].
16. L. D. Landau and E. M. Lifshitz, *Course of Theoretical Physics*, Vol. 3: *Quantum Mechanics: Non-Relativistic Theory* (Nauka, Moscow, 1989; Pergamon, New York, 1977).
17. D. Babic, R. Tsu, and R. F. Greene, Phys. Rev. B **45**, 14150 (1992).
18. A. Mimura, M. Fujii, S. Hayashi, *et al.*, Phys. Rev. B **62**, 12625 (2000).
19. T. van Buuren, L. N. Dinh, L. L. Chase, *et al.*, Phys. Rev. Lett. **80**, 3803 (1998).
20. S. Takeoka, M. Fujii, and S. Hayashi, Phys. Rev. B **62**, 16820 (2000).
21. S. Guha, B. Quadri, R. G. Musket, *et al.*, J. Appl. Phys. **88**, 3954 (2000).

Translated by Yu. Sin'kov

Semiconductors, Vol. 36, No. 10, 2002, pp. 1159–1162. Translated from Fizika i Tekhnika Poluprovodnikov, Vol. 36, No. 10, 2002, pp. 1237–1240.

LOW-DIMENSIONAL SYSTEMS

Dependence of Scattering of Quasi-Two-Dimensional Electrons by Acoustic Phonons on the Parameters of a GaAs/$Al_xGa_{1-x}As$ Superlattice

S. I. Borisenko

Kuznetsov Physicotechnical Institute, pl. Revolyutsii 1, Tomsk, 634050 Russia
e-mail: sib@elefot.tsu.ru

Submitted January 8, 2002; accepted for publication March 21, 2002

Abstract—The time of relaxation of quasi-two-dimensional electrons in a GaAs/$Al_xGa_{1-x}As$ superlattice in the case of scattering by acoustic phonons was calculated numerically in relation to the quantum-well width and the width and height of the potential barrier. The probability of scattering for electrons of the lower miniband was calculated using an approximate envelope wave function without consideration of the dispersion of the periodic component of the Bloch function in relation to the wave vector. A comparative analysis of the calculated relaxation times and the values obtained using the well-known approximate formula was performed.

1. INTRODUCTION

As is well known [1–3], many specific and electrical properties of superlattices (SLs) with a quasi-two-dimensional (quasi-2D) electron gas manifest themselves at low temperatures, in which case the charge carriers are mainly scattered by acoustic phonons. Typically, the following well-known formula for the relaxation time is used in calculations of the charge-carrier mobility governed by this type of scattering [3–5]:

$$\tau = \frac{2}{3}\frac{a\hbar^3 c_L}{m^* D_c^2 k_0 T}. \quad (1)$$

Here, a is the width of a rectangular quantum well (QW) in the SL, c_L is the elastic modulus for longitudinal acoustic vibrations, D_c is the deformation-potential constant at the conduction-band bottom, and m^* is the effective electron mass. The constants c_L, D_c, and m^* have the same values as those in the semiconductor material of the QW. The relaxation time defined by formula (1) depends only on the QW width since this formula was derived taking into account the envelope wave function of charge carriers, which corresponds to an infinitely deep QW. In this context, the question arises as to whether this formula is applicable to an analysis of the carrier mobility in SLs with fairly thin barriers whose height is comparable to the energy of electrons in the lower (main) miniband.

In this paper, we suggest a method for calculating the relaxation time of quasi-2D electrons due to scattering by the deformation potential of acoustic phonons with the envelope wave function accounting for the finite height and width of the SL potential barriers. We performed a numerical analysis of the relaxation-time dependence on the design parameters of the GaAs/$Al_xGa_{1-x}As$.

2. METHOD OF CALCULATION

In the tight-binding approximation, the probability of elastic scattering of quasi-2D electrons in the lower SL miniband by acoustic phonons from the state with the wave vector $\mathbf{k}$ to the state with the wave vector $\mathbf{k}'$ can be written as

$$w(\mathbf{k}, \mathbf{k}') = \frac{2\pi}{\hbar}\sum_{n=-N_z/2}^{N_z/2} \left|U_n(k_z', k_z)\right|^2 \delta(\varepsilon(\mathbf{k}') - \varepsilon(\mathbf{k})), \quad (2)$$

where N_z is the number of SL periods,

$$\varepsilon(\mathbf{k}) = \frac{\hbar^2 k_\perp^2}{2m^*} + \frac{\Delta}{2}[1 - \cos(k_z d)] \quad (3)$$

is the energy of electrons in the low miniband in the tight-binding approximation, d is the SL period,

$$U_n(k_z', k_z) = \frac{1}{d}\int_{-d/2}^{d/2} e^{i2\pi nz/d} C u_{k_z'}^* u_{k_z} dz, \quad (4)$$

$C = D_c\sqrt{k_0 T/c_L}$ is a parameter of interaction between electrons and phonons (the value of this parameter is different for the QW and for the barrier in the approximation of the volume phonon spectrum), and $u_{k_z}(z)$ is the part of the periodic envelope Bloch function whose period coincides with that of the SL.

In order to calculate expression (4), one typically uses the tight-binding approximation according to which the function u_{k_z} is represented as the Bloch sum over the lower localized state of an infinitely deep QW [4, 5]; i.e.,

$$u_{k_z}(z) = \sum_n e^{-ik_z(z-dn)}\varphi(z-dn), \tag{5}$$

where $\varphi(z) = \sqrt{d/a}\cos(\pi z/a)$ is a function normalized to the SL period; this function differs from zero in the QW region for $-a/2 \le z \le a/2$. With allowance made for function (5), the integral in (4) can be analytically expressed as

$$\begin{aligned} U_n(k_z', k_z) &= U(q_n) = CS(q_n) \\ &= C\frac{\pi^2\sin(aq_n/2)}{(aq_n/2)[\pi^2-(aq_n/2)^2]}, \end{aligned} \tag{6}$$

where $q_n = k_z' - k_z + 2\pi n/d$.

We now calculate the relaxation time, which is longitudinal or transverse in reference to the SL axis, using the well-known formula

$$\tau_i^{-1}(\varepsilon) = \sum_{\mathbf{k}'} w(\mathbf{k}', \mathbf{k})\left(1 - \frac{v_i(\mathbf{k}')}{v_i(\mathbf{k})}\right), \tag{7}$$

where the subscript i denotes $\perp$ or $\parallel$ and $v_i(\mathbf{k}) = \nabla_i\varepsilon(\mathbf{k})/\hbar$ is the electron-velocity component along the i axis. Taking into account formulas (2), (3), and (6) and using the quasi-2D approximation ($\Delta \ll k_0T$, $\varepsilon \approx E = \hbar^2k_\perp^2/2m^*$), we obtain

$$\begin{aligned} \tau_\perp^{-1}(E) &= C_{\mathrm{AC}}\int_0^\infty |S(x)|^2 dx, \\ \tau_\parallel^{-1}(E) &= C_{\mathrm{AC}}\int_0^\infty |S(x)|^2\left[1-\cos\left(2\frac{d}{a}x\right)\right]dx, \end{aligned} \tag{8}$$

where integration is performed with respect to the dimensionless variable $x = aq/2$,

$$C_{\mathrm{AC}} = \frac{2m^*C_a^2}{\pi\hbar^3 a},$$

and $C_a = C$ for the parameters' values corresponding to the QW. With allowance made for (6), the integrals in formulas (8) can be evaluated analytically, which yields the well-known formula [1]

$$\tau_\perp^{-1} = \tau_\parallel^{-1} = \tau_0^{-1} = \frac{3}{4}\pi C_{\mathrm{AC}}. \tag{9}$$

According to formula (9), the relaxation time of quasi-2D electrons in an SL due to scattering by acoustic phonons is isotropic and depends only on the parameters of the QW material and on the QW width.

In actual SLs, the relaxation time is bound to depend on the height and width of potential barriers since their values are finite (rather than infinite as was assumed when deriving formula (9)). In order to determine this dependence and estimate the applicability of formula (9) to actual SLs of the GaAs/$Al_xGa_{1-x}As$ type, we suggest using the periodic component of the SL envelope Bloch function for $k_z = 0$ as the $u_{k_z}(z)$ function; this function is to be calculated in the context of the Kronig–Penney model as

$$u_{k_z}(z) \approx u_0(z)$$

$$= \begin{cases} B\cosh\left[\chi\left(\frac{d}{2}+z\right)\right], & -\frac{d}{2} \le z \le -\frac{a}{2}, \\ A\cos(kz), & |z| \le \frac{a}{2}, \\ B\cosh\left[\chi\left(\frac{d}{2}-z\right)\right], & \frac{a}{2} \le z \le \frac{d}{2}, \end{cases} \tag{10}$$

where $k = \sqrt{2m_aE_0}/\hbar$; $\chi = \sqrt{2m_b(V-E_0)}/\hbar$; V and b are the height and width of potential barriers, respectively; m_a and m_b are the effective masses of electrons in the QWs and potential barriers, respectively; and E_0 is the energy corresponding to the bottom of the SL low miniband. The value of the latter energy is obtained as a solution of the secular equation

$$\sinh\left(\frac{b}{2}\chi\right)\cos\left(\frac{a}{2}k\right) - \frac{km_a}{\chi m_a}\cosh\left(\frac{b}{2}\chi\right)\sin\left(\frac{a}{2}k\right) = 0. \tag{11}$$

In formula (10), the quantities A and B are normalization constants defined as

$$\begin{aligned} B &= A\cos\left(\frac{a}{2}k\right)/\cosh\left(\frac{b}{2}\chi\right), \\ \frac{1}{A^2} &= \frac{1}{2d}\left\{a + \frac{1}{k}\sin ak + \left(\frac{B}{A}\right)^2\left[b + \frac{1}{\chi}\sinh(\beta\chi)\right]\right\}. \end{aligned} \tag{12}$$

Taking into account (10), we can represent formula (7) for the longitudinal and transverse relaxation times as

$$\tau_\perp = \tau_\parallel = \tau = \alpha\tau_0, \tag{13}$$

where $\alpha(a, b, x)$ is a function of the QW width and of the width and height (the alloy parameter x) of the potential barrier; i.e.,

$$\begin{aligned} a^{-1} &= \frac{2a}{3d}\sum_{n=-\infty}^{\infty} S_n^2, \\ S_n &= \frac{1}{C_a}U_n(k_z', k_z) = \frac{1}{d}\int_{-d/2}^{d/2} e^{i2\pi nz/d}\frac{C_{\mathrm{AC}}}{C_a}u_0^2(z)dz. \end{aligned} \tag{14}$$

Taking into account that the function $u_0(z)$ is even and C_{AC} is independent of the coordinate within both the QW and the potential barrier, we can represent the formula for S_n as

$$S_n = \frac{2}{d}A^2\left\{S_{an} + \left(\frac{B}{A}\right)^2\frac{C_b}{C_a}S_{bn}\right\}, \quad (15)$$

where

$$S_{an} = \int_0^{a/2}\cos^2 kz\cos\left(\frac{2\pi n}{d}z\right)dz,$$
$$S_{bn} = \int_{a/2}^{d/2}\cosh^2\left[\chi\left(\frac{d}{2}-z\right)\right]\cos\left(\frac{2\pi n}{d}z\right)dz \quad (16)$$

are integrals that can be expressed analytically and C_b is the C constant for the values of parameters corresponding to the potential barrier.

3. NUMERICAL ANALYSIS

Numerical analysis of the relaxation time was performed using formula (13) for a GaAs/$Al_xGa_{1-x}As$ SL. In the calculations, the following values of the parameters were used:

$m^* = 0.066m_0$, $D_c = 17.5$ eV, $c_L = 14.4\times10^{10}$ N/m^2,

for GaAs;

$$m^* = [-0.066 + x(0.0174 + 0.145x)]m_0,$$
$$D_c = 17.5 \text{ eV},$$
$$c_{11} = (12.21 + 0.14x)10^{10} \text{ N/m}^2,$$
$$c_{12} = (5.66 + 0.32x)10^{10} \text{ N/m}^2,$$
$$c_{12} = (5.99 - 0.05x)10^{10} \text{ N/m}^2,$$

for an $Al_xGa_{1-x}As$ alloy; and

$$V = 0.6x(1.18 + 0.4x) \text{ eV},$$

for the potential-barrier height.

Figure 1 illustrates the applicability of approximation (10), in which the dispersion of the periodic component of the Bloch envelope function over k_z is ignored, to the SL under consideration. In Fig. 1, we show the dependences of the squared magnitude of the $u_0(z)$ function calculated using formulas (10)–(12) and of the function $u_{k_z}(z)$ calculated according to the Kronig–Penney model for the largest value $k_z = \pi/d$ [7]. Both functions were calculated for a symmetric SL with $a = b = 5$ nm and $x = 0.36$. It can be seen from Fig. 1 that the difference between the aforementioned functions is indeed small in comparison with the difference between the functions $u_0(z)$ and $\varphi(z)$ for an infinitely deep QW.

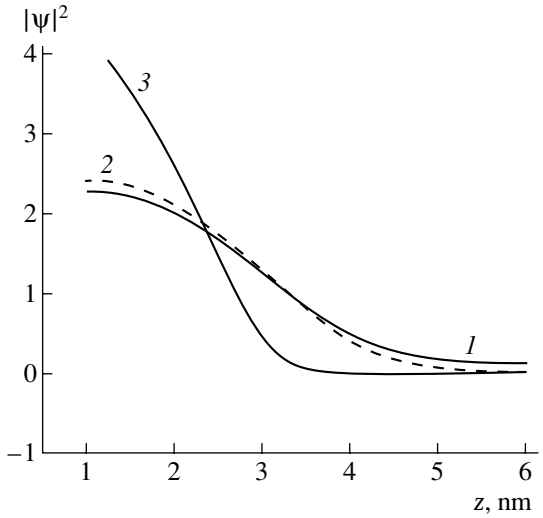

Fig. 1. Dependences of the squared magnitude of the envelope wave function $|\psi|^2$ on the coordinate z for a superlattice with $a = b = 5$ nm and $x = 0.36$. Curves *1–3* correspond to the (*1*) $|u_0(z)|^2$, (2) $|u_{\pi/d}(z)|^2$, and (*3*) $|\varphi(z)|^2$ functions.

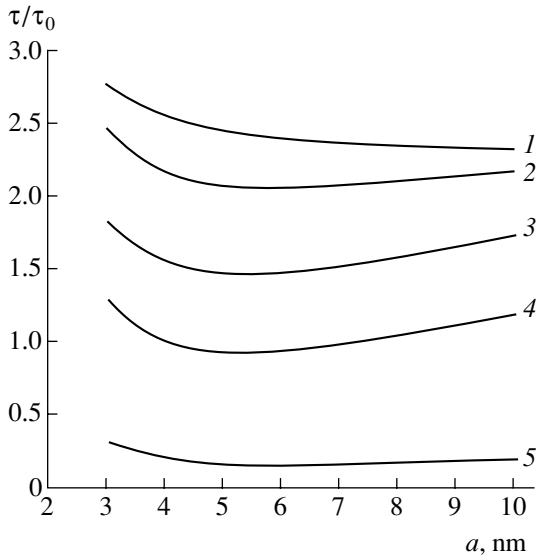

Fig. 2. Dependences of the function τ/τ_0 on the quantum-well width a in a superlattice with $x = 0.36$. The potential-barrier width $b =$ (*1*) 3, (*2*) 5, (*3*) 6, (*4*) 7, and (*5*) 10 nm.

Figure 2 shows the dependences of the parameter $\alpha = \tau/\tau_0$ on the QW width for several values of the potential-barrier width b of an SL with $x = 0.36$. It follows from the curves plotted in Fig. 2 that there is an appreciable dependence of the parameter α on the QW width for a fixed value of b; generally, this dependence is nonmonotonic. For $b < 5$ nm, the relaxation time far exceeds τ_0. Figure 3 shows the dependences of the parameter α on the potential-barrier width for several

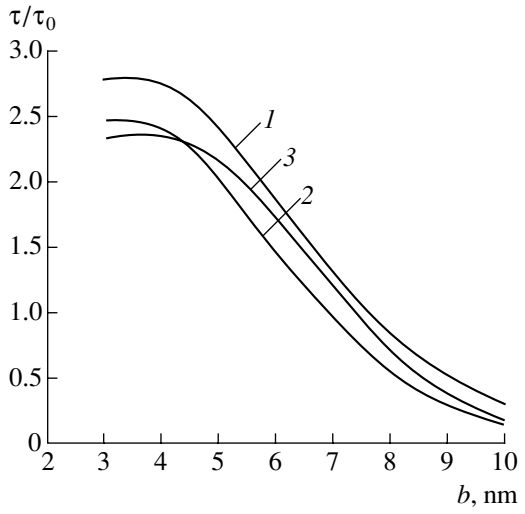

Fig. 3. The function τ/τ_0 in relation to the potential-barrier width b of a superlattice with $x = 0.36$. The quantum-well width a = (*1*) 3, (*2*) 5, and (*3*) 10 nm.

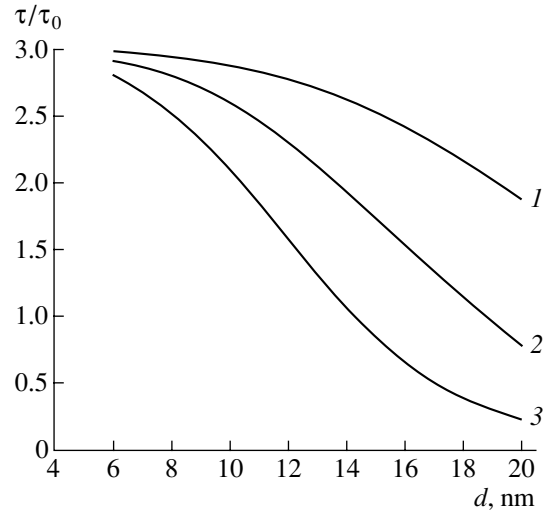

Fig. 4. Dependences of the function τ/τ_0 on the symmetric-superlattice period d for the composition parameter x = (*1*) 0.15, (*2*) 0.25, and (*3*) 0.35.

values of the QW width of a SL with $x = 0.36$. It follows from Fig. 3 that, as b increases with the value of a kept constant, the relaxation time decreases steadily. Dependences of the parameter α on the SL period d for a symmetric SL ($a = b$) with several values of the composition parameter are shown in Fig. 4. It can be seen from Fig. 4 that, as the composition parameter increases (i.e., primarily as the potential-barrier height increases) and the potential-barrier and QW widths remain constant, the relaxation times decreases steadily.

4. CONCLUSION

The above numerical analysis showed that the relaxation time of quasi-2D electrons due to scattering by acoustic phonons in a $GaAs/Al_xGa_{1-x}As$ superlattice decreases as the potential-barrier width and height increase. The consideration of this dependence may appreciably affect the calculated charge-carrier mobility derived using approximate formula (1).

REFERENCES

1. A. A. Dremin, V. B. Timofeev, D. Birkedal, and J. M. Hvam, Phys. Status Solidi A **164**, 557 (1997).
2. T. P. Pearsall, A. DiVergilio, G. Pierre, *et al.*, Appl. Phys. Lett. **72**, 76 (1998).
3. Yu. V. Ivanov, M. V. Vedernikov, and Yu. I. Ravich, Pis'ma Zh. Éksp. Teor. Fiz. **69**, 290 (1999) [JETP Lett. **69**, 317 (1999)].
4. L. Fridman, Phys. Rev. B **32**, 955 (1985).
5. B. K. Ridley, J. Phys. C **15**, 5899 (1982).
6. *Landolt-Börnstein: Numerical Data and Functional Relationships in Science and Technology, New Series*, Ed. by O. Madelung (Springer-Verlag, Berlin, 1987), Group III, Vol. 22a.
7. S. I. Borisenko and G. F. Karavaev, Fiz. Tekh. Poluprovodn. (St. Petersburg) **32**, 607 (1998) [Semiconductors **32**, 544 (1998)].

Translated by A. Spitsyn

Semiconductors, Vol. 36, No. 10, 2002, pp. 1163–1168. Translated from Fizika i Tekhnika Poluprovodnikov, Vol. 36, No. 10, 2002, pp. 1241–1247.

LOW-DIMENSIONAL SYSTEMS

Temperature Dependence of Conductance of Electrostatically Disordered Quasi-2D Semiconductor Systems Near an Insulator–Metal Percolation Transition

A. B. Davydov*^, B. A. Aronzon*, D. A. Bakaushin, and A. S. Vedeneev****

** Russian Research Centre Kurchatov Institute, 123182 Moscow, Russia*

*** Institute of Radio Engineering and Electronics, Fryazino, 141120 Russia*

^e-mail: davydov@imp.kiae.ru

Fax: 8 (0945) 1941994

Submitted January 14, 2002; accepted for publication March 26, 2002

Abstract—The experimental temperature dependence (4.2–300 K) of the conductance of mesoscopic quasi-2D electronic systems under conditions of the insulator–metal percolation transition are discussed for the case of metal–nitride–oxide–semiconductor silicon transistor structures with an inversion *n* channel and an extremely high ($\geq 10^{13}$ cm^{-2}) built-in charge density (source of electrostatic fluctuation potential). Saddle domains of the fluctuation potential are analyzed within the framework of the Landauer–Buttiker formalism. These domains, being *point quantum contacts* between wells in the chaotic potential distribution, determine both the nature of electron transport and the conditions of the insulator–metal transitions. The results of analyzing the dependence of the conductivity on temperature and field (on the gate voltage) are shown to be consistent. The shape of the effective potential barrier for the electron tunneling transport across the saddle domains is reconstructed. © *2002 MAIK "Nauka/Interperiodica".*

Interest in the electronic properties of quasi-2D electronic systems undergoing metal–insulator–semiconductor transitions (e.g., the dependence of the conductance G on gate voltage V_g and temperature) is related to the study of the fundamental features of an insulator–metal transition appearing due to the natural randomness of the objects (see [1]). Modern low-dimensional objects based on doped semiconductor structures are disordered mainly due to the high content of built-in charges (ionized impurities with a density of about 10^{12}–10^{13} cm^{-2}), which induce a random potential distribution in the plane of 2D electrons: the so-called fluctuation potential (FP) [2]. Then, the electronic transport is limited by the transition of charge carriers between wells of the potential relief via tunneling or activated hopping across the FP saddle domains. Such transitions determine both the field (as a function of V_g) and temperature dependences of G.

Of special interest are mesoscopic objects, particularly those whose length in the direction of the current L is small in comparison with the correlation radius L_c of a percolation cluster and the width $W > L_c$. The percolation cluster decomposes at these conditions into isolated percolation paths, and the conductance via the low-resistance path dominates in the transport. Therefore, the entire sample conductance is determined by a higher-resistance segment of such a path, which provides the possibility of studying the mechanism of electronic transport across a single FP saddle domain.

We experimentally realized this situation that is characteristic for contemporary field transistors with a submicrometer gate length (see [3, 4]), in particular, for the example of model objects: Si-MNOS (metal–nitride–oxide–semiconductor) transistor structures ($L = 5$, $W = 50$ μm [3, 4]). Using the method proposed in [5] for the determination of the percolation cluster correlation radius, we have established that $L_c \geq 10$ μm for these structures and, therefore, it satisfies the conditions $L \leq L_c < W$ [4]. A quasi-plateau segment on the $G(V_g)$ dependence for characteristic values $G \approx e^2/h$ was found at sufficiently high ($\geq 10^{12}$ cm^{-2}) built-in charge densities (at electron traps near the SiO_2–Si_2N_4 interface) within the temperature range 4.2–300 K (Fig. 1). The observed features demonstrate that the FP saddle domains are really *point quantum contacts* between wells of the chaotic potential relief [1]. These domains were analyzed in [3] within the framework of a model of parabolic saddle potential [6]. In particular, the energy parameters characterizing the potential curvature in the direction of electron motion ($\hbar\omega_x$) and in the transverse direction ($\hbar\omega_y \approx 100$ meV) were determined. The parameter $\hbar\omega_x$ was shown to decrease from ≈100 to ≤10 meV upon lowering the Fermi energy. This means that the real FP shape in the saddle domains differs from the parabolic one at the Fermi energies corresponding to weak inversion, when the Fermi level lies at the density-of-states tail. The electron transport at the insulator–metal transition is assumed to be totally con-

1063-7826/02/3610-1163$22.00

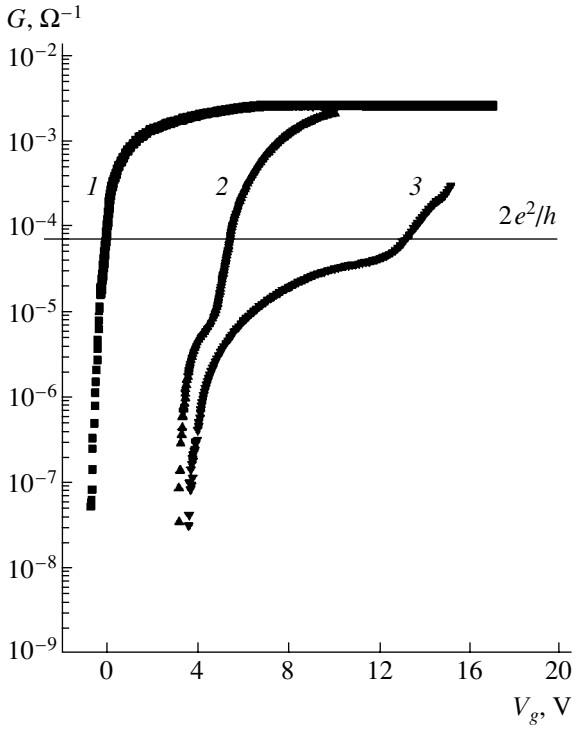

Fig. 1. Conductance G of the Si-MNOS structures as a function of the gate voltage V_g at various built-in charge densities: (*1*) $n_t \le 10^{10}$, (*2*) 5×10^{12}, and (*3*) 1.3×10^{13} cm^{-2}.

trolled by features of the saddle domains of the FP, which is characteristic of structures with two scales of fluctuations.

In this paper, experimental data for the conductance G temperature dependence are analyzed for Si-MNOS structures. Conditions for the electron transport to be controlled by the FP saddle-domains [3, 4] and for tunneling to be dominant in the transport across these domains are considered [1, 6]. The shape of the effective potential barrier controlling the conduction of the structures under conditions of the insulator–metal transition is analyzed.

Similarly to [3], the Si-MNOS transistor structures with an inversion *n*-channel on lightly doped (100) *p*-Si (L = 5 μm, W = 50 μm; thickness of the gate insulator layers: about 3 nm for SiO_2 and about 35 nm for Si_3N_4) were studied. Such objects are promising for modeling of electrostatically chaotic quasi-2D systems because of the possibility of controlling the density of the FP sources, i.e., n_t by using the field injection of electrons from the semiconductor into the traps at the SiO_2–Si_3N_4 interface. The charge state of traps was set at room temperature and the gate voltage 30 V (the current in the circuit gate–source–drain did not exceed 3 nA), which essentially exceeded the upper limit of V_g variation during the measuring of G. The objects retained the preset charge state of traps during the experiment, that is, for more than 10 h at low temperatures.

A typical dependence of the static conductance G on V_g at fixed n_t values within the range of 10^9–10^{13} cm^{-2} is shown in Fig. 1 ($G = I_d/V_d$, where I_d is the current, and $V_d \le 10$ mV is the source–drain voltage). In the "uncharged" state (curve *1*, $n_t \le 10^{10}$ cm^{-2}), the field effect exhibits the classical mechanism [7] of forming an inversion channel: the conductance exponentially depends on V_g at small V_g, which is characteristic of the weak inversion case. This dependence becomes linear as V_g increases (the strong inversion case). An increase in the built-in charge density (curves *2*, *3*) is followed by the appearance of an almost flat portion in the $G(V_g)$ dependence at the characteristic value $G \approx e^2/h$. This feature is observed within a wide range of temperatures (4.2–300 K) and built-in charge densities ($\approx 10^{11}$–10^{13} cm^{-2}), with an increase of n_t and/or a decrease of temperature accompanied by a clearer manifestation of the quasi-plateau portion with the asymptotic value $G = 2e^2/h$.

As was mentioned above (see [3–5]), the percolation cluster correlation radius L_c in the structures under consideration reaches values of ≥10 μm [3] in the weak inversion regime, which exceeds the gate length L = 5 μm. This means that the structures are mesoscopic (in terms of noncoherent mesoscopics [8]) objects; i.e., the percolation cluster reduces at these conditions into a system of parallel isolated percolation paths, and the main contribution to the conductance of the entire system comes from the one with the lowest resistance. Conductance of the latter is determined by the highest resistance portion of the path. In other words, the conductance in the weak inversion regime is controlled by a single saddle domain of the FP [3, 4]. The quantization of G (in units of e^2/h) means that this domain is a point quantum contact (see [1]) and is determined by the Landauer formula [9]

$$G(\varepsilon_f, T) = \frac{2e}{h}\int d\varepsilon\left(-\frac{\partial F}{\partial \varepsilon}\right)\mathfrak{T}(\varepsilon), \qquad (1)$$

where ε_f is the Fermi energy, F is the Fermi–Dirac distribution function, and $\mathfrak{T}(\varepsilon)$ is the tunneling transparency of the domain (see below). Following [6], i.e., approximating the FP saddle domain by the parabolic saddle potential

$$U(x, y) = U_s - \frac{m\omega_x^2 x^2}{2} + \frac{m\omega_y^2 y^2}{2} \qquad (2)$$

for the dependence of the $\mathfrak{T}$ factor on ε_f at conditions $\{kT \le \hbar\omega_y/2;\ \varepsilon_f \le U_s + \hbar\omega_y/2\}$, we obtain

$$\mathfrak{T}(\varepsilon_f) = \left[1 + \exp\left(-2\pi\frac{\varepsilon_f - U_s - \hbar\omega_y/2}{\hbar\omega_x}\right)\right]^{-1}, \qquad (3)$$

where U_s is the potential at the saddle point, which coincides with the classical percolation level; m is the effective carrier (electron) mass; ω_x and ω_y are parame-

ters characterizing the saddle potential curvature in the direction of electron transport (x) and in the transverse (y) direction.

The following estimates were obtained in [3] for the saddle potential curvature parameters from the experimentally obtained curves for the field effect $G(V_g)$ at low (liquid helium) temperatures near $G \approx e^2/\hbar$: $\hbar\omega_y \approx \hbar\omega_x \approx 100$ meV. A dependence of $\hbar\omega_x$ on V_g (at $G < e^2/h$) was found, thus indicating that the shape of the saddle potential differs from the parabolic one [6].

Let us consider the character of the temperature dependence of the conductance of these structures. The conductance G of the saddle domain and, therefore, of the whole structure, is thermally activated (because of the thermal excitation of electrons to the classical percolation level U_s), which is confirmed by the experimental results (see [5, 7]). In this paper, we consider another energy range, corresponding to conditions of the insulator–metal transition, where $\varepsilon_f - U_s > 0$. The conductance G calculated within the framework of the Buttiker [6] or Kamenev and Kohn [9] saddle-potential approach has at $T = 0$ and at conditions $0 \le \varepsilon_f - U_s \ll \hbar\omega_y/2$, $G \ll e^2/h$ a finite magnitude G_0 determined by the tunneling transparency $\mathfrak{T}$(3). As follows from (1) and (3), a temperature increase at $kT \le \hbar\omega_x/2\pi$ leads to the power-law increase of G (as distinct from the Mott law [7, 10]):

$$G \approx G_0\left[1 + \frac{2}{3}\pi^4\left(\frac{kT}{\hbar\omega_x}\right)^2\right]; \qquad (4)$$

this is a consequence of the power series expansion (1) in the small parameter $kT/\hbar\omega_x$ taking into account the dependence of $\mathfrak{T}$ on the Fermi energy (2).

A further temperature increase ($\hbar\omega_y \ge kT \ge \hbar\omega_x/2\pi$) must be accompanied by a transition to the quasi-activated $G(T)$ dependence with an activation energy of about ($\hbar\omega_y/2 - \varepsilon_f$) and a preexponential factor of about e^2/h [11], which, in contrast to the concept of minimal metal conductivity [7, 10], is a manifestation of the Landauer [9] character of conduction of the FP saddle domains (see (1)).

This qualitative reasoning is illustrated by the isothermal dependence of G on V_g, which was measured at a fixed built-in charge density $n_t \approx 1.3 \times 10^{13}$ cm^{-2} (Fig. 2), and by the temperature dependence of G (see below, Fig. 3).

Three regions with different types of temperature dependence of conductance are clearly seen in Fig. 2; they are separated by intersections of the isotherms $G(V_g)$ at $V_g \approx 8$ and 12 V.

In the first of these (weak inversion region, $V_g \le 8$ V), the conductance G drops abruptly with T decreasing, first by the Arrhenius law within the range of 300–40 K, and then the $G(T)$ dependence becomes weaker (see Fig. 3a). Such behavior, which is, in principle,

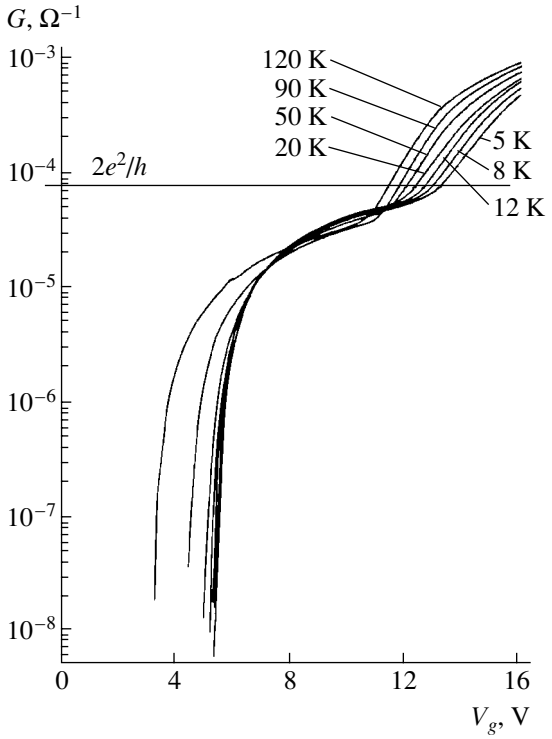

Fig. 2. Dependence of G on V_g for Si-MNOS structures at $n_t \approx 1.3 \times 10^{13}$ cm^{-2} and various temperatures.

characteristic of chaotic 2D systems, is usually related (see [7]) to a transition to the Mott hopping conductivity law with a variable hopping range. Taking into account real properties of the FP correlator [13], which implies the existence both of small-scale (about 30 nm) and large-scale smooth FP components, we shall consider another mechanism of the low-temperature behavior of G. The small-scale components are assumed to be responsible for forming the saddle domains of FP, which determine the electron transport features, while the large-scale components provide a spatial separation of these domains that exceed the electron free path. Thus, we consider the Landauer [6, 9] mechanism of electron transport in saddle domains of FP as controlling the conductance of the object in this region.

G slowly decreases with T in the second region (bounded from above by the intersection of isotherms $G(V_g)$ at the characteristic value $G \approx e^2/h$). We associate (see below) the presence of this region, which shows itself in experiments (see, e.g., [7]), with two points: (i) the Fermi energy temperature dependence in the semiconductor bulk at fixed V_g and (ii) the specificity of the electron tunneling transport, which is determined by the local potential distribution in FP saddle domains.

A further increase in V_g, accompanied by a sharp weakening of FP (due to the nonlinear electron screening of the potential fluctuations, beginning from the level of about 200 meV in the weak inversion regime [2]), leads to a transition from the initially percolation-type

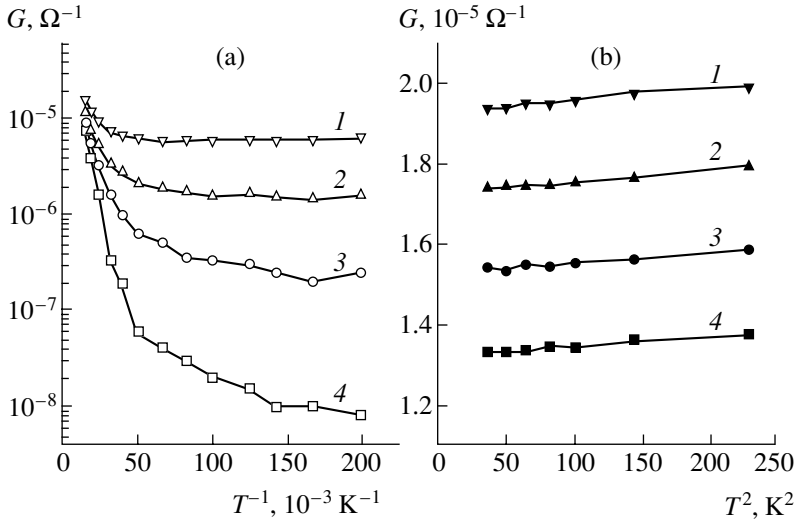

Fig. 3. Temperature dependence of the conductance G at fixed gate voltage values $V_g - V_{g0}(T) = \text{const}$ in (a) Arrhenius and (b) G–T^2 coordinates ($n_t \approx 1.3 \times 10^{13}$ cm^{-2}). The gate potential V_g = (a): (*1*) 6.3, (*2*) 5.8, (*3*) 5.5, and (*4*) 5.3 V; (b): (*1*) 7.6, (*2*) 7.4, (*3*) 7.2, and (*4*) 7.0 V.

quasi-1D medium to the weakly disordered 2D electron system, which is indicated, in particular, by the threshold behavior of the Hall effect with a characteristic conductance threshold value of about e^2/h [4]. The behavior of G in the region of strong inversion, on the whole, conforms to the classical picture [7].

Turning to a detailed analysis of the temperature dependence of conductance in regions of weak and intermediate ($G \le e^2/h$) inversion, we shall consider a range of small enough V_g values, bounded from above by the condition $U_s - \varepsilon_f > 0$. The expressions (1), (3) define G as a function of the Fermi energy ε_f, but not of the gate potential V_g. Here, ε_f is related to V_g by the relation

$$C(V_g - V_{g0}) = e\int_{\varepsilon_{f0}}^{\varepsilon_f} N_{ss}\,d\varepsilon, \qquad (5)$$

where C is the gate capacitance; N_{ss}, the effective density of electron states at the Si–SiO_2 interface; and V_{g0}, the V_g magnitude at some fixed value of $\varepsilon_f = \varepsilon_{f0}$, which is related to the temperature-independent point in the $G(\varepsilon_f)$ curves in [6], which must take place at $G = e^2/h$.

Let us explain the necessity of introducing the values ε_{f0} and V_{g0}. Analysis of experimental curves $G(T)$ at $\varepsilon_f = \text{const}$ is usually carried out at $V_g = \text{const}$ (see [7]), implying that, at $\varepsilon_f = \varepsilon_{f0}$, V_{g0} does not depend on T. Meanwhile, this dependence exists, e.g., due to changes of the Fermi level position in the bulk and of the mean potential at the surface with temperature, because of a redistribution of electrons in the space charge region [12]. In other words, the relation between V_{g0} and ε_{f0} values needs to be known at every temperature value in order to plot $G(T)$ for $\varepsilon_f = \text{const}$; this relation can be established in the following way. The conductance G has a constant value e^2/h (expressions (1)–(3)) at $\varepsilon_f = U_s + \hbar\omega_y/2$ within the formalism [1, 6]. We consider this fact as a useful criterion for determining the ε_{f0} value, which allows us to determine the dependence $V_{g0}(T)$. Indeed, if we put $\varepsilon_{f0} = U_s + \hbar\omega_y/2$, the $V_g(T)$ values will be determined by magnitudes of $V_g(T)$ corresponding to $G = e^2/h$ in the experimental field effect curves (Fig. 2). We analyze the dependence $G(T)$ on these grounds at fixed $V_g - V_{g0}$, which is equivalent to the condition $\varepsilon_f = \text{const}$.

$G(T)$ curves plotted for the weak inversion region at fixed $V_g - V_{g0}(T)$ values, i.e., at the condition $\varepsilon_f - (U_s + \hbar\omega_y/2) = \text{const}$, are presented in Fig. 3. According to the reasoning presented above (see (1)–(3)), G is thermally activated at sufficiently high temperatures ($kT \gg \hbar\omega_x/2\pi$, [3]) and has a preexponential factor of about e^2/h (Fig. 3a). The temperature dependence of G weakens as the temperature decreases ($kT \le \hbar\omega_x/2\pi$) to the liquid-helium range (Fig. 3a). As was mentioned above, unlike the classical picture [7, 10], we associate such behavior of the conductance with the Landauer mechanism of electronic transport, which is indicated (Fig. 3b) by the power-law (4) temperature dependence of G at low temperatures ($kT \ll \hbar\omega_x/2\pi$).

Estimates of the parameter $\hbar\omega_x$ for $\varepsilon_f = \text{const}$ from the range $0 < \varepsilon_f - U_s < \hbar\omega_y/2$, obtained on these grounds with the use of (4) from the temperature dependence of G at low temperatures (Fig. 3b), are represented in Fig. 4 by squares. Results of analysis (see [4]) of the isothermal field effect curves for the temperature range 4.2–15 K—the parameter $\hbar\omega_x N_{ss}/D$—are represented by stars in Fig. 4. Here, $D = 2m_0/\pi\hbar^2$ is the density of

states in the lower subband for the 2D electron channel at the interface Si–SiO_2. As was shown in [3], $N_{ss}/D \approx 1$, i.e., $\hbar\omega_x N_{ss}/D \approx \hbar\omega_x$ under experimental conditions.

The qualitative agreement of results of the analysis of independent experiments ($G(V_g)$ and $G(T)$ functions, Figs. 2 and 3b) in a wide range of conductance values (or ε_f) indicates the accuracy of estimates within the framework of the Landauer–Buttiker formalism and the prospects of applying the developed approach to the study of fundamental features of the insulator–metal transition in the topical electrostatically disordered quasi-2D electronic systems.

Let us consider the shape of FP saddle domains controlling the electronic transport in the intermediate and weak inversion modes. Inspecting Fig. 4, we notice that within the range $G \approx G_0 \le e^2/h$ (i.e., at $\varepsilon_f - U_s \le \hbar\omega_y/2$) the parameter $\hbar\omega_x$ has a constant value (≈100 meV), which is in agreement within the parabolic saddle potential model [6] with the present experimental results and with the experimental data and the results of numerical calculation presented in [3]. Meanwhile, the fall of $\hbar\omega_x$ observed upon a decrease of G means a deviation of the potential distribution from the parabolic law (2), which is enhanced as ε_f decreases in the direction $\varepsilon_f - U_s \le \hbar\omega_y/2$. We relate it to the nature of the generation and electronic screening of the chaotic potential relief in the plane of the quasi-2D electrons [2]. This implies the dominance of small-scale (on the order of the SiO_2 layer thickness, 3 nm in our case) FP components under intermediate and strong inversion, and also the subsequent manifestation of smoother (on the order of the nonlinear screening radius $R_s \approx (n_t/\pi)^{1/2}/n_s$ [2]; n_s is the density of quasi-2D electrons) large-scale components at the transition (with a decrease of ε_f, i.e., n_s) to weak inversion.

We then analyze, using experimental data, the effective quasi-2D potential barrier shape characterizing the electron transport at saddle domains of FP. We assume that this dependence determines the transport properties of point quantum contacts (see [1]), i. e., the fundamental features of the insulator–metal transition in modern quasi-2D electronic systems.

As was mentioned above, the temperature dependence of G in the weak inversion mode (Fig. 3) characterizes, at $kT \ll \hbar\omega_x/2\pi$, the tunneling mechanism of the electron transport in the saddle domains of FP. We trace this mechanism back to the transport of electrons under the effective potential barrier $U(x)$, assuming that, in the limit $T = 0$, the resulting conductance G_0 is determined by the transparency (transmission coefficient) $\mathfrak{T}$ of the barrier, which can be represented in the quasi-classical approximation as the integral

$$\mathfrak{T}(\varepsilon_f) \approx \exp\left[-\frac{2}{\hbar}\int\sqrt{2m[U(x)-\varepsilon_f]}\,dx\right] \qquad (6)$$

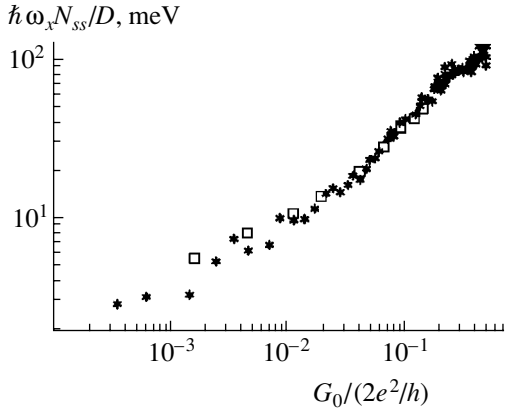

Fig. 4. Dependence of G_0 on the parameters $\varepsilon_x = \hbar\omega_x$ and $\varepsilon_x(N_{ss}/D)$ [3].

over the region $|x| \le x_0$, where x_0 satisfies the condition $U(x_0) - \varepsilon_f = 0$. Correspondingly, $G_0 \approx (2e^2/h)\mathfrak{T}$ ($\mathfrak{T} \ll 1$) within the framework of the formalism used [6, 9]. Notice also the agreement between the present experiments and those presented in [3] with the model [6] in the vicinity of the point $G \approx e^2/h$, which indicates that the barrier has a parabolic shape near the maximum

$$U(x) \approx U_s + \hbar\omega_y/2 - m\omega_x^2 x^2/2. \qquad (7)$$

The calculation of $\mathfrak{T}$ with the use of (6) and the substitution of (7) gives a solution that coincides with the one obtained in [6] (3) within the range of applicability of the quasi-classical approximation: at $G_0 \ll e^2/h$ in our case.

Taking these facts into consideration, to determine the effective barrier $U(x)$ shape from the experimental dependence $G_0(V_g)$ in the range of $G_0 \le e^2/h$, we used the interpolation expression

$$G_0(\varepsilon_f) \approx (2e^2/h)/[1 + \mathfrak{T}[(\varepsilon_f)]^{-1}], \qquad (8)$$

which is reduced to (3) in the vicinity of the maximum of the parabolic barrier (7), where $G_0 \longrightarrow e^2/h$, and is valid in the quasi-classical limit, i.e., at $G_0/(2e^2/h) \approx \mathfrak{T} \ll 1$.

The expressions (6) and (8) allow us to estimate the effective barrier $U(x)$ width, $x = x_0$, at the level $U(x) = \varepsilon_f$:

$$x_0(\varepsilon_f) \approx \pm\frac{1}{4}\ln\left(\frac{G_0}{2e^2/h - G_0}\right)\sqrt{\frac{\pi D}{U_s + \hbar\omega_y/2 - \varepsilon_f}}. \qquad (9)$$

The value of ε_f is, in turn, related to V_g by the expression $F(U_s + \hbar\omega_y/2 - \varepsilon_f) \approx C(V_{g0} - V_g)/e$, which was obtained from (5) taking into account the relation $N_{ss} \approx D$ [3], which relates x_0 with the G_0, V_g, and V_{g0} values being measured. (In the case of the parabolic barrier (7), the estimate (9) is in agreement with the exact value $x_0 = \pm[2(U_s + \hbar\omega_y/2 - \varepsilon_f)/m\omega_x]^{1/2}$ to within 20%).

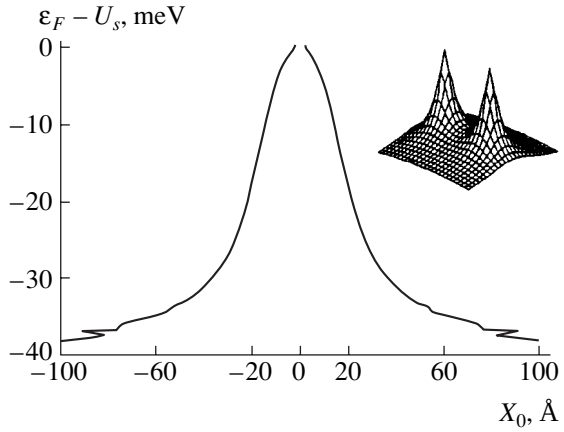

Fig. 5. The effective profile of the potential barrier controlling the tunneling electron transport across the FP saddle domains.

The effective barrier profile $U(x)$ for the electron tunneling transport across the FP saddle domains determined on these grounds is presented in Fig. 5. It is determined by a relationship of the parameter x_0 (considered as the argument) with the reduced Fermi energy $\varepsilon_f - U_s$. The barrier does have a parabolic shape (7) in the vicinity of the maximum ($x_0 \le 5$ nm), which concurs with the notions in [6], while it becomes smoother as ε_f decreases, so that $\varepsilon_f < U_s - \hbar\omega_y/2$. This manifests itself, in particular, in the abrupt fall of the $\hbar\omega_x$ value within the range of $G_0 \ll e^2/h$ (Fig. 4). Such behavior of $U(x)$ has a simple qualitative explanation. As was shown in [3], saddle points are formed between the peaks of FP, which appear in regions of the quasi-2D channel, where the local charge density exceeds the mean n_t (the corresponding potential distribution $V(x, y)$ in the saddle domain is presented in the inset of Fig. 5). Then, the shape of the effective barrier $U(x)$, on the whole, reflects the potential distribution in the saddle domain $V(x, 0)$ in the direction of electron movement with correction for the nonparabolicity of the $V(0, y)$ potential in the transverse direction.

Thus, the presented results clearly indicate the Landauer [9] character of the electron transport in the FP saddle domains controlling transport properties of disordered quasi-2D systems, including, in particular, their conductance within a broad range of temperatures and gate voltages. A concrete potential distribution in these regions determines the dependence of G on the Fermi energy (it is sharper in our case than in [6] but smoother than in [1]) and fundamentally influences the insulator–metal transition features in the class of objects under consideration.

ACKNOWLEDGMENTS

We are grateful to V. A. Volkov, V. A. Sablikov, and R. A. Suris for their interest in our work and for discussing the results.

This study was supported by the Russian Foundation for Basic Research (project nos. 01-02-17995, 99-02-16955, 01-02-06266), by the Interdisciplinary Program “Physics of Solid Nanostructures” (project nos. 99-1123, 97-1081), and by the Federal Foundation for the Development of Electronics.

REFERENCES

1. Y. Meir, Phys. Rev. Lett. **83**, 3506 (1999).
2. V. A. Gergel’ and R. A. Suris, Zh. Éksp. Teor. Fiz. **84**, 719 (1983) [Sov. Phys. JETP **57**, 415 (1983)].
3. B. A. Aronzon, D. A. Bakaushin, A. S. Vedeneev, *et al.*, Fiz. Tekh. Poluprovodn. (St. Petersburg) **35**, 448 (2001) [Semiconductors **35**, 436 (2001)].
4. B. A. Aronzon, D. A. Bakaushin, A. S. Vedeneev, *et al.*, Pis’ma Zh. Éksp. Teor. Fiz. **66**, 633 (1997) [JETP Lett. **66**, 668 (1997)].
5. B. A. Aronzon, A. S. Vedeneev, and V. V. Ryl’kov, Fiz. Tekh. Poluprovodn. (St. Petersburg) **31**, 648 (1997) [Semiconductors **31**, 551 (1997)].
6. M. Buttiker, Phys. Rev. B **41**, 7906 (1990).
7. T. Ando, A. B. Fowler, and F. Stern, Rev. Mod. Phys. **54**, 437 (1982).
8. A. I. Yakimov, N. P. Stepina, and A. V. Dvurechenskii, Phys. Low-Dimens. Struct. **6**, 75 (1994).
9. A. Kamenev and W. Kohn, cond-mat/0103488 (2001).
10. N. F. Mott and E. A. Davis, *Electronic Processes in Non-Crystalline Materials* (Clarendon, Oxford, 1979; Mir, Moscow, 1982).
11. D. G. Polyakov and B. I. Shklovskii, Phys. Rev. Lett. **74**, 150 (1995).
12. A. V. Rzhanov, *Electronic Processes on Semiconductor Surface* (Nauka, Moscow, 1971).

Translated by S. Ktitorov

Semiconductors, Vol. 36, No. 10, 2002, pp. 1169–1179. Translated from Fizika i Tekhnika Poluprovodnikov, Vol. 36, No. 10, 2002, pp. 1248–1258.

AMORPHOUS, VITREOUS, AND POROUS SEMICONDUCTORS

Photoluminescence and Recombination Luminescence in Amorphous Molecular Semiconductors Doped with Organic Dyes

N. A. Davidenko*, S. L. Studzinskiĭ*, N. A. Derevyanko, A. A. Ishchenko**, Yu. A. Skryshevskiĭ*, and A. J. Al-Kahdymi***

** Shevchenko National University of Kiev, Vladimirskaya ul. 64, Kiev, 01033 Ukraine*
e-mail: daviden@ukrpack.net
*** Institute of Organic Chemistry, National Academy of Sciences of Ukraine, Kiev, 02094 Ukraine*
Submitted November 14, 2001; accepted for publication February 5, 2002

Abstract—Photoconductivity, photoluminescence (PL), and thermally stimulated luminescence of photoconductive poly-*N*-epoxypropylcarbazole and poly-*N*-vinylcarbazole films and non-photoconductive polyvinylbutyral, polyvinyl alcohol, polystyrene, and polyethylene films doped with cationic, anionic, and neutral dyes are studied. It is found that the PL of cationic dyes in photoconductive polymer films is enhanced in comparison to nonphotoconductive ones. The PL enhancement correlates with an increase in photoconductivity, with the quenching effect of an external electric field on the PL intensity, and with an increase in the intensity of the recombination luminescence. It is assumed that this enhancement is related to the presence of predimer traps for holes in the vicinity of dye ions in the films of carbazolyl-containing polymers. A model describing the trap formation upon the photoexcitation of holes into predimer states is suggested. © *2002 MAIK "Nauka/Interperiodica".*

1. INTRODUCTION

Amorphous molecular semiconductor (AMS) films based on poly-*N*-epoxypropylcarbazole (PEPC) and poly-*N*-vinylcarbazole (PVC) doped with polymethine organic dyes [1] possess photoconductive properties, which is of interest for their application as recording media in electrography and holography [2–4]. These media can also be used in electroluminescent devices, since, at room temperatures, the bimolecular recombination of free charge carriers in dye molecules occurs radiatively [5, 6]. The radiative nature of the charge recombination at room temperatures is also evidenced by results on thermally stimulated recombination luminescence obtained previously [7]. This enables one to suggest that the luminescent properties of cyanines embedded in AMS are related not only to radiative transitions of excited dye molecules to the ground state, but also to radiative recombination of the photogenerated electron–hole pairs (EHPs) as well. To develop media suitable for the recording and modulation of optical radiation, it is important to understand the impact of the photophysical properties of the polymer matrix on the intensity of the polymethine photoluminescence (PL) and the dependence of the PL intensity on the photon energy of the exciting radiation. Thus, the purpose of this work is to study the luminescent properties of AMS containing polymethine dyes of different ionicity.

2. EXPERIMENTAL

We investigated the photoconductivity, PL, and thermally stimulated luminescence (TSL) of polymer films doped with polymethine dyes of different ionicity and chemical structure.

Photoconductive polymers were represented by PEPC oligomers and PVC polymers [8], while nonphotoconductive ones were represented by polyvinylbutyral (PVB), polyvinyl alcohol (PVA), polystyrene (PS), and polyethylene (PE) [9]. The molecular weights of the polymers under study are as follows: PEPC, 900; PVC_1, $(6–7) \times 10^3$; PVC_2, $(1–2) \times 10^4$; PVC_3, 7×10^4; PVC_4, 3×10^5; PS, 2.3×10^5; PVB, $(0.7–1) \times 10^5$; PVA, $> 10^5$; and PE, 1.25×10^5 amu.

The diagrams in Fig. 1 show cationic (1–3), anionic (4, 5), cationic–anionic (6), and neutral (7) polymethine dyes and cationic xanthene dye Rhodamine 6G (8) [1], which were used as dopants.

Anionic cyanine 4 has the same chromophore as cationic dye 1, although the net charge of the colored ion is –1 in the former case and +1 in the latter. This is related to the fact that sulfo groups, responsible for the negative net charge, are attached to the atoms that are not involved in the conjugation chain. Cationic–anionic dye 6 is composed of a cation and an anion from polymethines 2 and 5, respectively. Neutral (merocyanine) dye 7 is a hybrid of the cationic and anionic polyme-

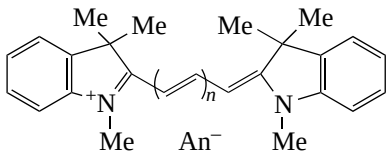

1: $n = 1$, $An^- = BF_4^-$; 1a: $n = 1$, $An^- = I^-$;
2: $n = 2$, $An^- = BF_4^-$; 3: $n = 3$, $An^- = BF_4^-$

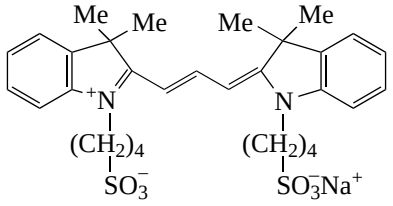

4

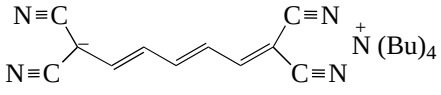

5

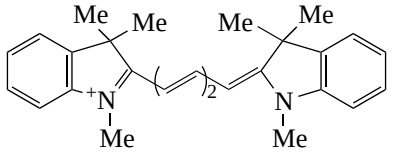

6

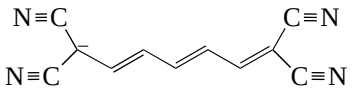

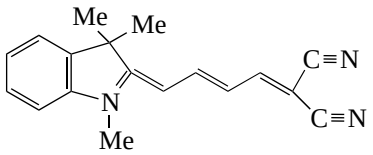

7

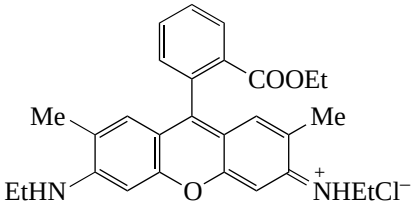

8

Fig. 1. Dyes used as dopants in amorphous molecular semiconductors.

thines 1 and 5, respectively. Thus, cyanines 1–7 belong to the same structural type of dyes but possess a different ionicity and chemical constitution; this makes them perfectly suited for studies of the photophysical properties of colored polymers.

The samples were prepared as free-surface structures [⟨glass substrate⟩–⟨amorphous polymer film⟩ or ⟨glass substrate⟩–⟨conductive SnO_2 layer⟩ ⟨amorphous polymer film⟩] and sandwich structures [⟨quartz substrate⟩SnO_2/AMS/Al]. The dye content in the films was 1 wt %. The colored films were obtained by drying the polymer/dye solution in methylene chloride deposited on glass substrates with or without a conductive layer. The films were dried in a furnace for 3 h at a temperature of +80°C. The film thickness, measured with an MII-4 interference microscope, was 1 μm. In sandwich structures, an aluminum electrode was deposited onto the polymer film by thermal evaporation in a vacuum chamber.

The absorption coefficient κ of the polymer films was measured for the samples without a conductive layer using a KSVIP-23 computerized spectrometer complex. In the PL measurements, the films were excited by visible light using glass optical filters. Both the angle of incidence of the excitation beam and the angle at which reemitted light is collected were 45° to the sample surface. In the samples with a conductive layer, we measured the PL intensity I_{PL} and its relative variation δI_{PL} under the influence of an electric field E; we used the relation $\delta I_{PL} = [I_{PL}(E) - I_{PL}(0)]/I_{PL}(0)$ (here, $I_{PL}(0)$ is the PL intensity without an electric field and $I_{PL}(E)$ is the PL intensity under an applied electric field of strength E). The following procedure was carried out. First, $I_{PL}(0)$ was determined for a chosen value of the wavelength λ_{irr} of the excitation light. Then, an electric field was applied to the polymer film, which remained continuously irradiated. The temporal variation of I_{PL} was recorded until some new quasi-steady intensity level $I_{PL}(E)$ was established. After switching off the electric field, the kinetics of the I_{PL} recovery to its initial level was recorded. The measurement runs

were repeated several times. Monochromator control, recording of the light intensity, and data processing were performed by a computer. For each λ_{irr}, the value of I_{PL} was determined as the average of five measurement results. κ and I_{PL} were measured in the wavelength range λ = 400–1000 nm, where the long-wave length dye absorption bands are present and the absorption in the polymers under study is absent. The measurements were carried out at T = 293 K.

For the free-surface samples, an electric field in the polymer film was induced by charging it in a corona produced using a special electronic unit, with a metal wire-shaped corona electrode placed above the sample surface at the side where the film is located. At the instant when the electric field between the wire electrode and the conductive SnO_2 layer is switched on, a high voltage (of several kilovolts) is applied, which leads to the ionization of the gas mixture with the formation of a corona discharge above the film. As a result, ions of a particular sign (e.g., positive ones) are uniformly deposited from the gas onto the free surface of the film. The strength of the electric field induced in the polymer film in the direction between the SnO_2 layer and the ions at the surface depends on the ion-charge density and is controlled by the voltage between the corona electrode and the SnO_2 layer. The electric-field strength in the film was $E = 1 \times 10^8$ V/m; it was determined from the potential of the free polymer-film surface with respect to the SnO_2 layer at the instant the voltage was switched off. This potential was measured by an electrostatic probe based on a V7-30 electrometer, with the probing electrode located above the free polymer-film surface and the second electrode connected to the conductive SnO_2 layer. The probe was calibrated before the measurements; the surface potential and the electric field were determined with an accuracy not worse than 5%. The electronic unit for charging polymer films in a corona and a measurement probe are described elsewhere [2]; they are used in devices for holography and electrography [2].

In the samples with a sandwich structure, the photocurrent was measured in the photoresistor mode using a storage oscilloscope. The samples were irradiated through the SnO_2 electrode by monochromatic light with a wavelength $\lambda > 400$ nm within the dye absorption region and outside the polymer matrix absorption region. The field strength in these experiments was varied from 2×10^7 to 2×10^8 V/m with the positive voltage on the aluminum electrode.

The TSL in free-surface samples was measured in the same way as described in [7]. The integrated luminescence intensity I_{TL} was measured with a photomultiplier, which operated in the photon counting mode and was placed in the immediate vicinity of the optical window of the cryostat. The temperature of the samples under study was varied linearly in the range T = 4.2–330 K at a rate of 0.1 K/s. To record the $I_{TL}(T)$ dependences, the sample in the cryostat was cooled to T_{irr} = 5 K and irradiated for 60 s by light with a wavelength λ_{irr} = 365 nm (in the absorption region of PVC and PEPC) or λ_{irr} = 400 nm (in the dye absorption region). After that, the sample was kept in the dark until the isothermal recombination luminescence decayed, and then linear warming-up was started. The duration of irradiation corresponds to the saturation of the I_{TL} dependence on the irradiation dose. A DRSh-500M mercury lamp with a set of optical filters was used as the light source.

3. RESULTS

Films of both photoconductive and nonphotoconductive polymers grown without the admixture of dyes 1–8 do not absorb visible light. The addition of 1 wt % of the dyes under study to these films leads to the appearance of strong absorption bands. The PL spectrum of a colored polymer film excited with light in the absorption band consists of a band whose shape is a mirror image of the shape of the absorption spectrum. Wavelengths λ^a_{max} and λ^L_{max} corresponding to the peaks in the absorption and luminescence spectra of colored PEPC and PS films are listed in the table. Replacement of the PEPC polymer matrix with PVC or PS ones does not have any significant effect on the position of absorption and PL bands (see Fig. 2), which results from a close coincidence of the refractive indices n_D of these polymers [8, 9]. The absorption spectrum of dye 6 has two bands, which correspond to the colored forms of anion 5 and cation 2, respectively. However, there is only a long-wavelength component in the PL spectrum, both under excitation into short- and long-wavelength absorption bands. This is an indication of the excitation energy transfer from the anion to the cation.

Spectral characteristics of PEPC and PS films doped with 1 wt % of different dyes

Dye	PEPC		PS	
	λ^a_{max}, nm	λ^L_{max}, nm	λ^a_{max}, nm	λ^L_{max}, nm
1	565	575	572	585
1a	565	575	572	585
2	667	678	675	687
3	755	762	760	775
4	665	672	673	687
5	557	585	560	592
6	563		565	
	673	693	680	700
7	535	592	540	603
8	543	557	552	566

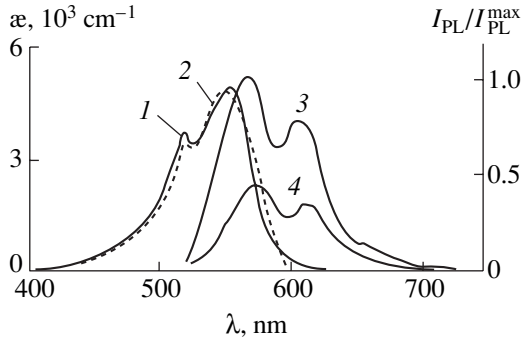

Fig. 2. Spectra of (*1*, *2*) optical absorption and (*3*, *4*) photoluminescence of polymer films containing 1 wt % of dye 1. Curves *1* and *3* correspond to PEPC and curves *2* and *4*, to PS. I_{PL}^{max} denotes the maximum PL intensity.

For cationic polymethine dyes 1, 1a, 2, and 3 and for xanthene dye 8, replacing the PS, PVB, PVA, or PE matrices with PEPC or PVC ones leads to an increase in the PL intensity under excitation in the short-wavelength wing of the absorption band. This is illustrated by Fig. 3, where, by the example of dye 1, the ratio of the PL quantum yield φ in colored photoconductive polymers to the quantum yield φ^{PS} in the PS matrix is plotted as a function of λ_{irr}. In photoconductive films (see curves *1–3*), the relative quantum yield increases with a decrease in λ_{irr}. The highest PL yield is achieved in the PEPC films. In this case, the intensity of the luminescence depends linearly on the photoexcitation intensity, while φ remains constant. In the chosen range of the excitation and emission wavelengths, PL is not observed in the polymer films without the admixture of dyes. The effect of the luminescence enhancement becomes less pronounced when the polymethine chain in the series of dyes 1–3 elongates (i.e., *n* increases) and when the PEPC matrix is replaced by the PVC one (see Fig. 4). This effect does not exist in polymer films doped with anionic dyes 4 and 5 or with neutral dye 7, but is observed in the cation band of the films containing cationic–anionic dye 6 under excitation both into the cation and the anion absorption bands. Thus, the anion PL itself is not enhanced in dye 5, but the anion is involved in the enhancement of the cation PL in cyanine 6 due to excitation energy transfer in the cation–anion pair. However, the intensity of the PL of cationic dyes in photoconductive polymer films depends on the nature of the anion An^-. For example, the PL intensity increases when the anion BF_4^- in compound 1 is replaced with the I^-.

The dependences of δI_{PL} on λ_{irr} for the samples with photoconductive polymer films are shown in Figs. 5 and 6. For a given film, the absolute value of δI_{PL} does not depend on the dye luminescence wavelength. This means that application of an external electric field does not change the spectral shape of the PL band, but leads to a decrease in the PL intensity. In PEPC and PVC films, electric-field quenching increases with a decrease in λ_{irr}. In the samples with PS, PVB, PVA, and PE films, no effect of the electric field on the dye PL was observed. The field also has no effect on the PL of polymer films with anionic dyes 4 and 5. Thus, it may be assumed that, similar to what was observed in [10], the quenching of the PL by an external electric field is

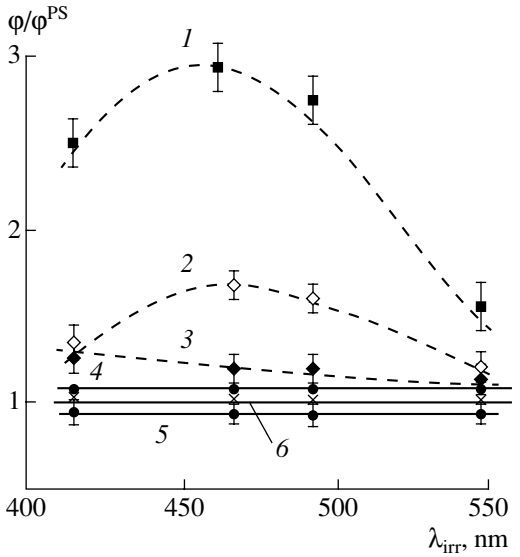

Fig. 3. Dependence of the relative quantum yield of photoluminescence in (*1*) PEPC, (*2*) PVC_1, (*3*) PVC_4, (*4*) PE, (*5*) PVB, and (*6*) PVA films containing 1 wt % of dye 1 on the excitation wavelength λ_{irr}. The luminescence was detected at λ = 575 nm.

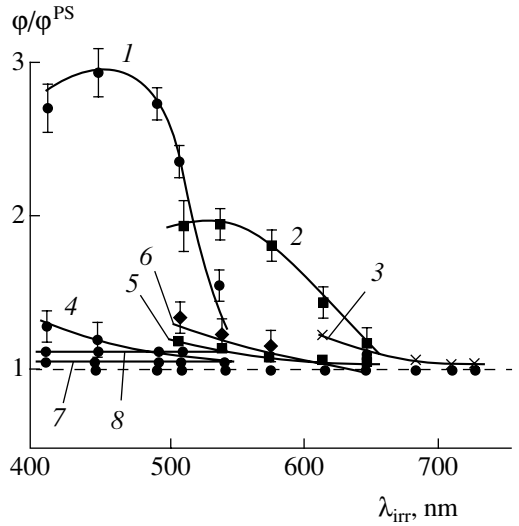

Fig. 4. Dependence of the relative quantum yield of photoluminescence in the films of (curves *1–3*, *6–8*) PEPC and (curves *4*, *5*) PVC_1 containing 1 wt % of dyes (*1*, *4*) 1, (*2*, *5*) 2, (*3*) 3, (*6*) 6, (*7*) 5, and (*8*) 7 on the excitation wavelength λ_{irr}. The luminescence was detected at the wavelength corresponding to the peak absorption of the dye.

related to the separation of the charge carriers in photogenerated EHPs accompanied by a decrease in the probability of their radiative recombination.

In the samples with a sandwich structure based on PS, PVB, PVA, and PE films doped with the dyes under study, photoconductivity was not observed. In similar samples based on PEPC and PVC with dyes 1–3 and 6–8, photoconductivity exists under excitation of the samples in the region of the dye absorption. The $j(E)$ dependence is linear in the coordinates $\log j = f(E^{1/2})$ and can be represented by an analytical expression often used to describe the photoconductivity in PEPC and PVC [2, 10]: $j \propto \exp[-(W_{0ph} - \beta E^{1/2})/kT_{eff}]$. Here, W_{0ph} is the photoconductivity activation energy; β is a constant, which is nearly equal to the Pool–Frenkel constant; $T_{eff}^{-1} = T^{-1} - T_0^{-1}$; and T_0 is the characteristic temperature, which usually amounts to (490 ∓ 15) K for PEPC. The experimentally determined value of $\beta = (4.2 \mp 0.1) \times 10^{-5}$ eV $(V/m)^{-1/2}$ agrees well with the known published data [2, 11]. In the sandwich structures with dye 3, the values of j are smaller by two orders of magnitude in comparison with the structures with dye 1 and by one order in comparison to the structures with dye 2. In the samples with dyes 4 and 5, no photoconductivity was observed.

The TSL curves recorded after irradiation at $T_{irr} = 5$ K of the samples with undoped PEPC films and PEPC films doped with dyes 1 and 7 are shown in Fig. 7. Curve *1* corresponds to the sample that was kept in the dark at room temperature for two days. In this case, there is a single TSL band peaked at about $T_{max\,1} = 150$ K. Curves *2–4* correspond to the samples that, prior to their cooling, were irradiated with light of wavelength λ_{irr} for 60 s at a temperature $T_{irr} = 290$ K. One can see that, after irradiation at room temperature of the PEPC film doped with dye 7, the corresponding TSL curve (curve *5*) does not differ considerably from curve *1*. For the PEPC film doped with dye 1, irradiation at room temperature results in the appearance of a high-temperature TSL arm in the range $T = 200$–300 K. However, if this sample is first irradiated at $T_{irr} = 290$ K, then, after switching the light off, it is rapidly (at a rate of 5–10 K/s) cooled to $T = 5$ K and, finally, irradiated to excite TSL, whereupon a new narrow band peaked at $T_{max\,2} \approx T_{irr}$ appears in the TSL curve. This band arises in the range 250 K $< T_{irr} <$ 320 K and varies with T_{irr}. The magnitude of the TSL peak at $T_{max\,2}$ increases with decreasing T_{irr} and attains a maximum value for $T_{irr} = 250$ K; the approximate equality $T_{max\,2} \approx T_{irr}$ is valid independent of the light wavelength and temperature at which TSL is excited.

Another feature of the PEPC samples with dye 1 is that the magnitude of the TSL peak in the temperature range 250–320 K appearing near T_{irr} depends on λ_{irr}. With a decrease in λ_{irr}, the TSL peak at $T_{max\,2}$ first increases and then starts to decrease. Similar effects

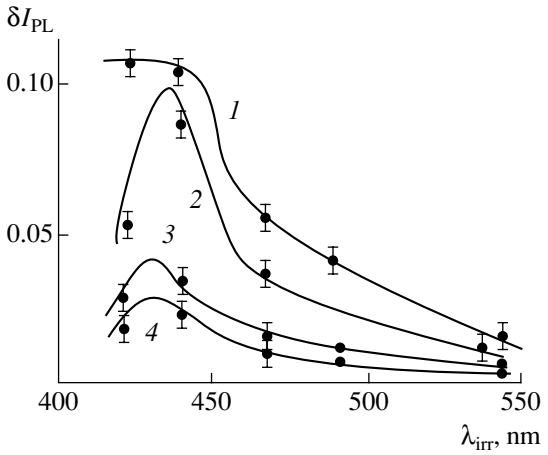

Fig. 5. Dependences of δI_{PL} on λ_{irr} in the films of (*1*) PEPC, (*2*) PVC_1, (*3*) PVC_2, and (*4*) PVC_4 containing 1 wt % of dye 1. The luminescence was detected at $\lambda = 575$ nm.

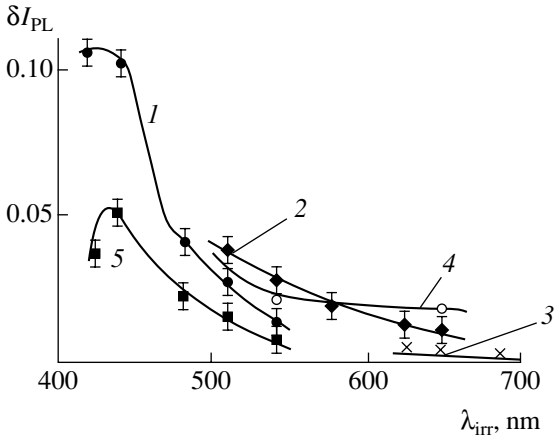

Fig. 6. Dependences of δI_{PL} on λ_{irr} in PEPC films containing 1 wt % of dyes (*1*) 1, (*2*) 2, (*3*) 3, (*4*) 6, and (*5*) 7.

were observed in the TSL of the polymer films based on PEPC and PVC doped with dyes 1a, 2, 3, 6, and 8. However, upon replacement of PEPC with PVC, the TSL at $T_{max\,2}$ decreases in intensity and vanishes for the samples based on PVC_4. In AMS films with dyes 4 and 5 irradiated with visible light, the TSL intensity both around $T_{max\,1}$ and $T_{max\,2}$ is lower by many orders of magnitude and is close to the noise level of the photomultiplier; thus, we failed to reveal any features of the TSL in this case.

Commonly, the TSL in photoconductive polymers is attributed to the radiative recombination of the charge carriers upon annihilation of photogenerated EHPs. It is assumed that photogenerated charge carriers are captured by traps and are released as the temperature is raised. The activation energy W_{TL} for the thermal escape of charge carriers from traps in the PEPC-based AMS samples was determined in the entire temperature range under study using the method of fractional-heat-

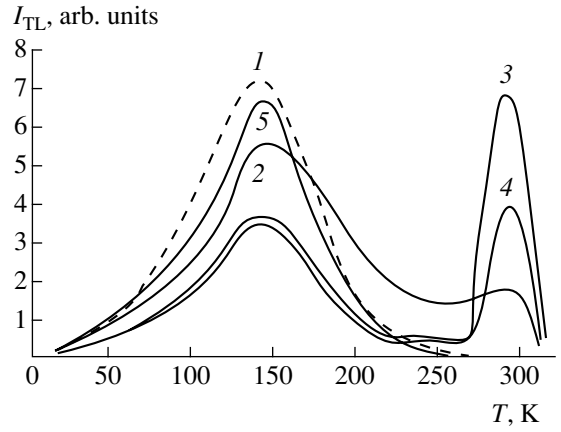

Fig. 7. Temperature dependences of I_{TL} in the sample with a PEPC film containing 1 wt % of dye 1: (*1*) upon irradiation with light of wavelength λ_{irr} = 365 nm at T_{irr} = 5 K; (*2*) upon irradiation with light of wavelength λ_{irr} = 600 nm at T_{irr} = 290 K and subsequent TSL excitation with light of the same wavelength, but at T = 5 K; (*3*) upon irradiation with light of wavelength λ_{irr} = 546 nm at T_{irr} = 290 K and subsequent TSL excitation with light of the same wavelength, but at T = 5 K; (*4*) upon irradiation with light of wavelength λ_{irr} = 436 nm at T_{irr} = 290 K and subsequent TSL excitation with light of the same wavelength, but at T = 5 K. Curve *7* represents the temperature dependence of I_{TL} in the sample with a PEPC film containing 1 wt % of dye 7 upon irradiation with light of wavelength λ_{irr} = 546 nm at T_{irr} = 290 K and subsequent TSL excitation with light of the same wavelength, but at T = 5 K.

ing TSL measurements. It was established that, independent of high-temperature pre-irradiation, the W_{TL} varies linearly as a function of T and this dependence remains unchanged around T_{irr}. Near T_{irr} = 250 K, $W_{TL} = (0.82 \mp 0.01)$ eV; this value is close to the activation energy for β-relaxation in PEPC, which was determined previously by another method [12].

4. DISCUSSION

Let us summarize the experimental results.

(i) Photoconductivity in the visible spectral range is exhibited by the films of PEPC and PVC doped with dyes 1–3 and 6–8. An increase in the length of the polymethine chain in the series of dyes 1–3 leads to a reduction of the photoconductivity effect. Photoconductivity is not observed in the films doped with anionic dyes 4 and 5. Photoconductivity is not detected in the polymer films of PS, PVB, PVA, and PE doped with the dyes under study.

(ii) Cationic dyes exhibit more intense PL when they are embedded in PEPC films in comparison to PVC and PS, PVB, PVA, or PE films; the effect of the PL enhancement increases with a decrease in λ_{irr} (for dyes 1 and 1a, the magnitude of this effect attains a maximum and then decreases). The PL enhancement becomes less pronounced with an increase in the length of the polymethine dye chain.

(iii) For anionic dyes 4 and 5 and for neutral merocyanine 7, enhancement of the PL in the PEPC polymer matrix in comparison with the PVC and PS, PVB, PVA, or PE matrices is not observed.

(iv) For cationic dyes 1–3 and 8 embedded in photoconductive polymers, luminescence originating from the recombination of the charge carriers captured after their photogeneration by traps and subsequently released due to thermal escape is observed even at room temperature along with isothermal recombination luminescence. The intensity of the recombination luminescence of this type increases with an increase in λ_{irr} (for dyes 1 and 1a, the intensity first increases, reaches a maximum, and then decreases) and is reduced as the length of the dye polymethine chain increases or if the PEPC matrix is replaced by a PVC one.

(v) The room-temperature recombination luminescence decreases in intensity as cationic dyes 1–3 and 8 are replaced by neutral dye 7 and vanishes in the case of anionic cyanines 4 and 5. It is also absent if photoconductive PEPC or PVC matrices are replaced with PS, PVB, PVA, or PE ones.

We believe that, in the polymer films under study, the dye luminescence includes conventional fluorescence and recombination luminescence originating from photogenerated EHPs. This inference is corroborated by a comparison of the dependences of φ and δI_{PL} on λ_{irr} (Figs. 3, 5) for photoconductive and nonphotoconductive polymers. One may assume that there is a correlation between the effects of the PL enhancement, photoconductivity, and an increase in the PL quenching by an electric field. When PS, PVB, PVA, or PE polymer matrices are replaced with PVC or PEPC ones, the photogeneration of EHPs from excited states of dye molecules becomes possible. For all of the dyes under consideration, there are two electrons in the highest occupied molecular orbital (HOMO). These electrons become unpaired upon excitation, since one of them is transferred to the lowest unoccupied molecular orbital (LUMO). The presence of unpaired electrons leads to a sharp increase in the reactivity of a dye ion in the S_1 state. Thus, an excited dye molecule can capture one of the photogenerated electrons from PEPC or PVC molecules with the formation of an EHP. Taking into account electrostatic forces acting between an ion and a free electron, one can expect that the electron capture probability will decrease sharply upon the replacement of a cationic dye with a neutral dye and, still further, with an anionic dye. Another reason for the decrease in probability is that electron capture by the dyes from the above sequence requires the formation of a neutral radical, an anion radical, and a dianion radical, respectively, which is related to a corresponding increase in the energy needed for the charge separation. As a result, anionic dyes cannot accept valence electrons from PEPC or PVC, and there is no photoconductivity and

no PL enhancement in the films with these dyes. The ability of the neutral merocyanine 7 to capture an electron is higher, which leads to the existence of photoconductivity. However, this is still insufficient for PL enhancement. For cationic dyes, the process of EHP photogeneration is most effective and, consequently, in PEPC and PVC films doped with these dyes, both photoconductivity and PL enhancement take place.

Annihilation of EHPs in PEPC and PVC occurs via recombination of the charge carriers due to a transition of the valence electron from the dye radical (a neutral radical in the case of cationic dyes, and an anion radical in the case of merocyanines) to the cation radical of the carbazolyl ring. As a result, an excited state of compound 1–3 or 6–8 is formed once again, its subsequent decay being radiative. Thus, in PEPC and PVC films (in contrast to PS, PVB, PVA, and PE ones), the emission from excited states formed due to recombination of the charges from photogenerated EHPs contributes to the dye PL. Upon the application of an electric field, EHPs dissociate and the charge carriers move from recombination centers to the collecting electric contacts, which leads to a reduction in the luminescence intensity (see Figs. 5, 6). It is known [2, 13] that the ability of dyes to form EHPs under photogeneration in carbazolyl-containing polymers is governed by the relation between the energies of the valence orbitals of the dye and the carbazolyl ring. The validity of this rule can be verified using the dyes under study as an example. For instance, upon increasing the polymethine chain length in the series of dyes 1–3, the HOMO and LUMO come closer to one another [1] and the energy difference between the dye and the HOMO of the carbazolyl ring decreases and may even become negative. Thus, replacing compound 1 with compounds 2 and 3 leads to a reduction in the photoconductivity of PEPC and PVC films.

The suggested model can be analyzed numerically. It is common [1, 14] that, in organic dye molecules, the first excited triplet state has a lower energy than the first excited singlet state, with the allowed transitions between S_1 and S_0 states being radiative and those between T_1 and S_0 states being nonradiative. The diagram in Fig. 8 illustrates the relation between the processes of conversion and the effect of an electric field on the PL. Here, P is the efficiency of photoexcitation of molecules from the singlet ground state S_0 to the unrelaxed first excited singlet state S_1^u of the dye; N_1 and N_3 are the densities of the dye molecules in relaxed singlet (S_1^0) and triplet (T_1) first excited states, respectively; n_1 and n_3 are the densities of EHPs in the singlet (S) and three triplet (T_0, T_-, T_+) states, respectively [15]; k_U is the rate constant of internal conversion S_1^u–S_0; k_{SU} and k_S are the rate constants of nonradiative and radiative transitions S_1^0–S_0, respectively; k_T is the rate constant of the transition T_1–S_0; k_2 and k_{-2} are the rate constants of intramolecular intersystem crossing S_1–T_1 and T_1–S_1; k_1 and k_{-1} are the rate constants of the formation and recombination of singlet EHPs; k_3 and k_{-3} are the rate constants of the formation and recombination of triplet EHPs; k_{ST} is the rate constant of the EHP spin conversion, which was estimated to be around 10^8 s^{-1} in doped PEPC films [2]; and k_η is the rate constant of the EHP dissociation into a free electron (e^-) and a free hole (p^+), which amounts to 10^6 s^{-1} for $E = 1 \times 10^8$ V/m (this estimate was obtained from the measurements of the photocurrent rise time in doped PEPC films upon their irradiation with light in the dopant absorption region [2]). Note that, usually, a linear dependence of the photocurrent on the excitation light intensity is observed in photoconductivity studies of thin PEPC films with low dopant concentrations (up to 1%). This means that the bulk recombination of free electrons and holes can be neglected in this model, which is thus described by the following set of kinetic equations:

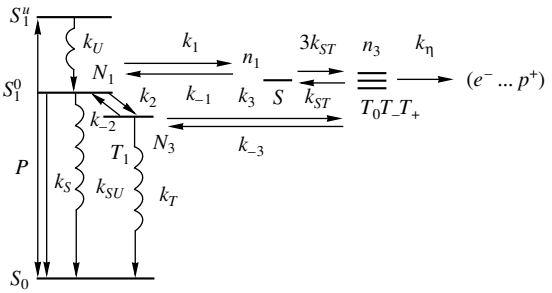

Fig. 8. Diagram representing the processes taken into account in the model calculation. See text for details.

$$dN_1/dt = P + k_{-2}N_3 + k_{-1}n_1 - (k_S + k_{SU} + k_2 + k_1)N_1, \quad (1)$$

$$dN_3/dt = k_2N_1 + k_{-3}n_3 - (k_T + k_{-2} + k_3)N_3, \quad (2)$$

$$dn_1/dt = k_1N_1 + k_{ST}n_3 - (k_\eta + k_{-1} + 3k_{ST})n_1, \quad (3)$$

$$dn_3/dt = k_3N_3 + 3k_{ST}n_1 - (k_\eta + k_{-3} + k_{ST})n_3. \quad (4)$$

If $k_2 \gg k_{-2}$, $k_3 \gg k_{-3}$, and $k_1 = k_3$ and, in addition, $dN_1/dt = dN_3/dt = dn_1/dt = dn_3/dt = 0$, we readily find from (1)–(4) that

$$I_{PL}(E) \propto k_SN_1 = Pk_S/\left\{k_S + k_2 + k_1 + k_{SU} - k_1k_{-1}\frac{k_\eta + k_{ST}[1 + k_2/(k_T + k_1)]}{k_\eta^2 + 4k_\eta k_{ST} + k_1(k_\eta + k_{ST})}\right\}. \quad (5)$$

For the case $E = 0$, let us determine the ratio of the PL intensity I_{PL} in the presence of EHP photogenera-

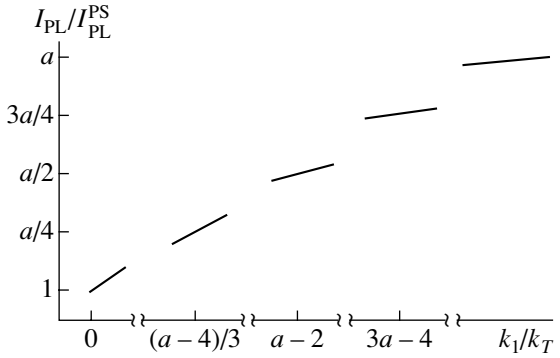

Fig. 9. Dependence of I_{PL}/I_{PL}^{PS} on k_1/k_T calculated by formula (6).

tion to the PL intensity I_{PL}^{PS} in the case where EHP photogeneration is absent and $k_1 = k_3 = 0$:

$$I_{PL}/I_{PL}^{PS} = a[1 + k_2/(k_S + k_{SU})], \quad (6)$$

where $a = 1 + k_2/(1 + k_1/k_T)$. It follows from (6) that PL enhancement should be observed if the ratio k_1/k_T increases. This can be clearly seen from Fig. 9, where the dependence of I_{PL}/I_{PL}^{PS} on k_1/k_T is plotted. Thus, the analysis of the kinetic model indicates that the observed effect of PL enhancement upon the replacement of nonphotoconductive polymer matrices with photoconductive ones is mainly related to the ability of dyes to take part in the EHP photogeneration process.

A difference between the PEPC and PVC matrices is that, in the former case, the strongest PL enhancement in cationic dyes is observed and the high-temperature recombination luminescence of the charge carriers formed due to photogeneration in these dyes is present, with both effects increasing in magnitude in a similar way as λ_{irr} decreases. We believe that these features are related to the molecular mobility of carbazolyl rings in PEPC and to the presence of predimer electron states (traps) capable of capturing photogenerated holes. After their thermal escape from the traps, these holes recombine radiatively in the course of the annihilation of the EHP. In what follows, we give our notion on the nature of the traps.

4.1. Trap Formation

AMS films based on PEPC and PVC are characterized by a broad energy spectrum of localized states of nonequilibrium holes. A TSL peak near T = 150 K (Fig. 7) is observed both in doped and nominally undoped films. At the same time, a new narrow TSL peak around $T = T_{irr}$ exists in low-molecular PEPC films and disappears with an increase in the polymer molecular weight in the series PVC_1, PVC_2, PVC_3, and PVC_4. Since neighboring carbazolyl rings belonging to the same polymer chain are arranged coplanarly and oriented by 180° with respect to the chain [8, 11], one should expect that neighboring carbazolyl rings belonging to different chains (segments) are involved in the formation of new traps for holes. In PEPC, carbazolyl rings are located at a larger distance from the chain, the chain is shorter, and the segment mobility is higher [8]. This explains why PEPC represents a matrix where predimer states, whose limiting form is a "sandwich" of carbazolyl rings, appear more readily.

Not only are the nature of the polymer and the colored cation of the dye important for the formation of traps, but so too is the nature of the dye anion. This is demonstrated by the dependence of the PL enhancement effect on the nature of An^- observed in this study (e.g., for dyes 1 and 1a). These traps appear in the course of the photogeneration of charge carriers and can exist only if they are being occupied. These traps are formed as a result of the rotation of PEPC carbazolyl rings, which compose a predimer state near An^- in the situation where a hole from a photogeneration center appears at these rings. The formation of such a trap, the capture of a charge carrier by the trap, the destruction of the trap, and the release of the charge carrier occur at the same temperature; the activation energy of these processes is close to the activation energy of β-relaxation in PEPC. Photogenerated holes may be transferred to the predimer states located near An^-, which, under the influence of the anion electrostatic field, may favor the transformation of predimer states into dimer ones as a result of the rotation of carbazolyl rings (β-relaxation). Thus, an occupied dimer trap for holes appears, with the energy necessary for its formation from a predimer state at a given temperature being supplied due to the polarization of the surrounding medium by the hole and the electrostatic interaction of this hole with An^-. In the course of recombination or dissociation, the hole leaves the trap, after which dimer destruction occurs via the rotation of the carbazolyl rings due to β-relaxation, and a predimer state (left unoccupied) appears again.

It is important to note that, although the energy spectrum of possible predimer states may be sufficiently broad due to the existence of a large ensemble of possible configurations of carbazolyl rings in amorphous PEPC films, only some of them are formed and remain stable at a given temperature: it is necessary that the thermal vibrational energy after the establishment of thermal equilibrium is insufficient to destroy such a state, while all states of a lower energy are thermally destroyed. This means that the distribution of predimer states over the energies W of traps created upon preirradiation corresponds to the Boltzmann law. Then, the distribution of the formed traps can be expressed as

$$F(W) = 1 - \exp(-W/k_B T_{irr}), \quad (7)$$

and the probability density is given by

$$f(W) = dF(W)/dW = \exp(-W/k_BT_{irr})/k_BT_{irr}. \quad (8)$$

In the course of the formation of predimer states, thermal equilibrium is not immediately established after the absorption of a photon with the energy $h\nu$: if $h\nu$ exceeds the energy of the 0–0 transition $h\nu_{0-0}$, then the thermal energy $U = h\nu - h\nu_{0-0}$ will flow out of the photogeneration center. This thermal-energy flow may facilitate the formation of predimer states with energies $W > W(k_BT_{irr})$, resulting in an increased density Q of formed traps even after the establishment of thermal equilibrium. At the same time, if U exceeds the maximum allowed energy W_m of the spectrum of traps, then, upon the formation of a trap, the thermally induced escape of a hole from the trap may occur, the activation energy of the escape process being W_{TL}. Finally, if $U > W_m + W_{TL}$, the charge carrier will escape from the predimer state immediately after being captured there, and the trap becomes empty and is destroyed. It should be noted that this mechanism of trap formation is unlikely to be of importance at low temperatures, since, in addition to thermal vibrations of separate carbazolyl rings, it requires involvement of the vibrations of entire segments.

Thus, the following formula can be used to express the dependence of the density Q of predimer states formed due to pre-irradiation on T_{irr} and λ_{irr}:

$$Q = Q_0\left\{\int_0^{U-\mathrm{sgn}(\mathrm{E}[U/W_m])(U-W_m)} f(W)dW - \int_0^{(U-W_{TL})\mathrm{E}[U/W_{TL}]} f(W)dW\right\}, \quad (9)$$

where Q_0 is the density of all possible predimer states and $\mathrm{E}[U/W_m]$ and $\mathrm{E}[U/W_{TL}]$ are the integer parts of the corresponding energy ratios. Taking this into account, we arrive at the conclusion that Q increases with increasing $h\nu$; however, when U exceeds the sum of the energies needed for charge escape from the trap and for trap destruction, a further increase in $h\nu$ will lead to a reduction in Q. It is such behavior that is observed for PEPC films doped with dye 1: with decreasing λ_{irr}, the TSL intensity first increases and then decreases.

4.2. Filling and Emptying of the Traps

To analyze the processes in which the charge carriers fill the formed predimer states and escape from them, we consider a set of kinetic equations that is similar to (1)–(4) but has one more equation added:

$$dN_1/dt = P + k_{-2}N_3 + k_{-1}n_1 - (k_S + k_{SU} + k_2 + k_1)N_1, \quad (10)$$

$$dN_3/dt = k_2N_1 + k_{-3}n_3 - (k_T + k_{-2} + k_3)N_3, \quad (11)$$

$$dn_1/dt = k_1N_1 + k_{ST}n_3 - (k_\eta + k_{-1} + 3k_{ST})n_1 - k_q(1 - q/Q)n_1 + k_{-q}q/4, \quad (12)$$

$$dn_3/dt = k_3N_3 + 3k_{ST}n_1 - (k_\eta + k_{-3} + k_{ST})n_3 - k_q(1 - q/Q)n_3 + 3k_{-q}q/4, \quad (13)$$

$$dq/dt = k_q(1 - q/Q)(n_1 + n_3) - k_{-q}q, \quad (14)$$

where q is the density of occupied predimer states at time t, k_q is the rate constant for the formation of occupied traps, and k_{-q} is the rate constant for charge release from traps. Here, we have taken into account that $k_{ST} \gg k_{-q}$ and EHPs composed of charge carriers captured by traps are uniformly distributed over four possible spin states prior to charge release [15].

When all of the traps are occupied, $q = Q$ and the set of Eqs. (10)–(14) becomes similar to (1)–(4). However, the traps affect transient luminescence and photoconductivity processes, especially those taking place for different temperatures and λ_{irr}. The latter statement is based on the following fact: when assuming the activation mechanism of filling, destruction, and charge escape from traps, we need to take into account that not only Q depends on T and λ_{irr}, but the rate constants k_q and k_{-q} do as well. For purposes of illustration, let us carry out a numerical calculation of the dependences of I_{TL} on t, T, and λ_{irr} for PEPC films with dye 1.

Considering the situation where traps are filled at low temperatures, in which case $k_{-q} \ll k_q$, k_{ST}, k_S, k_{SU}, k_2, k_{-2}, k_3, k_{-3}, k_1, if $dN_1/dt = dN_3/dt = dn_1/dt = dn_3/dt = dq/dt = 0$, we find from Eqs. (10)–(14) that, after the irradiation is switched on, the density of the charge carriers on traps varies with time as

$$q = Q[1 - \exp(-k_qt)], \quad (15)$$

and after all traps are filled and the light is switched off

$$q = Q\exp[-k_{q0}\exp(-W_{TL}/k_BT)t]. \quad (16)$$

Here, the parameter k_{-q0} was chosen on the basis of experimental conditions taking into account that, for the warm-up rate $dT/dt = 0.1$ K/s, the entire TSL curve falls within the range $T_{irr} = (250 \mp 7)$ K (Fig. 7). k_q was also regarded as a model parameter; it was determined taking into account that the results of the TSL measurements described above do not depend on the dose of irradiation at $T_{irr} = 5$ K for exposure times $t > 60$ s.

To calculate the dependences of I_{TL} on t and T, we used the relation

$$I_{TL} \propto dN_1/dt \propto dq(t)/dt. \quad (17)$$

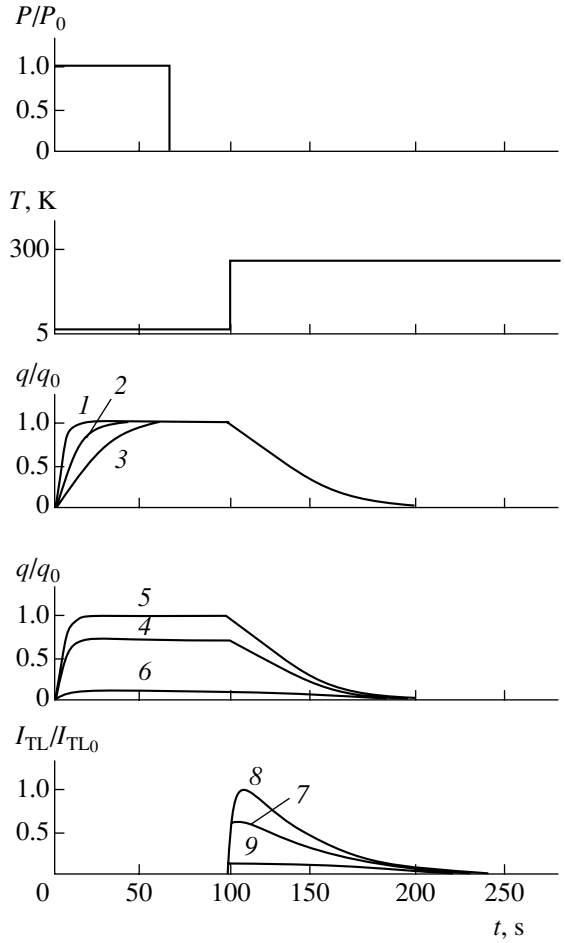

Fig. 10. Dependences of q on t and T calculated for P = (*1*) P_0, (*2*) $P_0/2$, and (*3*) $P_0/4$; dependences of q on t and T calculated for $P = P_0$ and λ_{irr} = (*4*) 600 nm, (*5*) 546 nm, and (*6*) 436 nm; dependences of I_{TL} on t and T calculated for $P = P_0$ and λ_{irr} = (*7*) 600 nm, (*8*) 546 nm, and (*9*) 436 nm. q_0 and I_{TL0} denote, respectively, the values of q and I_{TL} for $P = P_0$ and λ_{irr} = 546 nm.

The quantity $U = h\nu - h\nu_{0-0}$ was determined as the difference between the photon energy $h\nu$ of the light irradiating the sample and the energy $h\nu_{0-0}$ of an 0–0 transition in the dye, the latter being calculated from the spectral position of the intersection point of the curves κ/κ_{max} and $I_{PL}/I_{PL\,max}$ (Fig. 2). The value of Q was estimated from formula (9) assuming that T_{irr} = 250 K, W_{TL} = 0.82 eV, and W_m = 0.21 eV. The value of W_m was chosen taking into account that a maximum TSL effect around T_{irr} is observed for λ_{irr} = 546 nm, and, thus, it may be assumed that this corresponds to $U = W_m$.

Figure 10 shows the calculated dependences of q on P (curves *1–3*) and λ_{irr} (curves *4–6)* and of I_{TL} on t and T (curves *7–9*). One can see that an increase in the irradiation dose leads to a decrease in the trap filling time and the steady-state density of charges captured by traps is determined by the preirradiation wavelength. A narrow TSL peak occurs near T_{irr} = 250 K, and the variation in the magnitude of this peak with λ_{irr} correlates with similar dependences in Fig. 7.

5. CONCLUSION

In this study, we established that the replacement of nonphotoconductive polymers PS, PVB, PVA, and PE with photoconductive ones PVC or PEPC leads to an increase in the intensity and relative quantum yield of the PL of cationic dyes 1–3 and 8 and cationic–anionic dye 6 (in the cation band) embedded into these polymers. This effect is not observed for anionic dyes 4 and 5 and neutral dye 7. With a decrease in the excitation wavelength, the PL is enhanced, and so is the quenching effect of an external electric field on the PL in PVC and PEPC films. The electric field has no effect on the PL in PS, PVB, PVA, and PE films doped with any of the dyes under study and in PEPC and PVC films doped with anionic dyes 4 and 5. The intensity of room-temperature recombination luminescence in PEPC and PVC is reduced as cationic dyes 1–3 and 8 are substituted for neutral dye 7 and vanishes in the case of anionic cyanines 4 and 5; it also vanishes as photoconductive polymers are replaced with nonphotoconductive ones. An increase in the polymethine chain length in the series of dyes 1–3 leads to a reduction in the photoconductivity effect, which is related to a decrease in the energy difference between HOMOs in the hole photogeneration centers (i.e., in dye molecules) and in carbazolyl rings. If cationic dyes are replaced with anionic dyes 4 and 5, the photoconductivity in the dye absorption region disappears due to the existence of a high potential barrier for the transition of a hole from an excited anionic dye molecule to carbazolyl rings. The enhancement of the PL of cationic dyes becomes weaker as the polymer matrix is changed in the sequence PEPC, PVC_1, PVC_2, PVC_3, and PVC_4; this is related to an increase in the molecular weight of the polymer. The enhancement of the PL of cationic dyes in photoconductive polymers originates from the contribution of charge-carrier recombination luminescence that takes place upon the annihilation of EHP. This effect is more pronounced in PEPC in comparison to PVC, because predimer states are formed more readily in the former case owing to the higher mobility of the chromophore groups. Such states, located in the vicinity of dye anions, represent effective traps for nonequilibrium holes. The recombination of holes released from these traps occurs radiatively. A model describing trap formation and destruction, as well as trap filling with nonequilibrium charge carriers and charge release from traps, was suggested.

REFERENCES

1. A. A. Ishchenko, *Structure and Spectral-Luminescent Properties of Polymethine Dyes* (Naukova Dumka, Kiev, 1994).

2. N. G. Kuvshinskiĭ, N. A. Davidenko, and V. M. Komko, *Physics of Amorphous Molecular Semiconductors* (Lybin', Kiev, 1994).
3. K. Y. Law, Chem. Rev. **93** (1), 449 (1993).
4. P. M. Borsenberger and D. S. Weiss, *Organic Photoreceptors for Imaging Systems* (Marcel Dekker, New York, 1993).
5. N. A. Davidenko and A. A. Ishchenko, Fiz. Tverd. Tela (St. Petersburg) **40** (4), 629 (1998) [Phys. Solid State **40**, 576 (1998)].
6. N. A. Davidenko and A. A. Ishchenko, Dokl. Akad. Nauk Ukr., No. 9, 84 (1998).
7. N. A. Davidenko, A. A. Ishchenko, and A. K. Kadashchuk, Fiz. Tverd. Tela (St. Petersburg) **41** (2), 203 (1999) [Phys. Solid State **41**, 179 (1999)].
8. V. D. Filimonov and E. E. Sirotkina, *Chemistry of Monomers Based on Carbazole* (Nauka, Novosibirsk, 1995).
9. Yu. S. Lipatov, A. E. Nesterov, T. M. Gritsenko, and R. A. Veselovskiĭ, *Handbook on Chemistry of Polymers* (Naukova Dumka, Kiev, 1971).
10. N. A. Davidenko and A. A. Ishchenko, Chem. Phys. **247**, 237 (1999).
11. M. Pope and C. E. Swenberg, *Electronic Processes in Organic Crystals* (Clarendon, Oxford, 1982).
12. J. M. Pochan, D. F. Hinman, and R. Nash, J. Appl. Phys. **46** (10), 4115 (1975).
13. N. A. Davidenko and N. G. Kuvshinsky, J. Inf. Rec. Mater. **21**, 185 (1993).
14. S. P. McGlynn, T. Azumi, and M. Kinoshita, *Molecular Spectroscopy of the Triplet State* (Prentice-Hall, Englewood Cliffs, 1969; Mir, Moscow, 1972).
15. K. M. Salikhov, Yu. N. Molin, R. Z. Sagdeev, and A. L. Buchachenko, *Spin Polarization and Magnetic Effects in Radical Reactions* (Nauka, Novosibirsk, 1978; Elsevier, Amsterdam, 1984).

Translated by M. Skorikov

Semiconductors, Vol. 36, No. 10, 2002, pp. 1180–1183. Translated from Fizika i Tekhnika Poluprovodnikov, Vol. 36, No. 10, 2002, pp. 1259–1262.

AMORPHOUS, VITREOUS, AND POROUS SEMICONDUCTORS

Crystallization of Amorphous Hydrogenated Silicon Films Deposited under Various Conditions

O. A. Golikova†, E. V. Bogdanova, and U. S. Babakhodzhaev

Ioffe Physicotechnical Institute, Russian Academy of Sciences, Politekhnicheskaya ul. 26, St. Petersburg, 194021 Russia

Submitted February 27, 2002; accepted for publication February 28, 2002

Abstract—The possibility of using the magnetron-assisted silane decomposition technique for the deposition of *a*-Si:H films as the basic materials for the production of polysilicon is analyzed. It is shown how specific features of the film structure affect the crystallization process. *© 2002 MAIK "Nauka/Interperiodica".*

1. INTRODUCTION

The current interest in polycrystalline silicon (polysilicon) is due to its possible application in thin-film field-effect transistors, solar cells, and integrated circuits. It has been shown that polysilicon of device quality can be obtained though the crystallization of amorphous hydrogenated silicon (*a*-Si:H); the previously used technique for the thermal decomposition of silane and film deposition at the substrate temperature T_s = 625°C is unsuitable for this purpose [1].

Various methods for the crystallization of *a*-Si:H films are known: prolonged annealing in vacuum at a temperature of about 600°C, fast thermal treatment (with a series of fast heatings) [2], laser annealing [3], and, finally, the implantation of Si^+ ions with an energy of several tens of kV, which was recently demonstrated [4].

We must expect, however, that the properties of *a*-Si:H crystallized with a given technique will depend on the structure of the initial film, which depends, in turn, on the conditions of its deposition. In the present study, we consider the effect of structural characteristics, such as the hydrogen content in a film and the presence of various nanoinclusions in its amorphous matrix.

2. EXPERIMENT AND DISCUSSION

In the context of the above-listed problems, we analyze the potentialities of magnetron-assisted silane decomposition (MASD) technology using a 25%SiH_4 + 75%Ar mixture [4].

As is known, *a*-Si:H crystallization under an external influence is to a large extent defined by the hydrogen content in a film (C_H). First, the crystallization becomes slower as C_H rises [5]. Second, an intensive effusion of hydrogen during the crystallization results in mechanical damage in the film and, in extreme cases, even its destruction [6]. From this point of view, MASD seems highly promising, because it is one of the technologies that provides the lowest hydrogen content in a film for a given T_s.

Indeed, as seen by comparing C_H in films produced by MASD [4] and plasma-enhanced chemical vapor decomposition (PECVD) in a triode reactor with a glow-discharge plasma at an RF of 13.56 MHz [7], the C_H values are 2 and 3 at. % at T_s = 380–400°C, respectively. By contrast, in the films produced at the same T_s using HF (70 MHz) PECVD, remote-plasma, and hot-wire methods, C_H = 7, 10, and 4 at. %, respectively, [7].

Later, we shall discuss and compare the dependences of C_H on T_s for MASD and PECVD *a*-Si:H films with different structures. First, however, we will examine the methods used to control the film structure at T_s = const.

For a fixed anode voltage, magnetic field intensity, composition and feed rate of the gas mixture, the structure of MASD-films at T_s = const is controlled by varying the pressure of the gas mixture and by introducing an additional grid electrode. As a result, the obtained MASD films can be separated into three structural groups: standard *a*-Si:H homogeneous films, inhomogeneous nanostructured *a*-Si:H films containing $(SiH_2)_n$ polymer chains in an amorphous matrix, and inhomogeneous nanostructured *a*-Si:H films containing silicon nanocrystals in an amorphous matrix [4].

Groups of *a*-Si:H films with a similar structure can also be obtained by PECVD. The conditions of standard *a*-Si:H deposition using undiluted SiH_4 are well known (see, e.g., [5]). Nanostructured films were obtained in special conditions: films with $(SiH_2)_n$ chains, from silane strongly diluted with He (no more than 1% SiH_4 in He) [8]; and films with Si nanocrystals, at a much higher discharge power and SiH_4 pressure as compared with those in standard *a*-Si:H deposition [9].

† Deceased.

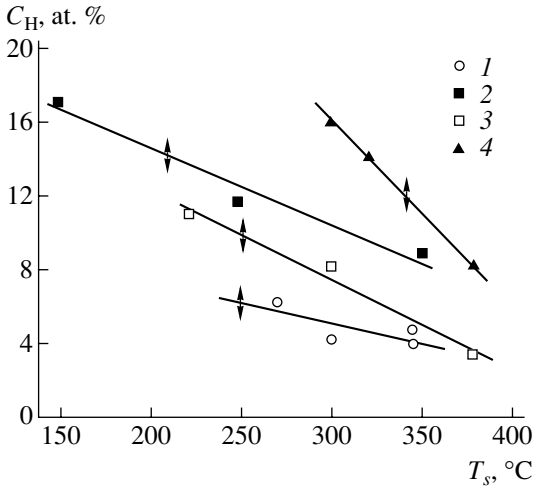

Fig. 1. Hydrogen content in standard *a*-Si:H films as a function of the deposition temperature: (*1*) MASD films and (*2–4*) PECVD films: (*2*) deposited from SiH_4 in a diode and (*3*) in a triode reactor; (*4*) deposited from a 25% SiH_4 + 75% He mixture in a triode reactor.

Figure 1 shows C_H vs. T_s dependences for standard *a*-Si:H produced by MASD and PECVD (in both diode and triode reactors). As seen, the MASD films (curve *1*) deposited with a gas pressure P = 7 mTorr and with a floating-potential grid in the magnetron chamber (the distance between the grid and the cathode d = 40 mm) demonstrate smaller C_H values as compared with PECVD films deposited under different conditions: from SiH_4 in a diode (curve *2*) and triode reactor (curve *3*), and also from 25%SiH_4 + 75%He mixture (curve *4*).

Figure 2 presents the C_H vs. T_s dependence for nanostructured *a*-Si:H films containing $(SiH_2)_n$ chains deposited by MASD at P = 7 mTorr without a grid (curve *1*) compared with films of similar structure deposited by PECVD in a diode reactor [8]. We can conclude that these dependences are alike, though C_H is slightly lower in MASD films than in PECVD films.

Figure 3 shows C_H vs. T_s for nanostructured *a*-Si:H films containing Si nanocrystals in an amorphous matrix, deposited by MASD at P = 3.5 mTorr without a grid (curve *1*), and also by PECVD in a diode [9, 10] (curve *2*) and triode reactor [11] (curve *3*). As seen, C_H values in nanostructured MASD films of this group are lower than in PECVD films at T_s = const.

Thus, MASD provides a reduced hydrogen content in films of all groups discussed; evidently this is due to specific features of this technology, which combines the silane decomposition process with the magnetron cathode sputtering of a crystal silicon target with argon. The interaction of argon species with the surface of a growing film raises the effective temperature of deposition and, consequently, reduces C_H in the films, thus favoring the further formation of polysilicon. From this position, the most interesting are the MASD films of standard *a*-Si:H and the nanostructured films with Si inclusions (the films with $(SiH_2)_n$ inclusions have a comparatively high C_H content, so they will not be discussed here).

The results of Si^+ ion implantation (the average ion energy is 75 keV, doses (D) up to 10^{13} cm^{-2}) performed at room temperature, with subsequent vacuum annealing at 200°C for 1 h, were used as a test to determine the tendency of films to crystallize.

It was shown earlier in the case of the partial crystallization of *a*-Si:H films that, first of all, the temperature dependence of dark conductivity σ changes: bends appear in the curves $\log\sigma = f(1/T)$; i.e., two activation energies $\Delta E_2 < \Delta E_1$ are observed (ΔE_1 and ΔE_2 refer to

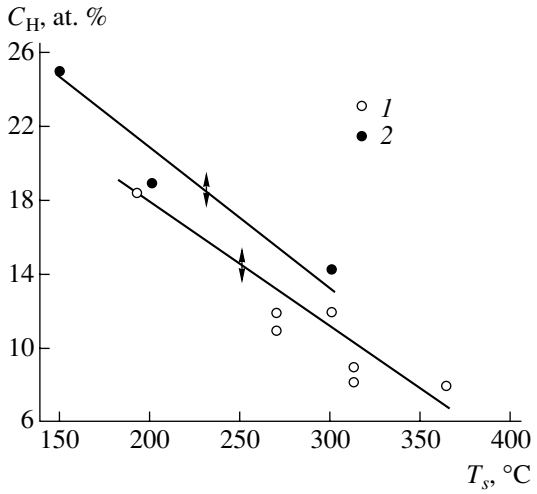

Fig. 2. Hydrogen content in films with $(SiH_2)_n$ nanoinclusions as a function of the deposition temperature: (*1*) MASD, (*2*) PECVD films.

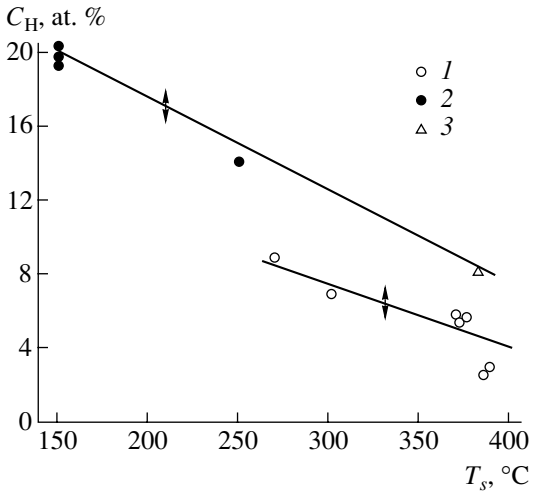

Fig. 3. Hydrogen content in films with Si nanoinclusions as a function of the deposition temperature: (*1*) MASD; (*2*) PECVD films deposited in a diode reactor from silane diluted with hydrogen and *(3)* in a triode reactor from SiH_4.

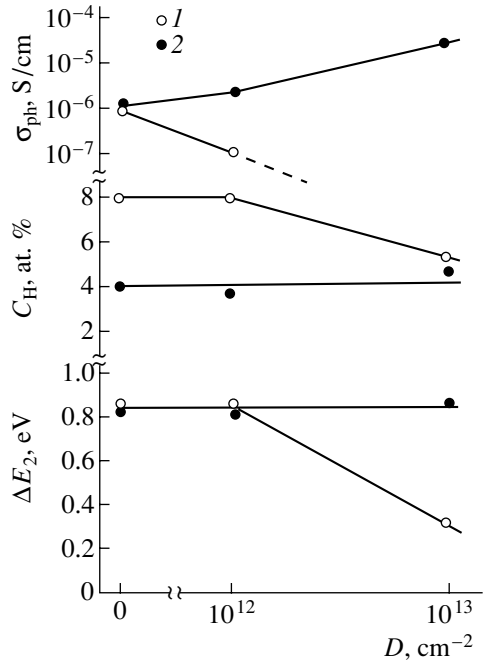

Fig. 4. The effect of Si^+ ion implantation (with dose *D*) on the activation energy of dark conductivity at low temperatures, photoconductivity (T = 300 K, the photon energy 2 eV, the rate of photocarrier generation 10^{19} cm^{-3} s^{-1}), and the hydrogen content in films: (*1*) standard *a*-Si:H MASD film; (*2*) MASD film with Si nanoinclusions.

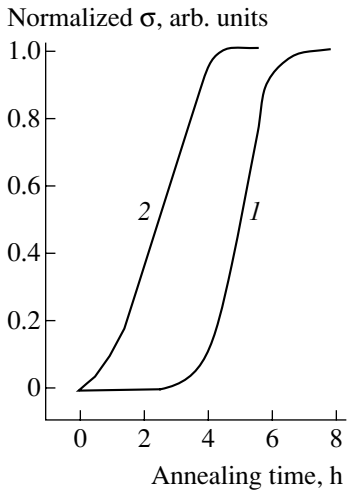

Fig. 5. Dark conductivity normalized to its saturated value vs. the time of annealing at 600°C: (*1*) standard *a*-Si:H MASD film and (*2*) MASD film with Si nanoinclusions.

the high and low temperature ranges, respectively). Second, the photoconductivity σ_{ph} falls [12]. Finally, as mentioned above, the C_H content decreases upon crystallization.

Figure 4 demonstrates the effect of ion implantation on the parameters of two "intrinsic" MASD films of standard and nanostructured *a*-Si:H. Prior to implantation, the $\log\sigma = f(1/T)$ curves exhibit only one activation energy, which is equal to half the mobility gap, i.e., $\Delta E_1 = \Delta E_2 = 0.85$ eV.

The data presented show that the effect of Si^+ implantation on *a*-Si:H films strongly depends on their initial structure.

Judging by the activation energy of the dark conductivity and C_H, a standard *a*-Si:H film is not crystallized. However, the strong enhancement of σ_{ph} leads us to the conclusion that, due to implantation, this film becomes nanostructured (with Si nanoinclusions with such a small size and such a low density that they cannot be identified using Raman spectroscopy) [9–11]. As an analogy, it is worth noting that the formation of carbon nanocrystals distributed in an amorphous matrix of carbon film subjected to ion irradiation has been observed recently [13].

We now discuss the impact of Si^+ implantation on an initially nanostructured film (Fig. 4). In this case, this effect corresponds to ordinary crystallization: the activation energies of σ, σ_{ph}, and C_H are correspondingly modified. Evidently, Si nanocrystals embedded in an amorphous matrix are crystallization centers. From the point of view of polysilicon fabrication, the MASD films of this structure are of primary interest, despite a hydrogen content substantially higher than in standard *a*-Si:H MASD films (Figs. 1 and 3).

Figure 5 shows the difference in the kinetics of crystallization under annealing between standard (curve *1*) and nanostructured (curve *2*) *a*-Si:H deposited at the same temperature T_s = 270°C. C_H values are, respectively, 6 and 10 at. %. The crystallization kinetics is judged from the variation in dark conductivity as a function of the annealing time. The conductivity remains constant during some "incubation period," when the centers of crystallization are formed. In contrast to standard *a*-Si:H, this time is virtually zero for nanostructured *a*-Si:H. However, the subsequent rate of the increase in conductivity is lower for a nanostructured film, presumably owing to a higher hydrogen content. Nevertheless, this does not result in a substantial increase in the crystallization time, which is defined as the time necessary to reach a leveling-off of the curves presented in Fig. 5.

3. CONCLUSION

The results obtained demonstrate the prospect of using MASD for the deposition of *a*-Si:H films, which can serve as a base in the fabrication of polysilicon. The technological conditions have been determined for the deposition of standard *a*-Si:H films with minimal hydrogen content, and of nanostructured films with Si inclusions in an amorphous matrix. The influence of specific features of the film structure on the efficiency of crystallization is demonstrated.

REFERENCES

1. M. Sudhar, D. D. Cyung, W. A. Anderson, and J. Coleman, Mater. Res. Soc. Symp. Proc. **356**, 921 (1995).
2. A. Szekeres, M. Garther, F. Vasiliu, *et al.*, J. Non-Cryst. Solids **227–230**, 954 (1998).
3. N. H. Nickel, Mater. Res. Soc. Symp. Proc. **378**, 381 (1995).
4. O. A. Golikova, A. N. Kuznetsov, V. Kh. Kudoyarova, *et al.*, Fiz. Tekh. Poluprovodn. (St. Petersburg) **34**, 86 (2000) [Semiconductors **34**, 87 (2000)].
5. K. Pangal, J. C. Sturm, and S. Wagner, Mater. Res. Soc. Symp. Proc. **507**, 577 (1998).
6. P. Lengsfield, N. H. Nickel, and W. Fuhs, in *Abstracts of ICAMS-18, USA, 1999*, FA2.1.
7. O. A. Golikova, M. M. Kazanin, O. I. Kon'kov, *et al.*, Fiz. Tekh. Poluprovodn. (St. Petersburg) **30**, 405 (1996) [Semiconductors **30**, 226 (1996)].
8. K. Akiyama, A. Ogiwara, and H. Ogawa, Jpn. J. Appl. Phys., Part 1 **33**, 5793 (1994).
9. P. Roca y Cabarrocas, N. Layadi, and M. Kunst, in *Proceedings of the 14th European Photovoltaic Solar Energy Conference, Spain, 1997*, P5A.20.
10. S. Vignoli, R. Butte, R. Meaudre, *et al.*, J. Phys.: Condens. Matter **11**, 8749 (1999).
11. O. A. Golikova and M. M. Kazanin, Fiz. Tekh. Poluprovodn. (St. Petersburg) **33**, 110 (1999) [Semiconductors **33**, 97 (1999)].
12. Yu. He, Ch. Yin, G. Cheng, and L. Wang, J. Appl. Phys. **75**, 797 (1994).
13. M. Fyta, I. Remediakis, P. C. Kelires, and E. Kaxiras, in *Abstracts of the ICAMS-19, France, 2001*, Th-B3/2.

Translated by D. Mashovets

Semiconductors, Vol. 36, No. 10, 2002, pp. 1184–1187. Translated from Fizika i Tekhnika Poluprovodnikov, Vol. 36, No. 10, 2002, pp. 1263–1267.

AMORPHOUS, VITREOUS, AND POROUS SEMICONDUCTORS

Electroluminescence from Porous Silicon in the Cathodic Reduction of Persulfate Ions: Degree of Reversibility of the Tuning Effect

A. A. Saren*, S. N. Kuznetsov, V. B. Pikulev, Yu. E. Gardin, and V. A. Gurtov

Petrozavodsk State University, Petrozavodsk, 185640 Russia

** e-mail: saren@mainpgu.karelia.ru*

Submitted February 7, 2002; accepted for publication March 13, 2002

Abstract—The temporal evolution of the spectra of cathodic electroluminescence from porous silicon in an electrolyte containing persulfate ions $S_2O_8^{2-}$ was studied in the galvanostatic mode. It was shown that irreversible changes in luminescence properties of porous silicon occur under cathodic polarization. These changes are manifested in a decrease in the signal intensity and a long-wavelength shift of the electroluminescence (EL) spectrum when the substrate potential remains virtually unchanged (pseudo-tuning). The irreversibility of the change in luminescence parameters is related to a concurrent electrochemical oxidation of the surface of porous silicon, which hinders the bipolar injection of carriers into luminescence-active crystallites. The results obtained suggest that the degradation phenomena observed under cathodic polarization are due to those same processes which are responsible for EL excitation, which casts doubt on the interpretation of the tuning effect, known in the literature, as a consequence of a purely electronic process in porous silicon. © *2002 MAIK "Nauka/Interperiodica".*

1. INTRODUCTION

The electroluminescence (EL) from porous silicon (*por*-Si) under cathodic polarization in contact with an electrolyte is observed in solutions containing strong oxidizing agents, such as persulfate ions $S_2O_8^{2-}$ [1–7].

In Si nanocrystallites, the source of EL is radiative recombination of electrons supplied from a cathodically biased substrate with holes injected into *por*-Si by sulfate radicals. It is assumed that the reduction reaction of the persulfate ion comprises two stages:

$$S_2O_8^{2-} + e_{cb}^- \longrightarrow SO_4^{2-} + SO_4^{-\bullet}, \quad (1)$$

$$SO_4^{-\bullet} \longrightarrow SO_4^{2-} + h_{vb}^+. \quad (2)$$

In reaction (1), an electron in the conduction band of the crystallite, e_{cb}, is captured to form a sulfate radical $SO_4^{-\bullet}$. The latter is a strong oxidizing agent and can inject a hole h_{vb} into the valence band of the crystallite [reaction (2)]. Then, if an electron is present in the conduction band of the crystallite, the injected hole can recombine with the electron, emitting a quantum of light $h\nu$:

$$e_{cb}^- + h_{vb}^+ \longrightarrow h\nu. \quad (3)$$

Of interest and importance for elucidating the mechanism of EL in *por*-Si is the so-called tuning effect, which is manifested in the dependence of the spectral position of the EL peak on applied potential: with increasing cathodic bias, the EL spectrum is shifted to shorter wavelengths and the intensity of the EL signal also changes [1, 3–6].

The mechanism of tuning of the cathodic EL was studied in [4, 5]. In [4], a model was proposed which attributes the tuning effect to a variation in the number of electrons in the conduction band of crystallites as the applied potential is varied. According to this model, the EL signal from a crystallite of a given size appears at a potential at which injection of electrons from the substrate into the conduction band of the crystallite becomes possible. Holes are injected by $SO_4^{-\bullet}$ radicals formed in the reduction of $S_2O_8^{2-}$ ions on the crystallite surface. Then, electron–hole pairs recombine in the crystallite emitting a quanta of light in the process. With a further increase in the cathodic bias, the rate of electron injection into the crystallite grows to such an extent that the injection of an electron during the time of existence of an excited state becomes possible. In this case, the fast nonradiative recombination of an electron–hole pair occurs with the transfer of energy to a third carrier, i.e., an electron (Auger process). The potential at which the onset of electron injection occurs depends on the crystallite size, since the energy gap and, consequently, the barrier to injection grow when this size decreases. Thus, the excitation and quenching of the EL occur successively with increasing cathodic bias in crystallites of various sizes, from larger to

smaller sizes, which gives rise to the observed tuning effect.

As stated by the authors of [4, 5], the EL peak position is determined solely by applied voltage, with an irreversible change in the EL signal intensity observed in repeated potential sweeps. The authors related such behavior of the EL signal to the oxidation of the *por*-Si surface.

Contrary to [4], the irreproducibility of the EL tuning effect under a repeated potential sweep was noted in [7] not only for the EL intensity, but also for the dependence of the EL peak position on bias. In the same study, a long-wavelength shift of the EL spectrum was observed when the substrate potential was kept constant. Based on an analysis of secondary ion spectra, the authors of [7] did not attribute the effect observed to *por*-Si oxidation: profiles of the object, obtained before and after the cathodic EL process, indicated a constant concentration of oxygen in the *por*-Si layer. However, this fact cannot serve as a conclusive argument against *por*-Si oxidation in cathodic EL, since the initial concentration of oxygen in the layer was high and its influence could markedly exceed the possible effect of oxidation in cathodic EL.

The data presented in this study indicate that irreversible degradation of the luminescence properties of the object occurs during the cathodic polarization of *por*-Si in an electrolyte containing persulfate ions. This degradation is accompanied by a change in the chemical composition of the *por*-Si surface. This fact complicates the interpretation of the tuning effect as something that results from a purely electronic process in porous silicon.

2. EXPERIMENTAL

Porous silicon samples were obtained through the anodic electrochemical etching of polished wafers of *n*-type single-crystal silicon with a resistivity of 0.3 Ω cm and (111) orientation. The etching was done for 5 min under dc current with a density of 100 mA cm^{-2} in a mixture of 49% hydrofluoric acid and isopropyl alcohol taken in equal volumes. The wafers were illuminated in the course of etching to create minority carriers. Then, the samples were placed for 10 min in an evacuated chamber to remove the liquid phase from pores.

The cathodic EL was studied on samples brought in contact with an aqueous electrolyte with a composition of 0.1 M $K_2S_2O_8$: 1 M H_2SO_4 = 1 : 1 (by volume) to which isopropyl alcohol (propanol-2) was added in an amount equal to 50% of the total solution volume; this was done to improve the wettability of the *por*-Si surface by the electrolyte. Platinum foil served as the counter electrode. The area of a sample in contact with the electrolyte was ≈1.3 cm^2. All the potentials are given relative to the platinum counter electrode.

Before and after measuring the EL response in the electrolyte, the photoluminescence (PL) properties of the samples were recorded in a vacuum (residual pressure 1 Pa). The PL was excited in a narrow range of energies of quanta around 4 eV at an incident power of ≈1 mW cm^{-2}. The PL and EL spectra obtained were corrected for the sensitivity of the spectrometric system.

IR transmission spectra of *por*-Si samples were measured on a Specord M-80 double-beam spectrophotometer, with a silicon wafer without a *por*-Si layer placed in the reference channel.

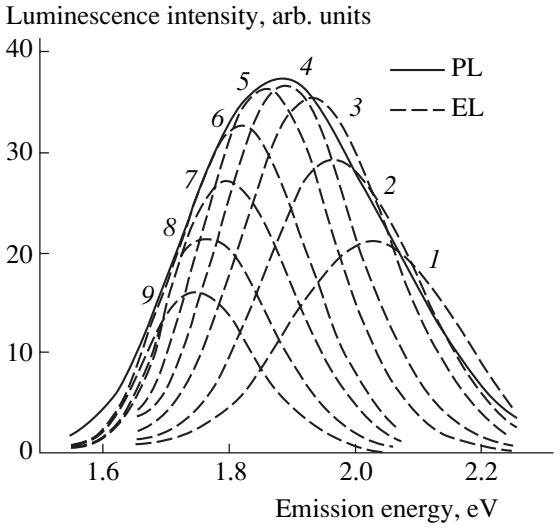

Fig. 1. Original PL spectrum (solid line) of a *por*-Si sample on an *n*-substrate and a set of EL spectra (dashed lines) obtained under the action of dc current with a density of 0.77 mA cm^{-2}. The numbering of the EL spectra starts from the beginning of the treatment.

3. RESULTS AND DISCUSSION

Figure 1 presents a PL spectrum (thick solid line) and a set of EL spectra (dashed lines) for a *por*-Si sample. The PL spectrum corresponds to the freshly prepared state of the object and is normalized to the peak value of the EL signal. The cathodic EL signal was measured under a dc current with a density of 0.77 mA cm^{-2} flowing in the circuit for 1.5 h. The EL spectrum shifted steadily to longer wavelengths with the time of treatment. The voltage across the cell was within –3.05 ± 0.05 V during the entire experiment.

The profile of the initial PL spectral line (normalized to the peak of the EL signal) is an envelope of EL spectra recorded at different instants of time after the beginning of treatment (Fig. 1). It should be emphasized that an outwardly similar pattern was observed in [6]; however, the set of EL spectra was obtained with a varied substrate potential. In terms of the quantum-confinement hypothesis for luminescence in *por*-Si, it may be suggested that, in both cases, the EL is excited in part of an ensemble of luminescing crystallites with different sizes.

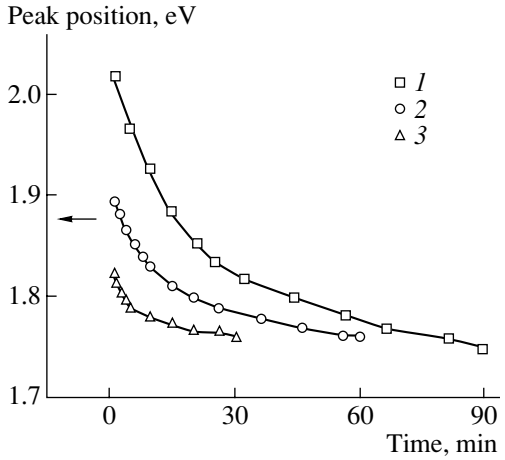

Fig. 2. Evolution of the peak position of the EL spectrum in three successive treatments in the dc mode. The arrow denotes the peak position of the PL spectrum for the initial state of the sample. The respective voltages across the cell: –3.05, –4.75, and –5.95 V (±0.05 V). Current density: (*1*) 0.77, (*2*) 3.85, and (*3*) 7.70 mA cm^{-2}.

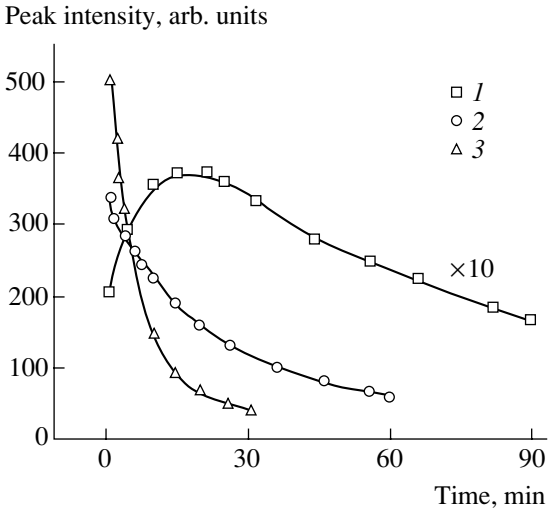

Fig. 3. Variation of the peak intensity of the cathodic EL in three successive treatments in the dc mode. Current density: (*1*) 0.77, (*2*) 3.85, and (*3*) 7.70 mA cm^{-2}.

The typical range of voltage variation, in which the EL tuning was observed, is 0.5–0.6 V [4, 6]. Apparently, the long-wavelength shift of the EL spectrum (named here as pseudo-tuning) cannot be accounted for in the given case by a change in potential, since the voltage across the cell changed during the experiment by no more than 0.1 V.

The given sample was subjected to two more successive treatments in the dc mode at current densities of 3.85 and 7.7 mA cm^{-2} (at the corresponding voltages of -4.75 ± 0.05 and -5.95 ± 0.05 V). The kinetics of the changes in the position and intensity of the EL spectrum is presented in Figs. 2 and 3, respectively.

According to Fig. 2, raising the cathodic bias leads, in successive treatments, to a short-wavelength shift of the EL peak relative to its position at the end of the preceding treatment at lower voltage. However, the position of the EL peak, recorded at the beginning of each successive treatment, shifts irreversibly to longer wavelengths. The PL spectrum, measured after three of the described treatments, exhibited a long-wavelength shift of the peak position (from 1.88 to 1.82 eV) and a decrease in the peak intensity by a factor of 3. Also noteworthy is the fact that the EL signal decreases more rapidly as the driving current increases (Fig. 3).

The probable reason for the observed degradation of the luminescence properties of *por*-Si in cathodic EL is the oxidation of the crystallite surface. The presence of holes in the surface layer of silicon gives rise to the electrochemical oxidation in electrolytes, which was studied in detail for the case of anodic polarization [8]. In cathodic polarization, holes are injected into the valence band of crystallites by sulfate radicals $SO_4^{-\bullet}$ and, therefore, it would be expected that the surface of the crystallites involved in EL is oxidized.

This assumption is confirmed by measurements of IR transmission spectra in the absorption ranges of Si–O (1000–1200 cm^{-1}) and Si–H (2000–2200 cm^{-1}) bonds. Figure 4 presents the IR spectra of a *por*-Si sample in a freshly prepared state and after cathodic polarization.

In the freshly prepared state, the *por*-Si surface is passivated by hydride bonds, which is indicated by the presence of a well-pronounced absorption band at 2050–2150 cm^{-1} consisting of three narrower bands

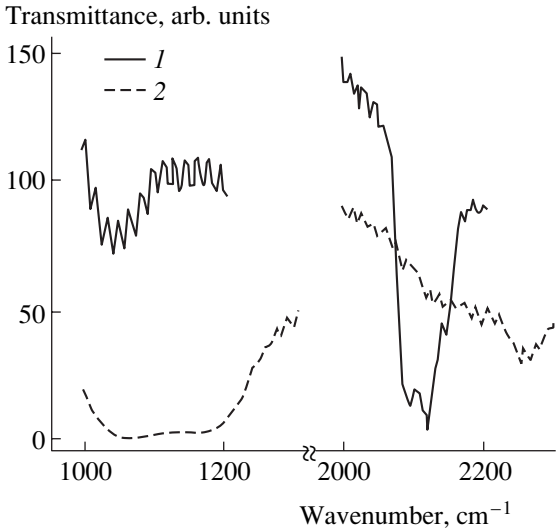

Fig. 4. Transformation of IR transmission spectra in the ranges corresponding to vibrations of Si–O–Si (1000–1200 cm^{-1}) and Si–H$_n$ (n = 1, 2, 3) bonds for a *por*-Si sample (*1*) in freshly prepared state and (*2*) after cathodic EL. The "fine" structure in the transmission spectrum, clearly seen in the long-wavelength band, is due to interference.

corresponding to the stretching vibrations of Si–H_n bonds (n = 1, 2, 3) on the silicon surface. The IR transmission spectrum of a *por*-Si sample subjected to cathodic polarization shows that absorption in the given spectral range almost completely disappears.

The absorption in the band at 1000–1200 cm^{-1} is determined by the concentration of Si–O–Si bonds. It can be seen from Fig. 4 that the absorption in the given spectral range of a *por*-Si sample subjected to cathodic polarization increased by more than a factor of 100 when compared with the freshly prepared sample.

Thus, it may be assumed that an oxide phase grows on the surface of luminescing crystallites in the course of cathodic EL. This process is accompanied by the loss of the hydride cover, which originally passivates the crystallites. The change in the surface passivation leads to the observed degradation of the luminescence properties of an object. The pseudotuning of EL under invariable external conditions (bias, current) can be accounted for by the exclusion of oxidized crystallites from the EL process: the formation of the oxide phase makes further charge exchange with ions in the electrolyte impossible. It may be assumed, in terms of the model described in [4], that electron injection into the oxidized crystallites is also hindered by an increased energy barrier and that the electron density in the conduction band of crystallites of a given size decreases as the oxide phase grows. Thus, crystallites with a higher emission energy cease to luminesce, and those with a lower energy become active. The probability of oxidation is higher for presently luminescing crystallites, since holes injected into the crystallites in which occupancy with electrons is high recombine nonradiatively (Auger recombination), having no time to cause oxidation.

A comparison of the quantum efficiencies of PL and EL shows that only a small number of luminescing crystallites are excited in *por*-Si under cathodic polarization. With the available data on the PL and EL signal intensities recorded under equal conditions of emission collection, it was possible to evaluate the ratio of the external quantum efficiencies of PL and EL. The quantum efficiency of PL, η_{PL}, is commonly defined as the number of emitted quanta per a single quantum of exciting radiation. The quantum efficiency of EL, η_{EL}, is defined here as the number of emitted quanta per elementary charge passing through the external circuit. A calculation in terms of these definitions gives a η_{PL}/η_{EL} ratio of about 15 for the object in a state corresponding to the beginning of the first treatment in Fig. 2, i.e., at the lowest degree of degradation of the luminescence properties.

This result correlates with the relatively small decrease in the PL intensity when there is a substantial change in the EL efficiency. The same circumstance accounts for the results reflected in Fig. 2, namely, the possibility of observing, on raising the current and the cathodic bias, an EL with a peak energy exceeding that in the preceding measurement. At a given voltage, the most accessible crystallites are involved in cathodic polarization. With increasing current and voltage, the excitation of EL becomes possible in *por*-Si fragments that are less accessible to current flow.

4. CONCLUSION

The temporal evolution of spectra of cathodic EL from *por*-Si on an *n*-Si substrate in an electrolyte containing persulfate ions $S_2O_8^{2-}$ was studied in the galvanostatic mode. It was shown that an irreversible change in the luminescence properties of *por*-Si occurs in the course of polarization. This change is manifested in a decrease in the EL signal intensity and in a long-wavelength shift of the EL spectrum with treatment time at a virtually constant potential of the silicon substrate. The temporal drift of the luminescence parameters is accompanied by changes in the IR transmission spectra, which indicate that the hydride cover is replaced by silicon–oxygen complexes on the *por*-Si surface. The data obtained allow for the following explanation of pseudotuning under cathodic polarization in the presence of persulfate ions. The formation of an oxide phase hinders the bipolar injection of carriers into luminescence-active crystallites. The change in the percolation process is most pronounced for the small-size fraction of the ensemble of luminescing crystallites, thereby leading to a shift of the EL band.

REFERENCES

1. L. T. Canham, W. Y. Leong, M. I. J. Beale, *et al.*, Appl. Phys. Lett. **61**, 2563 (1992).
2. D. N. Goryachev, O. M. Sreseli, and L. V. Belyakov, Fiz. Tekh. Poluprovodn. (St. Petersburg) **31**, 844 (1997) [Semiconductors **31**, 716 (1997)].
3. L. M. Peter and R. I. Wielgosz, Appl. Phys. Lett. **69**, 806 (1996).
4. L. M. Peter, D. J. Riley, R. I. Wielgosz, *et al.*, Thin Solid Films **276**, 123 (1996).
5. L. M. Peter, D. J. Riley, and P. A. Snow, Electrochem. Commun. **2**, 461 (2000).
6. A. Bsiesy, F. Muller, M. Ligeon, *et al.*, Appl. Phys. Lett. **65**, 3371 (1994).
7. Ji-Eun Lim, Won-Seok Chae, Yeonhee Lee, and Kang-Jin Kim, J. Electrochem. Soc. **144**, 647 (1997).
8. A. G. Revesz, J. Electrochem. Soc. **114**, 629 (1967).

Translated by M. Tagirdzhanov

Semiconductors, Vol. 36, No. 10, 2002, pp. 1188–1191. Translated from Fizika i Tekhnika Poluprovodnikov, Vol. 36, No. 10, 2002, pp. 1268–1271.

AMORPHOUS, VITREOUS, AND POROUS SEMICONDUCTORS

Space Charge Limited Current in Porous Silicon and Anatase (TiO_2)

É. A. Lebedev* and T. Dittrich**

** Ioffe Physicotechnical Institute, Russian Academy of Sciences, Politekhnicheskaya ul. 26, St. Petersburg, 194021 Russia*

*** Technische Universität München, Physics Department E16, D-85748 Garching, Germany*

Submitted April 11, 2002; accepted for publication April 15, 2002

Abstract—A comparative study of the transient space-charge-limited current in porous silicon and porous anatase (TiO_2) has been carried out. The room-temperature drift mobilities of electrons in porous silicon and porous anatase, determined from the transit times, are, respectively, 10^{-2} and 5×10^{-6} $cm^2 V^{-1} s^{-1}$. The specific features of space-charge-limited currents in porous anatase are discussed. © *2002 MAIK "Nauka/Interperiodica".*

1. INTRODUCTION

The strong interest in porous nanocrystalline materials is due to the possibility of their use in solar cells, gas analyzers, and light-emitting diodes [1–4]. Porous silicon (*por*-Si) is of interest, first of all, as a material exhibiting electroluminescence properties [4]. Layers of porous anatase (TiO_2) are used in solar cells, in which high quantum efficiency is achieved by using organic dyes, and porous anatase (PA) serves as a transport medium ensuring charge transfer in the space between the electrodes [1]. To elucidate the nature of photoelectric phenomena and optimize device characteristics, knowledge of the fundamental aspects of carrier transport in porous materials is necessary. Investigations show that the characteristics of carrier transport in these materials are rather similar to those in disordered materials [5, 6]. In this connection, the transport in *por*-Si and PA was analyzed using the methods and concepts developed in studying disordered materials. As an effective means of determining the drift mobility, the transient space-charge-limited current (TSCLC) was employed. The advantage of this technique over other methods consists in that it enables the determination of the mobility both from the transit time and from the current strength [7, 8]. Crystalline TiO_2, which, in contrast to crystalline silicon, has been relatively poorly studied, served as the starting material for obtaining PA. This material belongs to bipolar semiconductors, which are characterized by a high dielectric constant, strong electron–phonon coupling, and a high probability of the polaronic transport mechanism [9]. It seems of interest in this connection to reveal specific features of carrier transport in PA as compared with *por*-Si, whose optical and electrical properties are comparatively well understood. A comparative study of TSCLC in *por*-Si and PA may reveal both the general aspects of transport in porous materials and the specificity of each of these materials.

2. SAMPLE PREPARATION AND METHOD FOR STUDYING TSCLC

Porous silicon layers of thickness $L \approx 5$ μm were prepared electrochemically on a polished surface of *n*-type silicon with a resistivity of 2 Ω cm. The samples used in the measurements had a sandwich configuration. Crystalline silicon was used as one of the electrodes. A semitransparent chromium film deposited onto *por*-Si in a vacuum served as the other electrode. The sample resistance was 10^9–10^{10} Ω with an upper electrode area of 0.19 cm^2.

Porous anatase layers [1] were prepared from a paste containing ~16-nm TiO_2 nanoparticles and turpentine oil. The paste was thinly distributed over a glass substrate coated with a transparent SnO_2:F layer and then annealed in air at 450°C for 30 min. The layer porosity was ~50%. The thickness of the layers studied was 5–10 μm. The back contact was formed from the same paste mixed with carbon powder. The mixture was deposited over a preliminarily prepared TiO_2 layer and then annealed under the same conditions. Immediately before the measurements, the samples were kept in an atmosphere of oxygen at 450°C for 30 min. The measurements were also done in oxygen.

For TSCLC to be observed, it is necessary that the entire amount of charge, $q = CU$, generated at the electrodes of a sample with capacitance C enter the sample on applying a voltage U across the electrodes. In the case of effectively injecting electrodes, TSCLC can be observed by simply applying a voltage step across the electrodes. Since it is difficult to fabricate injecting electrodes and large capacitive currents mask the TSCLC, charge is commonly injected by a pulse of strongly absorbed light.

The TSCLC measurements were carried out on a setup for measuring transit times [11]; we used a voltage pulse of duration from 1 to 900 ms and a time delay

from 0.1 to 500 ms between the instants of application of voltage and the light pulse were applied to the sample. The charge was generated using a pulsed nitrogen laser with an emission wavelength of 0.337 μm and a pulse duration of 0.3 ns. The measurements were done in the mode of single pulses of space-charge-limited current (SCLC). On achieving the SCLC mode, the photocurrent became independent of the light pulse intensity.

3. RESULTS AND DISCUSSION

Figure 1 presents an oscillogram of TSCLC in porous silicon. The oscillogram is close to the ideal TSCLC shape [7, 8]. On applying a light pulse, an initial current I_0 is generated, whose density (in A cm^{-2}) is given by [8]:

$$J(0) = 4.4 \times 10^{-14} \varepsilon \mu U^2 / L^3,$$

where ε is the dielectric constant, μ is the mobility, and L is the sample thickness. Then, with the space between the electrodes filled with electrons, the current grows because of an increase in the field intensity at the front of the carrier packet and a rise in the effective capacitance, to $I_m = 2.7 I_0$ in a time t_m, which corresponds to the time in which carriers reach the back electrode. Since the carriers move in an increasing field, t_{tr} is shorter than the transit time t_m in the absence of the SCLC mode: $t_m = 0.78 t_{tr}$. The drift mobility is found from the transit time as $\mu = L^2/(t_{tr}U)$. For the sample studied, $\mu = 10^{-2}$ cm^2 V^{-1} s^{-1}. At a constant carrier injection, the current falls to $I = 2.3 I_0$ at a certain time after t_m. When carriers are generated by a light pulse, the injection is limited in time and the current falls to zero. Figure 2 presents the dependence of SCLC on the applied voltage in porous silicon. A quadratic dependence of the current, characteristic of the SCLC mode, is observed in a limited range of voltages below 2 V. At voltages exceeding 2 V, the limited light-induced injection results in that the SCLC mode gives way to the small charge mode, $q < CU$, to which corresponds a linear dependence of current on voltage.

The mobility calculated from the transit time coincides with that found from the currents I_0 and I_m at ε = 4–5, a value typical of porous silicon. Such a coincidence has been the case in all the known instances of TSCLC observation in porous silicon [12–14].

A photocurrent of electrons, close in shape to TSCLC, was also observed in porous anatase. As seen from Fig. 3, the photocurrent is characterized by an initial current I_0, with the subsequent gradual rise in current to its maximum value I_m. Commonly, the I_m/I_0 ratio did not exceed 2. The current increased with voltage, following a nearly quadratic power-law dependence. The time elapsed from the instant of light pulse application to the appearance of a maximum in the time dependence of the current varied in inverse proportion

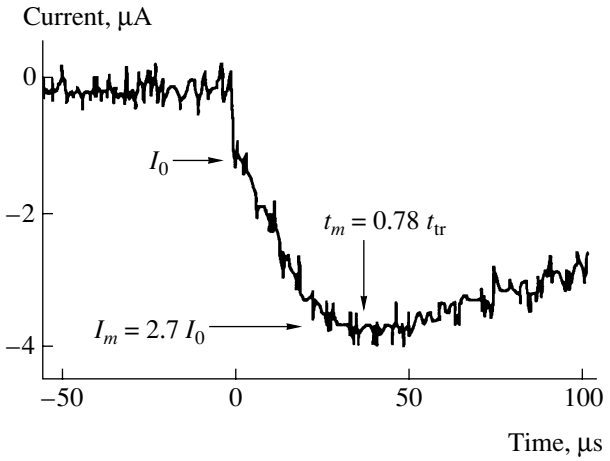

Fig. 1. Oscillograms of TSCLC of electrons in porous silicon. U = 0.41 V, L = 5 μm.

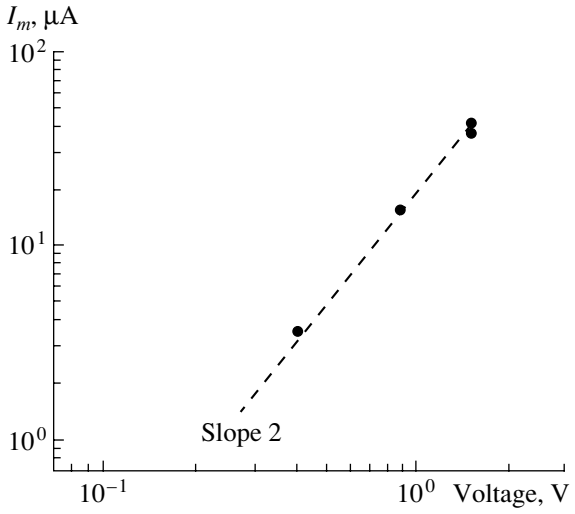

Fig. 2. Dependence of peak current I_m on voltage in porous silicon. L = 5 μm.

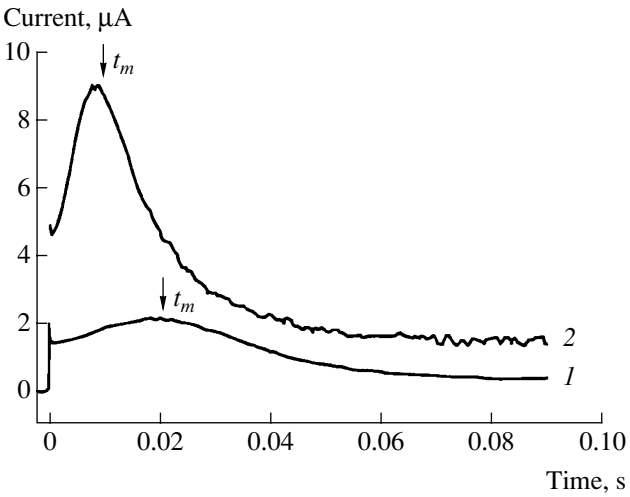

Fig. 3. Oscillogram of TSCLC of electrons in porous anatase. U = (*1*) 2.8 and (*2*) 5.7 V; L = 5.5 μm.

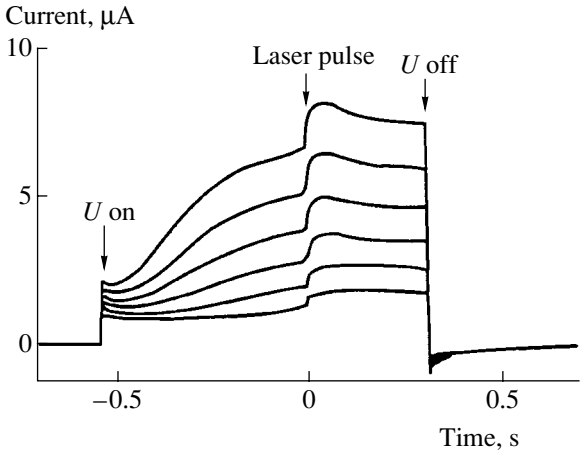

Fig. 4. Oscillograms of TSCLC generated by a laser pulse in porous anatase on the background of dark injection currents on switching the voltage on (*U* on) and off (*U* off). The voltage varies from 6 to 11 V with a step of 1 V; sample thickness 8 μm.

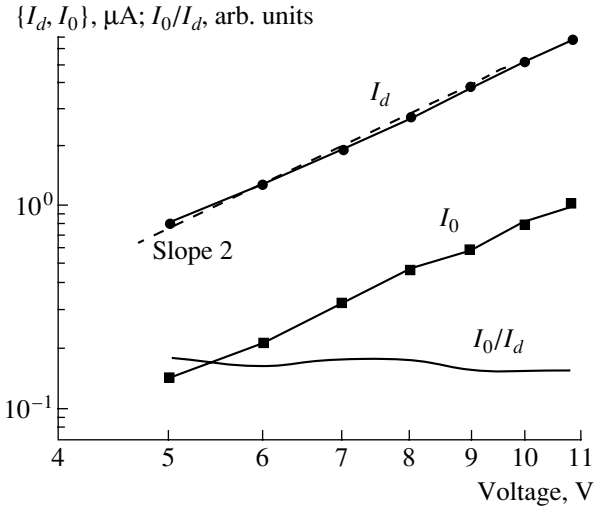

Fig. 5. Initial photocurrent I_0, dark current I_d at the instant of application of a light pulse, and ratio of these currents (I_0/I_d) vs. the voltage applied to a porous anatase sample.

to the voltage. As regards all the main parameters, the behavior of the photocurrent was the same as that in the case of TSCLC. The drift mobility found from the transit time was 5×10^{-6} cm^2 V^{-1} s^{-1}.

Commonly, the transit times are measured, for both weak and strong injection (TSCLC), under small dark currents. At the same time, the maximum in the time dependence of the current, $I(t)$, appeared in PA only in the presence of a high dark injection current. With blocking contacts and a thin insulating layer introduced between the electrode and the TiO_2 layer, transient currents decaying with time in ~100 μs were observed. The $I(t)$ dependences plotted in the log–log scale exhibited no bends, which are commonly used to determine the transit time in the case of dispersive transport. The appearance of a peak corresponding to carrier transit across the interelectrode space in the presence of dark injection may be due to field redistribution and the filling of localized states which capture carriers.

Figure 4 presents oscillograms of both the dark current, observed upon applying a varied voltage to a sample, and the photocurrent arising on applying a light pulse after a delay time of ~500 ms relative to the instant of voltage application to the sample. Figure 5 shows the initial photocurrent I_0, dark current I_d at the instant of application of the light pulse, and the ratio of these currents as functions of the voltage applied to the sample. At the instant of application of the light pulse, the dark current exceeds the photocurrent severalfold. The nearly quadratic dependence on voltage indicates the occurrence of the SCLC mode. In the presence of a dark SCLC, the injecting electrode creates an infinite reservoir of carriers and, at first glance, it seems that the additional charge generated by a light pulse near the injecting electrode cannot affect the current, since the current is only determined by the voltage applied to the sample. However, the photocurrent may appear because of the existence of a layer with a certain finite thickness in which light is absorbed. It was found in the present study that the thickness of this layer is $\Delta \approx 0.3$ μm. In this case, it seems as if the electrode is shifted to the distance along which light is absorbed, creating a high density of carriers. The effective thickness of the sample decreases instantaneously to become $L - \Delta$. Simultaneously, the sample capacitance grows and an additional charge is introduced into the sample. The drift of this charge causes a redistribution of the field and a further increase in capacitance, with the result that the current grows and a peak appears in the $I(t)$ curve when carriers reach the back electrode. In the absence of dark injection, the decrease in the effective thickness of the sample with increasing light pulse intensity leads to a rise in TSCLC and a decrease in the transit time [15]. The photocurrent can be evaluated by assuming that its value is equal to the difference between the SCLCs in samples of thickness $L - \Delta$ and L, where Δ is the distance along which light is absorbed:

$$I_0 = I_d[L^3/(L-\Delta)^3 - 1].$$

For a sample of thickness $L = 8$ μm with $\Delta = 0.3$ μm, the I_0/I_d ratio is ~0.12. As seen from Fig. 5, the experimental value of this ratio is 0.15–0.18, which is in good agreement with the above estimate.

Another important feature of SCLC in PA is that the mobility found from the transit time is much lower than that determined from the current density at $\varepsilon = 10$ [16], with the difference being occasionally as large as an order of magnitude. Since the SCLC is proportional to the dielectric constant, the behavior of the capacitance was studied in a wide range of frequencies in relation to the period of time during which voltage is applied to the sample. A strong rise in the dielectric constant was

observed at frequencies lower than 10^2–10^3 Hz and when the time during which voltage was applied to the sample increased [17].

The delay and transit times in porous TiO_2 correspond to the frequency range in which the dielectric constant greatly exceeds the value $\varepsilon = 10$ measured at a frequency higher than 10^3 Hz, which leads to an overestimated value of mobility determined from the current strength.

4. CONCLUSION

The investigation performed demonstrated that porous materials are characterized by low drift mobility. The transient SCLC in porous anatase exhibits a number of specific features. The appearance of light-induced SCLC on the background of a dark injection current and the disagreement between the mobilities found by different methods can be accounted for qualitatively by a decrease in the effective sample thickness, which occurs when carriers are generated by a light pulse, and by an increase in the dielectric constant at low frequencies. At the same time, a number of details concerning SCLC in porous anatase remain ambiguous. To these, in particular, belongs the contribution of the frequency dependence of the dielectric constant to TSCLC. Moreover, the reasons as to why the transit time cannot be measured in the absence of a dark current have not been revealed conclusively. These problems invite further investigation.

ACKNOWLEDGMENT

We thank F. Koch, V. Petrova-Koch, G. Polisski, and V. Kytin for helpful discussions and assistance.

REFERENCES

1. O. Regan and M. Grätzel, Nature **353**, 49 (1991).
2. W. Göpel and G. Reinhardt, in *Sensors Update*, Ed. by H. Baltes, W. Göpel, and J. Hesse (VCH, Weinheim, 1996), p. 47.
3. M. R. Hoffmann, S. T. Martin, W. Choi, and D. Bahnemann, Chem. Rev. **95**, 69 (1995).
4. A. G. Cullis, L. T. Canham, and P. D. J. Calcott, J. Appl. Phys. **82**, 909 (1997).
5. R. Konenkamp, Phys. Rev. B **61**, 11057 (2000).
6. E. A. Lebedev, E. A. Smorgonskaya, and G. Polisski, Phys. Rev. B **57**, 14607 (1998).
7. A. Many and G. Rakavy, Phys. Rev. **126**, 1980 (1962).
8. A. Many, S. Z. Weisz, and M. Simhony, Phys. Rev. **126**, 1989 (1962).
9. V. N. Bogomolov, E. K. Kudinov, and Yu. A. Firsov, Fiz. Tverd. Tela (Leningrad) **9** (11), 3175 (1967) [Sov. Phys. Solid State **9**, 2502 (1968)].
10. Th. Dittrich, E. A. Lebedev, and J. Weidmann, Phys. Status Solidi A **165**, R5 (1998).
11. W. E. Spear, J. Non-Cryst. Solids **1**, 197 (1969).
12. L. P. Kazakova, A. A. Lebedev, and É. A. Lebedev, Fiz. Tekh. Poluprovodn. (St. Petersburg) **31**, 609 (1997) [Semiconductors **31**, 517 (1997)].
13. N. S. Averkiev, L. P. Kazakova, É. A. Lebedev, and N. N. Smirnova, Fiz. Tekh. Poluprovodn. (St. Petersburg) **35**, 609 (2001) [Semiconductors **35**, 588 (2001)].
14. N. S. Averkiev, L. P. Kazakova, and N. N. Smirnova, Fiz. Tekh. Poluprovodn. (St. Petersburg) **36**, 355 (2002) [Semiconductors **36**, 336 (2002)].
15. G. Juska, M. Vilinas, O. Klima, *et al.*, Philos. Mag. B **69** (2), 277 (1994).
16. Th. Dittrich, Phys. Status Solidi A **182**, 447 (2000).
17. V. Kytin, Th. Dittrich, F. Koch, and E. Lebedev, Appl. Phys. Lett. **79** (1), 108 (2001).

Translated by M. Tagirdzhanov

Semiconductors, Vol. 36, No. 10, 2002, pp. 1192–1197. Translated from Fizika i Tekhnika Poluprovodnikov, Vol. 36, No. 10, 2002, pp. 1272–1277.

PHYSICS OF SEMICONDUCTOR DEVICES

Influence of the Design and Material Parameters on the Current–Voltage Characteristics of Two-Island Single-Electron Chains

I. I. Abramov*, S. A. Ignatenko, and E. G. Novik

Belarussian State University of Information Science and Radio Engineering, ul. Brovki 6, Minsk, 220027 Belarus

** e-mail: nanodev@bsuir.edu.by*

Submitted March 25, 2002; accepted for publication March 29, 2002

Abstract—The influence of the design and material parameters on the current–voltage characteristics of single-electron two-island chains of tunneling junctions was studied using a developed numerical model. It is ascertained that these characteristics are most sensitive to variation in the largest width of a tunneling junction and in the height of the potential barrier in the insulator. At the same time, variations in the background charges in the islands, in the relative permittivity of the insulator, and in the operating temperature bring about various transformations of the current–voltage characteristics. © *2002 MAIK "Nauka/Interperiodica".*

1. INTRODUCTION

The use of multiple-island chains of tunneling junctions is promising for the development of various single-electron device structures [1, 2]. The advantage of these chains over single-electron one-island transistors consists in a lower sensitivity of the characteristics of such chains to the parasitic cotunneling effect and also in the manifestation of both temporal and spatial correlations for fixed applied voltages. In this context, the use of many-island chains of tunneling junctions is justified for designing the memory elements [3, 4] of quantum integrated circuits.

An analysis shows that a theoretical study of such complicated structures as the chains under consideration is possible only in the context of a semiclassical approach. This is related to the fact that the models of a quantum-mechanical approach are still being developed and require substantial computing resources for their implementation. Therefore, the latter approach enables one to simulate only some of the processes in single-electron structures [5].

The known models of the semiclassical approach, which are based either on solving the master equation [1] or on the Monte Carlo method [6, 7], generally make it possible to simulate fairly complex single-electron many-island chains of tunneling junctions. However, a serious disadvantage of the aforementioned models is the fact that the capacitances and resistances of tunneling junctions are used in these models as the adjustable parameters to fit the calculation and experiment together. As a result, it is very difficult to study the effect of the design and material parameters on the characteristics of single-electron structures. At the same time, such studies would make it possible to determine the required sizes, select the appropriate materials, and predict the characteristics of single-electron devices at the design stage.

In this paper, we report the results of the theoretical study of two-island single-electron chains of tunneling junctions made of various materials; we used a developed numerical model. We also identified the most critical factors that influence the current–voltage (*I–V*) characteristics of these devices.

2. A MODEL

Abramov and Novik [8–10] suggested a two-dimensional numerical model for a metal single-electron transistor with a single island. The model is based on a semiclassical approximation and makes it possible to evaluate the characteristics of a device in relation to its design and material parameters; i.e., this model is devoid of the aforementioned drawback. In this paper, the suggested approach is generalized to the case of multiple-island (in particular, two-island) chains of tunneling junctions.

Let us consider the essence of the developed model. The input parameters in this model are the geometrical parameters of the device (see Fig. 1); the parameters of materials; the background charges at the islands; and also the external factors, such as the source, drain, gate voltages, and temperature *T*.

The model is based on the numerical solution of the Poisson equation (the effect of magnetic field is ignored); i.e., [8–10]

$$\nabla\varepsilon\nabla\varphi(x, y) = -q_M, \qquad (1)$$

where ε is the permittivity; φ is the electrostatic potential; x and y are coordinates; and q_M is the volume charge density, which includes the density of charge

1063-7826/02/3610-1192$22.00

carriers q_t directly involved in tunneling and the background-charge density q_0. The charge in the insulator is ignored.

In the model under consideration, a transition is performed from the continuous representation of the Poisson equation (1) to its discrete approximation in the *ABCD* region in Fig. 1. As the boundary conditions, we chose the Dirichlet conditions at the contacts and the Neumann conditions at the free boundaries. Numerical methods for the finite-difference approximation and for the solution of the emerging system of linear algebraic equations were described in detail elsewhere [9]. As a result of solving the equation, we obtain the distribution of potential in the structure in relation to the geometric parameters, parameters of the material, external factors, and also to the number of excess charge carriers at the islands.

We then determine the values of voltages across the tunneling junctions taking into account the electrostatic potential distribution in the structure. In this model, the partial currents through all tunneling junctions in the forward and reverse directions are calculated using the formula [1]

$$I = \frac{V_{\text{eff}}}{R}\left[1 - \exp\left(-\frac{eV_{\text{eff}}}{k_B T}\right)\right]^{-1} \quad (2)$$

with

$$V_{\text{eff}} = \frac{V_i + V_f}{2}, \quad (3)$$

where V_i and V_f are the voltages before and after electron tunneling, respectively; k_B is the Boltzmann constant; and e is the elementary charge. The expression for the tunneling junction resistance in relation to the potential barrier height was reported elsewhere [9]. Thus, in contrast to the model suggested previously [8–10], the model under consideration in this paper makes it possible to take into account more naturally the temperature effects using formulas (2) and (3).

In order to calculate the *I–V* characteristics of the chain, we used the master equation for single-electron structures [1]; however, we write this equation directly for the currents through the tunneling junctions rather than for the tunneling rates. As a result, this equation takes the following form for the two-island structures:

$$\begin{aligned}\frac{\partial\sigma(n_1, n_2)}{\partial t} &= I_{n_1-1, n_2 \to n_1, n_2}\sigma(n_1 - 1, n_2) \\ &+ I_{n_1, n_2-1 \to n_1, n_2}\sigma(n_1, n_2 - 1) \\ &+ I_{n_1+1, n_2 \to n_1, n_2}\sigma(n_1 + 1, n_2) \\ &+ I_{n_1, n_2+1 \to n_1, n_2}\sigma(n_1, n_2 + 1) \\ &- (I_{n_1, n_2 \to n_1+1, n_2} + I_{n_1, n_2 \to n_1, n_2+1} \\ &+ I_{n_1, n_2 \to n_1-1, n_2} + I_{n_1, n_2 \to n_1, n_2-1})\sigma(n_1, n_2).\end{aligned} \quad (4)$$

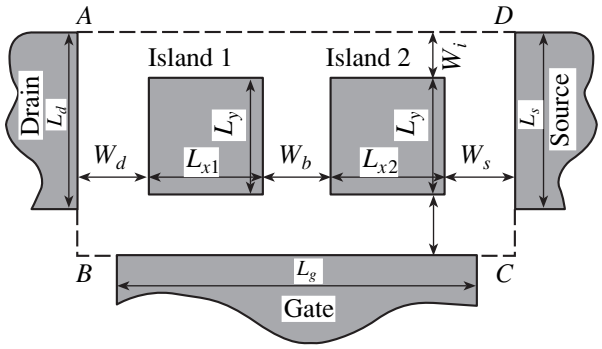

Fig. 1. Structure of a two-island single-electron chain.

Here, $\sigma(n_1, n_2)$ is the probability of finding the excess charge carriers at the islands; n_1 and n_2 are the numbers of excess charge carriers at the first and second islands, respectively; and $I_{n_1-1, n_2 \to n_1, n_2}$ is the sum of partial currents through the tunneling junctions as the number of charge carriers in the first island changes as $n_1 - 1 \longrightarrow n_1$.

Equation (4) was solved in the steady-state case. In order to find a nontrivial solution, we used the Seidel iteration method [11]. We will just note here that direct methods and a number of iterative methods cannot be used for the aforementioned purposes.

The total current through the structure was calculated using the formula

$$I = \sum_{n_1}\sum_{n_2}\sigma(n_1, n_2)[I^+(n_1, n_2) - I^-(n_1, n_2)], \quad (5)$$

where $I^+(n_1, n_2)$ and $I^-(n_1, n_2)$ are the currents through the tunneling junction in the forward and reverse directions, respectively.

The developed model was implemented using the MJT-SET-NANODEV software package for the many-island chains of tunneling junctions; this package was included in a NANODEV system for simulating nanoelectronic devices [9].

3. ADEQUACY OF THE MODEL

In order to assess the applicability of the suggested model to actual devices, we first compared the results of simulation on the basis of this model with experimental data for a number of two-island single-electron chains.

The results of calculations of the *I–V* characteristics for the first of the studied two-island structures based on the Au–Al_2O_3 film [12] are shown in Fig. 2a. Curve *1* corresponds to the experimental characteristic [12] obtained using a scanning tunneling microscope at a temperature T = 4.2 K. In this case, the insulating medium is aluminum oxide and the conducting islands are gold particles. Curve *2* represents the results of calculations performed according to the developed model,

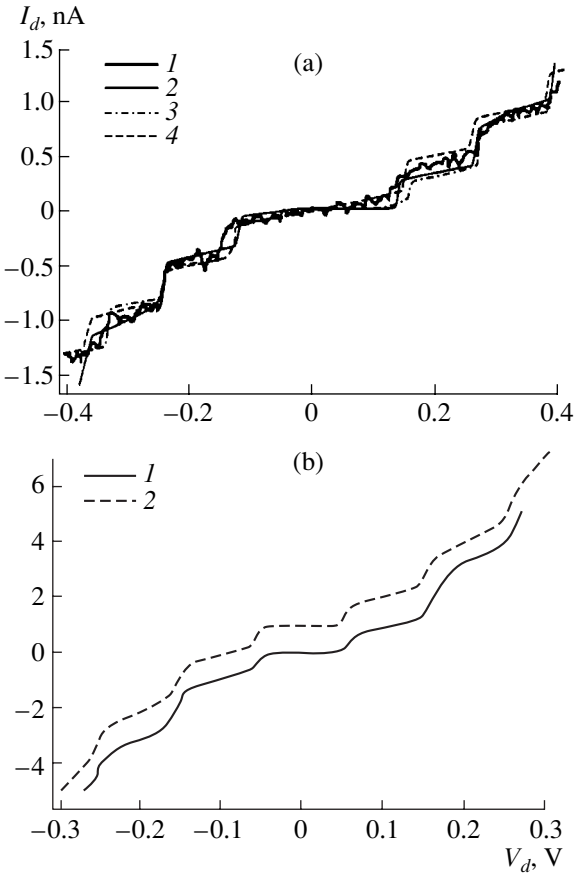

Fig. 2. Comparison of calculated *I–V* characteristics of two-island chains with experimental data. (a) A structure based on the Au–Al_2O_3 film: (*1*) experimental data [12]; (*2*) the results of calculations based on the developed model; (*3*) calculations based on a semiclassical model [12]; and (*4*) calculations based on the MOSES software package [13]. (b) A structure based on the $TlBa_2(Ca_{0.8}Y_{0.2})Cu_2O_7$ film: (*1*) experimental data [14] and (*2*) the results of calculations based on the developed model (for the sake of clarity, curve *2* is shifted upward by 1 nA).

curve *3* corresponds to the calculations using the semiclassical model [12], and curve *4* represents the results of calculations carried out using the MOSES program based on the Monte Carlo method [13]. It follows from Fig. 2a that all three models of the semiclassical approach make it possible to obtain satisfactory agreement with the experiment for the chain under consideration. However, it is appropriate to use the suggested model for calculating the *I–V* characteristic of two-island single-electron chains since, in this case, this characteristic is more clearly related to the parameters of both the design and the material (see Section 4).

The results obtained using the suggested two-dimensional numerical model are also in good agreement with other known experimental data on two-island single-electron chains which are made from a number of materials and operate at various temperatures. As an example, Fig. 2b shows the *I–V* characteristics of a structure based on $TlBa_2(Ca_{0.8}Y_{0.2})Cu_2O_7$ film at T = 9.8 K. Note that the experimental data (curve *1*) obtained using a scanning tunneling microscope [14] and the results of calculations based on the suggested model (curve *2*) almost coincide (for the sake of clarity, curve *2* in Fig. 2b is shifted upward by 1 nA).

Results similar to those represented in Fig. 2 were obtained for a chain based on $Co_{36}Al_{22}O_{42}$ film [15] at a temperature of 300 K. It is noteworthy that the model used for calculations involved the third approach (see [10]) for the consideration of the background charge at the island. Specifically, we used a slightly modified formula (6) from [10]; i.e.,

$$F = \frac{k_f(N_{ti} + N_{0i})}{kL_{\text{char}}}, \qquad (6)$$

where N_{ti} and N_{0i} are the number of excess charge carriers involved in tunneling and in the formation of the background charge at the ith island (i = 1, 2), respectively; and k_f is the coefficient that ensures the fit of the results of calculations to experimental data. Other designations correspond to those used in [10]. We note that the parameter k_f was chosen to be the same for both islands in each of the analyzed structures.

Thus, the suggested model makes it possible to obtain adequate results of simulation in calculations of the *I–V* characteristics of two-island single-electron chains, which are made from a number of materials and operate at various temperatures (including 300 K).

4. RESULTS AND DISCUSSION

We performed calculations for two-island single-electron chains based on two different films; the results of these calculations were compared with the experimental data in Fig. 2. It is worth noting that values of all variable numerical-model parameters that ensured the best fit to experimental data for each structure were used in the calculations, the results of which are reported below. With such a choice of parameters, we may anticipate with a high degree of confidence that the results of a theoretical evaluation of the effects of the design and material parameters on the *I–V* characteristics of the two-island single-electron chains are trustworthy. We believe that the above fact is important since all known models of single-electron structures (including the model we suggested) include a number of variable parameters that are used to fit calculations to experiment; furthermore, this stage of simulation is unfortunately still far from being sophisticated.

In Fig. 3a, we show the *I–V* characteristics of a chain based on $TlBa_2(Ca_{0.8}Y_{0.2})Cu_2O_7$ film for $W_d = W_b$ = 1.0 nm and W_s = 1.5 nm (curve *1*). Figure 3b shows the corresponding characteristic for a chain based on Au–Al_2O_3 film (curve *1*); in this case, $W_d = W_s$ = 2.0 nm and W_b = 2.3 nm. The results of calculations with vari-

ation in the geometrical parameters of the chains are also shown in Figs. 3a and 3b.

Let us analyze the obtained data. For the $TlBa_2(Ca_{0.8}Y_{0.2})Cu_2O_7$-based structure (Fig. 3a), a slight increase in the width of the junction between the source and the second island W_s from 1.5 nm (curve *1*) to 1.55 nm (curve *2*) brings about an appreciable decrease in current (by ~30%). At the same time, variations in the widths of the other two junctions W_d (curve *3*) and W_b (curve *4*) leave the current almost unchanged (Fig. 3a). Similar behavior of the *I–V* characteristic is also observed for the $Au–Al_2O_3$-based structure (Fig. 3b). Thus, an increase in W_b from 2.3 nm (curve *1*) to 2.35 nm (curve 2) reduces the current by about 40%, whereas, if the parameters W_d and W_s are increased (curves *3*, *4*), the current varies insignificantly.

These results suggest that the current flowing through a single-electron chain is very sensitive to variations in the maximal width of the tunneling junction. This can be attributed to the fact that the current in the system is mostly governed by the penetrability (the probability of the tunneling of an electron through the potential barrier) of the widest junction. Tunneling through the other two junctions proceeds with a much higher efficiency; consequently, slight variations in the widths of the latter junctions do not affect the total current. However, a variation in the range of the Coulomb blockade (this can be clearly seen in Fig. 3a) is related to the redistribution of voltages across the tunneling junctions.

Consequently, in the fabrication of many-island (two-island) single-electron chains, it is necessary that the maximal tunneling junction width be carefully controlled, since it is this width which most profoundly affects the *I–V* characteristic.

In Fig. 4, we show a family of *I–V* characteristics for a $Au–Al_2O_3$ two-island single-electron chain for several values of background charge at the islands $Q_{0i} = eN_{0i}$. The values of the parameters N_{0i} were chosen in the range typical of single-electron structures, i.e., $-1/2 \le N_{0i} \le 1/2$. For the sake of clarity, the curves in Fig. 4 are shifted relative to each other. Calculations were performed for the widths of tunneling junctions $W_d = W_s =$ 2.0 nm and $W_b = 2.3$ nm at an operating temperature of $T = 0.01$ K. It can be seen from Fig. 4 that the characteristics can be appreciably transformed by variations in the pairs (N_{01}, N_{02}). In this situation, the range of the Coulomb blockade can change (this range is widest for $N_{01} = N_{02} = 0$); the width and height of the steps in the Coulomb staircase can also vary. In addition, recurrence of the characteristics is observed if even one of the values in the N_{01} and N_{02} pair differ by an integer (in this case, by unity). In particular, this is valid for the following pairs of characteristics: curves *1* and *7*, curves *2* and *6*, and curves *3* and *5*. The coincidence between the characteristics for the second and third

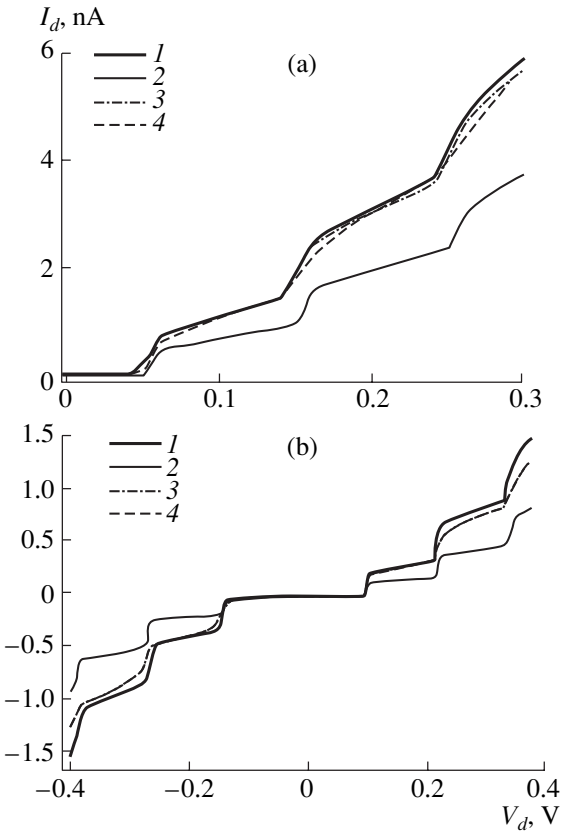

Fig. 3. The effect of widths of the tunnel junctions on the *I–V* characteristics of two-island chains. (a) A structure based on the $TlBa_2(Ca_{0.8}Y_{0.2})Cu_2O_7$ film: (*1*) fitting to the experiment, $W_d = W_b = 1.0$ nm and $W_s = 1.5$ nm; (*2*) $W_s =$ 1.55 nm; (*3*) $W_d = 1.1$ nm; and (*4*) $W_b = 1.1$ nm. (b) A structure based on the $Au–Al_2O_3$ film: (*1*) fitting to the experiment, $W_d = W_s = 2.0$ nm and $W_b = 2.3$ nm; (*2*) $W_b =$ 2.35 nm; (*3*) $W_d = 2.1$ nm; and (*4*) $W_s = 2.1$ nm.

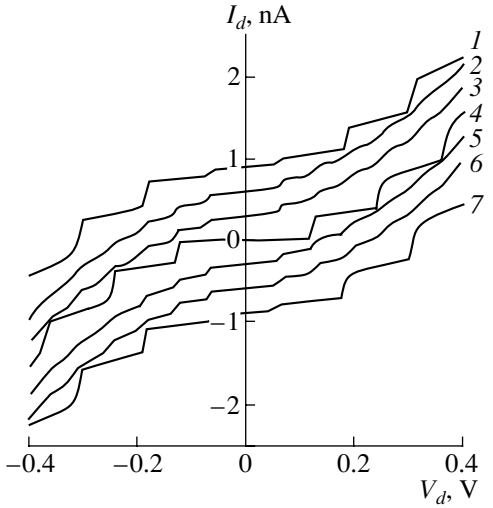

Fig. 4. The *I–V* characteristic of a two-island chain for several values of background charges (in elementary-charge units): (*1*) $Q_{01} = 0.5$ and $Q_{02} = 0.5$; (*2*) $Q_{01} = 0$ and $Q_{02} = 0.5$; (*3*) $Q_{01} = 0.5$ and $Q_{02} = 0$; (*4*) $Q_{01} = 0$ and $Q_{02} = 0$; (*5*) $Q_{01} = -0.5$ and $Q_{02} = 0$; (*6*) $Q_{01} = 0$ and $Q_{02} = -0.5$; and (*7*) $Q_{01} = -0.5$ and $Q_{02} = -0.5$.

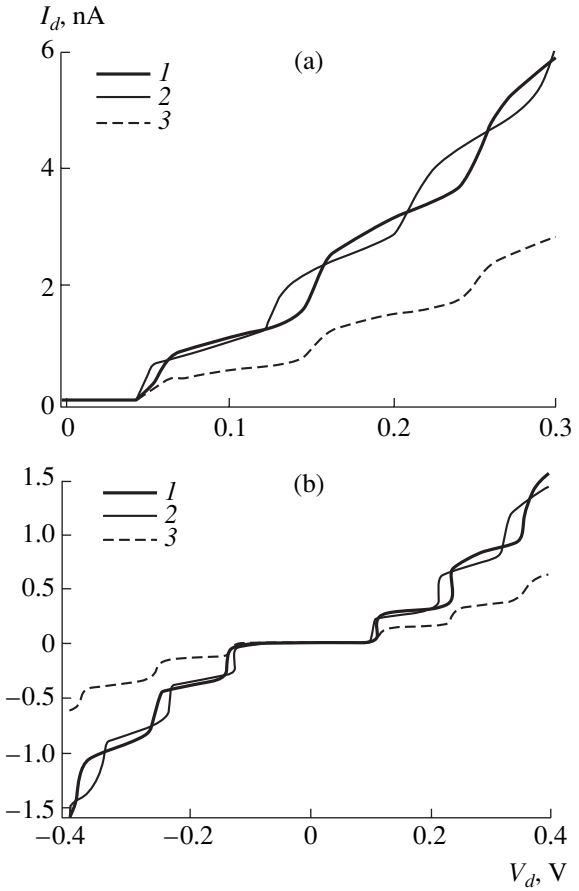

Fig. 5. Influence of material's electrical parameters (ε_d and ϕ) on the *I–V* characteristics of a two-island chain based on (a) the $TlBa_2(Ca_{0.8}Y_{0.2})Cu_2O_7$ film and (b) the Au–Al_2O_3 film. See the text for details.

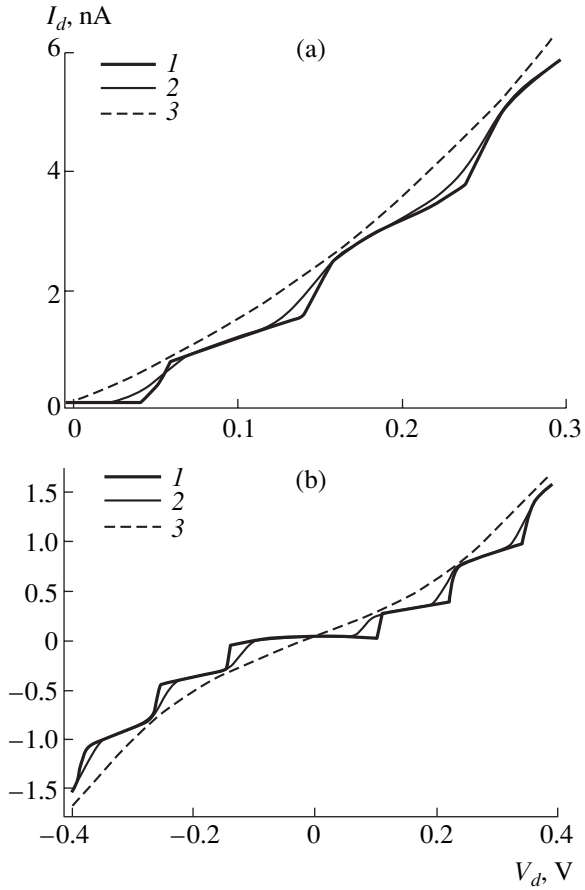

Fig. 6. The *I–V* characteristics of two-island single-electron chains based on (a) the $TlBa_2(Ca_{0.8}Y_{0.2})Cu_2O_7$ film and (b) the Au–Al_2O_3 film for several values of operating temperature: T = (*1*) 0.01, (*2*) 30, and (*3*) 300 K.

pairs is worth noting; in the case under consideration, this coincidence is caused by the symmetry of the chain (the islands are identical, so that $W_d = W_s$).

Thus, the calculations using the suggested numerical model showed that the shape of the *I–V* characteristic for two-island chains can vary appreciably as a result of changes in the background charge at the islands; this is completely consistent with the known data on a single-electron transistor [1].

The *I–V* characteristics of two-island single-electron chains were calculated using the suggested model and are shown in Fig. 5a for the $TlBa_2(Ca_{0.8}Y_{0.2})Cu_2O_7$-based structures and in Fig. 5b for the Au–Al_2O_3-based structures; two electrical parameters, i.e., the potential barrier heights of tunneling junctions ϕ and the relative permittivity of the insulator ε_d, were slightly varied. It is noteworthy that a possible variation in the aforementioned parameters of the material is characteristic of the insulating layers under consideration. The operating temperature was chosen to be 0.01 K. It can be seen from Fig. 5a that the increase in ϕ from 1.0 eV (curve *1*) to 1.1 eV (curve *3*) brings about an appreciable decrease in the current flowing through the structure (by about a factor of 2). It follows from Fig. 5b that the increase in ϕ from 1.65 eV (curve *1*) to 1.75 eV (curve *3*) leads to a similar decrease in the current through the second structure (by about a factor of 2.5). This tendency can be explained by the fact that an increase in the potential-barrier height reduces the probability of electron tunneling through this barrier and, consequently, reduces the current through the structure. It is worth noting that the Coulomb blockade range and the step width in the Coulomb staircase remained virtually unchanged.

Consequently, the potential-barrier heights in the tunneling junctions in single-electron chains affect the currents to a no lesser extent than does the tunneling-junction width characterized by a maximal value.

At the same time, an increase in ε_d from 5 (curve *1*) to 6 (curve *2*) in Fig. 5a and from 9 (curve *1*) to 10 (curve *2*) in Fig. 5b gives rise to only a slight variation in the current. However, it is noteworthy that a decrease in the range of the Coulomb blockade and in the step width are observed as the relative permittivity ε_d

increases. This can be attributed to the redistribution of voltages across the tunneling junctions.

Thus, a variation in the relative permittivity of the insulator brings about a transformation in the shape of the *I–V* characteristic; in particular, this variation leads to changes in the range of the Coulomb blockade and in the step width.

We also calculated the *I–V* characteristics of two-island single-electron chains based on $TlBa_2(Ca_{0.8}Y_{0.2})Cu_2O_7$ (Fig. 6a) and $Au–Al_2O_3$ (Fig. 6b) in relation to the operating temperature: $T = 0.01$, 30, and 300 K. It can be seen that an increase in temperature also causes the shape of the *I–V* characteristic to transform. However, in this case, the Coulomb staircase becomes smoothed and the phenomenon of single-electron tunneling disappears. These results are also consistent with known data on single-electron structures [1].

5. CONCLUSION

We developed a two-dimensional model for many-island (two-island) single-electron chains of tunnel junctions. This model makes it possible to obtain good agreement between the results of calculations and experimental data and predict the behavior of the *I–V* characteristics of these chains in relation to the material and design parameters. Using this model, we showed that the *I–V* characteristics of two-island chains are very sensitive to variations in the maximal width of the tunnel junction and in the potential barrier height of the insulator. Variations in the background charges at the islands, the relative permittivity of the insulator, and the operating temperature lead to diverse transformations of the *I–V* characteristics.

ACKNOWLEDGMENTS

We would like to thank A.N. Korotkov for his helpful comments concerning our model.

This study was supported in part by the Belarussian research programs “Electronics” and “Nanoelectronics” and by a grant from the Ministry of Education of the Republic of Belarus.

REFERENCES

1. *Single Charge Tunneling: Coulomb Blockade Phenomena in Nanostructures*, Ed. by H. Grabert and M. H. Devoret (Plenum, New York, 1992), NATO ASI Ser., Ser. B: Phys., Vol. 294.
2. I. I. Abramov and E. G. Novik, Fiz. Tekh. Poluprovodn. (St. Petersburg) **33** (11), 1388 (1999) [Semiconductors **33**, 1254 (1999)].
3. K. Nakazato, R. J. Blaikie, and H. Ahmed, J. Appl. Phys. **75** (10), 5123 (1994).
4. K. K. Likharev, Proc. IEEE **87**, 606 (1999).
5. A. Thean and J. P. Leburton, IEEE Electron. Device Lett. **22** (3), 148 (2001).
6. N. S. Bakhvalov, G. S. Kazacha, K. K. Likharev, and S. I. Serdyukova, Zh. Éksp. Teor. Fiz. **95** (3), 1010 (1989) [Sov. Phys. JETP **68**, 581 (1989)].
7. R. H. Chen, A. N. Korotkov, and K. K. Likharev, Appl. Phys. Lett. **68** (14), 1954 (1996).
8. I. I. Abramov and E. G. Novik, Fiz. Tekh. Poluprovodn. (St. Petersburg) **34** (8), 1014 (2000) [Semiconductors **34**, 975 (2000)].
9. I. I. Abramov and E. G. Novik, *Numerical Simulation of Metallic Single-Electron Transistors* (Bestprint, Minsk, 2000).
10. I. I. Abramov and E. G. Novik, Fiz. Tekh. Poluprovodn. (St. Petersburg) **35** (4), 489 (2001) [Semiconductors **35**, 474 (2001)].
11. V. M. Verzhbitskiĭ, *Numerical Methods (Linear Algebra and Nonlinear Equations)* (Vysshaya Shkola, Moscow, 2000).
12. E. Bar-Sadeh, Y. Goldstein, M. Wolovelsky, *et al.*, J. Vac. Sci. Technol. B **13** (3), 1084 (1995).
13. R. H. Chen and K. K. Likharev, Appl. Phys. Lett. **72** (1), 61 (1998).
14. T. G. Miller and R. Reifenberger, Phys. Rev. B **50**, 3342 (1994).
15. H. Imamura, J. Chiba, S. Mitani, *et al.*, Phys. Rev. B **61** (1), 46 (2000).

Translated by A. Spitsyn